A FOCUSED STUDY OF FUNDAMENTAL & FUNCTIONAL MATERIALS USING BEAMLINE TECHNIQUES TO INVESTIGATE MAGNETIC AND CRYSTAL STRUCTURE INTERACTIONS

by

ROBERT ARNOLD

A thesis submitted to
The University of Birmingham
for the degree of
DOCTOR OF PHILOSOPHY

School of Metallurgy and Materials
College of Engineering and Physical Sciences
The University of Birmingham
February 2021

Abstract

The development of functional materials is often built upon a cornerstone of knowledge provided by study of the underlying physics in more fundamental materials - understanding mechanisms and causality can pave the way to optimisation of application. Large scale beamline facilities offer unique opportunities to probe length scales and structures outside the remit of traditional laboratory equipment. Here, a two part study into magnetostrictive materials is presented - a small-angle neutron scattering study of $Fe_{68.8}Pd_{31.2}$ and a synchrotron X-ray diffraction study of $Tb_{1-x}Dy_xFe_2$ alloys. For iron-palladium, the results confirm the transition temperature from face centred cubic to face centred tetragonal and highlight a peculiarly high degree of scattering for the latter, hypothesised to arise from enhanced magnetisation. Furthermore details of an anisotropy along the [110] directions is shown, alongside the presentation of the physical sizes of the underlying scattering feature, before finally showing evidence for a direction sensitive high field, nanoscale feature. Morphotropic phase boundaries, composition and temperature sensitive dividing regions between tetragonal and rhombohedral phases, are found to be linked to physical property enhancement for a range of functional materials. This diffraction study, performed for a range of $Tb_{1-x}Dy_xFe_2$ samples with $0.56<x<0.87$, produces an expanded phase diagram, which shows the morphotropic phase boundary is rapidly fluctuating with sample composition, while also providing clear information regarding the makeup of the morphotropic phase boundary. The high temperature measurements show a slow melting toward 'cubic-like' reflection behaviour, likely caused by a reduction in lattice distortion, consequently decreasing the degree of peak splitting below that which is detectable. Lastly, evidence is presented for the discovery of a low temperature, low symmetry phase which is found to coexist with the rhombohedral phase at temperatures below 100 K.

In loving memory of Tony Arnold

Acknowledgements

I would like to start by expressing my most gracious of thanks to Dr Richard Sheridan, Dr Biao Cai and Dr Mark Laver - your expertise, patience and guidance are unfathomable and incredibly appreciated. I must give particular praise to Dr Sheridan who was instrumental in the final phase of this Doctorate, where his moral support, timely comments and positive attitude never failed to inspire.

To my colleagues and collaborators throughout this journey who have made the long days and sleepless nights filled with joy, you are unfortunately too numerous to mention by name! However please know that your contributions over the last few years, whether they were professional or otherwise (some names in particular come to mind there), are not forgotten. One set of extreme thanks has to go to my friends, who arguably all deserve an individual acknowledgement. From my colleagues in 1B20 who have had to cope with my endless holding of *Office Meetings*, my school comrades that have been with me throughout the entirety of my academic journey and to great friends I have made in recent years, words will never do justice my appreciation for your companionship.

Final praise must go to my immediate family: my mother Frances, brothers Ant & Phil, their partners Kyley & Claire, and my seven fantastic nephews & nieces, all of whom have had to cope with the ups and downs of the last four years. Your love, support and nurturing will last a lifetime. In its entirety, this thesis is dedicated to my father, who unfortunately passed away during its completion. Tony Arnold was the greatest dad I could dream of and it is without question that the knowledge and wisdom he bestowed to me, will forever eclipse any other.

Contents

Commonly Used Abbreviations

AFM	Antiferromagnetism
E	Electric field
FePd	$Fe_{68.8}Pd_{31.2}$
FM	Ferromagnetism
FSMA	Ferromagnetic shape memory alloy
FWHM	Full width at half maximum
H	Applied magnetic field
$\mathbf{H}_{C}$	Coercivity
$\mathbf{H}_{Sat}$	Saturating field
$\boldsymbol{K}$	Anisotropy constant
M	Magnetisation
$\mathbf{M}_{Sat}$	Saturation magnetisation
MCA	Magnetocrystalline anisotropy
MPB	Morphotropic phase boundary
PM	Paramagnetism
PMT	Pre-martensitic tweed
P	Polarisation
ppm	Parts per million
PZT	Lead zirconate titanate
$\boldsymbol{q}$	Scattering vector
RE	Rare-earth
SANS	Small-angle neutron scattering
sXRD	Synchrotron X-ray diffraction
T	Absolute temperature
$\mathbf{T}_{C}$	Curie temperature
Terfenol-D	$Tb_{0.27}Dy_{0.73}Fe_{2}$
TM	Transition metal
$\boldsymbol{\lambda}$	Strain
$\boldsymbol{\chi}$	Susceptibility

Chapter 1

Introduction

Advancements in scientific research have always provided a groundbreaking forefront upon which functional materials and systems can be developed. The advent of the current technological age has been driven by continued alloy development and research in decades past. Modern day functional materials are almost always within reach, whether this is loudspeakers in mobile phones, motors in recliner chairs or haptic feedback on smart watches, functional materials are more deeply entrenched in society today than they have ever been.[1–4] While functional materials are now a cornerstone of technology, it would be criminal to understate the importance of materials past, systems within which pivotal research has been performed to determine the underlying fundamental science which has allowed for the creation of optimised functional materials.

Producing complex and desirable responses (such as piezoelectricity[5–7] magnetostriction[8–10] or magnetoresistance[11,12]) requires a thorough understanding of the material system, the externally controlled behaviour and the complex interactions which govern the physical properties. Often the key to unlocking the optimised properties of a certain material system relies either on knowledge of precursor materials, as is the case for Terfenol-D ($Tb_{0.27}Dy_{0.73}Fe_2$) where knowledge of simple binary rare-earth/transition metal alloys ($TbFe_2$, $DyFe_2$, etc) provided suggestions for optimisation, or on the narrowed study of particular phenomena such as in $Fe_{68.8}Pd_{31.2}$ where the changing landscape of coexisting phases produces intriguing magnetic and crystal structure interactions.

The materials investigated within this thesis can be split into two categories - namely 'fundamental' and 'functional' materials. Fundamental materials are those which are limited in their application potential (often due to the need for liquid helium temperatures) but provide an excellent base from which to investigate their contained phenomena. Conversely, 'functional' is used to describe materials which have direct application potential. However, applied does not necessarily mean that they are completely understood and there is clearly further optimisation to be completed, particularly as the drive towards green technology and electrification will serve as impetus for both creation of new materials and improvement of old systems.

Table 1.1: Summary of the materials investigated and their categorisation.

Fundamental	$Fe_{68.8}Pd_{31.2}$
Functional	$Tb_{1-x}Dy_xFe_2$

Iron-palladium is a binary alloy which exhibits isotropic, hysteresis-free magnetisation and contains a nanoscale structure of twin clusters that can adapt their topography to minimise magnetic anisotropy, until a point at which they are overwhelmed and coalesce, resulting in a phase change that generates significantly higher values of magnetostriction.[13] $Tb_{1-x}Dy_xFe_2$ alloys are among the market leaders for magnetostrictive materials, generating large values of low coercivity strain at room temperature. Terfenol-D refers to a composition of $Tb_{0.27}Dy_{0.73}Fe_2$ and this delicate balance of the rare-earth (RE) elements creates an ideal material for room temperature application, where the presence of a morphotropic phase boundary (MPB) is suggested to be the cause of enhanced physical properties.[14] A function of both temperature and composition, morphotropic phase boundaries separate phase regions of specifically different symmetries, commonly tetragonal and rhombohedral, and tend to coincide with enhancement of desirable physical properties[15, 16] - this phenomena will be explored further in Chapter 5.

The continued investigation into both fundamental and functional materials is cardinal. For fundamental materials, further exploration of the underlying physics is crucial to the development of future materials and although already studied at length, the scrutiny of functional materials should not be discouraged despite their application prowess. Clearly, as new breakthroughs are made these can always inform previous research, which in turn will drive subsequent research.

Recent decades have seen the advent and widespread use of large-scale facilities for beamline scattering techniques such as small-angle neutron scattering and synchrotron X-ray diffraction. These complex techniques provide a large range of measurement options and the ability to probe otherwise difficult to study systems.[17,18] While neutrons and X-rays provide inherently different characterisation options, the ingenuity and innovation of the scientific community has helped to diversify the portfolio of beamline facilities. Beamline characterisation has a prominent foothold within the magnetic physics and materials science communities, although its use in other fields such as biology, geology and condensed matter is not to be trivialised.[19–21]

Since its discovery in the mid-19th century by James Joule, magnetostriction has been an ever-present phenomena for study due to the large range of application potential magnetostrictive materials have. Materials which exhibit magnetostriction are found to show a change in length when under the influence of an externally applied magnetic field.[22] This conversion of magnetic energy to kinetic (and vice versa) was identified to have huge application potential, and alongside piezoelectric materials, which convert mechanical energy to electrical energy and vice versa, magnetostrictive materials fulfil a large demand for functional materials. The ideal magnetostrictive material would have: low coercivity, magnetocrystalline anisotropy and saturating field, such as to easily turn 'on' and 'off' the length change, as well as high strain. The evolution of magnetostrictive applications has continued to develop over time with sensors, transducers, oscillators and actuators all now firmly part of the magnetostrictive market.[23] To facilitate these differing applications, there has been a natural growth in magnetostrictive materials created and optimised for application - among these materials sits Terfenol-D.

Discovered by the US Naval Ordnance Laboratory in the 1970's as a product of the alloying of rare-earth and transition metal (TM) elements,[24] Terfenol-D showed immediate promise due to its extremely high values of exhibited strain but was hindered due to the brittle nature of the rare-earth/transition metal alloy - the low fracture toughness meant that its operational temperature range was fairly fine to avoid critical failure.[25] Deriving from the family of rare-earth/transition metal alloys (RE-TM_2), $Tb_{0.27}Dy_{0.73}Fe_2$ was found to be a uniquely desirable composition that achieved high values of strain (for moderate values of applied field) and large energy density while also minimising the magnetocrystalline anisotropy of the alloy. Following optimisation of the manufacturing process in the 1980's,[25] specifically the move to larger scale crystal growth methods such as floating zone and sintered powder compacts, which reduced but did not completely address the problem of inherent brittleness, Terfenol-D went on to become the dominant magnetostrictive material for application purposes.

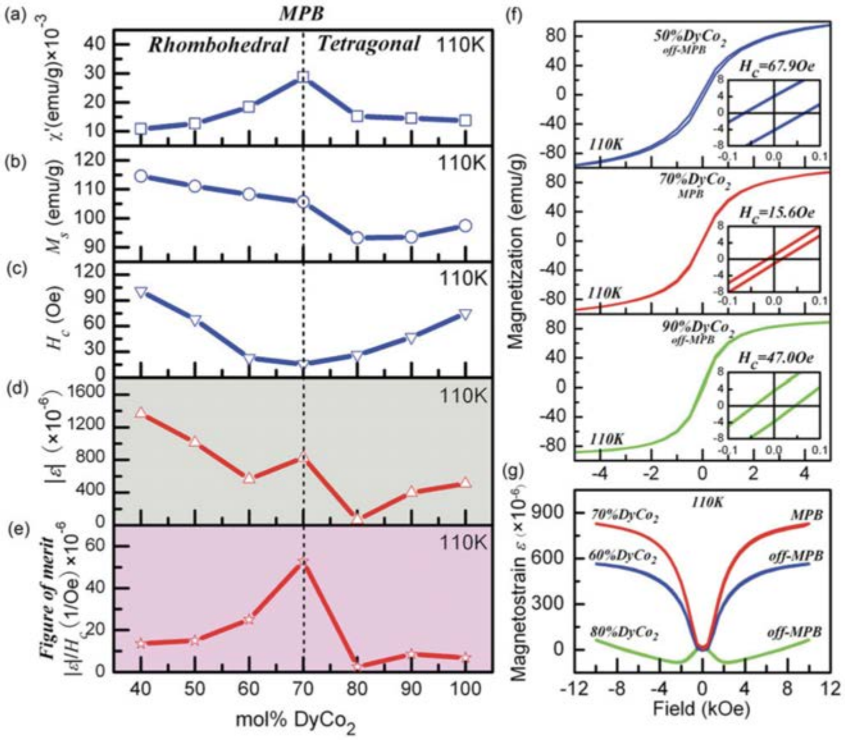

Figure 1.1: Physical property measurements of $TbCo_2$-$DyCo_2$ performed at 110K for a range of compositions centred around the MPB position. The figure of merit in e is used as a measure of optimisation based on the desire for low coercivity but high strain.[26]

The functional optimisation of the ferroic class of materials is maximised around morphotropic phase boundaries, with some of the current choice materials for applications employing such enhancement.[27] The short barrier between the opposing symmetries is effectively an elastic region, where lattice constants are enhanced or "softened". For materials such as piezoelectric and magnetostrictive materials, this elastic region aids in material function and application,[28] where the aforementioned enhanced lattice constants yield greater physical responses (polarisation, magnetostriction, etc) for the same values of applied field. Figure 1.1 summarises some physical property measurements performed on $Tb_{1-x}Dy_xCo_2$, a very similar compound which also exhibits an MPB. It has been found in this material, and others, that there is a maximisation of physical properties. This maximisation is represented by a figure of merit (e), derived from a minima in coercive field (c) and a local peak in strain (d), at the MPB composition. An extension of this is that there are clearly different magnetisation responses either side of the MPB, suggesting that the interplay is fine and the composition control must be thorough and well documented to achieve ideal optimisation.

It has previously been determined that the Terfenol-D composition, $Tb_{0.27}Dy_{0.73}Fe_2$, coincides with the presence of a morphotropic phase boundary between the parent phases of $TbFe_2$ and $DyFe_2$ at room temperature. Figure 1.2 shows the current MPB mapping within $Tb_{1-x}Dy_xFe_2$ alloys and combines various measurement techniques, with the synchrotron results most clearly showing the MPB position and width as a function of composition and field.[29] While enhancement of physical properties (such as strain and polarisation in magnetostrictive and ferroelectric materials respectively) is well known to occur around MPBs, the underlying physics that cause such an enhancement have not been widely studied. Furthermore, the nature of MPBs is continually up for discussion with some classes of materials exhibiting maximum enhancement on the MPB,[30] while others (including Terfenol-D) seem to achieve this 'around' the MPB. This infers that the type of material interactions affect the nature of the MPB, which is further supported by the evidence that the MPB width will change as a function of temperature.[31]

Ascertaining the mechanism for enhancement of physical properties within $Tb_{1-x}Dy_xFe_2$ is of keen interest for the future development of magnetostrictive materials and other ferroic responsive materials. Increased understanding of the nature of MPBs will open the

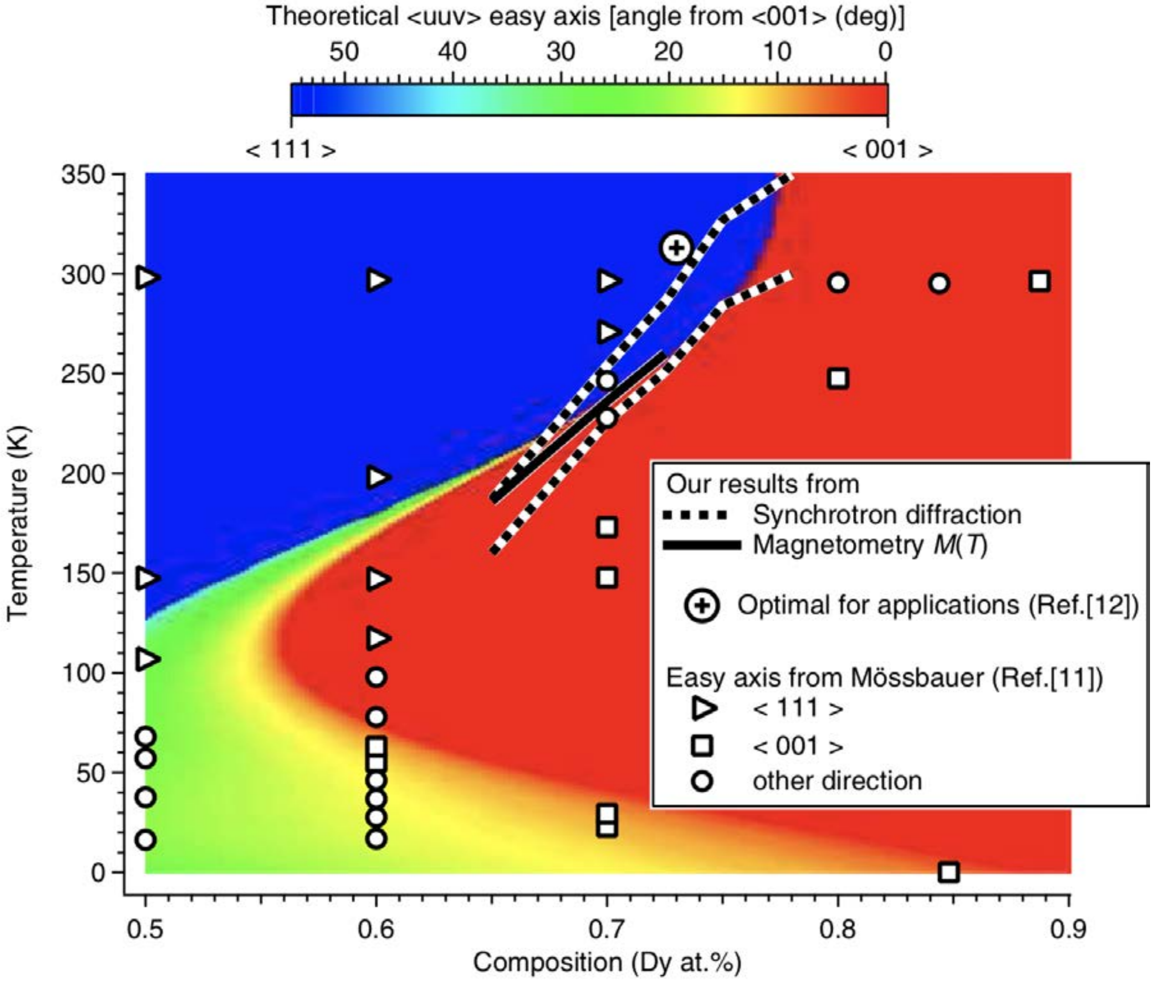

Figure 1.2: Synchrotron diffraction and magnetometry results showing the MPB position for varying compositions of Terfenol-D.[29] References 11 and 12 mentioned in the figure are [32] and [33] respectively.

door for compositional control of prototype materials, where the composition can be chosen to coincide with the MPB position and therefore achieve enhancement with minimal changes to the manufacturing process. Furthermore, the effect of temperature on MPB positions can offer an insight into the development of high temperature magnetostrictive materials, where the magnetic properties are negatively impacted by thermal fluctuations and therefore there is a strong desire to maximise the strain properties under field.

An induced change to the phase structure is also integral to the increased magnetostriction seen in $Fe_{68.8}Pd_{31.2}$. This ferromagnetic shape memory alloy exhibits considerable magnetostriction at temperatures not significantly below room temperature, showing strains on the order of 500 parts per million (10^{-6}) for single crystals (for comparison, market leading Terfenol-D used under load can reach strains of 2000 ppm[34]). The increase in strain with reducing temperature is due to an adaptive phase change to a martensitic, or twinned, structure.[35] The aforementioned phase change involves the coalescing of twin clusters, which exist as a nanoscale secondary phase at room temperature. This transition, mediated by the shifting dominance of primary and secondary phases, shows some similarities to morphotropic phase boundaries where the physical make-up of the MPB has yet to be fully determined.

1.1 Aims and Objectives

This thesis recounts a broad study of the magnetic and crystal structure interactions in the previously mentioned 'fundamental' and 'functional' materials. Beginning with background information on magnetism and its relationship to macroscopic magnetic phenomena (magnetostriction and the shape-memory effect), the current state of research on the fundamental material iron-palladium is presented. Subsequently, Terfenol-D alloys and the current knowledge on MPBs within them will be detailed, before an in-depth breakdown of the experimental methodology is outlined. Ending this thesis will be the results and findings, presented in separate chapters for the differing material groups, along with the discussion on these and their importance for future research. Finally, there will be a conclusion and summary to the thesis, which will also outline the next logical steps for research and suggestions for future work.

The main goal of this work is to improve and cement understanding of the suspected phenomena which arise within iron-palladium and $Tb_{1-x}Dy_xFe_2$ alloys, with a long term goal to help elucidate the maximum application potential for these intriguing compounds. By increasing the knowledge base of the underlying mechanisms and interactions, the future application potential for all functional materials is augmented. Experimentation was performed using a variety of beamline techniques, namely small-angle neutron scattering and high resolution X-ray diffraction, utilising the full range of sample environment and analytical options available.

Specifically, this will be achieved through a comprehensive reciprocal space study on a range of $Tb_{1-x}Dy_xFe_2$ alloys and $Fe_{68.8}Pd_{31.2}$ single crystal samples. As well as further mapping the position of the MPB within the phase diagram of the $Tb_{1-x}Dy_xFe_2$ alloy system, the nature of the MPB shall be determined, while the potential existence of other phases with non-trivial easy axis directions is also investigated. Iron-palladium has an intriguing magnetic response, with behaviour changing rapidly as a function of both temperature and applied magnetic field - these properties attract a desire to determine the cause of such features, likely arising on the nano length scale.

Main objectives for this thesis are to:

- Perform a comprehensive small-angle neutron scattering study of $Fe_{68.8}Pd_{31.2}$ to investigate the effects of temperature and field on the micro- and nano-scopic features.
- Use the arc melting facilities at the University of Birmingham to fabricate a range of $Tb_{1-x}Dy_xFe_2$ alloys, with approximate range $0.5 < x < 0.8$.
- Investigate the potential existence of a low symmetry phase in $Tb_{1-x}Dy_xFe_2$ alloys by performing a synchrotron X-ray diffraction experiment.
- Study the presence, structure and phase composition of the morphotropic phase boundary within $Tb_{1-x}Dy_xFe_2$ alloys.

Chapter 2

Magnetism & Magnetostriction

In this chapter the theory of magnetism is detailed, beginning with a discussion of the various underlying anisotropy constants which determine a material's magnetic response. Following this, the fundamentals of the different forms of magnetism are detailed before finishing with a comprehensive explanation of the magnetostriction phenomena.

2.1 Magnetic anisotropy

Isotropy comes from the Greek 'iso', meaning equal, and 'tropos', meaning turn. Anisotropy is now commonly used to describe systems within which there is a directional bias. The origin of anisotropy is complex, deriving from a combination of individual anisotropic parameters, all of which are entirely dependent on the system in question.

2.1.1 Magnetocrystalline anisotropy

Magnetocrystalline anisotropy (MCA), sometimes referred to simply as magnetic anisotropy, is the relationship between magnetisation and a specific crystal direction within a lattice. Arising from the spin-orbit coupling, the interaction between the spin and angular momentum of an orbiting electron, MCA is an inherent property of ferromagnetic materials, being effectively a measure of the minimum energy to drive the magnetic moment from the easy to hard directions in a single crystal.[36] Measurement of this anisotropy is achieved by performing magnetisation curves along these different directions, as seen in Figure 2.1 for iron. Given the cubic nature of iron, the saturation magnetisation is the same in all directions with the only change being the amount of field necessary to achieve saturation. In non-cubic materials, such as Co, the MCA is significantly stronger in the c-axis than the others, leading to a noticeably different magnetisation behaviour for that specific direction.[37] More specifically, the c-axis is the hard axis and it requires large values of saturating field to drive the magnetisation to either of the basal, or easy, axes. When considering MCA, the energy density (E/V), or energy (E) per unit volume (V), of the system can be described by a sequence of anisotropy constants, K, and the respective angles within the crystal systems. Equations 2.1, 2.2 and 2.3 show the energy density for cubic, tetragonal and rhombohedral systems respectively,[38] where θ is the angle between magnetisation and c (or long) axis, ϕ is the azimuthal angle, $\alpha = cos\phi sin\theta$, $\beta = sin\phi sin\theta$ and $\gamma = cos\theta$. It should be noted that the K_3 anisotropy constant is not included in the cubic example because higher order powers are often negligible in cubic materials - in fact, it is not uncommon for K_2 to also be insignificant and therefore be ignored.

$$\frac{E}{V} = K_1(\alpha^2\beta^2 + \beta^2\gamma^2 + \gamma^2\alpha^2) + K_2\alpha^2\beta^2\gamma^2 \tag{2.1}$$

$$\frac{E}{V} = K_1 sin^2\theta + K_2 sin^4\theta + K_3 sin^4\theta\, sin2\phi \tag{2.2}$$

$$\frac{E}{V} = K_1 sin^2\theta + K_2 sin^4\theta + K_3 cos\theta\, sin^3\theta\, cos3\phi \tag{2.3}$$

It will soon be discussed how magnetisation is inversely related to temperature, in that magnetisation increases as system temperature approaches absolute zero, see Chapter 2.2.1. Additionally, the anisotropy constants can also vary with temperature meaning that magnetocrystalline anisotropy, and therefore the magnetostriction of the material, will not necessarily follow the path of the magnetisation with respect to temperature.[40,41] Figure 2.2 shows how the bulk anisotropy constants in $DyFe_2$ can vary as a function of temperature. T_C is the Curie temperature below which materials begin exhibiting ferromagnetism and will be expanded upon in Chapter 2.2.2. It is clear to see that the magnitudes of these constants are at their peaks when T/T_C approaches zero, implying

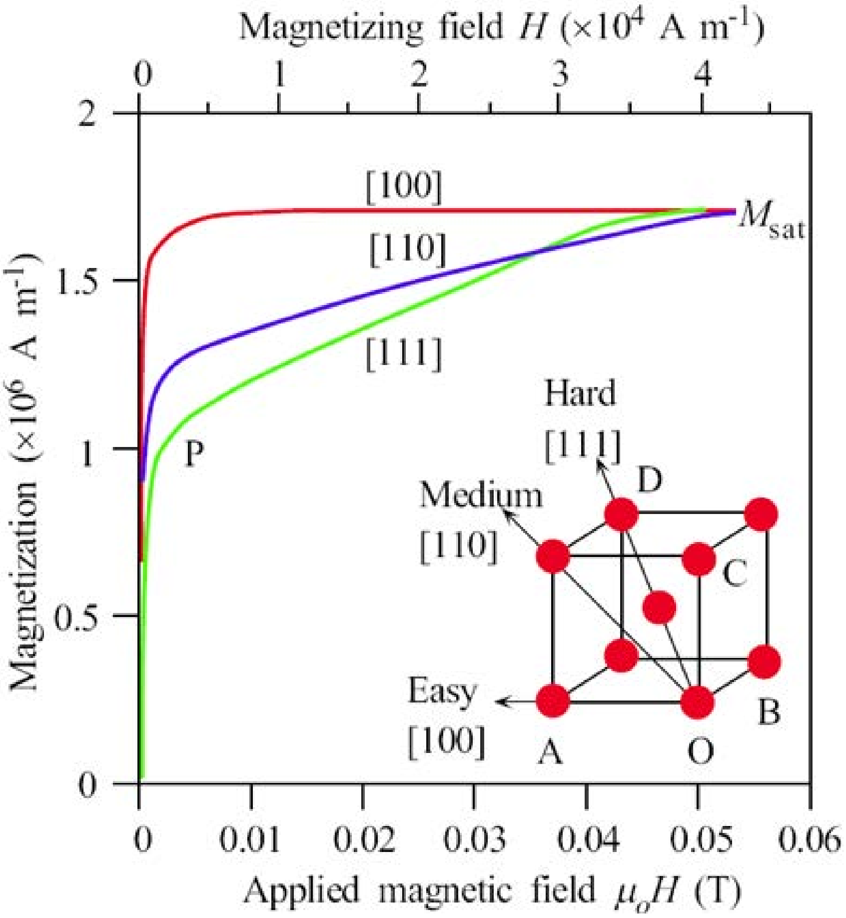

Figure 2.1: Representation of magnetocrystalline anisotropy in a single crystal of iron, showing that the saturating field is significantly larger for the [111] hard direction than for the [100] easy direction.[39]

that in general higher values of MCA are expected at lower temperatures. However, one can also see that there is a sign dependancy associated with these elastic constants as well, of which can also be switched as a function of temperature.

This dependence on temperature will complicate the picture around structural transitions, especially so in Terfenol-D, where it has been found that reducing the temperature to -21 °C increased the field required to reach the strain saturation, λ_S, with a positive slope remaining at 500 kA/m. At this field, saturation had been reached at 0 °C.[43] Figure 2.3 shows this data, which suggests that while the saturation magnetostriction may increase, so will the magnetocrystalline anisotropy - unfortunately creating a balance problem between performance and ease of use.

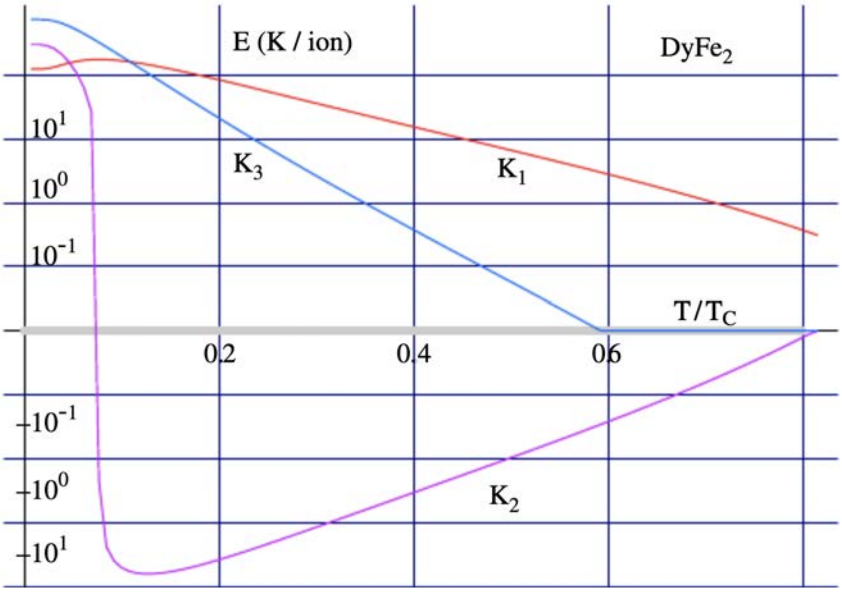

Figure 2.2: Calculated measurements of bulk anisotropy constants in DyFe$_2$ as a function of temperature.[42] Calculations are a second-order extension of the Callen-Callen model.

2.1.2 Shape anisotropy

Shape anisotropy is a direct competitor for anisotropy domination with magnetocrystalline anisotropy. Shape anisotropy heavily favours in-plane magnetism, such as that demonstrated by thin films, where the magnetostatic energy is favoured when the dipoles are orientated along the internuclear axes, as opposed to perpendicular to them.[44] Shape anisotropy is heavily controlled by the macroscopic physical shape of a material. Shape anisotropy is composed of three components: one from dipoles on fixed lattice positions within a spherical volume, another from pseudo-charges on the surface of said assumed sphere and a final macroscopic contribution birthed from the demagnetising field. The demagnetising field is itself controlled by the geometry and characteristics of the external sample surface, in that non-spherical samples will have a demagnetising field that allows for certain easy axes of magnetisation.[45] The strength of the demagnetising field is generally an order of magnitude (or more) bigger than the sum of the microscopic contributions, therefore it can be said that shape anisotropy is heavily dependent on the physical geometry of the sample. As previously mentioned shape anisotropy dominates for thin film samples, whereas magnetocrystalline anisotropy will dominate for layered

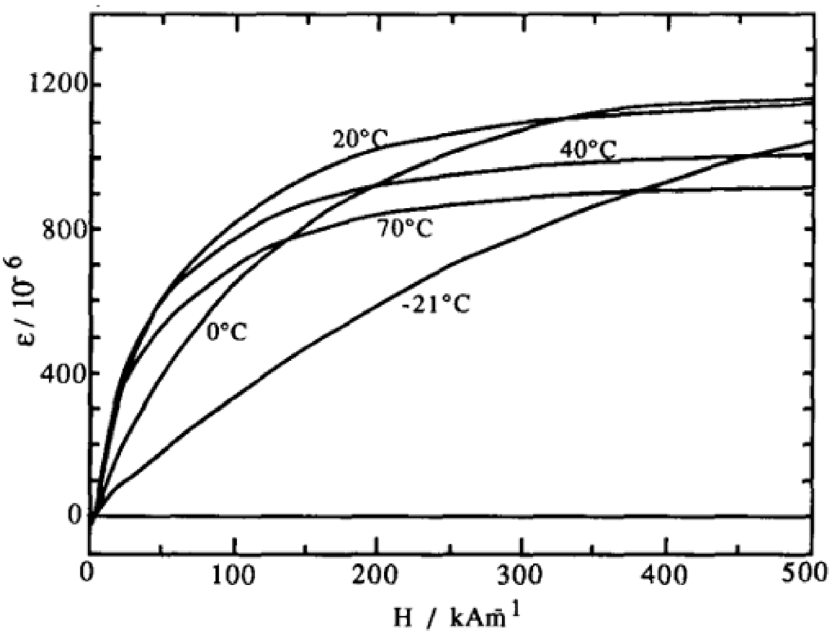

Figure 2.3: Magnetostriction of $Tb_{0.27}Dy_{0.73}Fe_{1.90}$ as a function of applied field, across a variety of temperatures.[43]

samples which are typically alternating layers of magnetic and non-magnetic material.[46] So called 'magnetic multilayers' have vast application potential for magnetic reading devices, magnetoresistive sensors and utilisation in future applications may lead to their deployment in fields such as spintronics.

2.1.3 Stress anisotropy

The most situationally dependent of the anisotropies mentioned, the application of a uniaxial stress can significantly alter the magnetic response of a material. Sufficient application of stress, can 'force' an easy axis of magnetisation onto a sample therefore yielding more desirable magnetisation properties in that direction.[47,48] It should be noted that the degree of stress applied is material dependent and would need to be significant enough to overcome the other anisotropies discussed.

While slightly outside the scope of this thesis, it is important to mention the role that stress anisotropy plays in the Villari effect, which is often considered to be inverse magnetostriction. As will be discussed in Section 2.3, magnetostriction is the induction of strain due to a change in magnetisation. Conversely, the Villari effect is the changing of the magnetisation due to the application of an external stress. Studies of the Villari effect determined that within cubic materials, all magnetisation axes are formed by combinations of the standard easy and hard axes for cubic materials, namely [001] and [111].[49, 50]

2.2 Magnetism

When discussing the origin of ferromagnetism, it is first important to discuss the inherent properties of electrons through which magnetism is itself birthing. Electrons carry a half-integer spin which can be simplified to exist in either an 'up' or 'down' state.[51] When filling the electronic structure of atoms, electrons will follow Hund's first rule. Pauli exclusion principle, the phenomenon that two electrons cannot be identical (in that they share quantum numbers), informs that a maximum of two electrons can exist in a single electron orbital.[52] Hund's first rule follows this, proving that the ground state is the one with the largest spin. Therefore, when one considers the filling of electron orbitals, it is energetically favourable to maximise the spin, more specifically, by half-filling each orbital before then pairing spin up and spin down electrons, therefore yielding a net zero spin and increasing the system energy.[53] In reality, this is a simplification of the complex interactions happening within the atom.

2.2.1 Paramagnetism (PM)

For all materials, the application of an external magnetic field, H, will induce a change in the magnetisation, M, of the material in question. Materials can be grouped based on their magnetic response to this applied field. The degree of magnetisation generated for a fixed applied field, is dependant on the material parameter, χ, which is the volume magnetic susceptibility. Susceptibility is a dimensionless constant which links the applied field and magnetisation.[54]

$$\boldsymbol{M} = \chi \boldsymbol{H} \tag{2.4}$$

If the value of susceptibility is greater than zero (and there is no spontaneous magnetisation), then the material is considered to be paramagnetic, in that an applied field will induce an increased magnetisation in the same direction as the applied field. For a value of $\chi < 0$, the material is diamagnetic and will induce a magnetisation that opposes that of the applied field. Paramagnetism and diamagnetism both appear to be linear with magnetic field. For diamagnetism, this is in fact the case, whereas the paramagnetic response is slightly more detailed. The strict definition of paramagnetism involves a hyperbolic tan function, which becomes negligible at relatively low fields and high temperatures. However, as applied field becomes large and/or temperature becomes small, the $tanh$ becomes significant and the shape of the magnetisation will slowly begin to saturate. Susceptibility is not only a material property, but is also temperature dependant[55] - Equation 2.5 shows the relationship between the material dependent Curie constant, C, and the absolute temperature, T.

$$\chi = \frac{C}{T} \tag{2.5}$$

$$\boldsymbol{M} = \frac{C}{T}\boldsymbol{H} \tag{2.6}$$

It can be seen from Eq. 2.6 that magnetisation is inversely proportional with temperature. This arises due to the constant appearance of thermal fluctuations for non-zero temperatures, which cause disruptions to the spin orientation and therefore reduces the magnetic anisotropy within the material. Saturation magnetisation and properties such as magnetocrystalline anisotropy (explored in Section 2.1.1) assume a maximum at absolute zero due to the absence of these thermal fluctuations.[56] While impractical for application purposes, this provides the reason for many milli-Kelvin studies of low magnetic moment materials, where the thermal fluctuations are capable of dominating the magnetic signal.[57]

2.2.2 Ferromagnetism (FM)

The form of magnetism most commonly attributed to conventional magnets, ferromagnetism is responsible for the creation and use of both permanent and soft magnets. A ferromagnetic material will undergo various changes as a function of both applied magnetic field and temperature. Above the critical (Curie) temperature, T_C, the material will behave in a paramagnetic fashion, in that an applied field will generate a magnetisation in the material.

Below the Curie temperature, a Heisenberg, or exchange interaction will begin to cause a spontaneous alignment of the unpaired electron spins in the material, causing the creation of regions called domains. Exchange interactions arise as a quantum mechanical relationship between two identical particles, which differ for bosons as for fermions.[58] For the purpose of this work, only the behaviour of fermions is discussed as this ties directly to electron behaviour, which are the drivers for magnetism. Summarising exchange interactions is not trivial, specifically due to the combination of spatial and spin waveforms which must be considered as part of the system but the underpinning rule is that no two fermions can take the same state, which is known as the Pauli exclusion principle.[59,60] Combining the position and spin waveforms of the relevant electrons, produces the spin-orbital for that particle, which is then found to have a distinct ruling system when exchange occurs with an identical particle - namely that when the orbital relationship is anti-symmetrical, the spin relationship must be symmetric and vice-versa. Following this, both Heisenberg and Dirac settled on a simplified form of the exchange interaction, which only uses the spin momenta for the electrons, alongside the exchange integral for the system. The Hamiltonian for the Heisenberg interaction is given as Equation 2.7.

$$\mathbf{H_{Heis}} = \sum_{<i,j>} -J_{i,j}\, \mathbf{S_i} \cdot \mathbf{S_j} \tag{2.7}$$

where $\boldsymbol{S}$ represents the spin momenta of the electrons, i and j denote the nearest neighbour positions and J is the exchange co-efficient which is system dependent. The value of the exchange co-efficient can greatly affect the magnetic properties of the system, for example a negative J would suggest an anti-ferromagnetic response within the material (described in Section 2.2.3).

We can define a domain as a region of uniform magnetic alignment, more specifically a region where all of the individual spins are aligned along a single direction. Magnetic domains are analogous to grains in conventional metallurgy. The domains formed when $T < T_C$ will have a net magnetisation in some direction, with the direction of alignment being a product of the magnetocrystalline anisotropy of the material. Importantly, if the material is heavily isotropic, it is possible to have a material where $T < T_C$ and still have a net magnetisation equal to zero.[61] However, once a magnetic field is applied to the material, then the domains will align, either by re-orientation of similarly aligned domains or by sacrificial growth into counter-aligned domains, leaving a material with all of the domains aligned on the applied field direction.[62] An example of this is shown in Figure 2.4, where it should be highlighted that the dashed lines seen in the saturated case represent the position of domain walls which are absent. From the definition of a domain being a region of uniform magnetic alignment, then a fully saturated material has only one single domain. Note how below T_C domains are formed and that this can still lead to a net magnetisation of zero - it is in these situations where the various anisotropies (see Section 2.1) would introduce a directional bias to the magnetic moments.

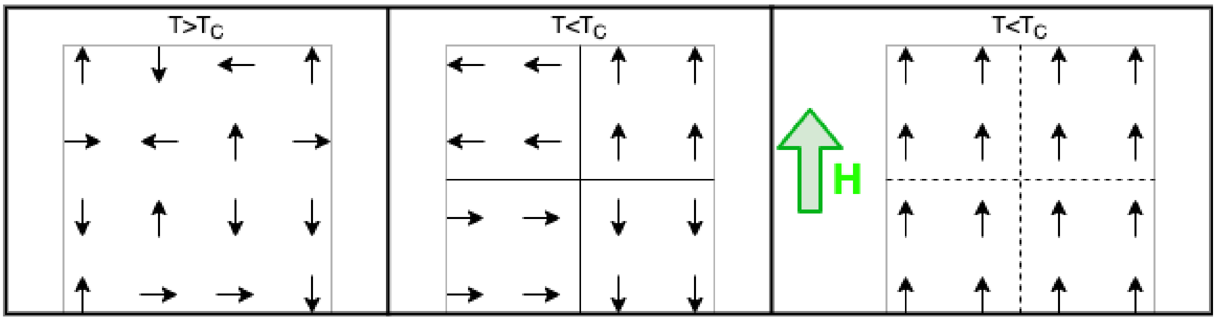

Figure 2.4: Schematic representation of the magnetic moments within a ferromagnetic material, for different temperature and field conditions.

Crystallinity of a sample is a factor in the degree of magnetisation within a sample - this becomes particularly important when one considers domain rotation and thus magnetostriction.[63–65] Polycrystalline materials will have a given number of grain boundaries within the material and when magnetic domains rotate under the influence of an external field, these grain boundaries can act as pinning sites to hinder the magnetic rotation within the sample.[66] Magnetostriction relies on rotation of domains, so this has a knock on effect which can hinder a material's functionality. In comparison, single crystal materials will have no grain boundaries and therefore the energy needed to rotate the domains is vastly reduced by not having to overcome the resistance of the grain boundaries. It would be fair to say that the degree of crystallinity in a sample has an inverse relationship with the magnetisation potential, therefore the ideal scenario for magnetostrictive functional materials is for them to be single crystal.[67]

The inverse relationship between magnetism and temperature was earlier described for paramagnetism through use of the Curie law (Equation 2.6). With regards to ferromagnetism, the inverse mathematical relationship is no longer valid (in that the relationship is no longer strictly inverse) however as temperature increases, the magnetisation will decrease. While the presence of thermal fluctuations does not change, the presence of a transition in ferromagnetic materials is one of note. Following the Ehrenfest system and assuming decreasing temperature, the order parameter is continuous to the first order and discontinuous in the second derivative. Physically, this relates to the magnetisation and susceptibility, which exhibit behaviour across the transition temperature, T_C, that is characteristic of a second order, or continuous transition.[36,68]

Applying this to mean field theory, or Landau theory, one can present a mathematical representation of the behaviour of the order parameter for a material through the transition temperature.[69,70] Equation 2.8 shows how the degree of magnetisation is a function of the saturation magnetisation, M_S, the temperature, T, with respect to the Curie temperature, T_C, and the critical exponent, β. β is another system dependant parameter and examples of the effect this will have on the shape of the ferromagnetic response are given in Figure 2.5.

$$M = M_S\left(1 - \frac{T}{T_C}\right)^{\beta} \tag{2.8}$$

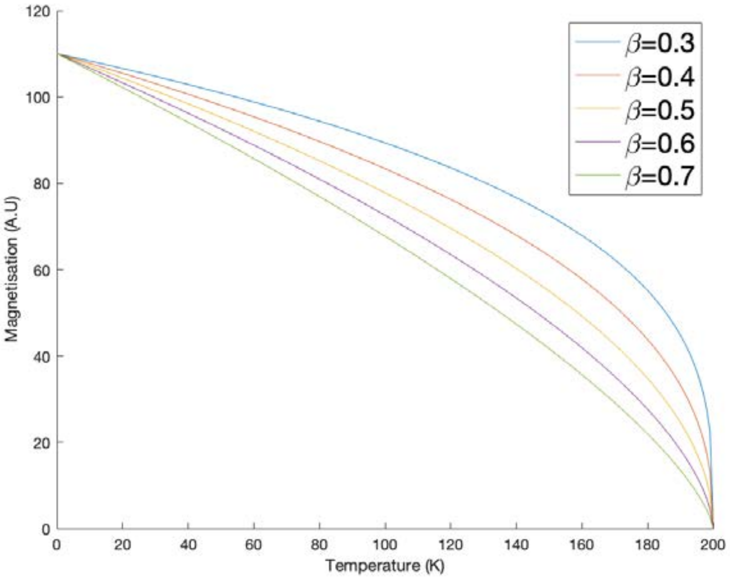

Figure 2.5: A Landau plot showing the effect of the critical exponent, β, on the second order transition. Note that the magnetisation units are arbitrary, however the Curie temperature for this plot is taken as 200 K.

Hysteresis

Following the application of a strong magnetic field on a material in the ferromagnetic state, the domains are all aligned in a single direction and the magnetisation is considered to be saturated. When the field is removed, a portion of this magnetisation is retained and this residual magnetisation is known as the remanence, or remanent magnetisation of the material. To completely remove the magnetisation on the material, a reverse field must be applied to combat the alignment previously instilled within the system. This amount of negative field to achieve zero net magnetisation is known as the coercivity or coercive field, H_C. The phenomena here results in the creation of hysteresis within ferromagnetic materials.[71] An example of a hysteresis loop, as well as other magnetic responses are given in Figure 2.6. Magnetic materials are commonly defined as hard and soft, which relate to their coercivity. Materials with large H_C ($>$ 10 kA/m) are *hard* to demagnetise, whereas the *soft* magnets have significantly smaller degrees of coercivity ($<$ 1 kA/m).

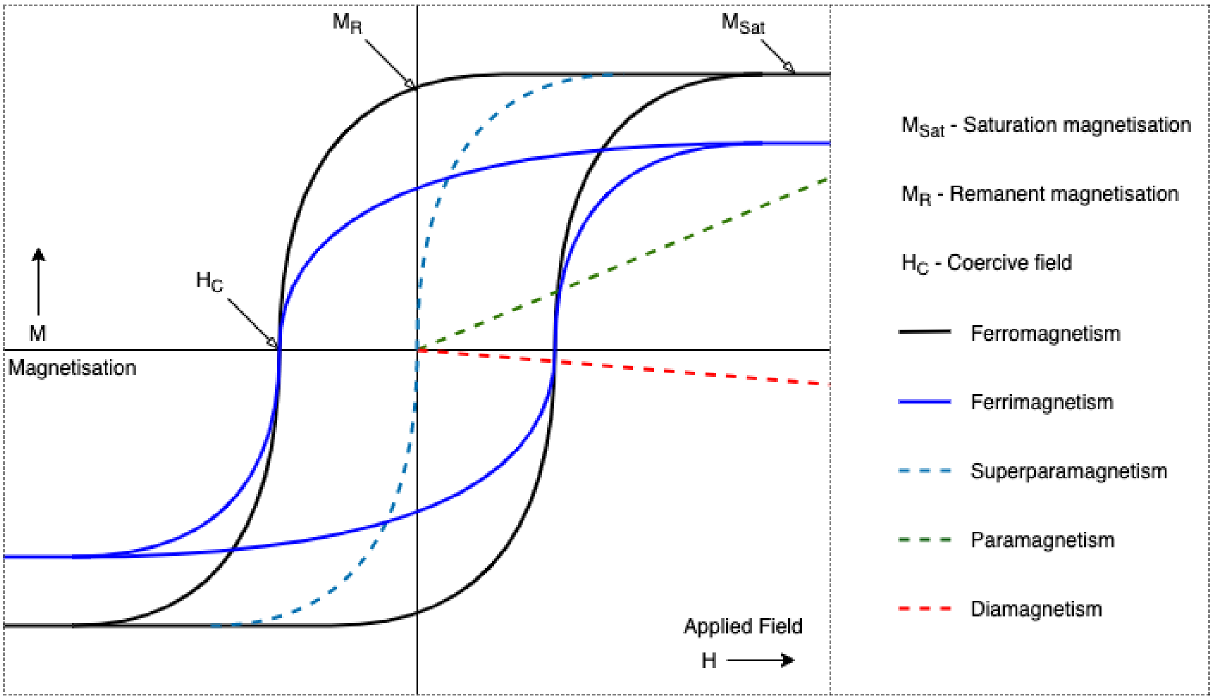

Figure 2.6: Behavioural examples of the magnetic response to an applied field for different types of magnetic material. Paramagnetism is shown in the Curie regime, with magnetisation being linear with applied field.

2.2.3 Other forms of magnetism

Anti-ferromagnetism (AFM)

Here the exchange integral ($J < 0$) causes the atomic moments to align anti-parallel, therefore yielding a net magnetic moment of zero for no applied field, below the Néel temperature. Note - the Néel temperature is for AFM materials what Curie temperature is for FM materials. Visually, AFM materials seem to exhibit a similar magnetic response to PM materials, with the magnetisation increasing linearly with applied field.[72–75]

Ferrimagnetism

An arrangement of moments from multiple magnetic elements, which can be in both parallel and anti-parallel orientation, yielding a net moment in a given direction. Ferrimagnetism can be thought of as a consequence of AFM, or vice versa.[76] It is ferrimagnetism within $Tb_{1-x}Dy_xFe_2$ alloys which leads to the particularly large magnetic moment exhibited, due to the rare-earth ions having a significantly larger magnetic moment than that of the iron atoms. Ferrimagnetism relies not only on an anti-parallel arrangement of electrons, but also on the need for different magnitudes of magnetic moment, therefore ferrimagnetism only exists in compounds or alloys and cannot exist in elements.[77] The M vs H response for a ferrimagnetic material takes a familiar shape to that of a ferromagnetic material.

Diamagnetism

When an external field is applied to a diamagnetic material, the interior moments will align opposite to the external field to minimise its effect. It is the weakest magnetic response and is easily masked by any other magnetic behaviour.[78]

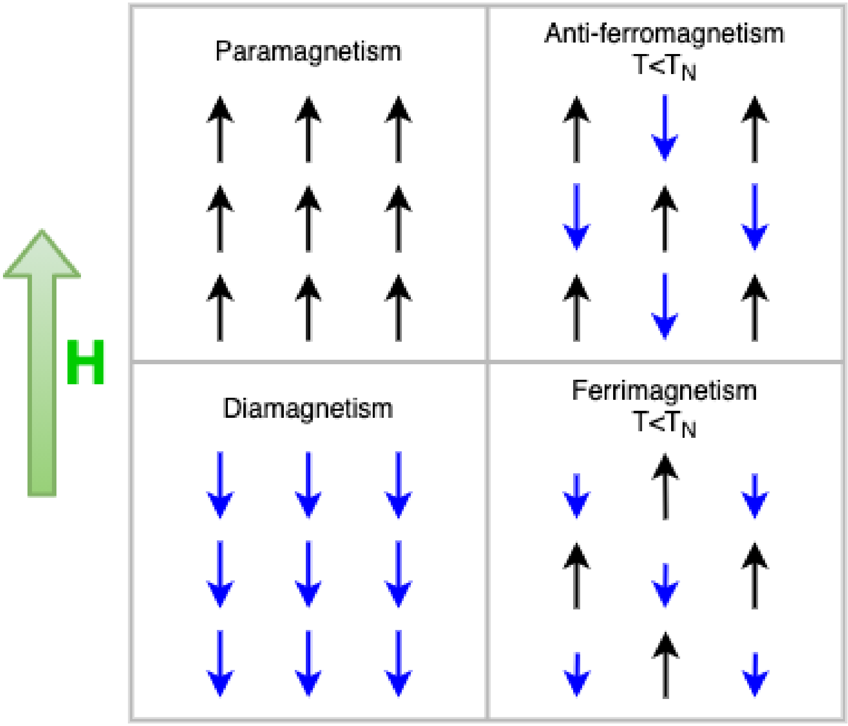

Figure 2.7: Pictorial representation of magnetic moment alignment in non-ferromagnetic materials. Arrows denote spin-up or spin-down electrons, while arrow size represents magnitude of the magnetic moment.

2.3 Magnetostriction

First discovered by James Joule in the 1840's, magnetostriction is the phenomenon of an induced length change in a material when under the application of a magnetic field.[22] While first observed in a rod of BCC iron, it has now been found to occur in all ferromagnets to varying degrees and has since become one of the more utilised materials phenomena.[79,80] Modern day sensors, actuators, transformers and many pieces of medical equipment all feature magnetostrictive materials in some capacity, making them a mainstay in the modern economy.[81]

Joule first suggested that bulk tetragonal magnetostriction is caused by the reorientation and/or repopulation of domains, where the easy magnetisation directions lie along the c axis of each tetragonal domain. In Joule theory there is no volume change, however it has been found through studies of the linear thermal expansion that there are anomalies upon cooling through the Curie temperature. By comparing the thermal expansion coefficients between measured values and the "hypothetical thermal expansion it would experience if it were non-magnetic", a spontaneous magnetostriction can be found to cause a small effect.[82]

Macroscopically, the length change that occurs is visually just a stretching of the material along a given axis, which to preserve volume must also lead to a related shrinking in a separate axis. While this is a rather simplistic picture to appreciate, the microscopic scale is significantly more difficult.

Consider a small rod of magnetic material which is only one domain wide but i domains long. The set of domains comprising this rod, all carry their own direction that is assigned randomly with no directional bias. Label the long axis of this rod to have a length L and the individual domains to have a length of l in the same long-axis direction (considering a 2D picture). Figure 2.8 visualises this approach. It should not surprise the reader that the values of l will take a distribution of values between zero and a maximum, as determined by the orientation of the domain itself. Therefore, summing over i domains, the value of

L is defined as

$$L = \sum_i l_i \tag{2.9}$$

As saturating field is applied along the long-axis direction, it is trivial to appreciate that the domains will rotate to run parallel with this field and consequently it can be seen that all values of l will reach a maximum. This in turn will lead to an increase in L, therefore yielding a length change in response to an applied field. This length change, ΔL, is mathematically defined as the difference between the initial and final lengths, L and L', such that $\Delta L = L' - L$. Commonly, this change in length is given the symbol λ and is typically measured in units of parts per million (ppm). This logic can then be applied to a single crystal with many domains, wherein the length change arises from the orientation of the domains such that the easy axis direction is aligned with the applied field.

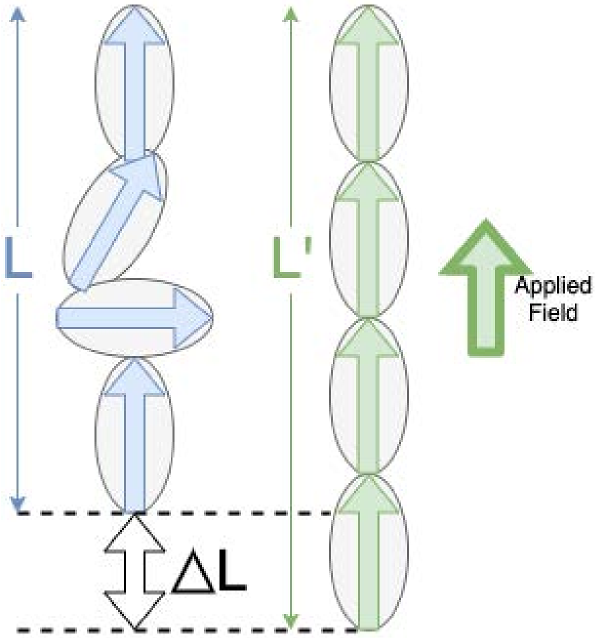

Figure 2.8: Visual representation of magnetostriction occurring in a rod of single domain width, with total length L and comprised of a number of domains, each having an individual length of l.

Furthermore, if one re-examines this setup, but instead considers the width of the domains and still applying a field in the long-axis, it can be evaluated that there must be a shrinking in the short-axis as the domains realign. This is representative of the volume preservation seen in materials that causes a shrinking in, for example, the a and b axes where elongation occurs in the c axis. While this picture is simplified, ignoring the huge contributions that magnetocrystalline anisotropy plays on the easy axis and domain pinning, it does go a long way to present the results of magnetostriction that are known. Nickel-based alloys were the first widely investigated material, exhibiting around 50 ppm length change at room temperature.[83,84] The major breakthrough in development of magnetostrictive materials is generally attributed to the discovery that the rare-earth elements would display huge values of strain, on the order of 10,000 ppm, when measured at low temperatures.[85,86] This prompted the alloying of these rare-earth elements with the $3d$ electron transition metals, such as iron or cobalt.[87] Further experimentation with Fe-based alloys was launched after the discovery that solid solution structures like FeGa could also exhibit high amounts of magnetostriction.[9,88] Measurements of magnetostriction are commonly performed along both the [100] and [111] directions, yielding values for $\lambda_{[100]}$ and $\lambda_{[111]}$ respectively. The most simple experimental setup for measurement employs the use of commercial strain gauges in conjunction with resistivity measuring equipment, as simple as Wheatstone bridges, or as complex as Physical Property Measurement System (PPMS) or Super conduction Quantum Interference Device (SQUID) instruments. An ideal measurement would be one performed on a single crystal sample, wherein the directions of applied field and strain can be very carefully considered, controlled and recorded. Table 2.1 shows the effect that directionality and single crystal samples can have on the magnetostriction of a material and attention should be brought to the difference in magnitude between single crystal and polycrystal samples, due to the presence of competing domains.

2.3.1 Examples of magnetostriction in RE-TM$_2$ alloys

Magnetostriction is a common phenomenon in RE-TM$_2$ alloys. The observation of high magnetostriction in these compounds was a driving force behind the development of

Table 2.1: Examples of magnetostrictive co-efficient for the magnetic transition metal elements.[89] Iron is an example wherein the sign of the co-efficient will change dependant on the direction of applied field.

Material	Crystal Axis	Magnetostriction coefficient, $\lambda(ppm)$
Fe	[001]	+(11-20)
Fe	[111]	-(13-20)
Fe	Polycrystal	-8
Ni	[001]	-(50-52)
Ni	[111]	-27
Ni	Polycrystal	-(25-47)
Co	Polycrystal	-(50-60)

Terfenol-D, where it was found that alloying of RE-TM$_2$ compounds with opposing signs of MCA constants was an effective way of reducing the necessary field to induce large values of strain.[25, 90] Table 2.2 summarises a fleet of calculation (single ion model) and experimental work (magnetostriction, magnetic anisotropy and elastic moduli), presented so as to show a small collection of magnetostriction and MCA constants - further depth will be provided in Chapter 4. It is clear to see that the rare-earth binary alloys have significantly larger values of strain than the pure transition metals, however they do suffer with higher anisotropy. The reader is encouraged to pay close attention to the results for TbFe$_2$ and DyFe$_2$, which paints the picture for why Terfenol-D, Tb$_{0.27}$Dy$_{0.73}$Fe$_2$, is such a successful and widely used magnetostrictive material. It is clear that when alloyed in the correct ratio (roughly 1:3, Tb:Dy) the value of the K_1 constant is reduced due to the opposing signs and relevant magnitudes of the individual constants. Meanwhile, the values of exhibited strain are not opposed and therefore remain significant.

It should be noted that while the magnetostrictive properties of RE-TM$_2$ alloys are desirable, the properties of the individual RE elements are not necessarily so. The strain exhibited by pure RE elements is often huge in comparison to those when alloyed as described, however the Curie temperature of these pure elements is so low that any direct application potential is impossible. This is due to the changing in crystal structure, which in turn leads to a significantly more favourable magnetocrystalline anisotropy - this will be explored in Chapter 4 where the importance of the Laves phase structure is made clear.

Table 2.2: Example data of calculated and measured values of magnetostriction values and the room temperature magnetocrystalline anisotropy constant, K_1, for Fe, Co and various RE-TM$_2$ alloys.[25] The reader should note that Tb$_{0.3}$Dy$_{0.7}$Fe$_2$ is roughly equivalent to the composition of Terfenol-D.

Material	Magnetostriction (ppm) & temperature (K)	K_1 (x 10^4 Jm^{-3})
Fe	$\lambda = 9$ @ 300 K (Measured)	+4.5
Co	$\lambda = 62$@ 300 K (Measured)	+45
PrFe2	$\lambda_{[111]} = 5600$ @ 0 K (Calculated)	
TbFe2	$\lambda_{[111]} = 4400$ @ 0 K (Calculated)	-760
DyFe2	$\lambda_{[111]} = 4200$ @ 0 K (Calculated)	+210
NdFe2	$\lambda_{[111]} = 2000$ @ 0 K (Calculated)	
Tb0.3Dy0.7Fe2	$\lambda_{[111]} = +1500\text{-}2000$ @ 300 K (Measured)	+5

Chapter 3

Fundamental Materials: $Fe_{68.8}Pd_{31.2}$

Within this section, the fundamental material $Fe_{68.8}Pd_{31.2}$ is detailed. This ferromagnetic shape memory alloy (FSMA) material displays a complex interaction between the magnetic and crystal structure, currently in a region far below room temperature where the application potential is vastly reduced. Further knowledge of the underlying physics within this material is crucial to future development of functional materials which exploit these complex magnetic-crystal structure interactions. Iron palladium is currently not used for application and therefore there are no conventional methods of manufacture for this binary alloy. Current synthesis methods being used for research purposes involve chemical reduction for suspended nanoparticle assemblies,[91] alongside Bridgman growth and float zone melting which will be discussed in the following Chapter.

Enhanced magnetostriction in Fe-based binary alloys have been reported in multiple systems: FeCo, FeGa and FePd are examples of this.[9,92,93] Within these compounds, the magnetostriction is significantly larger than that recorded for bulk BCC iron, a result which is curious given that gallium and palladium are non-magnetic additions. An example of this is ≈400 ppm for FeGa alloys compared to ≈20 ppm for BCC iron, and this large enhancement was a driver behind research that coincided with that for Terfenol-D (Chapter 4) and resulted in the naming of certain FeGa alloys as Galfenol.

The iron-palladium material discussed henceforth will pertain to the composition $Fe_{68.8}Pd_{31.2}$ (shortened to FePd). With regards to the magnetic properties of FePd, it has an almost entirely isotropic response to magnetisation at room temperature.[35,94,95] Figure 3.1 shows the room temperature hysteresis loop for the common cubic crystal directions - coercivity is low and isotropy is present at all but extreme fields, wherein [111] and [001] directions have the highest and lowest saturation magnetisation (M_{Sat}) values respectively and even at these extreme fields the different in M_{Sat} is negligible. The low coercivity and large isotropy are very desirable for magnetically induced strain applications, where complete removal of magnetism with removal of external field is vital and many desired directions can exist.

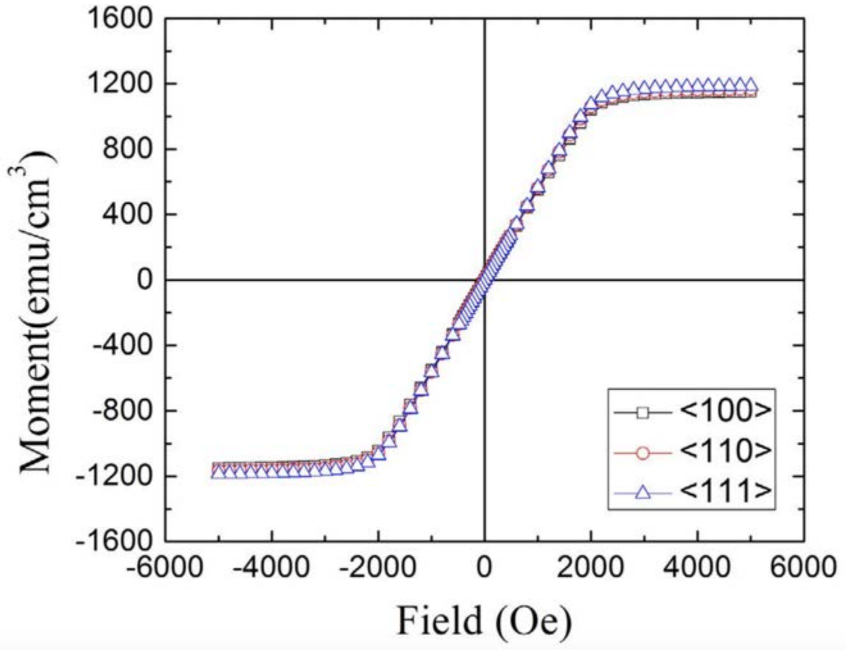

Figure 3.1: Room temperature hysteresis loop of a single crystal $Fe_{68.8}Pe_{31.2}$ sample in the $< 100 >$, $< 110 >$ and $< 111 >$ directions.[35]

This composition was specifically chosen for synthesis following the pioneering works performed by Schmidt & Berger,[96] where they measured the saturation magnetostriction for a large number of samples in the full range of Fe_xPd_{1-x} alloys (Figure 3.2). The range of samples produced for Figure 3.2 were created by entwining strips of constituent material (roller milled to facilitate this entwining) before melting in a resistance furnace. Following melting, a 20 hr homogenisation was performed before a final heat treatment - the 'quenched' samples received a further 2 hr anneal before being quenched into water, whereas the 'annealed' samples had a 20 hr anneal before a very slow furnace cool.

The two different processes were designed to minimise (quench) and maximise (anneal) the degree of atomic ordering and homogeneity within the samples. As the quantity of iron increases, the difference between quenched and annealed samples becomes more pronounced. This likely arises due to the increased iron content being more affected by the reduction in diffusion caused by quenching, thus causing an inherently strained matrix as seen in the case of ferrite to martensite transitions in steels.

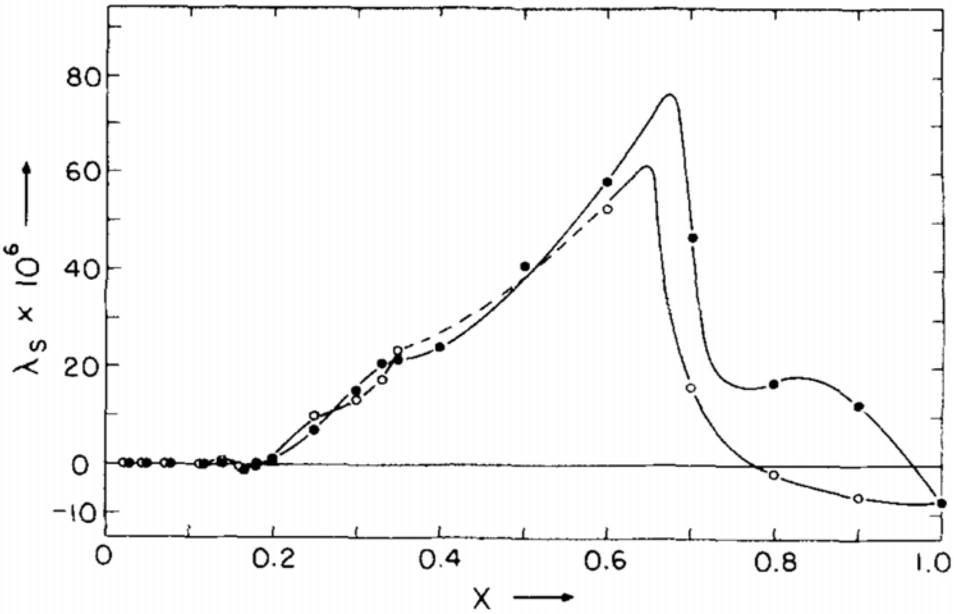

Figure 3.2: Room temperature saturation magnetostriction measurements as a function of sample composition for Fe_xPd_{1-x} polycrystal alloys.[96] Solid circles represent quenched alloys, while open circles are for annealed alloy samples.

Advancing towards the modern day, the magnetostriction of a single crystal sample of $Fe_{68.8}Pe_{31.2}$ has been determined at temperatures slightly below room temperature (Figure 3.3). The [001] magnetostriction response across a small temperature range (centred roughly on 250 K) is approximately 500 ppm, a value which is significantly larger than that measured at room temperature for the polycrystalline samples, yet continues to be larger still when the measurement direction is shifted to [110].[35] While an increase in strain is anticipated with the change to lower temperature and single crystal samples, Schmidt & Berger did perform polycrystalline measurements at base temperature (4.2K) and found that the magnetostriction did not exceed 100 ppm. These intriguing results, performed at two vastly different temperature regions by both Steiner and Schmidt & Berger, suggest that the crystallinity and anisotropy have a far more integral part to play than the magnetisation results alone would suggest.

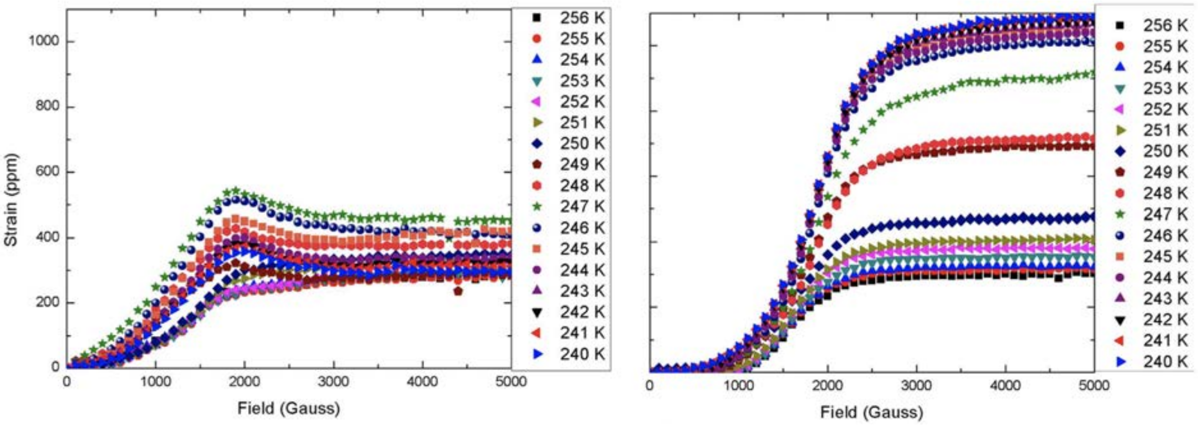

Figure 3.3: Temperature dependent magnetostriction measurements, taken along the [001] **(Left)** and [110] **(Right)** directions, for a single crystal of $Fe_{68.8}Pd_{31.2}$.[35]

At room temperature, FePd exhibits the $L1_0$ or $P4/mmm$ crystal structure which is a disordered face-centred cubic structure, comprised of alternating layer stacking in the [001] planes,[97] which is shown as Figure 3.4a. There is a lack of extensive crystal structure work for FePd alloys, however there are significant similarities with the iron-platinum series which has been studied more at length, such as the addition of Increasing amounts of palladium leading to a shift towards an $FePd_3$ or $L1_2$ type structure, as also seen in FePt materials. It has been found that the ferromagnetic ordering in these alloys is a function of the degree of disorder within the phase structure, where the random positioning of Fe and Pt atoms on lattice sites induces a ferromagnetic ordering.[98] Further complicating the picture for iron-palladium alloys, particularly the composition studied in this thesis, is the presence of the precursor pre-martensitic tweed phase - the nature of which is yet to be completely determined, and may have significant impact on the non-stoichiometry of the bulk material.

As expected for cubic systems, the anisotropy is low as has been highlighted previously in

Figure 3.1, where the measurements were performed at room temperature. Interestingly however, the magnetic properties appear to change dramatically when temperature is reduced, with a drastic increase in the magnitude of strain. While an increase in strain with decreasing temperature is expected, the magnitude of the change in FePd is particularly large given the temperature range for the increase is only ≈50 K from room temperature, where the strain is small. This can be explained via an adaptive phase change, which is driven by the presence of pre-martensitic tweed.

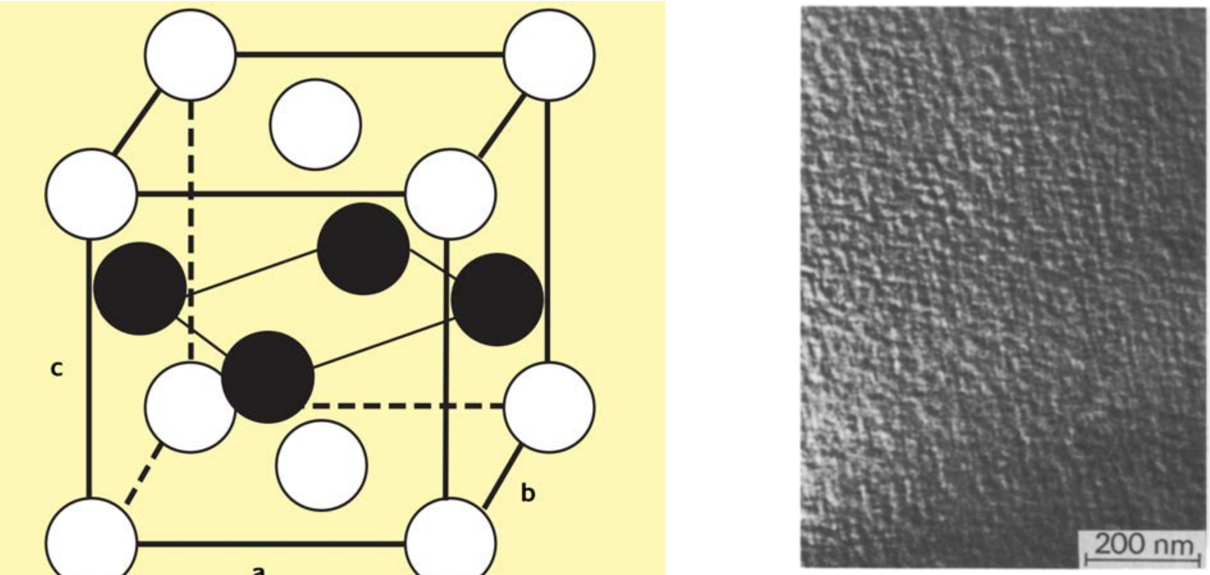

(a) The $L1_0$ structure of FePd. White and black atoms represent Fe and Pd respectively.[97]

(b) An electron micrograph of the tweed structure of Fe-30wt.%Pd alloy at 325 K.[13]

Figure 3.4: Room temperature crystal structure and elevated temperature tweed structure within FePd.

Coinciding with the cubic structure at room temperature, is the presence of a pre-martensitic tweed (PMT) second phase which is not yet fully understood, particularly relating to the composition of the PMT.[99] Consisting of nanoscale domains, PMT acts as a precursor phenomena which exists in plate like topography which gives the appearance of a 'tweed' pattern on electron microscopy images (Figure 3.4b). Fujita was among the first to highlight that the PMT within FePd alloys can be treated as embryos for nucleation sites, heralding the phase transition of the bulk from FCC to FCT. While subcritical nucleation sites are expected to appear and disappear in the theory of nucleation (as the ever shifting kinetics allow for brief appearances that do not lead to phase change), it was found that the PMT regions within FePd could be considered as static and stable with respect to time. Given that temperature is found to drive the FCC to FCT transition, it is a logical conclusion to say that a reduction in temperature stabilises the PMT phase and allows for growth, which in turn generates a phase change in the bulk, resulting in a martensitic twinned structure with a favoured direction of strain in the [110] direction.[100] The effect of the PMT is more far reaching than simply a precursor to phase change. The magnetic response of FePd in the cubic phase is independent of temperature - a consequence of this would normally mean a system wherein all domains are pinned and only spin rotation towards the applied field is allowed. This fully pinned system is only possible when there is no crystallinity, such as in a frozen glass or metglass system. Given the long range order and repeating unit cell, this cannot be the case. Instead, it is proposed that the PMT clusters have an 'ultra-low' anisotropy, which in turn generates an almost isotropic internal demagnetisation field.[101] This thinking is further compounded with the magnetic torque results presented by Steiner et al, which show a combination of two- and four-fold anisotropies in the torque data. The two-fold anisotropy is dominant for low values of field and is believed to arise from the low anisotropy seen in FePd. One theory suggests that the twin clusters can 'fold and unfold' to minimise the anisotropy energy, however as the temperature approaches that for the FCC to FCT transition, the twin clusters instead coalesce as part of a second-order transition, to form the FCT phase.[100] Figure 3.5 shows the strain vs temperature map for FePd. The presence of a low symmetry, adaptive phase which is reactive to temperature and magnetisation, while also being elastically sensitive is of particular interest and identifying the mechanism of the twin clusters may lead to future exploitation of the versatility of this peculiar nanofeature. As in the case of morphotropic phase boundaries, a more complete understanding can pave the way for technological advancements via informed alloy development.

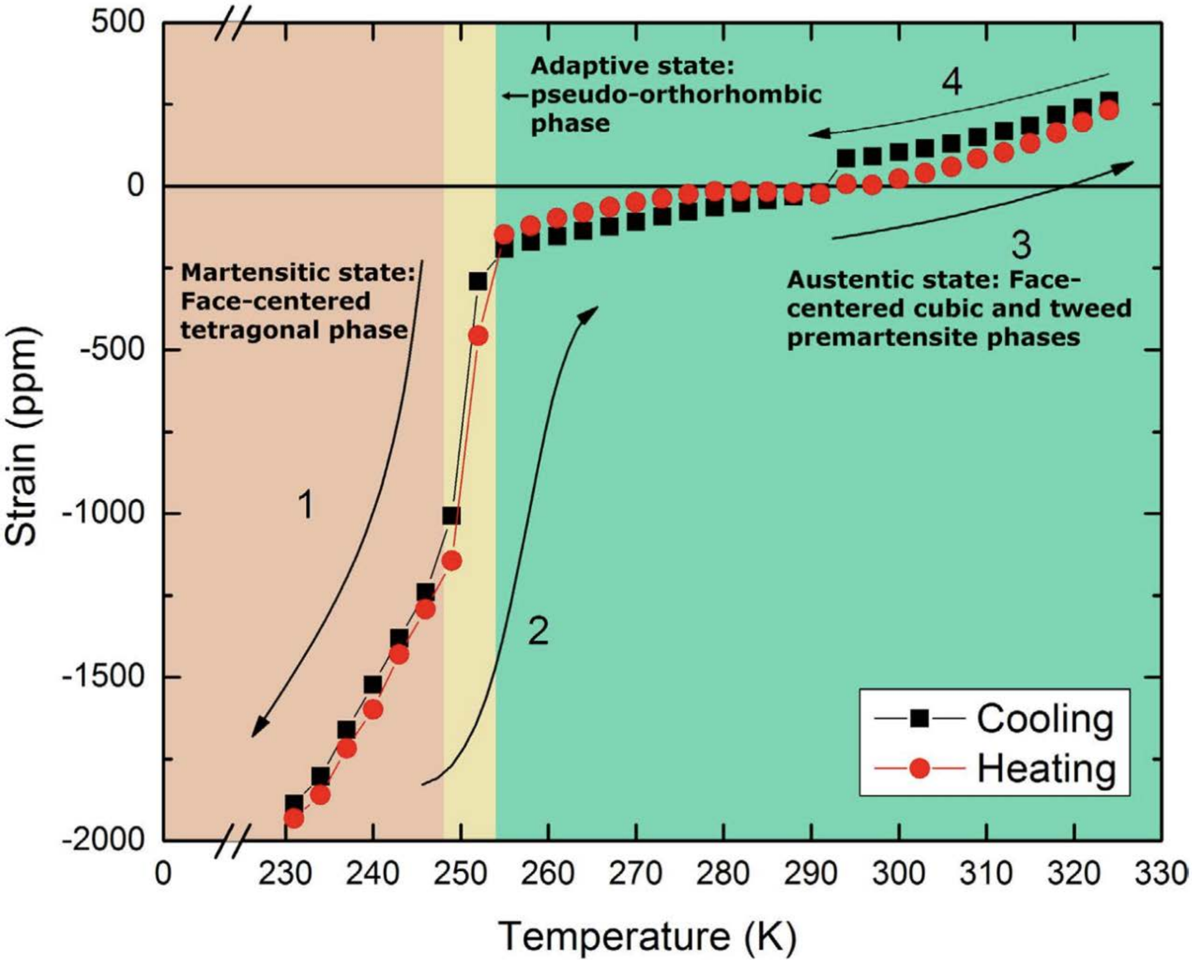

Figure 3.5: Single crystal strain [100] of FePd as a function of temperature, with phases annotated to show the adaptive phase (yellow vertical region)[35] which acts as a preliminary between the low strain austenite state (green) and high strain martensitic state (orange).

Chapter 4

Functional Materials: $\mathbf{Tb_{1-x}Dy_xFe_2}$ alloys

This investigation into functional materials is based around the $Tb_{1-x}Dy_xFe_2$ alloy system, from which the market leading Terfenol-D originates. Beginning with a rough timeline and description of the characterisation and alloying efforts which led to the creation of Terfenol-D, this chapter continues to explore the crystal structure, magnetic properties and magnetostriction properties of this alloy system. Finally, the conventional manufacturing methods for $Tb_{1-x}Dy_xFe_2$ are outlined, along with the effects that alloying additions can generate.

4.1 Discovery and use as Terfenol-D

Throughout the 1960's, there was significant work performed on understanding the phenomena of magnetostriction in rare-earth materials, which attracted significant interest as their strains were orders of magnitude larger than previously reported values of magnetostriction.[85–87] The heavy rare-earth elements, Tb and Dy, led the way in this field as their strains approached 1% (10,000 ppm), a figure which is still considered large in the modern scientific world. Considering the high values of strain, there was an inherent desire to try and unlock the large magnetostrictions for use in room temperature applications. Unfortunately, the rare-earth elements have generally very low ordering temperatures[25] (with all but Gd having a T_C below room temperature) and as previously discussed, magnetostriction increases with decreasing temperature due to the reduction in thermal fluctuations. Table 4.1 display the Curie temperature for some rare-earth elements.

Table 4.1: Curie temperature of the pure rare-earth elements which have some inherent magnetostriction.[25]

Element	Curie Temperature (K)
Gd	292
Tb	222
Dy	87
Ho	20
Er	32
Tm	25

In the 1970's, work began on producing alloys of rare-earth (RE) and transition metal (TM) elements, with the three room temperature ferromagnetic elements, Ni, Fe and Co, being alloyed to multiple RE elements in differing ways. RE-TM$_2$, RE-TM$_3$, RE$_6$-TM$_{23}$ and RE$_2$-TM$_{17}$ were among the compositional balances investigated. Initial results were promising, showing that room temperature magnetostriction for these alloys was not negligible and that the composition had a significant effect on the resultant magnetic properties. Figure 4.1 shows the results of different investigations using Fe as the base transition metal. It is important to spotlight the vast difference in peak magnetostriction displayed by the RE-TM$_2$ type systems in contrast to others, with TbFe$_2$ peak values on the order of 2500 ppm, drastically different to the ≈1000 ppm seen for TbFe$_3$. Another key results from these investigations is that the saturation behaviour and limit can vary within alloys of the same type - an example of this is best seen in Figure 4.1b, where TbFe$_3$, DyFe$_3$ and SmFe$_3$ clearly have different saturating field (H$_{Sat}$) values, with SmFe$_3$ not even approaching saturation at an applied field of 25 kOe. Following initially promising results with rare-earth transition metal alloys, namely of type RE-TM$_2$, it was found that combinations of these alloys can lead to a minimisation of the magnetocrystalline anisotropy while retaining the high exhibited strain seen in the parent compounds. TbFe$_2$ and DyFe$_2$ both exhibit positive magnetostriction, however their anisotropy constants are of opposing sign. Alloying this pair leads to minimisation of the MCA, while retaining the desirable large values of strain.

With this new breakthrough, the composition of $Tb_{0.27}Dy_{0.73}Fe_2$ was created. Dubbed Terfenol-D (derived from the parent compounds of $TbFe_2$, providing the "Ter" and "Fe", combined with the acronym for the lab responsible "NOL" and "D" represents the designation used to specify the alloying of $DyFe_2$), this alloy was almost immediately recognised as the new standard for the optimum magnetostrictive material. Despite a low ductility which causes fracturing problems during fabrication, Terfenol-D has remained as the market-leading magnetostrictive material since its introduction.

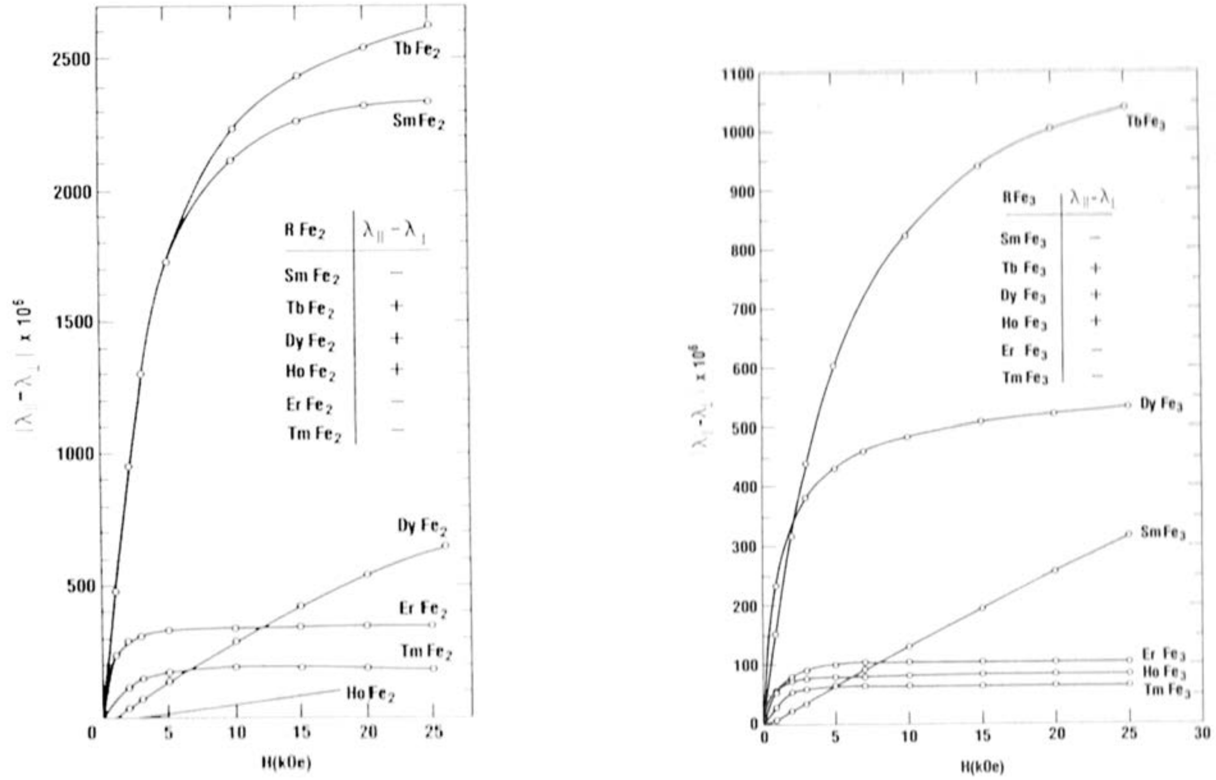

(a) Magnetostriction of various RE-TM_2 alloys.

(b) Magnetostriction of various RE-TM_3 alloys.

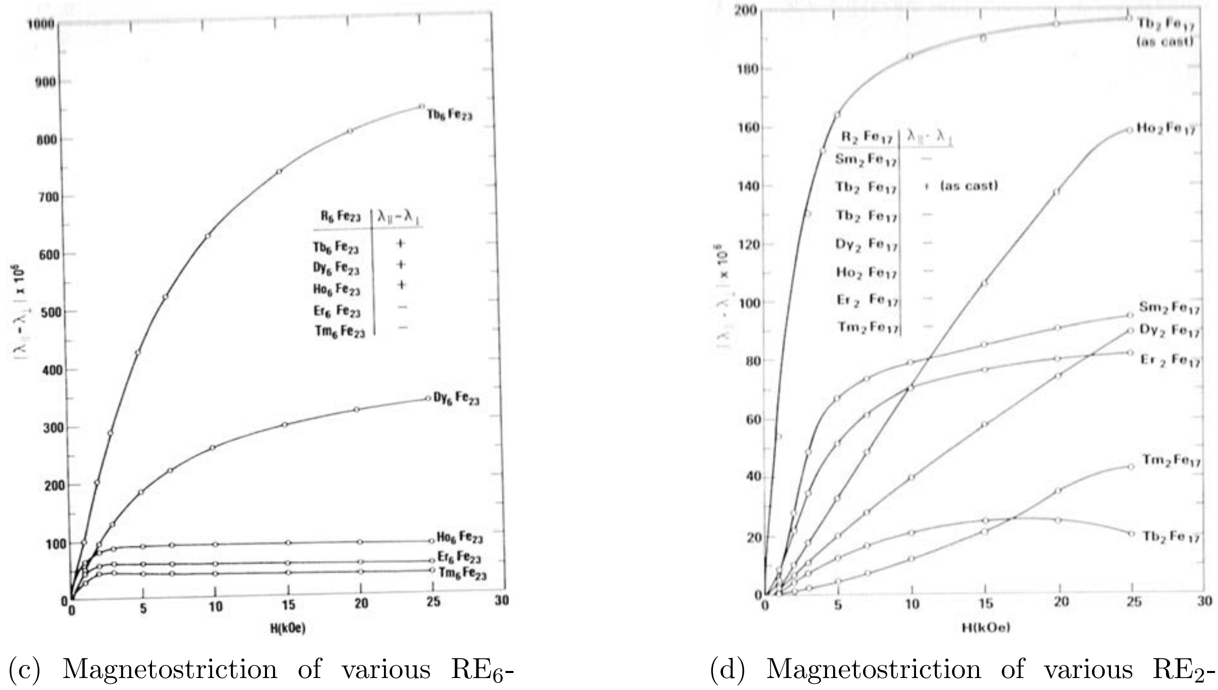

(c) Magnetostriction of various RE_6-TM_{23} alloys.

(d) Magnetostriction of various RE_2-TM_{17} alloys.

Figure 4.1: Summary of the magnetostriction seen in the rare earth/transition metal alloying investigations performed by Clark et al.[25] Label on the y-axis is $|y_\parallel - y_\perp| * 10^{-6}$.

4.2 Crystal structure

Before discussion into the crystal structure and lattice interactions of Laves phase compounds, it is first imperative to briefly discuss some of the different crystal structures possible. Figure 4.2 shows the four crystal structures that will feature prominently in this report. Cubic structures, where the three lattice distances are equal and all angles are 90°, form the high temperature state of almost all RE-TM$_2$ compounds discussed in this thesis. Tetragonal structures are merely a single direction stretching of the cubic structure, yielding a structure where a=b≠c with all angles remaining 90°. In contrast, the rhombohedral crystal can be seen as a canting, or sloping, of the cubic system. All lengths and angles remain equal, with the angle being non-trivial ($\neq 90°$). Finally, the monoclinic structure has all lengths unequal to another and two axis perpendicular, such that $a \neq b \neq c, \alpha = \gamma = 90°, \beta \neq 90°$.

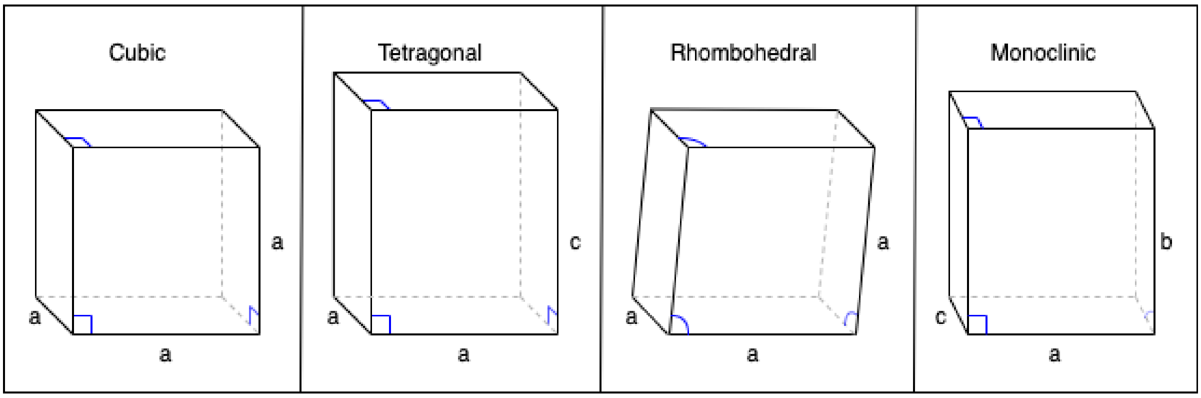

Figure 4.2: Schematics of the cubic, tetragonal, rhombohedral and monoclinic lattices.

The crystal structure of Terfenol-D is the Cu$_2$Mg structure, more commonly known as the cubic Laves phase or C15 structure.[102,103] Figure 4.3 shows a detailed model of the cubic unit cell for Terfenol-D at elevated temperatures.

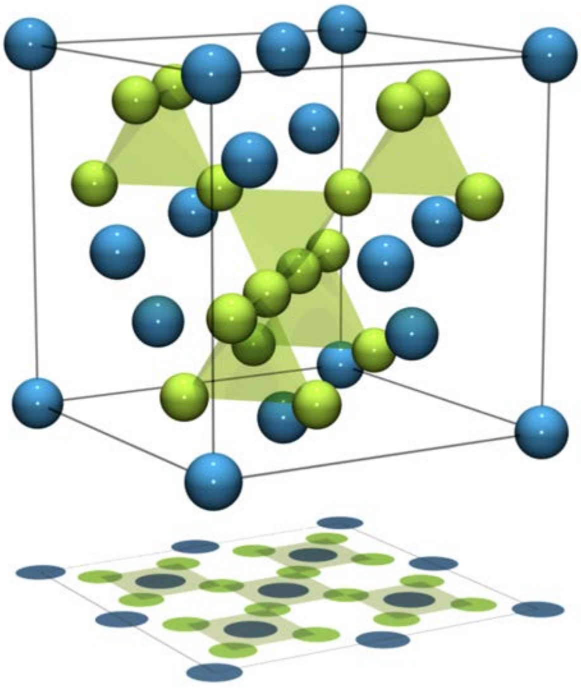

Figure 4.3: Representation of the C15 Laves unit cell, where the blue and green spheres represent the rare-earth atoms and transition metal atoms respectively.[104]

4.2.1 Laves phase

Fritz Laves first described the collection of structures as a series of intermetallic compounds, all of which take a form of AB_2.[105] Broadly, Laves phase encompasses three separate crystal structures, all of which are considered to be tetrahedrally close packed. $MgCu_2$ type (C15), hexagonal $MgZn_2$ type (C14) and the second hexagonal $MgNi_2$ type (C36) structures can all be considered as minor alterations of each other, wherein the stacking and rotation of the unit cell is altered.[106] Laves phase compounds are of significant interest because of the interactions between the localised $4f$ and itinerant $3d$ electrons. Normally, $3d$ electrons display small anisotropy (due to quenching of their orbital angular moments), however when in the Laves structure the $3d$ electrons will form narrow bands, putting the Fermi level in such a position where the magnetic properties can be altered via the substitution of other transition metal atoms for Fe atoms. The occupancy levels of the 3d, 4f and 5d orbitals, alongside the change in inter-atomic distance (which affects the exchange interaction) leads to hybridisation of the 3d-4f orbital.

This change in hybridisation is tied to the electronic structure and therefore the elements comprising the Laves phase material.

Due to this complex landscape of structural and electronic interactions, Laves phase compounds have continued to draw interest and research due to their relative lack of predictability. In 2004, Stein noted that the presence of Laves phase (and which of the three structures) within a particular alloy system was difficult to predict. This system was only complicated further when expanded to binary or ternary alloy systems. Factors that have been found to affect the presence of Laves phase are:[106]

Atomic radii While there is little to no correlation between the ratio of atomic radii and the existence (and type) of Laves structure formed, there is indeed a relationship between the stability of phases and atomic radii. It has been found that the most stable phases, i.e. those with the highest formation enthalpies, are those with $r_a/r_b \approx 1.225$. As the radii ratio deviates from this desired value (closest packing of hard spheres), the enthalpy of formation shifts to destabilise the phase - this is speculated to occur due to the rise in elastic interactions in the lattice.

Electronegativity The structural contraction between the A and B type atoms is proportional to the square of the difference between the electronegativities of the two atoms. Laves phase compounds which have almost the ideal atomic radii ratio and are yet unstable, are thought to suffer from this effect.

Concentration of valence electrons As has been mentioned briefly in this subsection, the electronic structure is one of the main contributing factors to the Laves phase and its attractive properties. Stability and determination of phases can be performed to a degree, providing that the alloy system is known and compatible. There is unfortunately no single model which will determine Laves phase stability based on valence electron concentration.

Laves phase compounds are therefore of significant interest, due to their desirable properties as functional materials, however the lack of predictability and complexity to the various interactions are a stumbling block for future application. Transition metal based Laves materials (such as Terfenol-D like compounds) have also been found to exhibit a mixed bonding system, where ionic, covalent and metallic bonding is found to coexist. This further complication means that synthesis and analysis of compounds is one of the more critical avenues of work for Laves phase development.

More recent work on prediction of Laves phase compounds has been performed using the density functional theory (DFT) method of simulation. By examining the electronic structure, using a quantum mechanical approach to evaluate the effect that potentials will have on the system electrons, the attained electronic structure can then be studied through the use of mathematical operators, allowing for the calculation of multiple parameters (such as elastic moduli, stiffness, magnetic anisotropy, etc).[107] Further to determination of the lattice structure, modern simulation can also predict other behaviour such as optical properties, bonding chemistry and physics properties as a function of crystallinity (single vs poly).[108] The major limitation of DFT lies in its reduced ability to predict properties at increasing temperatures, with a significant amount of DFT work being simulated at absolute zero (T=0 K). Recent work has developed expansion codes to DFT,[109] which can 'layer' temperature onto existing DFT work although it is thought that the initial starting T=0 K model must be incredibly robust to correctly track upwards in temperature and ultimately, these results must be confirmed with physical measurement.

4.2.2 Changes to crystal structure with temperature

At temperatures exceeding 700 K (in reality it will be lower than this figure, as ≈700 K is that of the $TbFe_2$ parent phase) the crystal structure of Terfenol-D will be in the cubic form.[102] Here the material is simply paramagnetic, with no preferential easy axis of magnetisation - the magnetisation will simply rotate to follow the direction of any applied field. Below 700 K the crystal structure is determined by the Tb-Dy ratio of the alloy in question.[110]

Dy-heavy alloys have a tetragonal structure. This tetragonal structure has a [001] easy axis and therefore if one considers the *hkl* reflections, there will be a 2:1 splitting in the (800) reflection, while the (440) will show a 1:2 splitting and the (222) reflection will exhibit a single peak (unity). Tb-heavy alloys have a rhombohedral structure giving a [111] distortion, therefore the (222) reflection will split 1:3, (440) will exhibit an equal splitting, whereas the (800) reflection will show no splitting.

The low temperature region of these alloys is of particular interest. There appears to be a re-emergence of the tetragonal direction at approximately 50 K, even in the Tb-heavy alloys, with the lattice distortions (at the key reflections) approaching unity. Furthermore, there is a non-trivial region of the phase diagram which suggests that there could be regions where the MPB itself is metastable (a phase which only occurs at specific conditions) and therefore, there is an anticipation that the lattice distortion exists at some direction between the [001] and [111] directions. Figure 4.4 shows examples of the room temperature X00, XX0 and XXX lattice distortions of tetragonal $CoFe_2O_4$ and rhombohedral $Tb_{0.3}Dy_{0.7}Fe_2$. It is clear that with sufficient resolution, it is possible to distinguish between the different structures, therefore synchrotron X-ray diffractions allows the work in this thesis to be performed and phase determination achieved.

4.3 Magnetostriction of $Tb_{1-x}Dy_xFe_2$

In the 1960's, studies into the magnetostrictive properties of the rare earth elements were able to determine that the heavy rare earths (Tb and Dy) showed incredible magnetostriction properties. Unfortunately for application purposes, the ordering temperature of these elements is significantly below room temperature, limiting the functionality of the materials. Another factor preventing the use of rare earth metals directly for function is the extreme cost, something which has only become more of a concern since these initial works.[111] In contrast with the RE elements, the ferromagnetic transition metal elements (Fe, Ni and Co) exhibit higher magnetic ordering temperatures but experience magnetostrictive strains which are far from those needed for application purposes.

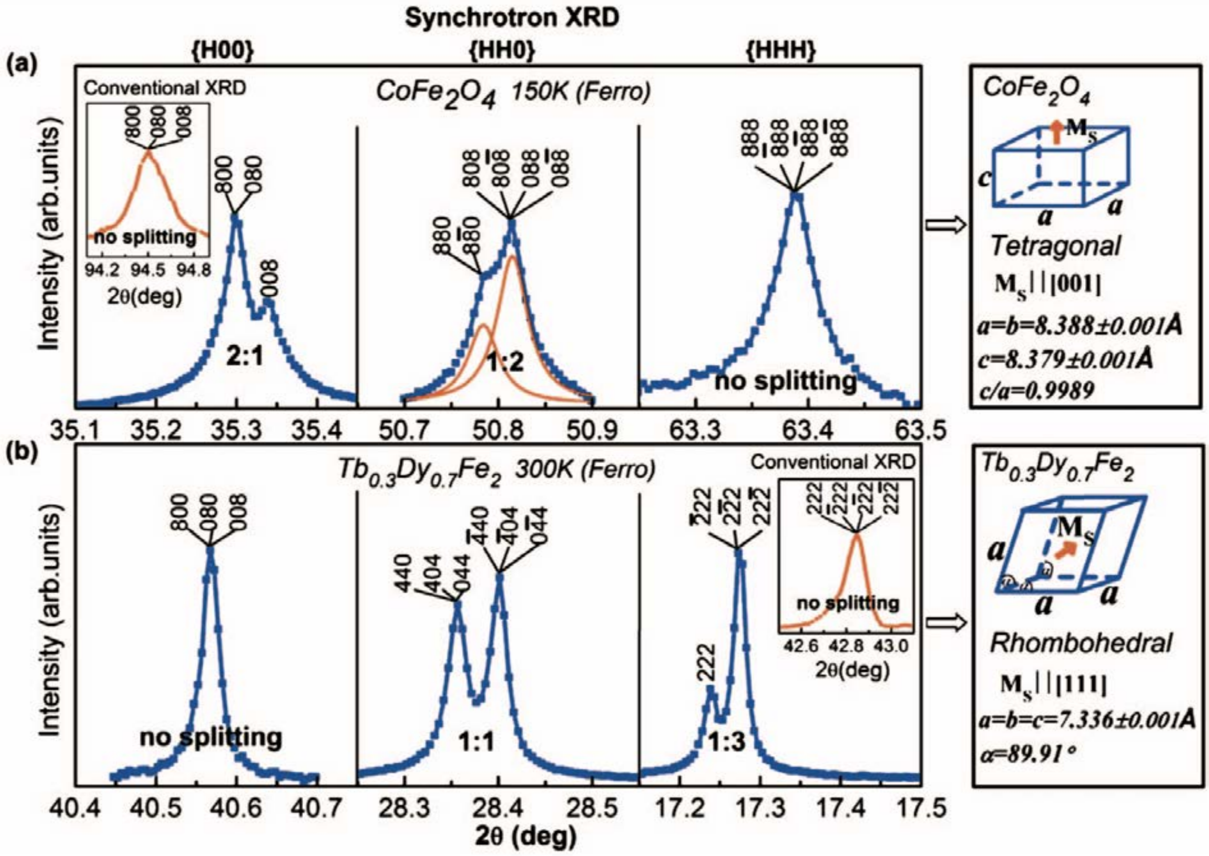

Figure 4.4: Representation of the expected peak splitting for X00, XX0 and XXX type reflections in tetragonal and rhombohedral crystal structures.[110]

To try and create a middle ground material that is ideal for application, multiple alloys were synthesised and their physical properties assessed. Initial alloying attempts yielded mixed results, with little to no correlation being found between the addition of TM to RE and the improvement of Curie temperature. Ni-based RE compounds were found to have low ordering temperature (T_C < 200 K). Co-based systems had a huge range to their ordering temperature generally with increased Co content leading to higher T_C - some of the RE_2Co_{17} compounds exhibited T_C up to 1200 K. In contrast, iron content seemed to have a reverse effect (when compared to cobalt), the relationship between iron content and Curie temperature was found to be inversely proportional. It was clear from the initial synthesis results, that RE-TM systems have a degree of complexity which overshadows that of the parent elements.[112]

As alloying investigations continued, certain alloy systems were identified to be of keen interest for their large strains. RE-TM_2 materials were found to exhibit particularly large magnitudes of magnetostriction in comparison to sister alloys RE_2-TM_{17} and RE-TM_3. $TbFe_2$ and $SmFe_2$ recorded room temperature polycrystalline strains in excess of 1500 ppm. The high magnetostriction in these compounds can again be linked to the large anisotropy - large MCA is not desired for application purposes as large values of field are needed to induce strain. Anisotropy is directly related to the electronic structure, more particularly to the shape of the RE atoms and their electron clouds. Samarium atoms take an extreme prolate shape, whilst terbium is oblate and it is this extreme shape which has a different contribution to the strength of the magnetic anisotropy.[113] In combination with this, the exchange interactions between these RE and iron atoms has strength, resulting in a persistence to the magnetisation with increasing temperature (a feature which the reader should remember is not seen for pure RE materials). This is crucial as increasing the Curie temperature unlocks multiple functional material possibilities, however the large anisotropy is not an ideal parameter. $DyFe_2$ has magnetostriction which is about a factor four smaller than $TbFe_2$ and of the same direction. Furthermore, $DyFe_2$ has large magnetocrystalline anisotropy.

Study of the magnetisation directions in each of the RE-TM_2 compounds found that those displaying smaller value of strain had an easy magnetisation direction of [001] ($DyFe_2$, $HoFe_2$), whereas those with a [111] easy magnetisation direction resulted in larger magnetostriction. It is now known that the rhombohedral [111] lattice distortion is significantly larger than the tetragonal [001] distortion.[24,90,114]

Within the cubic Laves phase structure and assuming an easy magnetisation direction of [111], the rare earth electron cloud ($4f$) is aligned perpendicular to magnetisation. The electron cloud is in plane with other RE atoms and when the electron cloud shape is heavily oblate (as in the case of $TbFe_2$), there is a stronger electrostatic interaction with those in plane atoms. This reduction in symmetry allows an elongation along the [111] direction, which is then mapped onto the whole structure, causing large rhombohedral distortions. In contrast, prolate electron clouds would experience a contraction along the magnetisation direction and therefore exhibit negative [111] strain. For a [001] easy axis direction, as is the case with $DyFe_2$ the shape of the electron cloud is irrelevant - all nearest neighbour interactions will be equidistant and there is no internal distortion from the electrostatic potentials.[115]

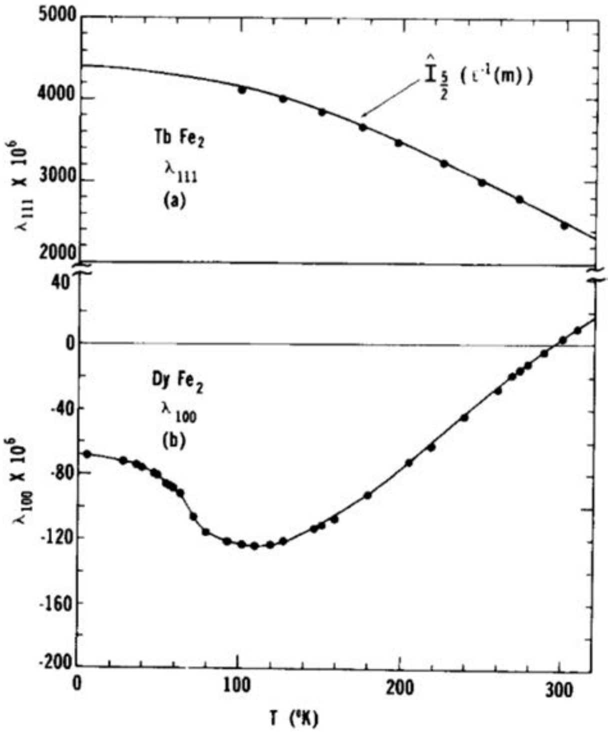

Fig. 1. Magnetostriction of $TbFe_2$ and $DyFe_2$.

Figure 4.5: Temperature dependence of the magnetostriction in single crystal samples of $TbFe_2$ and $DyFe_2$.[115] Strains are measured along the easy axis of magnetisation for each compound, such as to compare the maximum strains achievable by each material.

In combination with the difference in magnetisation directions, the thermal behaviour of single crystal samples of $TbFe_2$ and $DyFe_2$ are significantly different (Figure 4.5). As discussed, the exchange interaction between the Tb and Fe atoms is strong, leading a defined smooth transition that persists well with increasing temperature. Contrasting again, $DyFe_2$ exhibits positive magnetostriction at high temperatures, which becomes negative shortly after room temperature before having a change of gradient around 100 K, before settling on the approach to 0 K. The region of negative magnetostriction $DyFe_2$ is one of the modern limiting factors with regards to the use and cost efficiency of Terfenol-D alloys. As temperature is decreased, the $DyFe_2$ sublattice magnetostriction switches sign and begins to oppose the large, positive magnetostriction from $TbFe_2$, although it must be stated that $TbFe_2$ is larger by almost a factor 40 and therefore the effect of this switching is minimal. If temperature decrease is sufficient, then the magnetostriction will collapse towards zero. This can be countered by using an alloy with slightly higher Tb content and manufacturers now produced Terfenol-D alloys which have a range of Tb-Dy ratio, however the increased price of Tb does reduce the feasibility of large scale application at reduced temperatures (Figure 4.6).

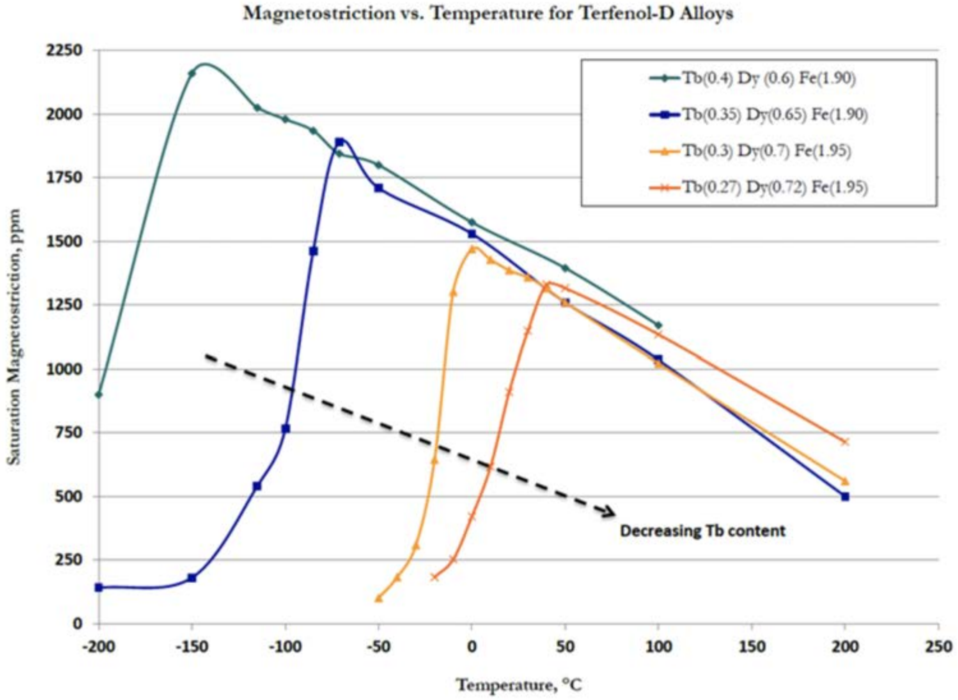

Figure 4.6: Magnetostriction of manufactured single crystal Terfenol-D rods of varying composition, as a function of temperature.[116]

As the feasibility of RE-TM_2 materials become increasingly clear, it was evident that most applications would benefit from the high strains expected. However, one stumbling block for such materials was the desire for low activation fields. The large magnetocrystalline anisotropies of the RE-TM_2 alloys creates a problem for applications where the magnitude of applied field to induce strain needs to be minimised, as they require a significant amount of magnetic energy to switch the alignment direction.[117,118] An anisotropy summary of some of the RE-TM_2 alloys is given in Table 4.2, showing the signs of the

the magnetostrictive strain and elastic constants. The reader should be reminded that the elastic constants in Table 4.2 have a direct effect on the energy density of the crystal system (Eq. 2.1).

Table 4.2: Summary of polarity of magnetostriction (λ and elastic constants for various RE-TM$_2$ alloys.[25]

	PrFe$_2$	SmFe$_2$	TbFe$_2$	DyFe$_2$	HoFe$_2$	ErFe$_2$	TmFe$_2$	YbFe$_2$
λ	+	-	+	+	+	-	-	-
$K^{\alpha 4}$	+	-	-	+	+	-	-	+
$K^{\alpha 6}$	-	0	+	-	+	-	+	-

Based on the data shown in Table 4.2 it is evident why the alloying of TbFe$_2$ and DyFe$_2$ was pursued. Both materials had exhibited high strains, which persisted reasonably well with temperature and yet suffered with large anisotropy. The opposing nature of the anisotropy constants in the parent compounds were of significant interest, which was only compounded when the room temperature magnetostriction of the alloy series was measured. Given the different thermal behaviour with magnetostriction for the parent compounds (Figure 4.5) and the large difference in magnetostriction between the parent compounds (Figure 4.1a), it was expected that the magnetostriction would decrease linearly approaching the Dy side. However, around the composition which is considered as Terfenol-D (Tb$_{0.27}$Dy$_{0.73}$Fe$_2$) there was an unexpected peak in the room temperature magnetostriction, shown in Figure 4.7. While higher degrees of strain can be achieved with the parent phase of TbFe$_2$ it is important to remember that the MCA is large, requiring large amounts of energy to switch magnetisation direction. Likewise, while the peak is less pronounced at higher values of applied field, it is important to remember that the optimal magnetostrictive material is one which can be driven to large strains, using low values of applied field (which inherently determine the practicality of application). There is also a cost incentive to reducing Tb content, as Dy is approximately one third of the price (based on current markets). The identification of this peak is the beginning of what will come to be known as an MPB region (Chapter 5) and the widespread application of Terfenol-D.

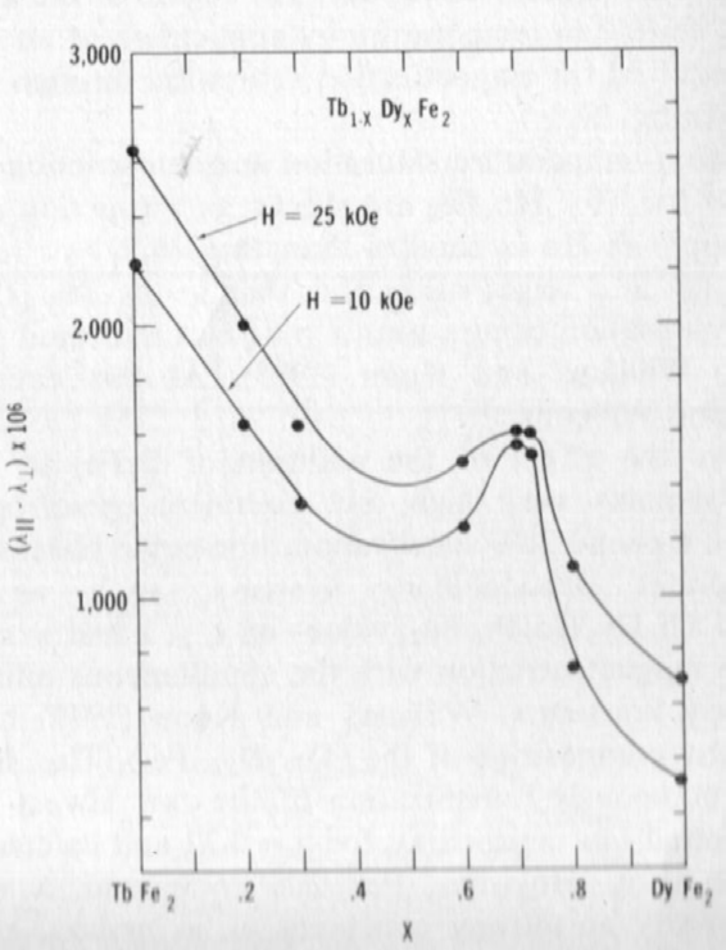

Figure 4.7: Room temperature magnetostriction of the $Tb_{1-x}Dy_xFe_2$ alloy series.[90]

Follow up work on this peculiar phenomenon uncovered a temperature dependence to the magnetostriction, wherein the strain (for a composition within the peak) could be altered significantly by a change in temperature. Reducing the temperature would lead to a reduction in exhibited strain and the magnetisation direction would cant to a [001] direction. It is now known that this is due to the material leaving the MPB region and sitting firmly on the Dy side of the phase diagram.

Explorations into the addition of $HoFe_2$ (creating a ternary alloy system) were performed and while this did lead to a slight increase in the magneto-mechanical coupling factor (k_{33}), the magnetostrictive properties were negatively enhanced by a significant degree, rendering the materials poor in comparison.[115]

4.4 Conventional manufacture of Terfenol-D alloys

As the practicality and potential of Terfenol-D became realised, the problem of successful, large-scale manufacturing was swift to follow. The unavoidable low ductility, poor fracture toughness and necessity for precise composition meant that significant work had to be undertaken to create a suitable process method. Figure 4.8 shows an example of a Terfenol-D rod - attention should be drawn to the fracture surface which highlights the brittle failure mode common for this material. The method used to create $Tb_{1-x}Dy_xFe_2$ alloys in this thesis was the arc melting technique. Desirable due to its easy control of process parameters and operational ease, arc melting is suitable for the production of polycrystalline samples. Limited by low sample size, batch restrictions and inability to produce single crystal samples, arc melting is not used to produce Terfenol-D for commercial purposes and is therefore not considered a conventional method of manufacture, however the ability to have complete control over the melting parameters, constituent materials and degree of homogenisation made arc melting the preferred option for this thesis.

Figure 4.8: Terfenol-D rods are typically formed in cylindrical or bar shaped geometries.[119] Attention should be drawn to the brittle fracture surface which is indicative of both the catastrophic failure mode and limitations of Terfenol-D.

There are currently four main methods for commercial production of Terfenol-D (and similar) alloys:

- Float zone melting
- Bridgman
- Powder sintering
- Polymer bonded composites

Float zone melting

During localised heating, solid/liquid boundaries exist within the material. The segregation coefficient is the ratio of the impurity concentration in the solid phase and the impurity concentration in the liquid phase. If this coefficient is less than one, which it often is for intermetallic compounds, the impurity atoms will have a driving force to drift into the liquid phase. Zone melting relies upon this principle.[120,121] By creating warm and cold zones within the melting area, a solid/liquid boundary is created and the impurities diffuse to the liquid phase. The heating control then shifts the warm zone (normally melting is vertical), such that the impurities will solidify at the beginning of the produced rod and the purity of the final product improves along the length. The removal of impurities promotes a reduction in crystallinity, allowing for single crystal growth with relative ease. The use of a seed crystal is often employed as this can 'set' directions for the pure, single crystal section of the product rod.[122,123]

The main limitation of this technique is one of sample diameter. As the process is reliant on movement of the seed crystal and/or pressed powder rod, then the limiting factor is the surface tension of the liquid phase. As sample diameter increases, the cohesion at the surface is reduced - at some physical limit, the material will no longer adhere together. This maximum limit is around 8mm for Terfenol-D.[124]

Bridgman

The Bridgman (or Bridgman-Stockbarger when given full credits) method also utilises a seed crystal for production of single crystal materials. Differently to the float zone technique, Bridgman produced crystals will have an orientation which directly matches that of the original seed crystal, e.g. if the z axis in the seed crystal is [001], then the resultant final product and assuming a cylindrical rod, will have a long axis of 001 direction.[125–127] As the single crystal nature in float zone growth is due to a lack of impurity concentration, the seed crystal need not necessarily be a single crystal. Methods to improve the purity of Bridgman samples do exist - controlled atmosphere sublimation of constituent materials and repeated Bridgman melting are two such methods.[128,129] Bridgman melting relies on having a two zone furnace, split into hot and cold zones. By creating a temperature gradient within the furnace and again utilising motion of the sample, the molten precursor material (hot zone) is lowered slowly into the cold zone, where the seed crystal is located. Due to the created thermal gradient, the solidifying material will take the crystallographic characteristics of the seed crystal used. Negatives of this method mainly arise from the inconsistency in sample composition along the length of the produced rod - as the impurity concentration is not reduced (unlike in float zone melting) the composition, and therefore physical properties, may alter along the length of the rod.[130] In contrast to float zone melting, Bridgman produced rods must have a minimum diameter of 10 mm.

Powder sintering

As with conventional magnet manufacture, Terfenol-D rods can be produced by powder sintering. Powder of desired composition is aligned and pressed into shape, which can be complex for powder processing, before sintering to melt the powder together and create the final product. While this does provide some benefits, such as unlocking complex geometries, the samples produced are polycrystalline and suffer with reduced magnetostrictive properties, such as porosity which was found to negatively affect the density to a degree of 70% the expected value.[131–133]

Polymer bonded composites

The low ductility of Terfenol-D can be somewhat countered by mixing with a polymer binding agent before setting. This creates composites, which are more desirable from a fracture toughness perspective but do suffer with regards of their physical properties - achievable strain and magnetic properties are both diluted. Some results from these materials show enhanced electrical response, something that would be advantageous to minimise eddy current losses, however the suffering magnetic properties would mean that large amounts of this material would be needed to produce the desired magnitudes for functional materials.[134–136]

4.5 Effect of alloying on $Tb_{1-x}Dy_xFe_2$

There are two methods of alloying within the Terfenol system; either by substituting the rare-earth or the transition metal atoms. Both of these methods affect the material properties due to the changes in the crystal sublattices and magnetic exchange interactions. Sections 4.5.1 and 4.5.2 show some examples of the effect of substituting the RE and TM atoms respectively. A summary of the information presented in this section (and indeed the fabrication methods formerly presented) is given in a comprehensive review by Wang.[137]

4.5.1 Rare-earth substitution

Neodymium

The $NdFe_2$ sublattice has an anisotropy constant opposite to that of Tb and therefore the small addition of Nd can minimise the MCA without drastically lowering the saturation magnetostriction. Specific compositions of $Tb_{0.4-x}Nd_xDy_{0.6}(Fe_{0.8}Co_{0.2})_{1.93}$ display magnetostriction coefficients in excess of 1000 ppm.[138, 139]

Holmium

$HoFe_2$ has a lower value of saturation magnetostriction than desired, however it has been found that additions of Ho reduce the hysteretic response. Furthermore, the reduction in magnetostriction is less significant than the desired reduction in hysteresis exhibited. While $HoFe_2$ exhibits small room temperature values of strain, there is an order of magnitude increase with temperature approaching absolute zero.[140–142]

Praseodymium

$PrFe_2$ has high magnetostriction and K_1 anisotropy constant opposite in sign to $TbFe_2$.[143, 144] Interestingly, studies of $PrFe_{1.9}$ have found that the easy magnetisation direction changes from [111] to [001] as a function of decreasing temperature, with the RE sublattice moment increasing sharply with decreasing temperature.[145] When alloying with Pr, one does need to consider the ideal radius ratio for the Laves compound, which is found to be 1.225. In fact, Pr^{3+} are too large to preserve this and therefore alloying of Pr is limited to $Pr<0.2$ at% otherwise it becomes easy to form the RE-Fe_3 impurity phase which negatively affects saturation magnetostriction.[146]

4.5.2 Transition metal substitution

Aluminium (Paramagnetic)

Small additions of Al can lower the MCA and saturating field of the compound, however alloying will lead to a reduction in magnetostriction for the compound. A portion of the lost strain can be recovered if the material is used under compressive load. Furthermore, with increasing Al% the Curie temperature of the material will drop. Al addition is however found to increase resistivity and ductility.[147]

Manganese (Antiferromagnetic)

Mn is an excellent alloying choice because the magnetostriction of Mn-containing compounds is found to be greater than that for Mn-free compounds, when the material is used under load. At 21 MPa, the [111] magnetostriction of $Tb_{0.5}Dy_{0.5}(Fe_{0.9}Mn_{0.1})_2$ is almost three times larger than the [111] magnetostriction of $Tb_{0.5}Dy_{0.5}\ Fe_2$. Unfortunately, applications with no external load will suffer from significantly reduced magnetostriction. Furthermore, inclusion of Mn will drop the magnetocrystalline anisotropy, allowing for applications to use lower values of applied field.[147]

Cobalt (Ferromagnetic)

Capable of stabilising the Laves phase but does reduce the magnetostriction possible in the compound. Small additions of Co have been found to improve T_C, but this effect reverses upon the Co content exceeding 0.3 at%, at which the Curie temperature is enhanced to a maximum.[148,149]

Zirconium (Paramagnetic)

Small additions of Zr (<0.1%, to replace Fe) can inhibit the formation of malignant RE-Fe_3 phases and will slightly enhance the magnetic properties. However, addition of excess Zr will lead to precipitation of RE-rich Zr phases which become detrimental to the magnetostriction.[150]

Silicon (Diamagnetic)

Eddy currents form easily in Terfenol-D, reducing their efficiency as transducers. Adding Si increases resistivity by promoting more localised electron positions. This in turn can improve the efficiency of operation. However, additions of silicon will negatively affect the magnetostriction, although this can be suppressed with pressure application.[151]

4.6 Oxide impurities in $Tb_{1-x}Dy_xFe_2$ alloys

Oxygen intake during sample fabrication may occur via two potential pathways: contamination of the raw metals used and non-sufficient vacuum/argon pressure during arc melting. Previous studies have shown that oxygen contamination within samples of $Tb_{0.3}Dy_{0.7}Fe_2$ stoichiometry will negatively affect both the saturation magnetostriction and the magnetostrictive coefficient (d_{33}). Kim et al report that the system will form rare-earth oxides, that grow as dendrite structures which have composition $Tb_{0.27}Dy_{0.73}O_{0.68}$.[152] These RE oxides have significantly higher melting point than the Laves phase, therefore the dendrites appear within the Laves phase. The oxide inclusions are responsible for the decrease in magnetostrictive potential because they hinder the reorientation of magnetic domains. Other key findings from this report are that an increase in oxygen content will lead to an increase in iron content (of the matrix) due to the "oxidation loss of the rare earth element". It should be highlighted at this point that the ratio of Tb and Dy is preserved from the parent alloy, to that of the oxide - this is crucial as it suggests the x value of the produced samples, and therefore the credibility of these results, will not be overtly affected by the presence of minor oxide phases.

A study of Terfenol-D growth in quartz crucibles by Kwon et al was able to determine the oxide growth occurring during fabrication.[153] Wavelength-dispersive X-ray spectroscopy measurements on the oxide layers showed that the RE-oxide tends to form as a Dy heavy compound, specifically $Tb_9Dy_{50}O_{41}$. Furthermore, the silicide also studied is found to be Dy dominant as well. While Tb is the more magnetostrictive compound, the reader is reminded that a fine balance of opposing polarity anisotropy constants is needed to minimise the magnetocrystalline anisotropy of the material, which is crucial for application purposes. In fact, the presence of oxides may cause a two-fold decrease to the magnetostriction, as RE-Fe_3 phase can evolve due to oxidation. Following the oxidation of RE atoms from the matrix, there is an excess of Fe, which in turn will increase the driving force for formation of RE-Fe_3 in preference to RE-Fe_2. As the RE-Fe_2 phase produces more desirable magnetostriction the formation and stability of this phase is crucial, therefore oxides and impurity phases should be kept at a minimum.[25,154]

Given the nature of the results presented in this work and the drive to map the MPB further, the degree of impurities is not of particular concern as long as the impurity concentration does not dilute the x-ray diffraction (XRD) results. Follow up work which measures the magnetostriction should however aim to produce samples which are entirely RE-Fe_2 phase.

Chapter 5

Morphotropic phase boundaries

The functional optimisation of the ferroic class of materials is maximised around morphotropic phase boundaries (MPB), with some of the current choice materials for applications employing such enhancement. Morphotropic phase boundaries divide two phase regions of distinctly different symmetry and crystal structure, commonly rhombohedral and tetragonal. This chapter will explore the nature and definition of a morphotropic phase boundary, before analysing the nature of MPBs in other ferroic systems, as well as detailing the current knowledge on the MPB present within Terfenol-D alloys.

5.1 Nature of morphotropic phase boundaries

5.1.1 Definition of an MPB

Morphotropic phase boundary is the name given to a composition-driven phase transition, which yields a significant change to the crystal structure of the material.[15,28,30,155] Given that these boundaries are often not sharp (in that they have a non-negligible width which is composition and temperature dependent), then they may also be referred to as morphotropic phase regions. In recent years, MPB is typically used to discuss specifically the change from a tetragonal to a rhombohedral structure (and vice versa), such as the one seen in Terfenol-D alloys, where the $DyFe_2$ and $TbFe_2$ parent phases contribute tetragonal and rhombohedral structures respectively.[156–158] It is important to make the distinction that when a material is stated to have an MPB at a given composition, the MPB often only applies over a fixed temperature range. As will be seen in the sections to follow, MPB compositions can be vastly different across a fairly slim temperature range.

5.1.2 Changes to crystal parameters at MPB

Given the nature of the changing crystal structure of MPB materials, it is important to discuss the changes to the lattice parameter of these materials during an MPB transition. As the crystal structure melts across the boundary, the lattice parameters must similarly adjust to reflect the changes. Figure 5.1 shows how the characteristic XRD reflections change with temperature for a given composition of $Tb_{0.3}Dy_{0.7}Co_2$ alloy, which bears many similarities to the $Tb_{1-x}Dy_xFe_2$ system which is a focus of this thesis.[26] The lattice parameters and α angle (extracted from curve fitting) are then plotted with respect to temperature to show how the overlap between structures is achieved within the MPB region, in turn suggesting that there is a co-existence of phases within the MPB itself. The α angle tends towards 90° as the material becomes increasingly tetragonal in their nature.

5.2 Morphotropic phase boundaries in ferroic systems

MPBs are consistently found in many different ferroic systems. The physical property effects of the MPB is wholly dependent on the system, as will be discussed in the remainder of this Chapter. Figure 5.2 shows four examples of morphotropic phase boundaries in different ferroic systems. As has become convention, these boundaries separate regions of rhombohedral and tetragonal symmetry but otherwise take on different characteristics. For example, Figures 5.2a and 5.2d show near-vertical boundaries - these materials exhibit very sharp phase transitions. Meanwhile Figure 5.2b exhibits a far more flat MPB, suggesting that the parent phases are more stable in their co-existence.

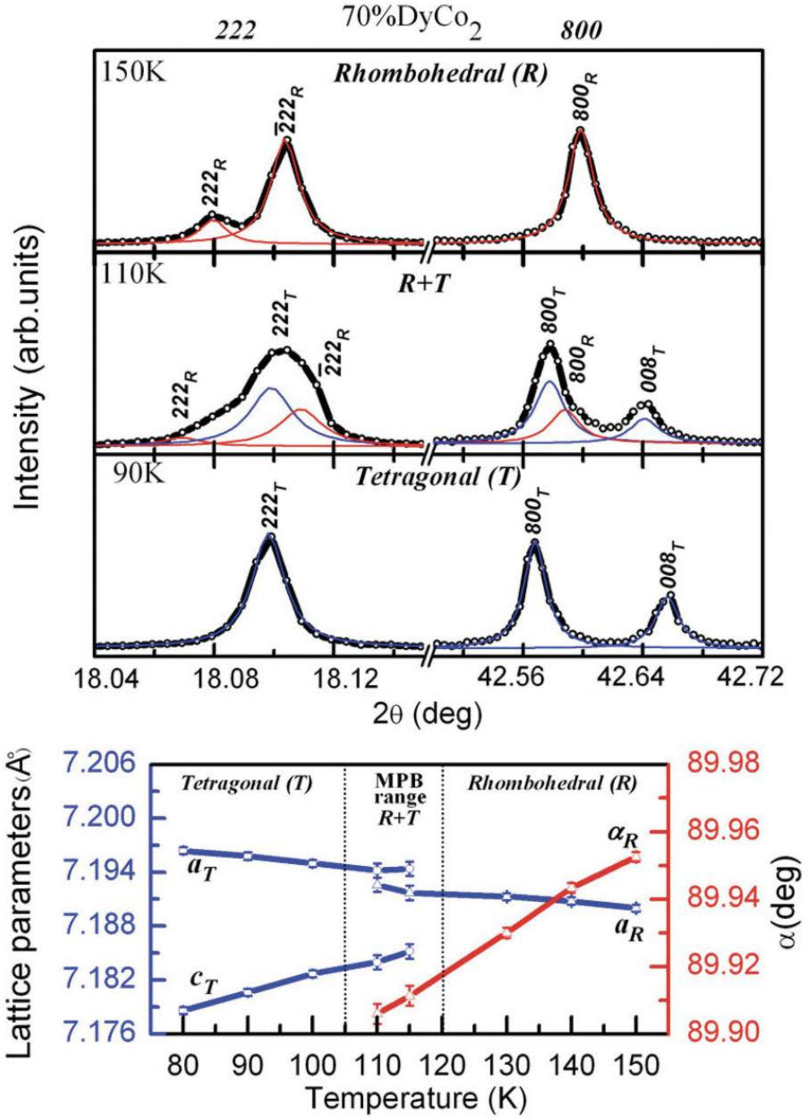

Figure 5.1: Lattice parameter shows mixing of tetragonal and rhombohedral phases within the MPB. Sample is single composition $Tb_{0.3}Dy_{0.7}Co_2$ alloy.[26] It is important to solidify the point that the temperature range for the MPB here is specific to the given composition.

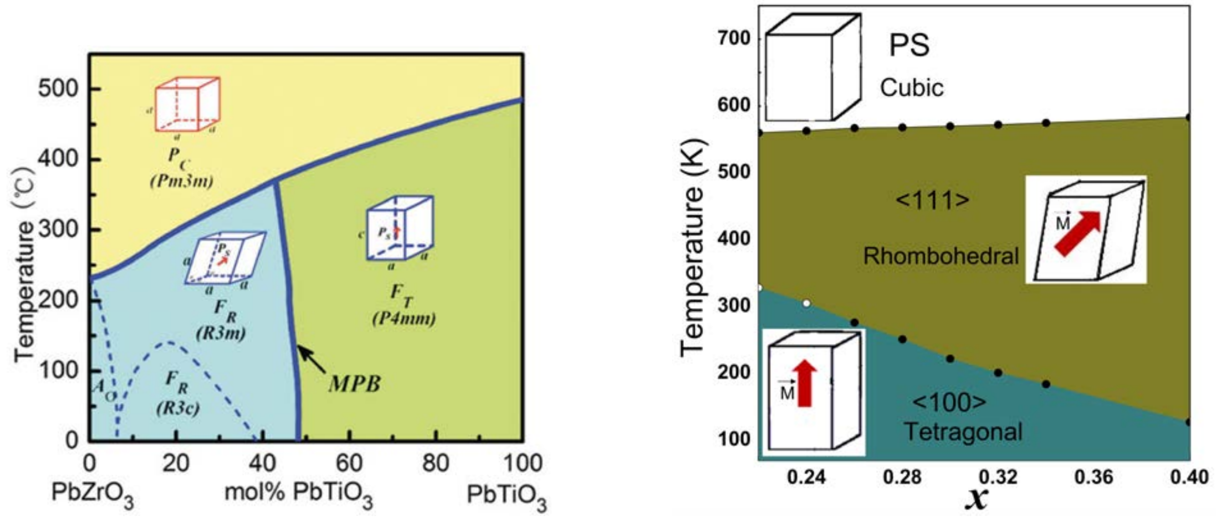

(a) $PbZr_{1-x}Ti_xO_3$[28]

(b) $Tb_xDy_{1-x}(Fe_{0.9}Mn_{0.1})_{1.93}$[159]

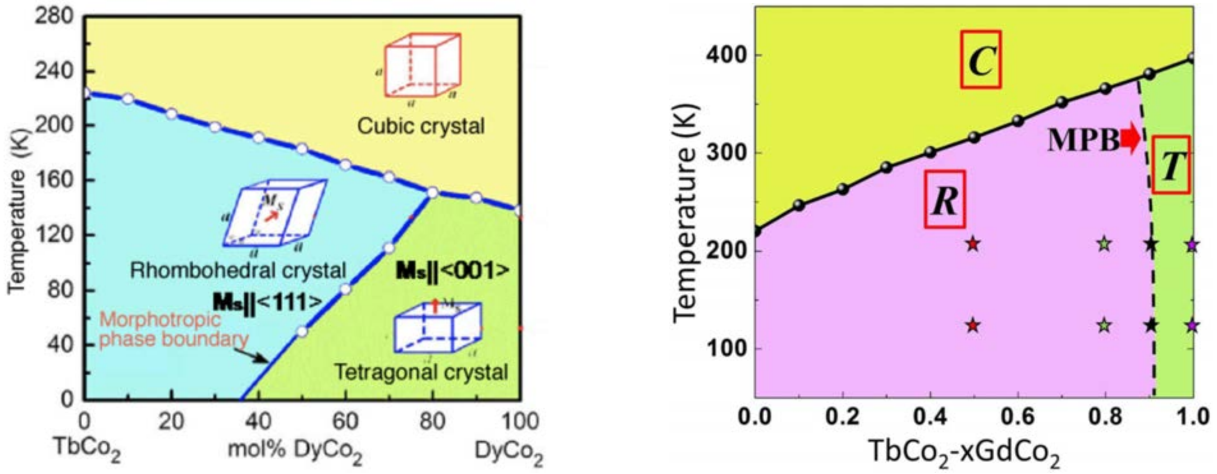

(c) $Tb_{1-x}Dy_xCo_2$[26]

(d) $Tb_{1-x}Gd_xCo_2$[160]

Figure 5.2: Collection of MPB phase diagrams in various different systems.

5.2.1 MPBs in ferroelectrics

Ferroelectricity is the phenomenon of spontaneous polarisation occurring in materials, which is inherently analogous to the phenomena of ferromagnetism which has been discussed in Chapter 2. Examples of polarisation behaviour can be seen in Figure 5.3, which emphasise the similarity in behaviour to magnetic behaviour in ferroic systems by showing the polarisation (P) as a function of electric field (E).[161,162] While following a similar shape in polarisation behaviour, paraelectricity is not widely used for application purposes. The lack of ordering and relatively weak response to an externally applied electric field leaves ferroelectric materials as the stand out candidate for application purposes. Further, antiferroelectricity is another magnetically analogous phenomena, with the polarisation domains aligning anti-parallel with respect to each other[163–165] Antiferroelectricity has large potential in terms of its energy storage density properties and takes a particularly peculiar shape for its $P-E$ hysteresis loop.[166]

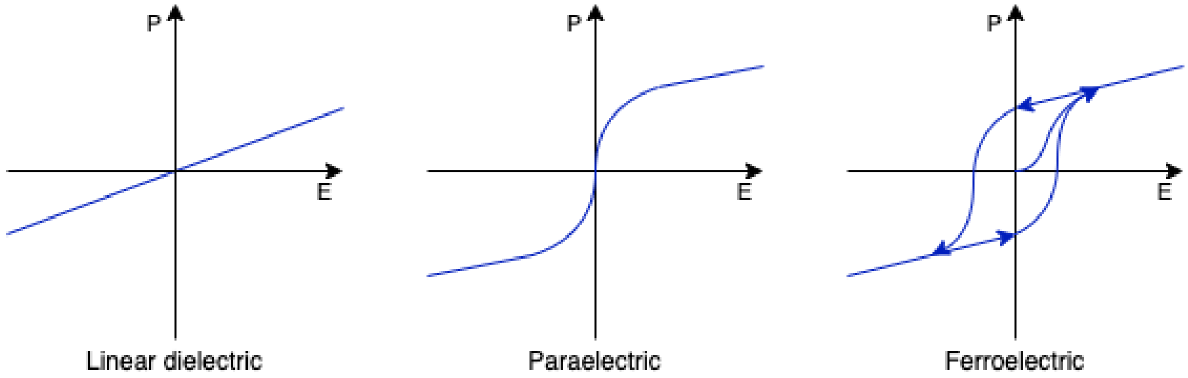

Figure 5.3: Example schematic of different types of polarisation behaviour in ferroic systems. Note, how the hysteretic phenomena in ferroelectric compounds is directly analogous to that in ferromagnetic materials.

The use of morphotropic phase boundaries to enhance physical properties is widespread for ferroelectric materials. Lead zirconate titanate, abbreviated and more commonly referred to as PZT, is a commonly used material due to its large ferroelectric response.[167–169] PZT is a solid solution perovskite, which has an associated MPB between the tetragonal and rhombohedral phases of the parent lead titanate and lead zirconate materials. Jaffe et al first reported the phase diagram of PZT materials and highlighted the presence of a morphotropic phase boundary separating the rhombohedral and tetragonal structures. Figure 5.4 shows some of the data presented by Jaffe et al, specifically the phase diagram and respective unit cell distortions for PZT. It is clear to see that the MPB exists between the ferroelectric rhombohedral and tetragonal phases, with an almost instantaneous jump in the unit cell distortions across the boundary. It is important to mention that a second boundary exists within PZT, however the transition from ferroelectric rhombohedral to anti-ferroelectric orthorhombic is of diminished interest as no mechanical change is induced by external field application, limiting the application potential.[170,171] However, some potential for application exists in other branches, such as microelectronics.

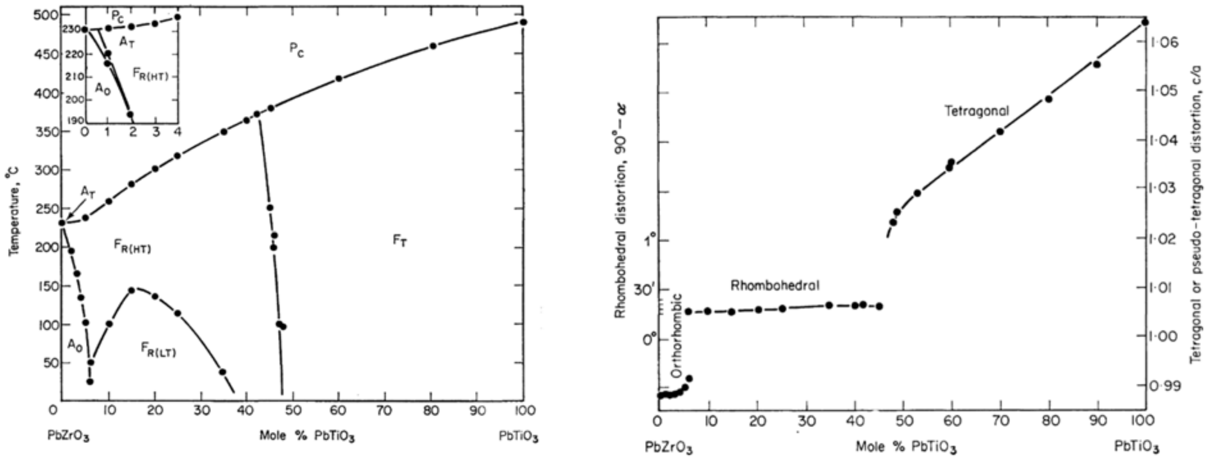

(a) Phase diagram showing the tetragonal-rhombohedral MPB as a function of composition and temperature.

(b) Room temperature unit cell distortion as a function of composition.

Figure 5.4: Phase diagram and unit cell distortions for the PZT system, as found by Jaffe.[30] Phase symbols denote the electric response (**F**erroelectric, **P**araelectric and **A**ntiferroelectric) and the crystal structure (**C**ubic, **T**etragonal, **R**hombohedral (high & low temperature) and **O**rthorhombic).

The mechanism for such large property enhancement at the MPB is a combination of both structural and polarisation factors. Approaching the MPB, the elastic constants soften while the polarisation directions increase due to the co-existence of multiple phases. Within PZT, the tetragonal phase contains six polarisation directions and rhombohedral contains eight.[172] Co-existence of the two phases help to compound the polarisation directions, allowing for a total of fourteen, yielding a large polarisation response while the lattice constants are also more malleable. This combination of properties is the mechanism for the large piezoelectric response seen in the ferroelectric MPB. Figure 5.5 shows how the dielectric coupling and planar constant are significantly enhanced at the MPB position ($PbZrO_3 \approx 52$ mol%).[28]

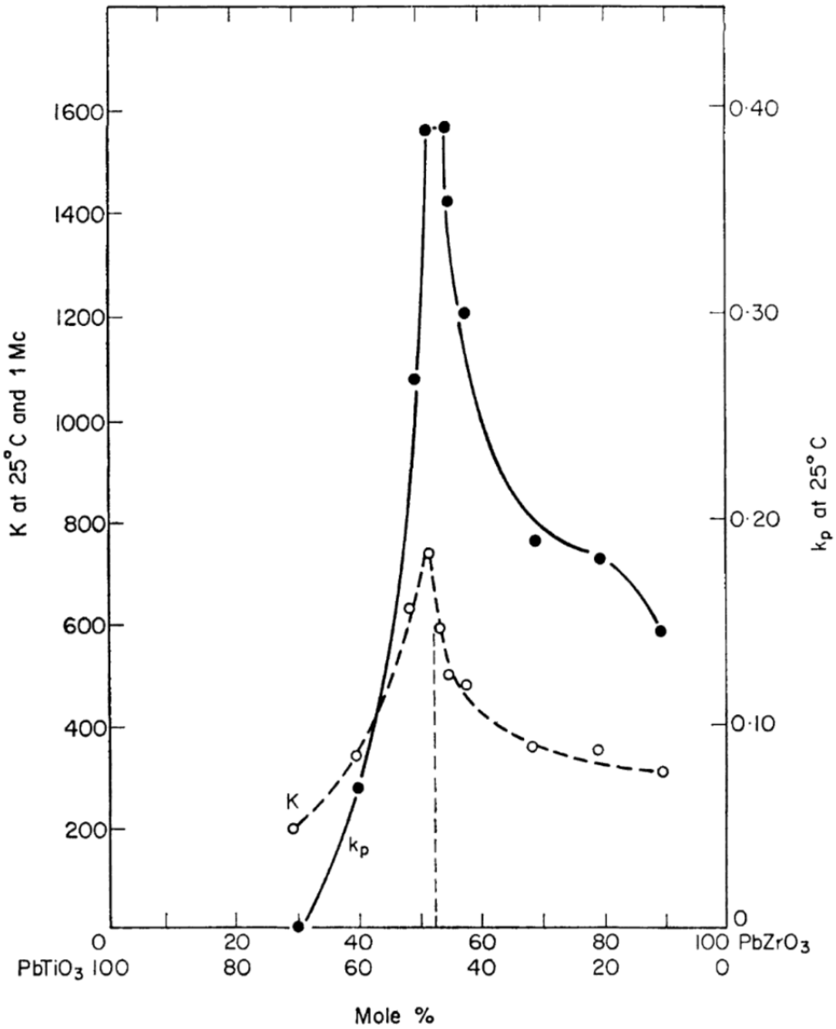

Figure 5.5: Dielectric constant (black circles) and planar coupling factor (white circles) as a function of composition for the PZT system.[28]

Similar enhancement of the physical properties at the MPB position can be seen in other ferroelectric materials. Given the harmful properties of lead, there is a desire to move to lead-free piezo-ceramics, with bismuth sodium titanate ($Bi_{0.5}Na_{0.5}TiO_3$) - bismuth potassium titanate ($Bi_{0.5}K_{0.5}TiO_3$) - barium titanate ($BaTiO_3$) system (abbreviated henceforth as BNT-BKT-BT) showing desirable properties in the exhibited MPB region.[173–175] Figure 5.6 shows the phase diagram of the system, as well as the effect on the piezoelectric constant (d_{33}) with increasing BNT concentration. The piezoelectric constant is a measure of the induced polarisation per unit stress, parallel to the polarisation axis.[176] It is seen that the MPB again separates a rhombohedral and tetragonal structure, occupying a thin region in the phase diagram, with the measurements of d_{33} showing a peak is clearly visible around the MPB composition ($x \approx 0.9$).

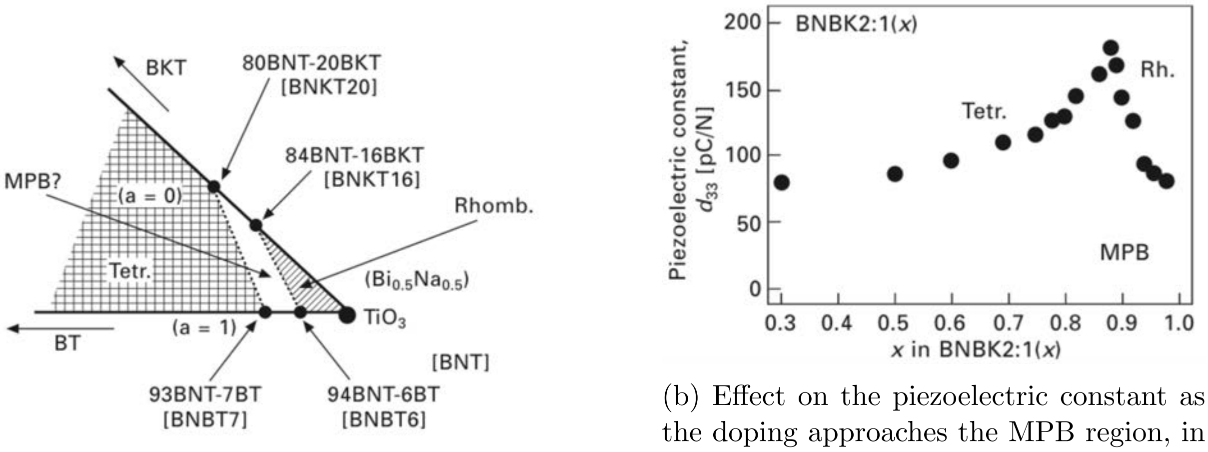

(a) Section of the BNT-BKT-BT phase diagram, encompassing the MPB region.

(b) Effect on the piezoelectric constant as the doping approaches the MPB region, in between the parent tetragonal and rhombohedral structures.

Figure 5.6: Phase diagram section and piezoelectric constant dependancy for varying compositions of the BNT-BKT-BT system.[177]

When considering the application of functional materials, it is crucial to determine their effectiveness at temperature as this ultimately dictates the conditions and opportunities where the material can be utilised. Figure 5.7 shows how the electromechanical coupling factor, k_{33}, differs with temperature for varying compositions in the rhombohedral, MPB and tetragonal regions.[178,179] It is clear to see that the MPB provides superior properties, however, the thermal stability of this region does bring into question the application potential - the 'top shelf' of high coupling factor magnitude is only stable until approximately 100 °C. In contrast, the slightly reduced physical properties of both the tetragonal and rhombohedral reasons are mostly preserved with increasing temperature, with some samples still existing in their 'top shelf' region at temperatures in excess of 200 °C. As

k_{33} is a measure of efficiency for a piezoelectric material to convert mechanical energy to electrical or vice versa, these thermal stability differences may arise to the co-existence of tetragonal and rhombohedral structures limiting the mechanical response. Clearly if a material is designed to be 'on MPB' composition, it is imperative that any temperature changes during operation must not shift the material away from the property enhancement region.

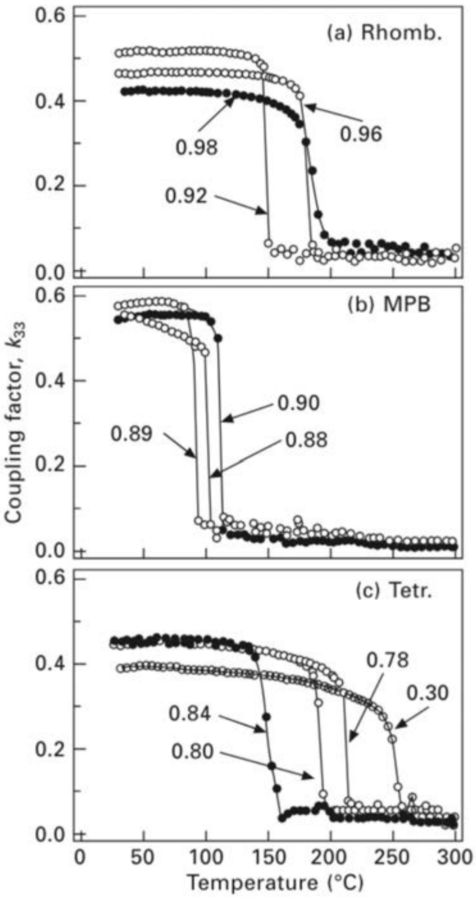

Figure 5.7: Electromagnetic coupling factor as a function of temperature, in three different structural positions a) rhombohedral, b) MPB and c) tetragonal, for various compositions.[177]

The depolarisation temperature, T_d, was interpreted from the results by Takenaka and found to vary significantly around the structural transition. It appears that the depolarisation of the material is highly reflective of the level of tetragonality within the structure, such that T_d crashes at the MPB composition before recovering and continuing its decrease with increasing rhombohedral component.[180]

Combining the results for the piezoelectric constant and depolarisation temperature, the application potential of the MPB region can be visualised. Figure 5.8 shows how d_{33} varies with T_d, while also showing the different structures associated with each region. Application purposes show that the optimal region is one of high depolarisation temperature and high piezoelectric constant (upper right region). Interestingly, the MPB region is shown to widen with increasing temperature for the BNT-BKT-BT system, suggesting that the induced thermal instability allows for greater mixing of the different structural phases at the cost of reduced physical properties. This widening of the MPB is often not seen in ferroelectrics but is seen more frequently in ferromagnetic compounds, such as $Tb_{1-x}Dy_xFe_2$.[31,181,182]

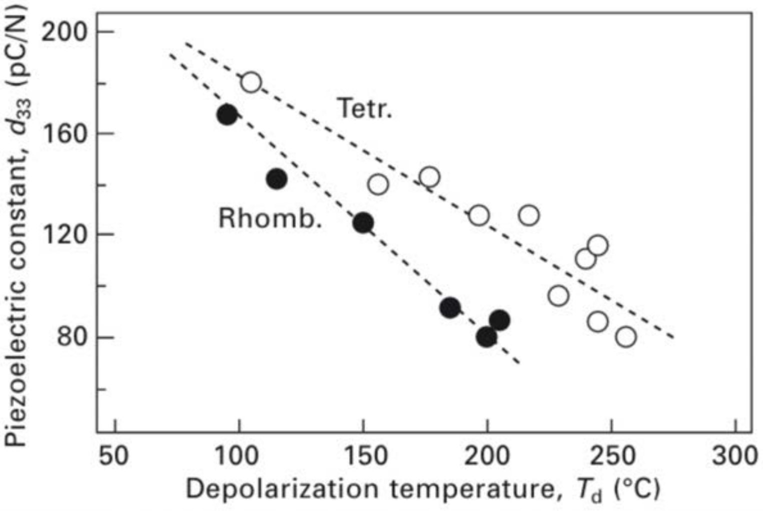

Figure 5.8: Representation of the application potential of the BNT-BKT-BT system, as a function of piezoelectric constant, d_{33}, and depolarisation temperature, T_d.[177]

Finally, the presence of monoclinic phases within the MPB region is of particular importance.[183] As discussed previously, the polarisation potential of a material is a function of the number of equal symmetry polarisation axes. Figures 5.9 and 5.10 show how the number of polarisation axes vary across different crystal structures, with a monoclinic having double that of the slightly higher symmetry orthorhombic structure. Monoclinic structures dwarf those often seen either side of the MPB, providing a potential explanation for the large rise in performance.

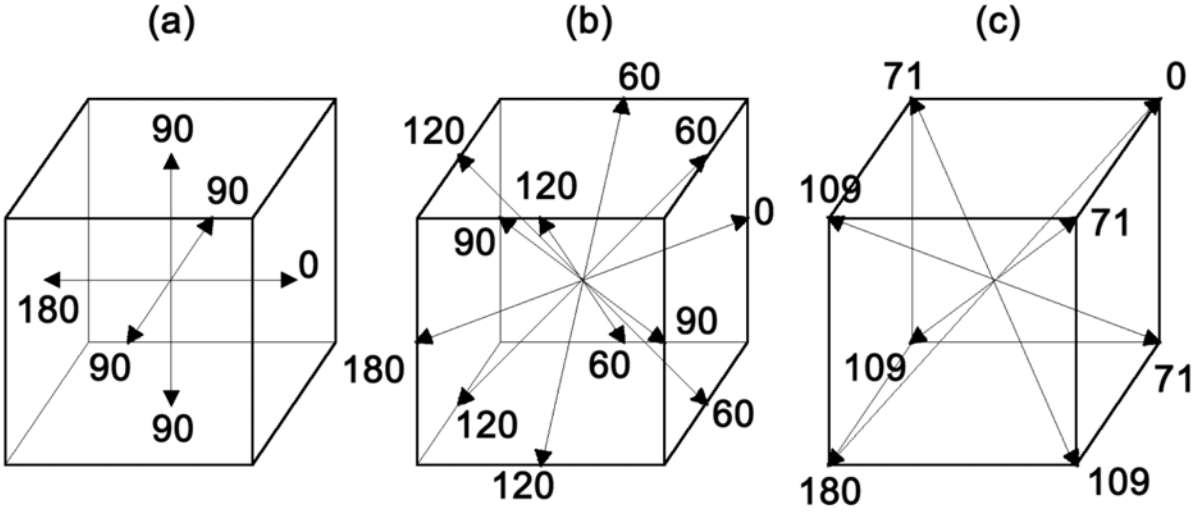

Figure 5.9: Representation of the polarisation axes in **(a)** tetragonal, **(b)** orthorhombic and **(c)** rhombohedral phases. The numbers dictate the angle between the equal symmetry directions.[184]

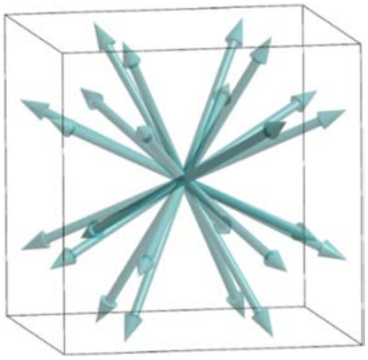

Figure 5.10: Possible polarisation directions for a monoclinic ferroelectric phase.[185]

This phenomenon, predicted and theorised to occur in ferroic materials, largely remained unseen due to the resolution limits on diffractometers until recently. Since then, experimental evidence for briefly appearing monoclinic phases has been discovered.[186,187] One particular example is that by Gorfman et al which presents high resolution, single crystal x-ray diffraction results for two different alloys of lead zirconate titanate.[188] Figure 5.11 shows reciprocal space maps of the Bragg peaks within the $PbZr_{0.69}Ti_{0.31})O_3$ and $PbZr_{0.54}Ti_{0.46})O_3$ single crystal samples studied, with the white lines showing the simulated reflection positions (see caption). By analysing different *hkl* reflections, then mapping the expected reflection positions over the colour maps, it can be seen that a co-existence of rhombohedral and monoclinic phases exists. The presence of a monoclinic

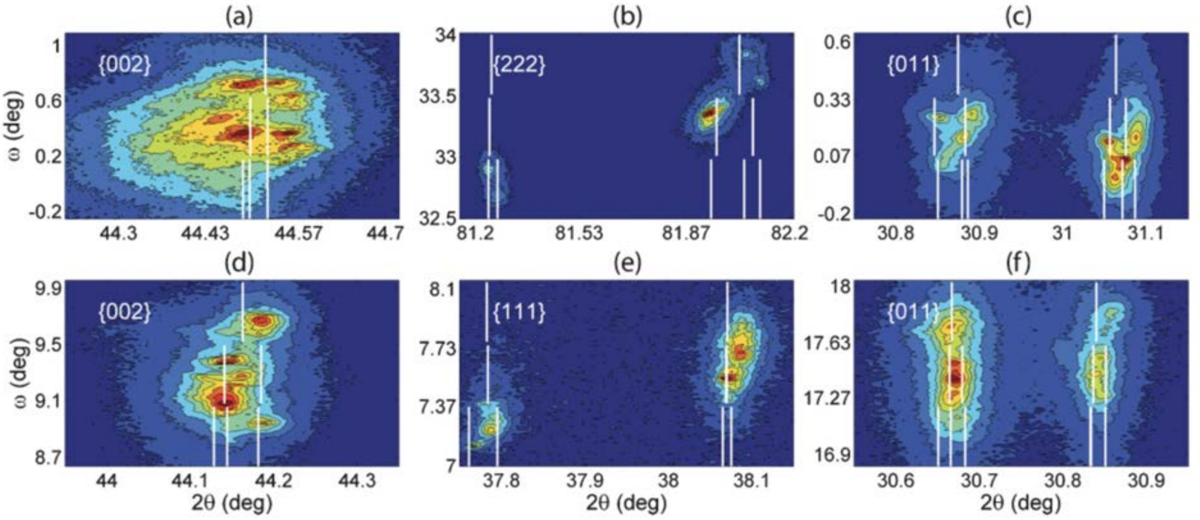

Figure 5.11: Room temperature colour maps for different *hkl* reflections.[188] **(a)**, **(b)**, **(c)** are for $PbZr_{0.54}Ti_{0.46}O_3$, while **(d)**, **(e)** and **(f)** show results for $PbZr_{0.69}Ti_{0.31}O_3$. White lines are the simulated positions for a rhombohedral **(top)**, monoclinic **(middle)** and co-existence **(bottom)** structure.

phase around the MPB does cast some doubt onto previous thinking, where the MPB was considered to be a co-existence of rhombohedral and tetragonal phases.[189,190] While it may be the case that a very small monoclinic phase region exists, this appears to be significantly small. Furthermore, it should be noted that there is an element of inconclusivity with regards to the presence of a third phase or a lower symmetry lattice phase. Compounding this study shortly after, simulation work on PZT compounds were used to investigate the hypothesised monoclinic domains within the MPB.[191] Using a 'standard' MPB model of a rhombohedral-tetragonal barrier, long range electrostatic and elastic interactions were simulated in conjunction with a sixth order Landau polynomial. Results show that the monoclinic phase is expected, existing as hierarchical nanodomains with temperature change. The successful simulation, and therefore hypothesised presence of, monoclinic domains within the MPB is thought to arise due to the long range interactions between the electronic and elastic lattices and the minimisation of polarisation anisotropy approaching the MPB.

5.2.2 MPBs in ferromagnets

Following the chronological drive towards MPB materials being used in application, there has been major interest in replicating MPB-like behaviour in other ferroic materials.[192,193] In 2010, the prospect of MPB behaviour in ferromagnetic materials was observed when Yang et al performed a characterisation study on $TbCo_2$-$DyCo_2$ alloys, with a focus on ascertaining the crystal structures around and within the MPB region.[26] Initial results from Yang showed significant promise, there was indeed a structural change to coincide with the previously seen spin reorientation transition, suggesting that MPBs are indeed evident within ferromagnetic systems (Figure 5.12). This is of particular importance as there are similarities between $TbCo_2$-$DyCo_2$ and $TbFe_2$-$DyFe_2$, most notably in the crystal structure either side of the boundary, as well as the electronic structure and exchange interactions involved, with the RE coupling antiferromagnetically to the transition metal atoms in both systems.[194]

Following the confirmation of an MPB, assisted by their AC susceptibility results which highlighted the MPB existence at 70% $DyCo_2$, the physical properties of the material were explored. As had been performed for the ferroelectrics, the application potential of better performing functional materials was of paramount interest. Study of the MPB region showed a peak in magnetostriction while coercivity was minimised. Optimal properties for a magnetostrictive material can be summarised as a 'figure of merit' (FoM), which can be described as:

$$FoM = \frac{|\varepsilon|}{H_C} \tag{5.1}$$

where ε is the strain and H_C is the coercivity.

Figure 5.13a summarises the measurements. While the magnetostriction shows an unexpected peak during the decrease from rhombohedral to tetragonal structures, the strain measured is not significantly enhanced in itself. However, the coercivity is found to be at a minimum at the MPB composition. This reduced coercivity means that the switching of magnetic moment is less energy intensive, a feature which is incredibly desirable for

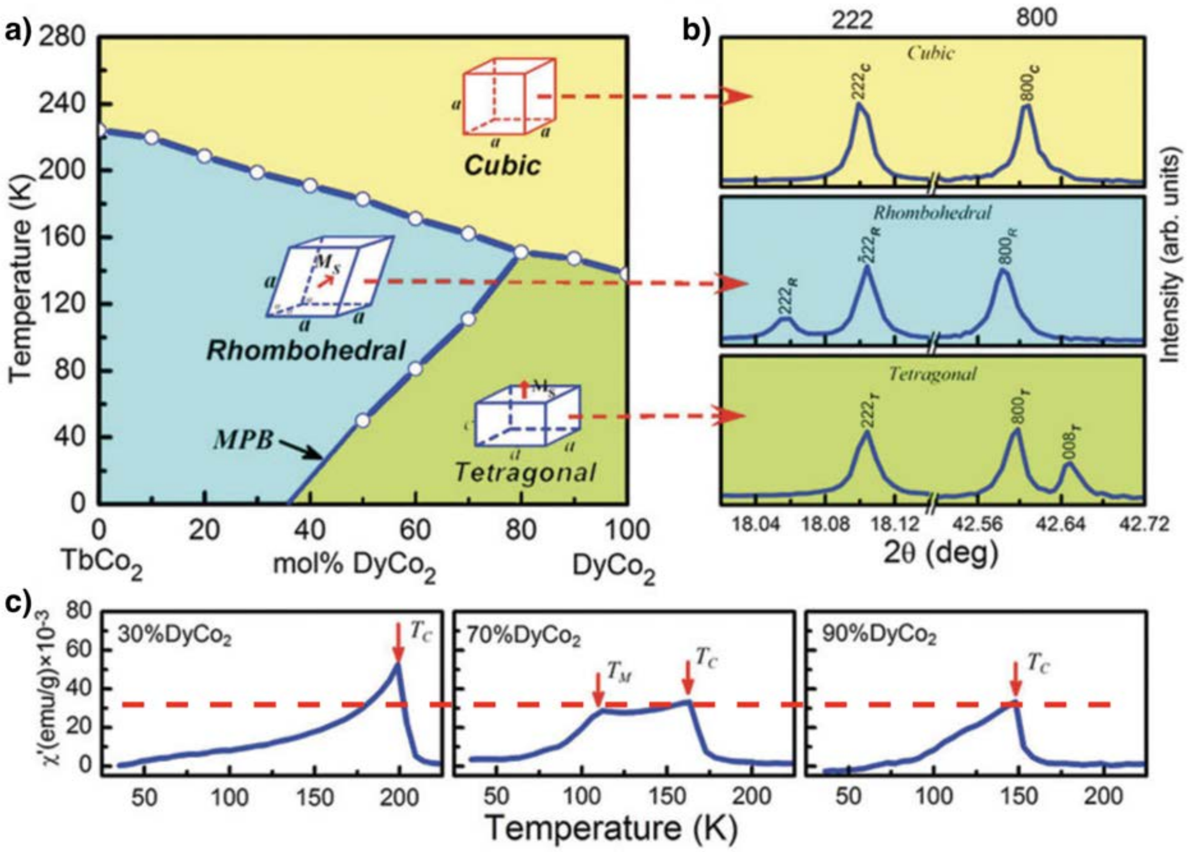

Figure 5.12: Characterisation of $TbCo_2$-$DyCo_2$ system:[26] **(a)** Phase diagram, **(b)** synchrotron XRD results and **(c)** AC susceptibility results as a function of temperature. T_M represents the temperature of MPB transition.

application. This softening of the magnetisation at the MPB composition, with the coercivity being almost a factor three smaller for the 'off-MPB' compositions, implies that the MPB itself has a significant effect on not only the crystal landscape but also the magnetic. Interestingly, the reader should note that the tetragonal side (80% $DyCo_2$) of this compound exhibits switching magnetostrictive behaviour, with the direction of the magnetostrictive coefficient changing sign at approximately ±2 kOe before magnetostriction becomes positive at approximately ±6 kOe (Figure 5.13a.g). This is an example of the peculiar temperature dependence of magnetism-crystal interactions.

Figure 5.13b presents a brief portion of the synchrotron measurements performed by Yang et al.[26] Here they show the rhombohedral to tetragonal transition with decreasing temperature. Notice how the peak broadening arises from the co-existence of the two phases, with the (222) peaks increasing separation and widening (with a Gaussian characteristic)

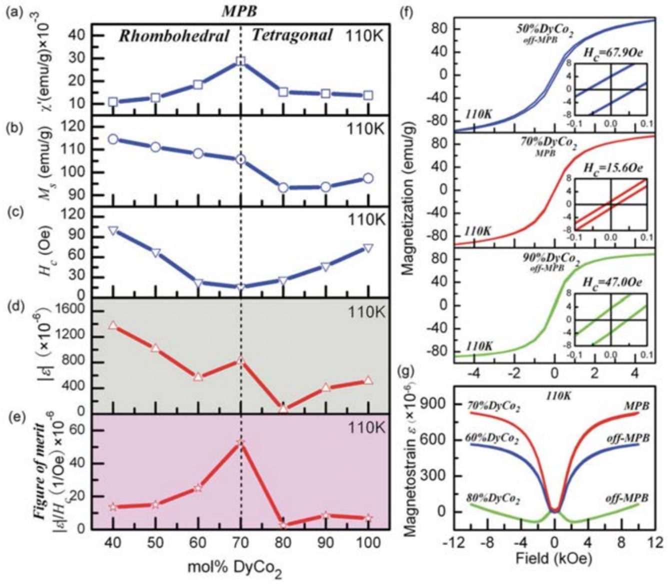

(a) Summary of the magnetic property measurements performed around the MPB. **(a)**, **(b)**, **(c)** and **(d)** are AC susceptibility, saturation magnetisation, coercivity and magnetostriction respectively. **(e)** is the figure of merit calculated using Eq. 5.1. **(f)** and **(g)** show magnetisation and magnetostrictive behaviour with applied field.

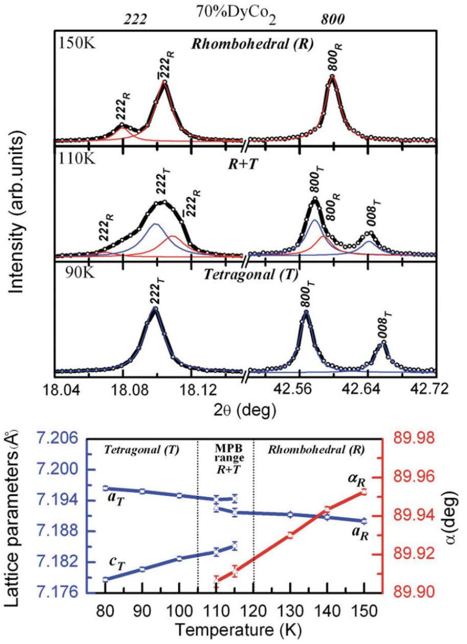

(b) Synchrotron XRD results showing the change in peak splitting and lattice parameters as a function of temperature across the MPB.

Figure 5.13: Summary of results for $TbCo_2$-$DyCo_2$ system.[26]

as the single tetragonal peak forms. The opposing situation happens at the (800) peak, with the rhombohedral reflection melting and the tetragonal peaks forming and separating. Extracted lattice parameters show a discontinuity for the a_T and a_R parameters within the MPB region, while the rhombohedral angle α_R is found to rise with increasing temperature, tending towards 90° upon approach to the rhombohedral-cubic transition. The maximisation of magnetostriction within the MPB region is not unique to $Tb_{1-x}Dy_xCo_2$ based systems. Following their work on confirming the structural transitions occurring in $DyFe_2$ and Terfenol-D,[110] Yang and Ren continued their investigation in the $TbFe_2$-$GdFe_2$ MPB system.[195] While this MPB was found to be significantly more compositionally stable across a wide temperature range (remaining fairly vertical, Figure 5.14a), the enhancement of magnetic properties at the MPB was confirmed to exist in this system (Figure 5.14b). Near vertical MPBs, i.e. phase boundaries which are stable with temperature, are desirable for application purposes as the stability of the physical properties unlocks new potential uses.

One difference between the otherwise similar MPB systems of $TbCo_2$-$DyCo_2$ and $TbFe_2$-$GdFe_2$ is the behaviour of the magnetostriction curve around the MPB region. For the cobalt based samples the magnetostriction retains a positive gradient up to 10 kOe for the MPB composition, whereas once the structure becomes dominantly tetragonal the magnetostriction is negative for low fields before switching and recovering to a positive magnetostriction at high fields (Figure 5.13a). In comparison, the iron based $TbFe_2$-$GdFe_2$ shows a visibly more rapid change to the 'switching gradient' type curve upon movement to the tetragonal side of the MPB. Furthermore, the change is reverse, initially having positive gradient and then switching and recovering to take negative magnetostriction values, however this is easily attributed to the magnetostrictive properties of the parent compounds being inherently different, highlighted previously by AE Clark et al.[25] Further information of importance is the field dependency of the magnetostrictive response and the underlying mechanism which can be attributed to that. It was found that for all values of field, the rhombohedral domains would elongate with the field direction, leading to a positive and diminishing gradient to the magnetostriction (V-shape). Less trivially, at low magnitudes of applied field the tetragonal domains would elongate with the field (caused by the elimination of domains which directly oppose the field) before the perpendicular domains collapse and there is a shrinking in the field direction, producing an M-shape to the magnetostriction curve.

Examining the magnetostrictive curves within the MPB region, the low field behaviour of the two lattice structures work in tandem, yielding a V-shape to the magnetostriction curve. Approaching high fields, the second step of domain switching causes the shrinking seen in the tetragonal region while there is also a sacrificial quenching of the rhombohedral domains, in turn creating a loss in strain. While the values are expected to remain positive up to very high fields for the MPB composition, it is imperative to highlight that the parent compound $GdFe_2$ showed net negative magnetostriction at high fields due to the 180° domain switching. Conclusions drawn from this suggest that the parent compounds of any MPB system must have sufficiently different magnetisation directions (which is so for rhombohedral-tetragonal MPB) such that the anisotropy of the system is reduced approaching the MPB, allowing for easier domain switching. To coincide with this, there must also be a resolvable difference in magnitude of lattice distortion for the parent phases, such that there is a net distortion occurring.

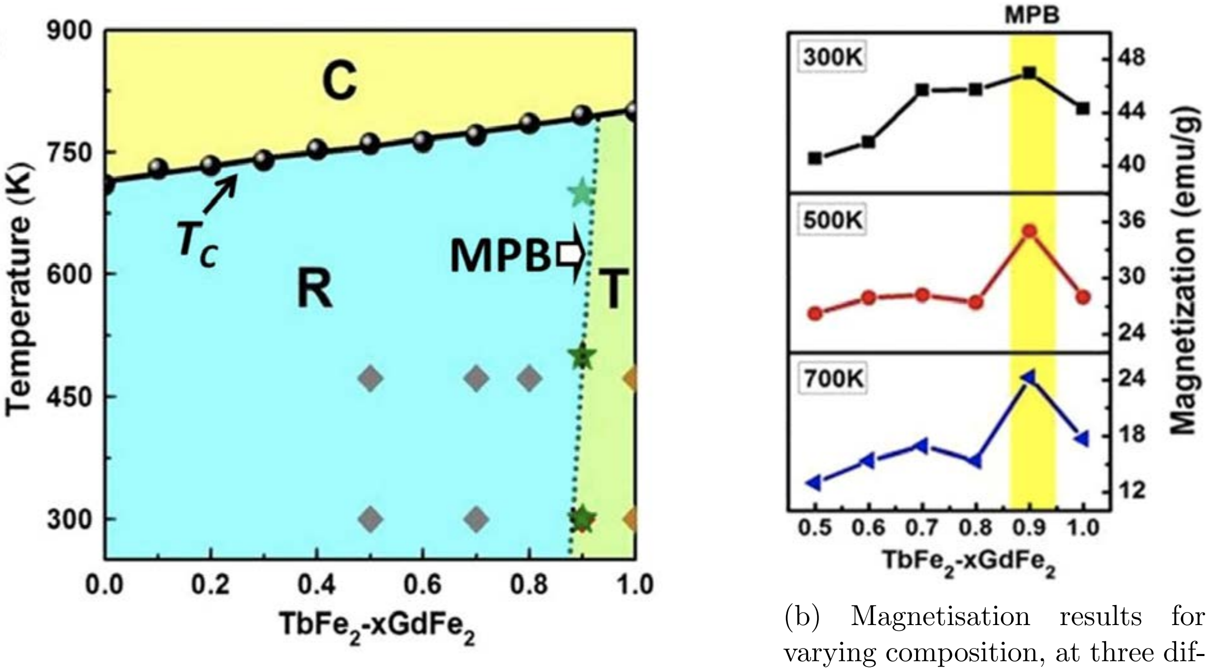

(a) Phase diagram for the $TbFe_2$-$GdFe_2$ system.

(b) Magnetisation results for varying composition, at three different temperatures.

Figure 5.14: Summary of results for $TbFe_2$-$GdFe_2$ system.[195] Symbols within the phase diagram represent Curiie temperature measurements (circles), XRD structure measurements (diamonds) and magnetic hysteresis measurements (stars).

To anticipate MPB behaviour, one can use these two metrics as a representation of the types of MPB behaviour possible. When considering the magnetisation directions of the phases either side of the MPB, there exists two scenarios: one where the directions are sufficiently different leading to a reduction in anisotropy at the boundary, and one where the directions have a degree of common alignment (which may occur with some of the lower symmetry phases hypothesised to appear around MPBs), therefore the system will retain a larger degree of anisotropy. However, as the directions converge, the anisotropy will remain but the energy requirement will lessen. The impact of this will determine the ease of domain switching and magnetisation. Regarding lattice distortions, it has previously been shown that the co-existence of rhombohedral and tetragonal phases can lead to a reduction in magnetostriction at high values of field due to domain switching losses.[196] For the case of $TbFe_2$-$GdFe_2$, a positive magnetostriction is retained at the MPB due to the rhombohedral distortion being significantly larger than that of the tetragonal, however this may not necessarily be the case for all materials. Magnetostrictive coefficient of the relevant distortions will also play a factor.

Hence, there is an interplay at the MPB which is heavily dependent on the parent compounds - a phenomena which is echoed in the ferroelectric systems discussed prior. The effects of differing magnitudes of lattice distortions is fairly well documented:

$TbCo_2$-$DyCo_2$ system Here the magnetostriction of the Tb parent phase is sufficiently higher than Dy parent phase. Therefore, this leads to relatively high values of magnetostriction at the MPB composition (Figure 5.13a).[26]

$TbCo_2$-$GdCo_2$ system Within this system, the lattice distortions of the parent compounds are roughly equal, leading to a negligible magnetostriction at the MPB.[160]

$TbFe_2$-$GdFe_2$ system Difference in distortion is quantifiable but small, resulting in a low magnetostriction at the MPB. Within the system, the enhanced saturation magnetisation at the MPB is found to become more prominent, in comparison to the parent phases, as temperature increases.[195]

Later work performed on $TbFe_2$-$GdFe_2$ presents data which expands their previous work, suggesting that the saturation magnetisation is minimised at the MPB for all temperatures for high values of field.[197] Room temperature measurements performed at 60 kOe show that the MPB composition has the lowest M_{Sat}, whereas the previous measurements (300 K, 10 kOe) found the saturation magnetisation to be higher than the surrounding phase region. Not only would this suggest a very large anisotropy (explaining why saturation is not reached even at large fields) but also that the interactions between the rare-earth and transition metal sublattices are heavily dependent on the elements involved.

MPB regions have also been found to show anomalous, or reverse, behaviour. $TbCo_2$-$NdCo_2$ was found to exhibit a minimised saturation magnetisation within the MPB (Figure 5.15), a phenomenon not often seen in other similar binary alloys.[198] This minimisation is believed to occur due to the compensation of rare earth sublattices at the MPB position. Light RE elements (in this case Nd) will couple ferromagnetically to the transitional metal (Co), whilst heavier RE elements (Tb) will form an anti-ferromagnetic exchange. When the structure is heavy on the Tb side, the anti ferromagnetic coupling will lead to a net magnetisation in the direction of the Tb atom, or more importantly, in the opposite direction to that of the Co atom. Approaching the MPB position, there is an increasing opposing magnetisation from the Nd side, as the magnetisation lines up with the Co atom, leading to a compensation of the magnetisation at the MPB.

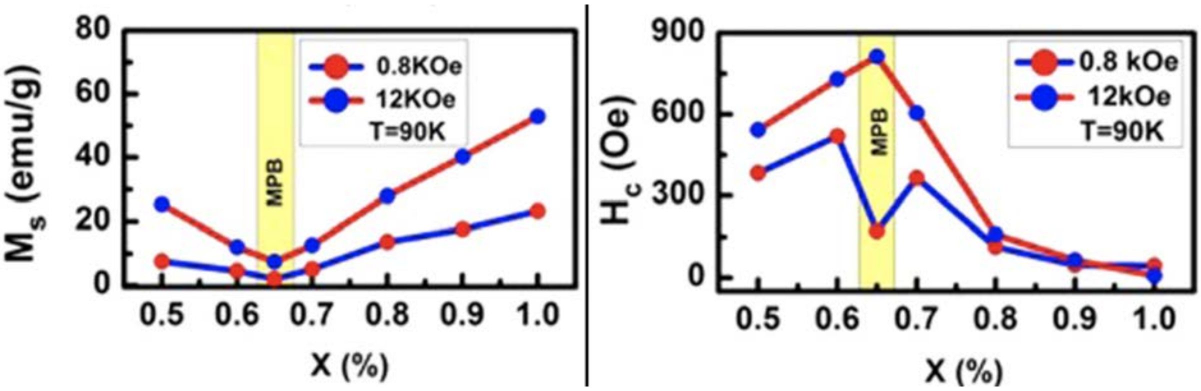

Figure 5.15: Saturation magnetisation **(left)** and coercivity **(right)** results as a function of composition for the alloy $Tb_{1-x}Nd_xCo_2$.[198]

Another phenomenon seen in $Tb_{1-x}Nd_xCo_2$ alloys is that of a low temperature magnetic transition. Believed to be caused by the temperature dependence of the RE and TM sublattices, the stabilisation of easy magnetisation direction is affected by the temperature reduction. The low temperature phase for this material is orthorhombic but other low symmetry phases, such as monoclinics, could be expected as the ionic radii of the elements involved can differ relatively largely.

Simulation results on ferromagnetic MPBs have been performed in similar capacities to that of the ferroelectric compounds. Monte Carlo calculations combining the anisotropy, exchange, magnetostatic and external field energies were used to investigate the differences in domain structure for low and high barrier cases of MPB.[199] It was found that the formation of a monoclinic phase is heavily dependent on the degrees and dominance of the interacting energy terms. Monoclinic domains are energetically favourable for magnetostatic and exchange energies but not so for the anisotropy energy. Where anisotropy energy is dominant, such as sufficiently far from the MPB, then monoclinic domains are not developed. However, as the anisotropy collapses at the MPB and providing the magnetostatic and exchange energies are sufficiently high, then monoclinic domains will exist among the expected tetragonal and rhombohedral domains.

5.2.3 Morphotropic phase boundary vs spin reorientation boundary

It is important to make a clear distinction between the process of transition through a morphotropic phase boundary and a spin reorientation transition (SRT). While both result in the shifting of the magnetic easy axis due to a compositional or thermal change, the mechanism behind the change is significantly different.

Take the cases of $TbCo_2$-$DyCo_2$ and $HoFe_2$-$ErFe_2$ as presented in Figure 5.16.[199,200] Both materials are ferromagnetic in nature and were studied using XRD and Mossbauer (for $TbCo_2$-$DyCo_2$ and $HoFe_2$-$ErFe_2$ respectively) to determine the phase diagram. Upon cooling, both materials exhibited a shift from a magnetic easy axis of [111], with the Co system preferring a [100] and the Fe system favouring the [110] direction.

The significant difference between the systems is not one of directionality, but of shifting mechanism - importantly an MPB transition involves a movement from one crystal structure to another, as well as a changing in magnetisation direction. SRT do not undergo a lattice change. $TbCo_2$-$DyCo_2$ changes its easy axis via an adaptive phase - whether that is a low symmetry phase such as a monoclinic or a co-existence of tetragonal and rhombohedral phases through the MPB is yet to be confirmed. This phase mixing is roughly analogous to that of nucleation and growth in metallurgical systems. In contrast, the

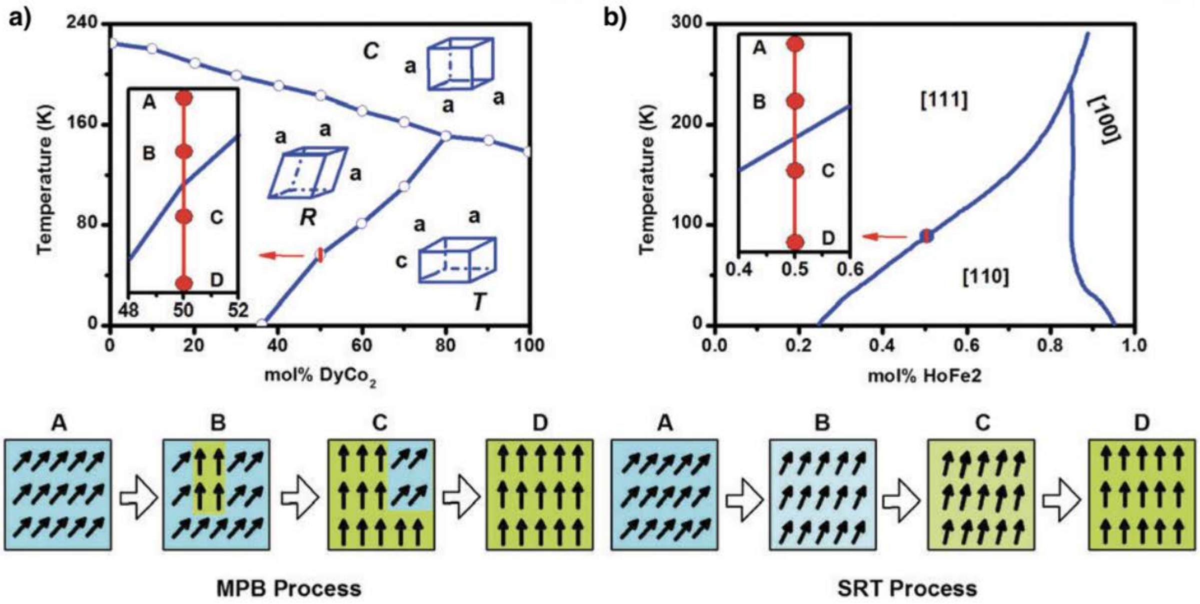

Figure 5.16: Phase diagrams and schematic mechanisms of MPB and SRT for the $TbCo_2$-$DyCo_2$ and $HoFe_2$-$ErFe_2$ systems respectively.[199,200]

cooling transition in $HoFe_2$-$ErFe_2$ occurs by spin reorientation - the magnetic moments remaining in parallel alignment and rotating through the transition, with no structural change exhibited.

The difference between these two transition types is crucial. Monoclinic phases have been speculated to appear within MPB materials, however their presence and mechanism for appearance is yet to be determined. Across a bulk material, a non-trivial easy magnetisation direction (some arbitrary angle between the [001] tetragonal and [111] rhombohedral, $0 < \theta < 54.7$) can be achieved with both mechanisms. A shifting concentration of phases in a co-existence will lead to the same net direction rotation as a direct spin reorientation of the magnetic moments. Monoclinic phases could exist as part of both mechanisms, either as a dominant phase in a co-existence or as a naturally occurring phase seen during the reorientation. It has been speculated by simulation, that the energetics of the system will determine the type of transition. Anisotropy favours a co-existence, arising due to the preference for domains to remain aligned to the so called 'trivial' easy axis directions of the parent phases. Conversely, when anisotropy is weak and the energetics are dominated by magnetostatic and exchange energies, the presence of a monoclinic is confirmed (by simulation) to appear.

5.3 Morphotropic phase boundaries within $\mathbf{Tb}_{1-x}\mathbf{Dy}_x\mathbf{Fe}_2$ alloys

When first manufactured, Terfenol-D was almost instantly a market leader for its large magnetostriction, with significantly desirable properties found to exist at particular compositions. Subsequent research proved that these properties came from a precise balance of the magnetocrystalline anisotropy constants and heralded the presence of a morphotropic phase boundary between the parent rhombohedral and tetragonal phases.[14]

This thesis builds upon the synchrotron XRD work performed by Bergstrom et al, which is currently the most comprehensive phase diagram for $TbFe_2$-$DyFe_2$ alloys and is shown as Figure 5.17.[29] Comprising of XRD measurements (dashed line), magnetometry data (solid line), Mossbauer results (symbols)[32] and single ion mean field theory calculations (shading), the phase diagram shows how the MPB separates the [111] and [001] easy magnetisation directions, while also highlighting that non-trivial directions exist within the MPB and at low temperatures. Synchrotron measurements were performed over a relatively small composition and temperature range (0.65<Dy at%<0.78, 150K<T<350K). All of the measurement techniques agree well in the region of synchrotron data, thusly the MPB position is confirmed to exist in that composition and temperature range, clearly dividing regions of tetragonal and rhombohedral structures as expected. However linear extrapolation of the diffraction results would begin to contradict with the Mossbauer and theory results - both of which suggest the existence of non-trivial easy axis directions at low temperatures ($0.5<x<0.6$, $T<100$ K). As has been seen in other MPB-containing materials, the MPB width is shown to widen with increasing temperature as the co-existence of rhombohedral and tetragonal phases becomes easier. The expansion of synchrotron XRD data calculated in this thesis, is aimed to explore the higher temperature regions of the MPB, while also attempting to probe the low temperature, non-trivial directions

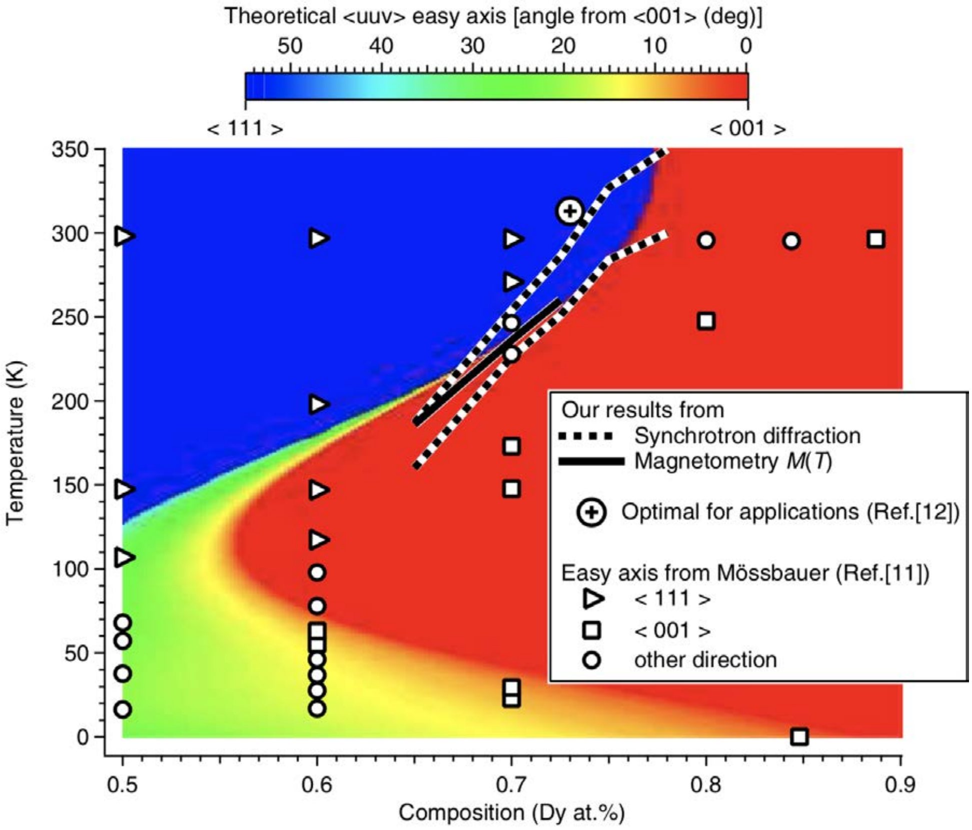

Figure 5.17: Summary of work created by Bergstrom et al on the near room temperature MPB in $Tb_{1-x}Dy_xFe_2$.[29] The colours show the easy magnetisation direction, derived from crystal field theory simulations, while the other symbols are detailed in the key. Mossbauer and application data taken from refs[32,33]

predicted by the crystal field theory results.

Chapter 6

Methodology

This chapter will present the planning, experimentation and data analysis practices which were used throughout the studies enclosed in this thesis. Beginning with a discussion of the material preparation steps, with a specific focus on the arc melting fabrication method used to create alloys of $Tb_{1-x}Dy_xFe_2$, the focus will then shift to a discussion of the beamline techniques used for measurements - specifically small-angle neutron scattering (SANS) and synchrotron X-ray diffraction (sXRD). As the theory, instrumentation and data analysis of these processes are all paramount, they will be presented thoroughly with a spotlight on the specific conditions and experimental set-up used in this thesis. Finally, the analytical methods of peak fitting and parameter tracking will be presented alongside a brief discussion of the packages and fitting profiles used.

6.1 Material preparation

The samples used in this study were $Fe_{68.8}Pd_{31.2}$ and a range of $Tb_{1-x}Dy_xFe_2$ alloys. The FePd single crystal samples were prepared by Takashi Fukuda & Tomoyuki Kakeshita at the Department of Materials Science and Engineering, Osaka University, using the floating zone method. To maximise the efficiency of this study, a 24 hr heat treatment at 1100 °C was performed before the encapsulated sample was quenched into ice water to maximise the degree of martensitic character. Finally, the produced single crystal rods were cut into disks of 6 mm diameter and 2 mm thickness, resulting in single crystals with well defined crystallographic directions that are suitable for SANS (where transmission is crucial and therefore sample thickness must be controlled).

For the fabrication of $Tb_{1-x}Dy_xFe_2$ alloys, the dysprosium and terbium constituent materials used were solid samples of the respective RE metals of 99.99% purity. These hexagonal close-packed materials were kept under vacuum in the rare-earth store (10^{-7} mbar) at the School of Metallurgy & Materials, University of Birmingham when not in use to prevent oxidation and preserve quality. During use, care was taken to limit the material's exposure to air during processing, however exposure to air cannot be helped when loading the samples into the arc melting furnace as there is no option for inert loading. However, while Dy and Tb oxidise quite rapidly in moist conditions or at elevated temperatures, visual inspection showed very little oxidation during the loading process and was used to mitigate against unintentional addition of oxygen to the samples. Constituent materials were measured to within a tolerance of 1 mg and the resultant compositions were calculated, using the measured masses to determine the atomic % of each element.

6.2 Alloy fabrication using the arc-melting technique

Comprising of an airtight chamber (with controlled inlet flow of high purity argon and connected to a rotary pump for evacuation), water cooled Cu sample hearth, sparking electrode and the relevant high current sources and transformers - arc melting is a versatile technique which employs the use of a localised high energy spark from the electrode tip, directed at the constituent materials to induce melting, while the argon atmosphere acts as an inert fill gas for spark transmission. The localised heating of the spark, or "arc" allows for the melting of high melting temperature (T_m) materials within short time scales, as well as easy alloying of transition metal and rare-earth elements. The Ar atmosphere is necessary to transmit the spark but also plays a role in reducing the possibility of sample oxidation. The equipment used for the alloy preparation is shown in Figure 6.1.

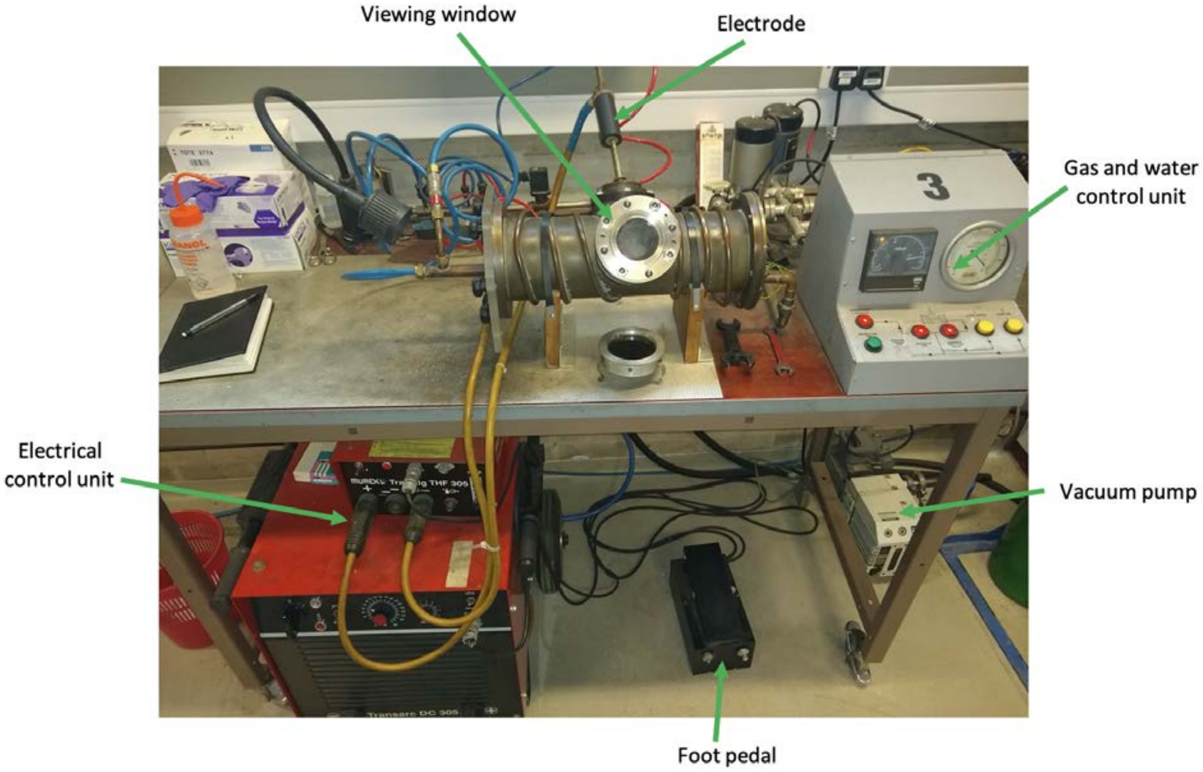

Figure 6.1: The arc melting kit at the University of Birmingham used for this project.

The importance of a low oxygen content in the melting chamber is significant, therefore a number of steps were taken to ensure that the melting environment was as desired. Firstly, the Ar purity was 99.998%, with a preference to using a fresh bottle when starting batch melting - this reduces the chance of moisture ingress into the system, an undesirable factor when bottle pressure drops to ≈50 bar. Secondly, there was a minimum of three pumping and flushing operations which were recommended and considered a standard for operation. In reality, for samples of high sensitivity, the chamber was pumped for longer and flushed more frequently before operation to further reduce the oxygen content. Finally, multiple heating of a titanium getter inside the chamber was employed to lock up any residual oxygen not removed during pumping and flushing. Ti getters are commonly large samples, designed so that heating does not cause melting and to absorb the maximum amount of oxygen possible.

The arc is generated through use of a voltage transformer which in turn generates a large current (on the order of 90 A) enabling easy melting of materials with T_m in the region of 1500 °C, namely those used in this experimentation: terbium, dysprosium and iron. The contact temperature of the arc is variable with the distance of arc travel and the localised temperature often exceeds that of T_m, however superheating is avoided due to the constant water cooling supplied to the copper hearth, on which the samples sit. To promote homogeneity in the samples, multiple melting and solidification operations were performed (minimum of three) and the sample was manipulated in between melts, such that the melting occurred at multiple surface points. Given the small volume of powder needed for synchrotron XRD and the large price for both Dy and Tb, sample sizes were kept to a minimum where possible. The average sample mass was approximately 0.5 g and the resultant sample shape was spherical, with mild shape inconsistencies that have little consequence as samples are eventually pulverised into powder for characterisation. Larger samples were attempted however it was found that porosity and rare-earth boil off became significant in these samples, producing detrimental samples with undesired compositions and morphology.

Table 6.1: Sample number designation and compositional details of the $Tb_{1-x}Dy_xFe_y$ samples created and measured in the synchrotron XRD study. x_f and y_f represent the fabricated (or calculated) composition, whereas x and y are the assumed composition to a lower precision.

Sample	x_f	y_f	**x**	**y**
1	0.562	2.006	**0.56**	**2.01**
2	0.599	2.006	**0.60**	**2.01**
3	0.642	2.020	**0.64**	**2.02**
4	0.650	2.049	**0.65**	**2.05**
5	0.664	2.027	**0.66**	**2.03**
6	0.701	2.010	**0.70**	**2.01**
7	0.752	2.011	**0.75**	**2.01**
8	0.787	2.015	**0.79**	**2.02**
9	0.871	2.012	**0.87**	**2.01**

Table 6.1 details the sample number and compositional information for the arc melted samples which were used for the synchrotron XRD investigation into the MPB. An assumption is made that as arc melting is known to produce a slight amount of RE boil off, which will have some small effect on the fine composition balance between the Tb and

Dy elements. Furthermore, it is fair to assume and allocate an uncertainty of ±0.01 to both x and y which factors in the RE boil off but also a consideration of the presence of impurity phases (in low concentrations, on the order of $< 1\%$) - some of which may be oxide compounds that form readily with RE phases.

6.3 Neutron and X-ray scattering techniques

Reciprocal space scattering techniques probe the surface as well as the bulk of samples and can retrieve information about sample properties such as overall crystal structure and/or size distributions of scattering bodies within the sample.[201–203] Small-angle neutron scattering and synchrotron X-ray diffraction are two such techniques which rely on elastic scattering between incident radiation and localised material features. One of the key parameters in scattering is that of the scattering vector, $\boldsymbol{q}$, which is defined as the difference between the incident neutron wavevector, $\boldsymbol{k_i}$, and the resultant wavevector, $\boldsymbol{k_f}$.

$$\boldsymbol{q} = \boldsymbol{k_f} - \boldsymbol{k_i} \tag{6.1}$$

In the elastic limit, where the scattering angle between incident and final waveforms is approaching zero, the small-angle approximation allows for $\sin\theta \approx \theta$ and the scattering vector becomes a measure of the momentum transfer and the modulus of q can be taken to produce a relationship between the scattering vector, wavelength and scattering angle.

$$|\boldsymbol{q}| = \frac{4\pi}{\lambda_N} \sin\theta_B \tag{6.2}$$

The wave-particle duality of neutrons and photons is of particular importance when one considers the Bragg condition (Eq. 6.3) which is necessary for scattering theory, especially so for the case of uniform, long-ordered crystal structures. Bragg's law is:

$$2d \sin\theta_B = n\lambda_N \tag{6.3}$$

where d is the physical distance between scattering planes, θ_B is the Bragg angle (or half the scattering angle), n is the order of scattering and λ_N is the wavelength of the neutron (or scattering particle). Figure 6.2 is a schematic representation of the Bragg condition.

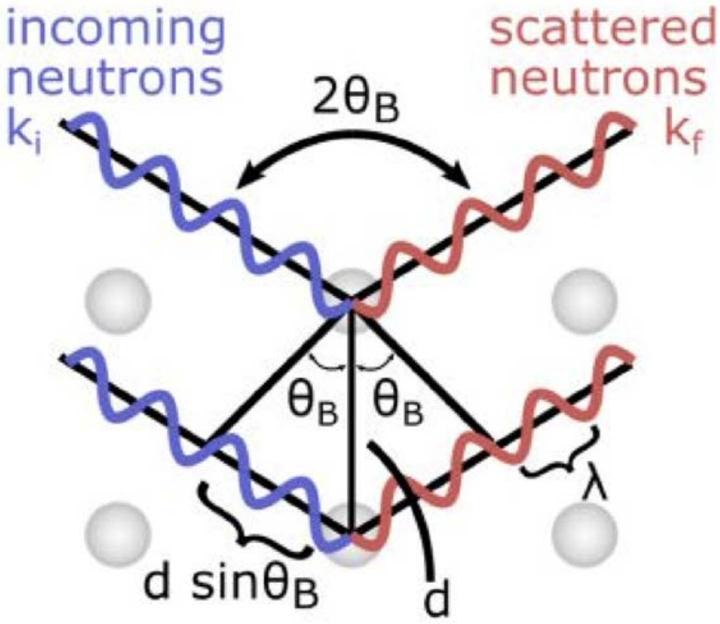

Figure 6.2: Schematic representation of elastic scattering, particularly the Bragg condition which is crucial for SANS.[56]

Rearrangement of Eq. 6.3 and insertion into Eq. 6.2 yields the important relationship between the reciprocal space scattering vector (units of $\mathring{A}^{-1}$) and the real physical distance, providing the features are ordered and long ranged.

$$q = \frac{2\pi}{d} \tag{6.4}$$

The measured scattered intensity, $I(q)$, is given by Eq. 6.5. The measured scattered intensity is equivalent to the differential cross section, $d\sigma/d\Omega$ - the probability of an incident neutron being scattered into a particular solid angle, $d\Omega$. The form of the differential cross section can be expanded to include form and structure factors, which are beyond the scope of this thesis but are crucial for analysis in some material systems.

$$\frac{d\sigma}{d\Omega} \equiv I(q) \sim \left| \sum_j b_j e^{i\boldsymbol{q}\cdot\boldsymbol{R_j}} \right|^2 \tag{6.5}$$

where b is the bound scattering length of the object and R is its position. Peaks in the scattered intensity at specific values of q provide information on structural features and the physical size of said peaks can be calculated using Eq. 6.4.

6.3.1 Small-angle neutron scattering (SANS)

Neutrons scatter primarily via nucleon-nucleon interaction, meaning that structures in liquids, crystals and biological material can all be investigated with SANS.[204] The inherent magnetic moment of neutrons also leads to a magnetic interaction, allowing for detection and study of magnetic properties.[205] With regards to probing of magnetisation using SANS, the scattered intensity, $I(q)$ is proportional to the change in magnetisation squared, as shown in Eq. 6.6. Physically this means that ferromagnetic material which is fully aligned will have zero contribution from magnetisation, as all domains will have parallel alignment and therefore the change in magnetisation is zero. In comparison, a ferromagnetic sample that has no external field will have random domain orientation (providing there are no strong anisotropy effects which might create spontaneous alignment) and will therefore see a 'maximum' in magnetic contribution to scattering signal.

$$I \propto |\Delta M|^2 \tag{6.6}$$

Instrumentation

Neutrons are generated using a continuous reactor or spallation source, before being moderated (to different degrees of thermal energy, depending on the end-instrument) and directed towards the instrument with the use of neutron guides whose interior is coated with reflective material. Neutron optical components that are commonly employed include focusing/beam defining slits, collimators, monochromator/velocity selectors, choppers and beam polarisers. For SANS applications a pin-hole collimator is used after the so called source aperture/slit, following the neutron guides, to ensure a well focused beam at the sample position. For wavelength selection a rotating drum velocity selector is most commonly used (providing a wavelength resolution in the order of 10%) while choppers are employed for time-of-flight measurements. Following scattering at the sample position, deflected neutrons enter the evacuation tube where they travel before encountering the He^3 detectors and are converted into a signal. The position of the detectors within the evacuation tube is one of the control parameters, as it determines the range of scattering vectors accessed for a particular measurement.

For the scope of the current study, SANS measurements were performed on the D11 and D33 beamlines of the High Flux Reactor at the Institut Laue-Langevin (ILL) in Grenoble, France. These two SANS instruments have been optimised for slightly different modes of study - D11 is capable of measuring at very low values of momentum transfer, therefore probing large scale structures on the micron scale. Figure 6.3 shows the basic layout of the D11 instrument which is also representative of a typical SANS instrument. In comparison, D33 is a multi-detector instrument, often utilised in time-of-flight mode (via the use of choppers) where the 'white beam' of wavelengths leads to extremely large q ranges, and/or paired with other options, such as polarisation analysis which uses an RF flipper before the sample and a He^3 analysis cell after scattering.

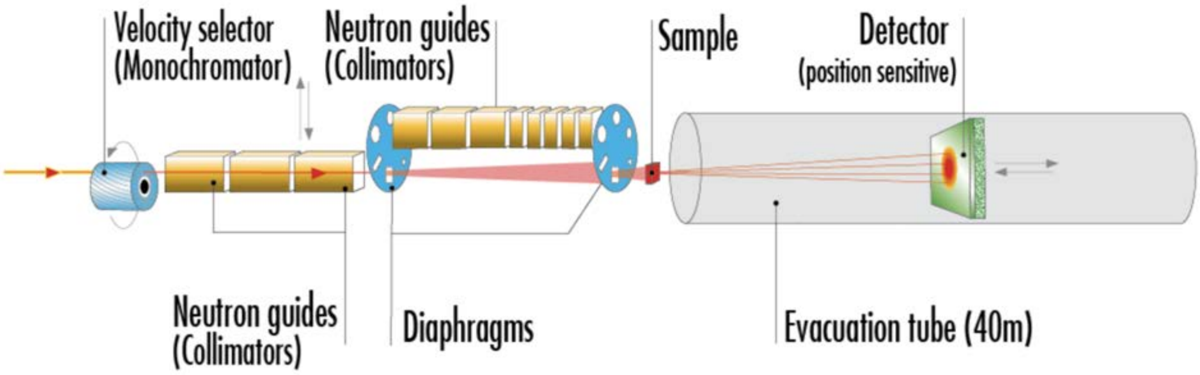

Figure 6.3: The D11 SANS instrument.[206]

Sample environment flexibility is imperative to most SANS studies, as the cutting edge phenomena studied often appear at extreme conditions (liquid helium temperatures, large magnetic fields, etc).[207] For this experiment, liquid helium cryomagnets and electromagnets were used in both parallel and perpendicular orientation (respective to the beam direction), as this allows for the greatest depth of study with regards to the crystallographic dependency of the appearing features, something which is of particular importance for the magnetic anisotropy study in FePd.

Measurements and Analysis

The SANS work performed in this thesis is comprised of multiple different types of physical property dependencies. Prior to measurements, the single crystal samples of iron-palladium were properly aligned using a local lab-based X-ray Laue diffractometer and then were fixed to the relevant sample holder and inserted into the sample environment stage being used (electromagnet or cryostat). With regards to measurement sequences, scans were typically performed as a function of field and/or temperature, from which further information regarding the anisotropy (or azimuthal angle) and scattering vector dependence can be determined. Given that the degree of scattered intensity is a function of the interaction type and the q range, effort was made to ensure that the counting times (which determine uncertainty) were sufficient enough to produce reasonable error bars. For the raw data treatment and analysis, the GRASP package was used,[208] which is arguably the most robust and widely used tool for SANS analysis. Created by Charles Dewhurst, it is a graphical interface which runs as a MATLAB script application and an example of the interface is shown in Figure 6.4. GRASP is designed to directly interface and extract any relevant data during analysis. The freedom of this analysis is paramount, particularly so when the sample environment demands of the experiment are high. Further to the analysis capabilities of GRASP, which include the ability to load and reduce multiple data sets, the visualisation of the 2D detector image should not be understated. The raw scattering image visible on the multi-detector is often an indicator of anisotropic effects.

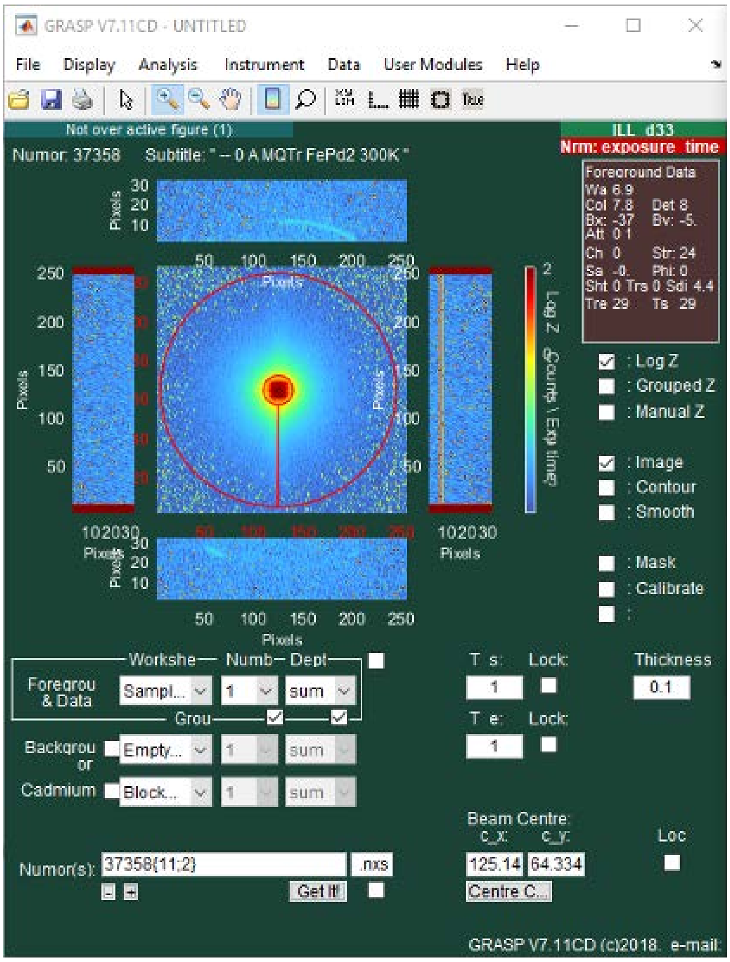

Numor: 37358 Subtitle: " -- 0 A MQTr FePd2 300K "

Foreground Data
Wa 6.9
Col 7.8 Det 8
Bx: -37 Bv: -5.
Att 0 1
Ch 0 Str: 24
Sa -0. Phi: 0
Sht 0 Trs 0 Sdi 4.4
Tre 29 Ts 29

Foregrou & Data: Sampl... 1 sum ☑ ☑
Backgrou or: ☐ Empty... 1 sum
Cadmium: ☐ Block... 1 sum
T s: 1 Lock: ☐
T e: 1 Lock: ☐
Thickness: 0.1
Beam Centre: c_x: 125.14 c_y: 64.334
Numor(s): 37358{11;2} .nxs

Figure 6.4: The GRASP graphical interface showing the 2D detector visualisation and the various reduction options.[208]

6.3.2 Synchrotron X-ray diffraction

For synchrotron XRD the majority of the scattering theory discussed for SANS applies for this photon-based technique, however the scattering object is the atomic form factor caused by the atomic electron cloud.[209] Synchrotron XRD employs the use of large scale beamline facilities (such as the ESRF (France), DESY (Germany) and Diamond (UK)) to perform complex experimentation, that would otherwise be impractical to do in a normal lab space. The high flux and high brilliance offered by synchrotron light is orders of magnitude above that achievable by even the best of lab-scale XRD machines or neutron sources. Furthermore, the large flux allows for the achievement of good statistics within exceptionally small time frames, meaning that results which often take hours or days on a conventional XRD machine, can now be completed in minutes, if not seconds.

Another benefit of synchrotron XRD against conventional XRD is one of resolution. The multiple analyser crystals and complex sample stage options used on most beamline diffractometers yield increasingly superior resolution to that of most tabletop XRD instruments. This increased resolution allows for the distinguishing and analysis of peaks that share very similar angular position. Certain instruments, such as ID22 which provided the data for this thesis, are capable of investigating the individual reflections within a particular crystallographic direction.

Instrumentation

Measurements were performed on the ID22 high resolution powder diffractometer at the ESRF.[210] ID22 has an energy range of 6-80 keV and uses a bank of nine silicon [111] analyser crystals to achieve the very fine resolution that is necessary for these peak splitting explorations. All nine crystals are mounted on a singular rotation stage, which reduces alignment error and allows for easier adjustment of the Bragg angle if wavelength is changed. Acceptance for the Si is on the order of arcseconds and the combination of multiple crystals helps to tightly cement 2θ. Figure 6.5 is a schematic of the analyser crystals on ID22.

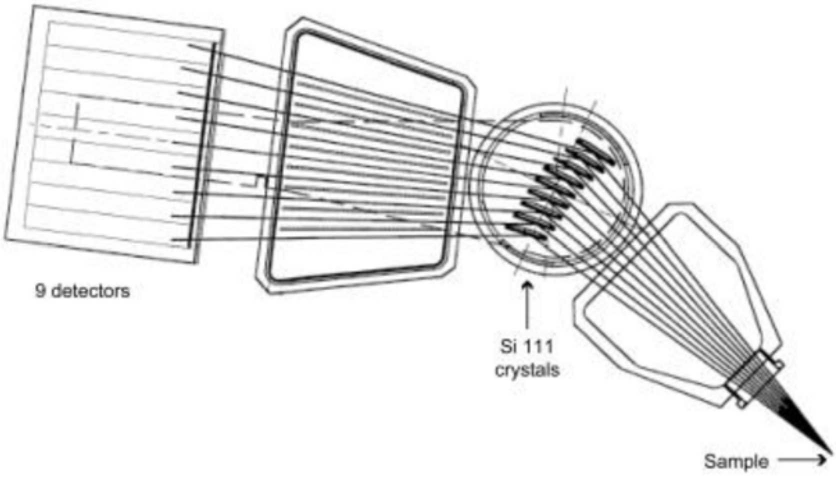

Figure 6.5: Silicon 111 analyser crystals.[210]

Pulverisation of the metallic samples was performed using a mortar and pestle under Ar (to remove the risk of ignition and oxidation) for around 15 minutes per sample to ensure that the powder was fine and homogenous (the degree of pulverisation necessary was assessed during an early measurement). Following this, the powder was loaded into 0.5 mm diameter borosilicate glass capillaries, which were then spun in the beam to remove any preferred orientation effects.

The ID22 sample environment capabilities are vast, allowing for measurements from base temperature up to ≈1000 K through the use of a He^3 cryostat, an Oxford Instruments Cryostream and a hot air blower. The latter two options can be remotely driven in and out of position via use of a sample table, allowing for swift scanning of a large temperature range.

Further to the sample environment capabilities of ID22, the use of a robot was employed for automatic handling and loading of samples to ensure speed and accuracy while also reducing the amount of human handling time inside the experimental hutch. Other experimental parameters (such as sample environment options, robotic handling, beam parameters and detector controls) were controlled using commands and executables programmed in C.

Measurements

Given the extremely high resolution of ID22 in its configuration for this experiment, two distinctly different methods of measurement were employed.

Full trace Full angle scans were performed up to a maximum angle of 70°. An example of such a trace is given as Figure 6.6. These measurements were used to check for sample purity, inspection of the trace was used to determine whether or not a sample had an acceptable level of purity or not. The majority of these measurements were performed near base temperature, so as to remove the effects of lattice expansion and thermal vibrations. The primary use for obtaining a quick, full trace is to ensure that the RE-TM_2

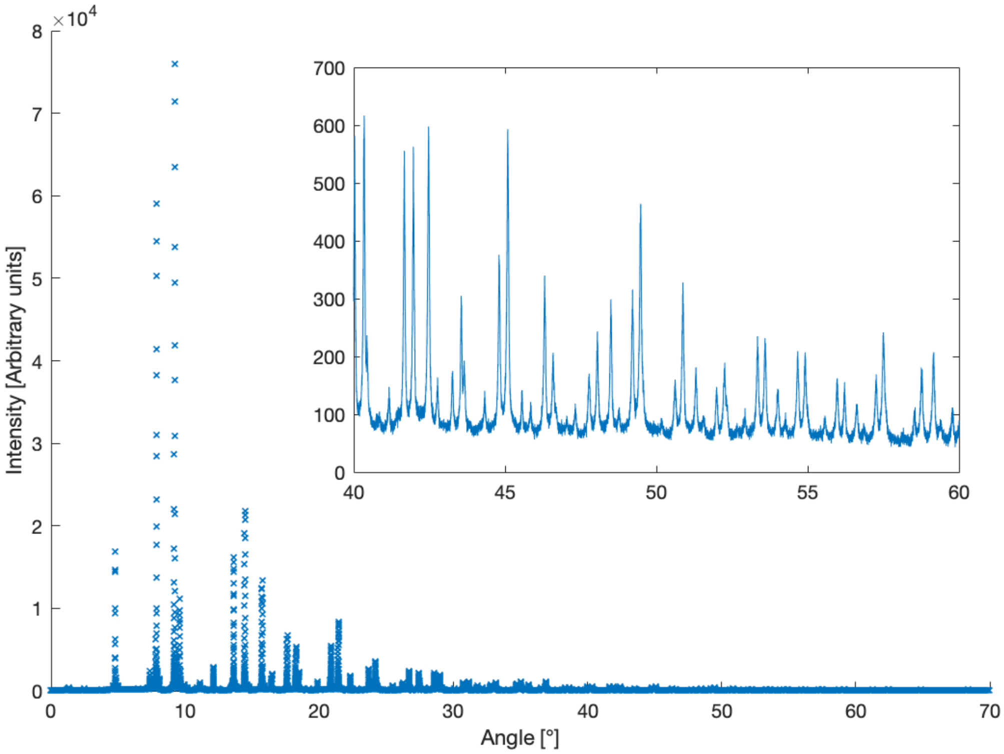

Figure 6.6: An example of a complete X-ray diffraction scan performed on the ID22 instrument at the ESRF. The inset shows that the resolution is sufficient to isolate individual peaks even at large angles.

phase is dominant and that the impurity peaks will not cause interference during the peak scanning. Undesirable phases can have negative impacts on the physical properties however for determination of the MPB position, their impact is negligible.

Peak scanning Once the desired samples for further study had been decided, the majority of the measurement time was spent scanning at specific angle positions. Certain reflections are of significantly more use for analysis than others. The chosen reflections for further study were (222), (440) and (800) as these reflections provided a great deal of insight into the structure of the material - explanation of this is given in Chapter 4.2. An example of these three reflections for one material at a fixed temperature is shown in Figure 6.7.

6.4 Data analysis

Data analysis was performed using two computational packages: GRASP and MATLAB. Information about both of these can be found in their respective websites and it is important to state that the versatility of these programs was influential in their use throughout this thesis.[208, 211]

6.4.1 Pseudo-Voigt function

Voigt functions, which are a convolution of a Gaussian and Lorentzian function, can be used for analysis, however these are significantly more computationally demanding and are therefore considered a more rigorous, but not necessary option.[212] The pseudo-Voigt function is an alternative which requires significantly lower computational power while still achieving reliable and agreeable results.[213] Eq. 6.7 shows the pseudo-Voigt approximation.

$$PV = \eta L + (1 - \eta)G \tag{6.7}$$

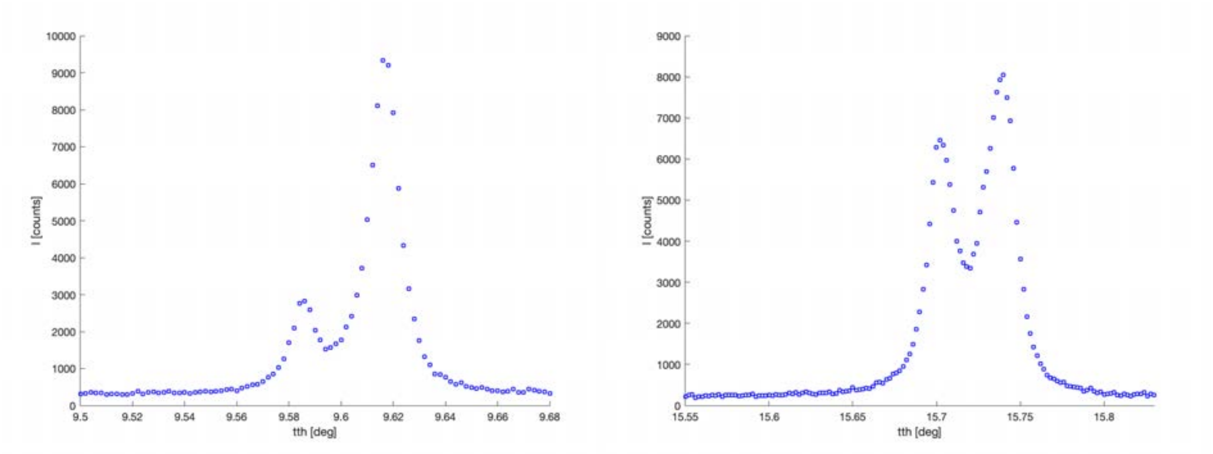

(a) (222) (b) (440)

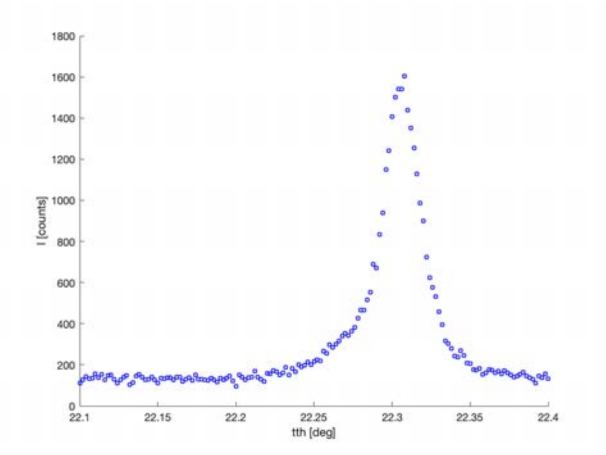

(c) (800)

Figure 6.7: Example of the low range scans used to monitor specific peak reflections with changing temperature.

where L and G represent a Lorentzian and Gaussian peak shape respectively and η is the mixing factor between Lorentzian and Gaussian contributions that is inherent to a pseudo-Voigt function. The effect of different η values is shown in Figure 6.8. Eqs. 6.8 and 6.9 show the Lorentzian and Gaussian functions, respectively, which were used in this analysis.

$$L = \frac{A}{\pi}\frac{c}{(x-b)^2+c^2} \tag{6.8}$$

$$G = \left[\frac{1}{c\sqrt{2\pi}}\right] exp\left[\frac{-(x-b)^2)}{2c^2}\right] \tag{6.9}$$

where A is the amplitude scaling factor, b is the peak centroid and c is the peak width.

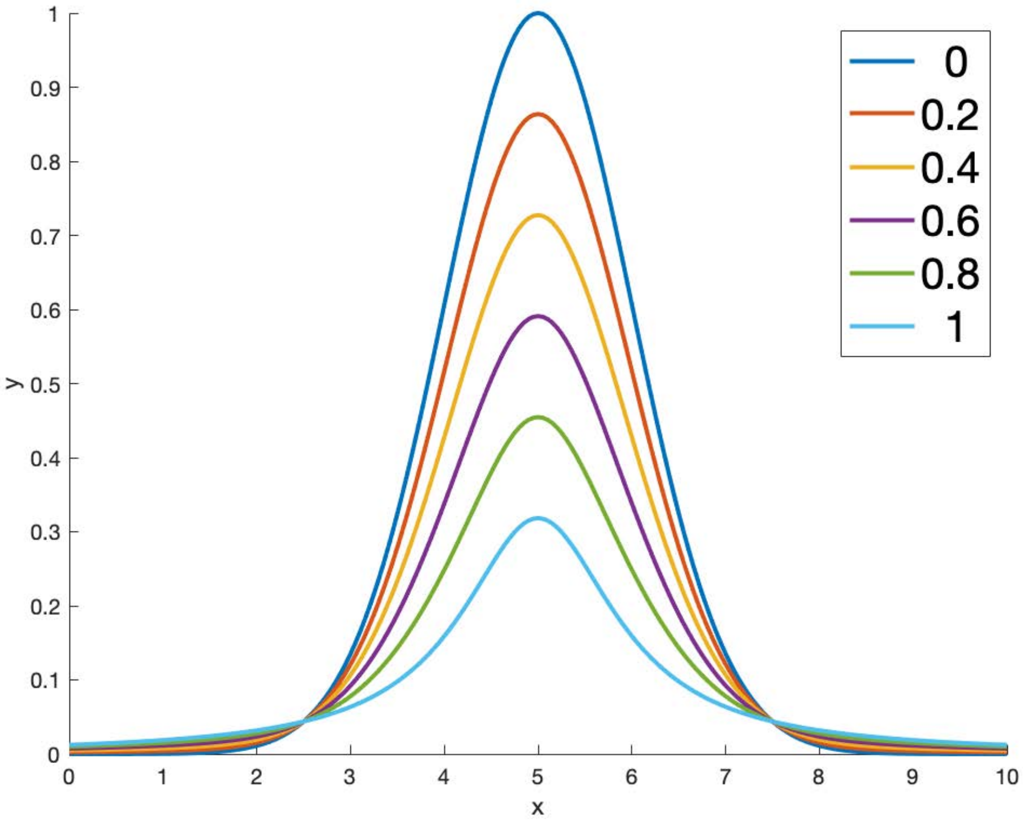

Figure 6.8: The effect of the η on the peak shape of a Pseudo Voigt function. $\eta = 0$ corresponds to a Gaussian, while $\eta = 1$ is a full Lorentzian peak.

6.4.2 Double Pseudo-Voigt fitting

Figure 6.7 shows that depending on the reflection and crystal structure of the alloy, there can be multiple peaks present within a small data region. To perform efficient fitting, a model was designed to allocate for single or multiple peak fitting of pseudo-Voigt profiles. MATLAB was employed mostly for its visual representation and customisable peak fitting options. Measurement data for specific peaks was imported into MATLAB and peak fitting was then performed across the peak range. To account for the splitting of the peaks, a double Pseudo-Voigt (DPV) function was used and this is given as Eq. 6.10.

$$\begin{aligned} DPV = BG + A_1(1-\eta_1)exp\left[\frac{-(x-b_1)^2)}{2c_1^2}\right] + \left(\frac{\eta_1 A_1}{\pi}\right)\frac{c_1}{(x-b_1)^2+c_1^2} \\ +A_2(1-\eta_2)exp\left[\frac{-(x-b_2)^2)}{2c_2^2}\right] + \left(\frac{\eta_2 A_2}{\pi}\right)\frac{c_2}{(x-b_2)^2+c_2^2} \end{aligned} \tag{6.10}$$

where BG is a simple, constant background term - there is no need to include the more complex background term used in typical refinement calculations because the fitting is only over a small angle range.

The fitting for this equation uses so-called "preliminary fitting" to obtain good starting parameters for the DPV function. By first fitting a single Gaussian and single Lorentzian peak, the results of this fitting are used as starting variables for the DPV fitting. It was found that a good estimation of the starting variables had a significant effect on the accuracy of the fitting and was therefore an important consideration throughout analysis.

The key resultant parameter from the DPV fitting is that of the amplitude ratio, which is defined as

$$Amplitude\ Ratio = \frac{High\ angle\ intensity}{Low\ angle\ intensity} = \frac{A_2}{A_1} \tag{6.11}$$

and is used to clearly identify the phase regions, by comparison with the expected peak splitting for the inherent lattice distortions.

Following the above extraction of key parameters, the aim is to accurately and succinctly present an expanded phase diagram for the MPB in $\mathrm{Tb_{1-x}Dy_xFe_2}$ alloys, with a particular focus on portraying the MPB width. This will be done by monitoring the movement of peak centroid positions and peak amplitude ratios around the transition - the temperatures and ratio magnitudes at which point they settle will mark the edges of the MPB width for that particular sample.

Chapter 7

Fundamental materials (Iron-Palladium): Results & Discussion

The following chapter encompasses the experimental results and subsequent analysis on the fundamental material, iron-palladium. The chapter begins with a presentation of the comprehensive SANS study into the underlying physics and mechanisms of the interplay between the magnetic and crystal structures of this intriguing material. Closing this chapter is a brief mention of the other fundamental studies undertaken during this thesis. The data used in this section was primarily collected at the ILL on the D11 and D33 instruments, however there will also be some low q preliminary data shown that was collected at the FRM-II reactor in Munich. The sample orientation was varied to best investigate the anisotropic effects and will be discussed when necessary. Two single crystal samples were studied, both of 'disc like' shape and the orientation of the crystals was determined with the use of X-ray Laue. Figure 7.1 shows the orientation of FePd Sample 1 for the ILL data. The orientation of the low q measurements was random outside of the beam direction being parallel to [001], as at the time of measurement the in-plane directions had yet to be determined.

A second experiment was performed on FePd, using an additional sample with different orientation, where an attempt at polarised neutron scattering was attempted. Unfortu-

Figure 7.1: Sample orientations used during experimentation.

nately, due to the stray fields of the ferromagnetic FePd the polarisation analysis was not a success, however some unpolarised SANS measurements were completed, to supplement those already performed on the previous experiment.

This Chapter present results from both crystal orientations ($n \parallel [001]$ and $n \parallel [110]$), with multiple different q ranges probed for each sample. It should be noted that different experimentation conditions resulted in a slight difference in q ranges (i.e. medium q from the first experiment overlaps with medium q from the second experiment, but is not exactly similar in width) - this is however not a problem as the q ranges were selected to cover features of note.

7.1 Results - $n \parallel [001]$

This section presents results where both the neutron direction and sample normal are aligned along the [001] direction of the disc-shaped sample. Unless otherwise stated, intensity measurements are integrated across the whole detector area (minus the beam and sample space).

7.1.1 Low q (LQ) - FRM-II

Figure 7.2 shows the magnetic field dependence on the intensity for FePd in the low q range, with field applied perpendicular to the beam direction and corresponds to a horizontal direction on the detector image. H-Up and H-Down dictate the scan direction, either increasing positive magnetic field for H-Up or decreasing positive field followed by increasing negative field for H-Down. Magnetic field values used in this scan are: ± 0 T, 0.005 T, 0.01 T, 0.02 T, 0.05 T, 0.1 T, 0.2 T, 0.5 T, 1 T and 2 T. Empty beam measurements were used to provide a background file - an artefact of instrument scattering is visible on 2D detector images and is not a scattered signal, therefore the empty beam is used to remove this. The knock-on effect of this is that high field measurements (where magnetic scattering is negligible) will register as negative intensity because some signal is lost following interaction at the sample position.

As expected for a ferromagnetic material approaching saturation, the scattered intensity decreases in a Landau fashion (Figure 2.5) as the magnetic domains align, until ±0.5 T at which point saturation is assumed. Hysteresis is exhibited between H-Up and H-Down and a degree of anisotropy is visible on the 2D detector image. Figure 7.3 shows the analysis sectors used to investigate this anisotropy between the horizontal and vertical directions and presents the resultant magnetic field dependency. There is a clear difference in scattered intensity for the horizontal direction that aligns with the magnetic field, with the difference in magnitude most pronounced at the saturation value of H=0.2 T, before reducing as magnetic field is further ramped towards 1 T. Figure 7.4 shows the scattering vector dependence on the intensity at the four fields of interest and informs that the anisotropy in scattered signal is uniform across this q range. The degree of scattered intensity is found to drop significantly between H=0.2 T and H=0.5 T, suggesting that saturation is indeed reached at some point between these two data points. The raw signal images (Figure 7.5) show a collapse in scattering signal at H=0.5 T when compared to H=0.2 T.

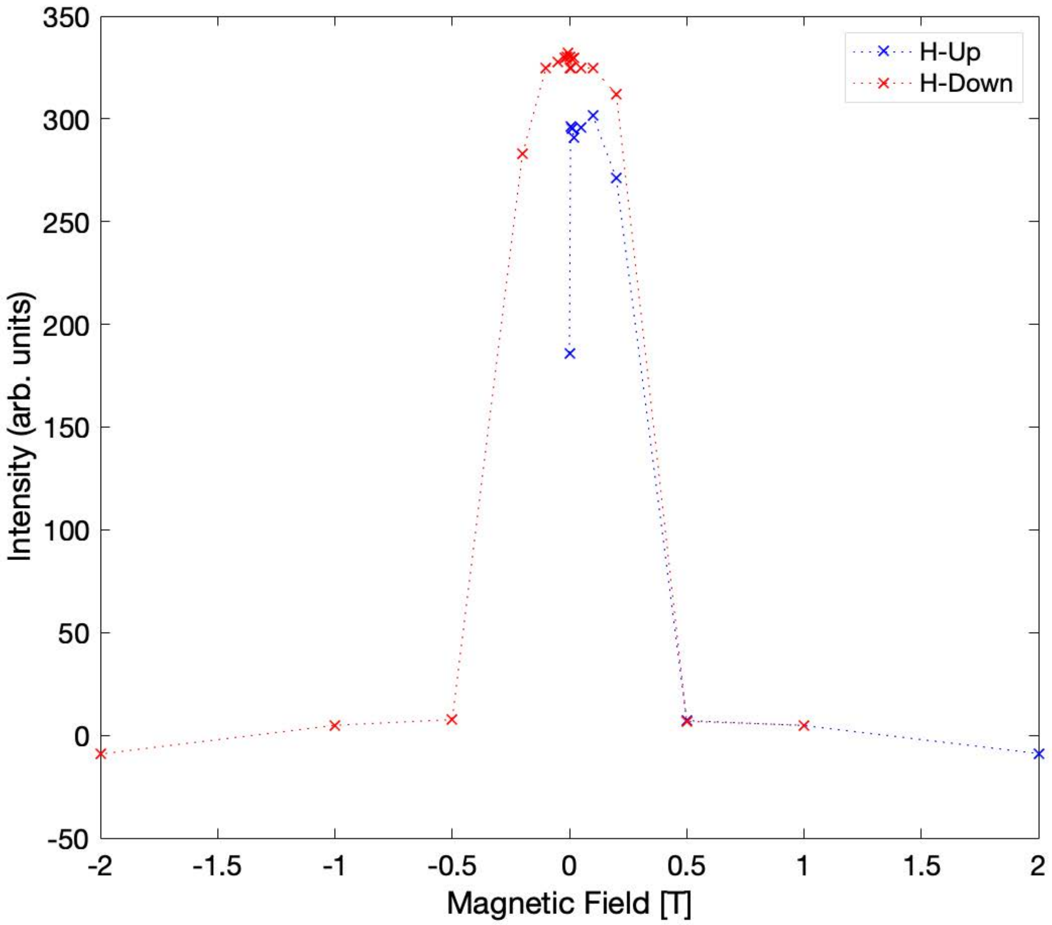

Figure 7.2: Magnetic field dependence at room temperature for H=0 T to H=2 T (H-Up) and H=2 T to H=−2 T (H-Down).

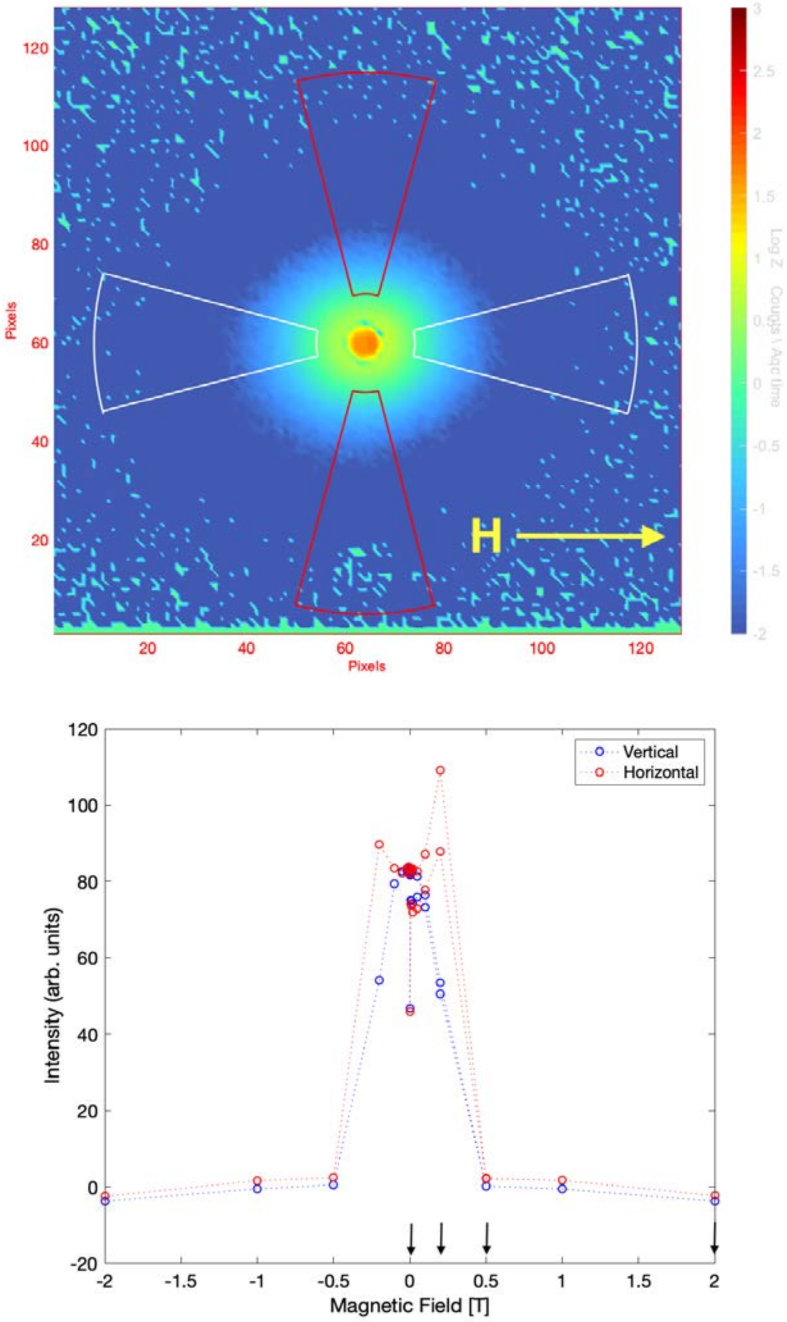

Figure 7.3: **Top** Detector image and analysis sectors used to determine the anisotropic magnetic field dependence. Field direction is marked with a yellow arrow. **Bottom** Split sector analysis of the intensity vs field scan in the horizontal and vertical directions (Figure 7.2). Black arrows show the fields of interest for analysis of the scattering vector dependence.

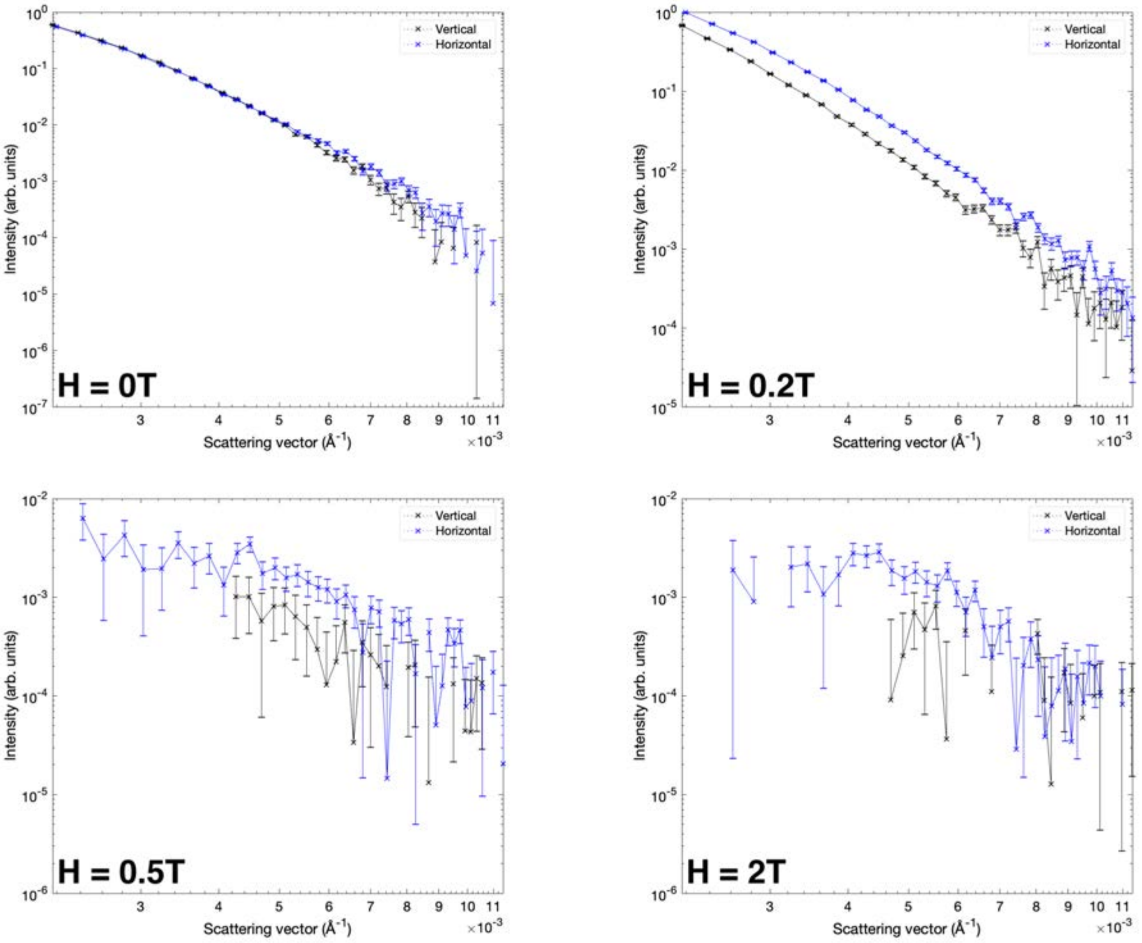

Figure 7.4: Intensity as a function of scattering vector at room temperature for a range of magnetic fields in the horizontal and vertical directions, chosen as key points from Figure 7.3.

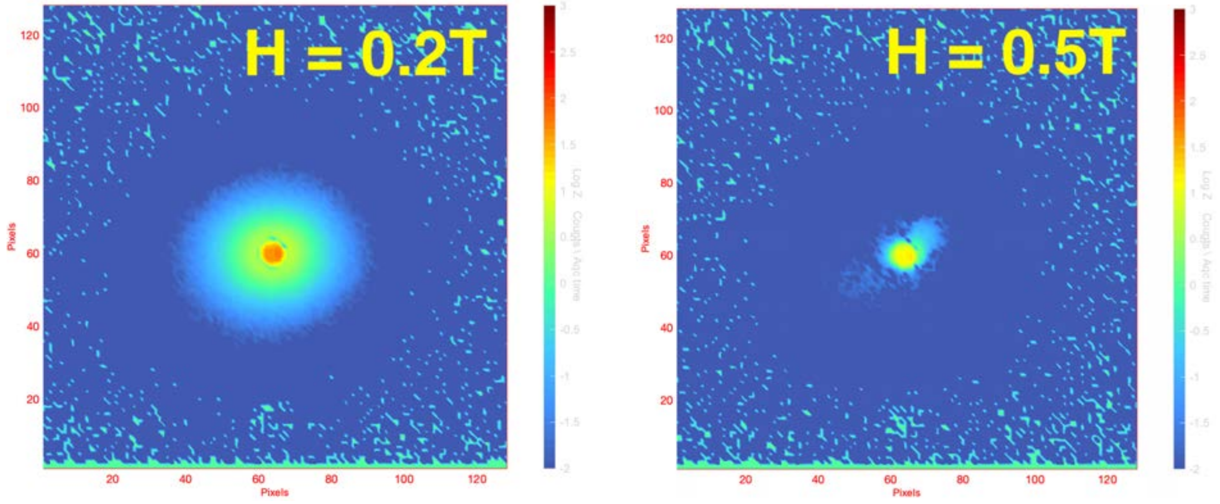

Figure 7.5: Detector images showing the collapse in scattering intensity either side of the anticipated saturation field, for the low q region.

7.1.2 Medium *q* (MQ) - ILL

Figure 7.6 shows the room temperature (RT) magnetic field dependency in the medium q range. The expected decrease in intensity with increasing field is seen however there is also an unexpected peak in the intensity centred around H=0.5 T. Furthermore, the hysteresis seen for H-Up and H-Down is consistent with the low q results, in that the intensity at H=0 T is larger after the material has been fully saturated. Interestingly however, the newly discovered peak at H=0.5 T shows the ramping measurements (H-Up) more strongly than with decreasing field (H-Down).

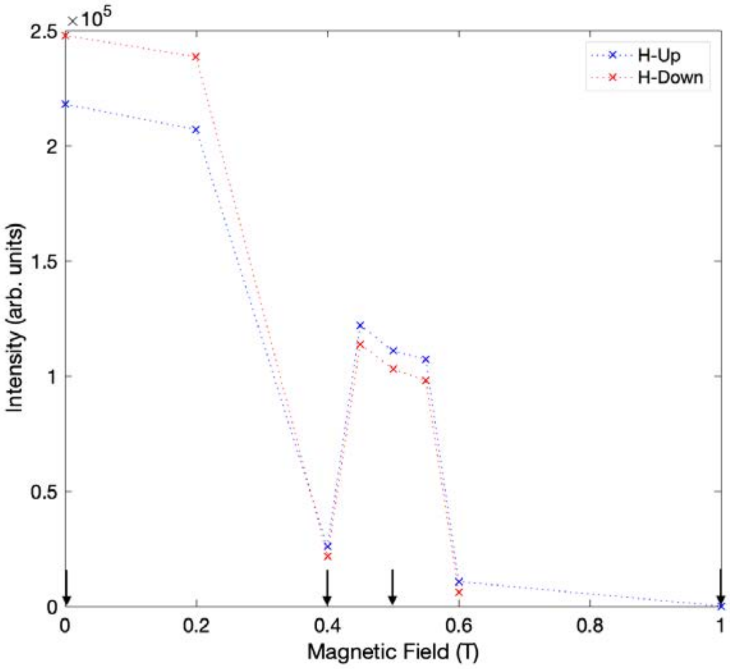

Figure 7.6: Intensity against field for the medium q arrangement at RT. Field range is H=0 T to H=1 T (H-Up) and H=1 T to H=0 T (H-Down). Black arrows dictate the fields of interest (c.f Figure 7.7)

Analysis of the scattering vector dependence shows significant, non-uniform variation with altering field strength. Figure 7.7 shows the slope for the different fields - at the extremities of the MQ range, the slope is uniform for all fields. However, the H=0 T data shows a shifting in the slope of the data, suggesting that a change in the scattering features in this size range. Furthermore, the H=0.5 T data shows the expected intensity peak (compared to H=0.4 T) with the dependence on q showing no irregularities, suggesting that the increased intensity comes from uniform scattering features. The high field measurements (H=0.6 T) have the lowest overall signal, characteristic of magnetic saturation and therefore a reduction in contribution to the scattering. Errors increase at high q due to reduced counting statistics - a reduction in intensity leads to an increased percentage error, following Poisson statistics.

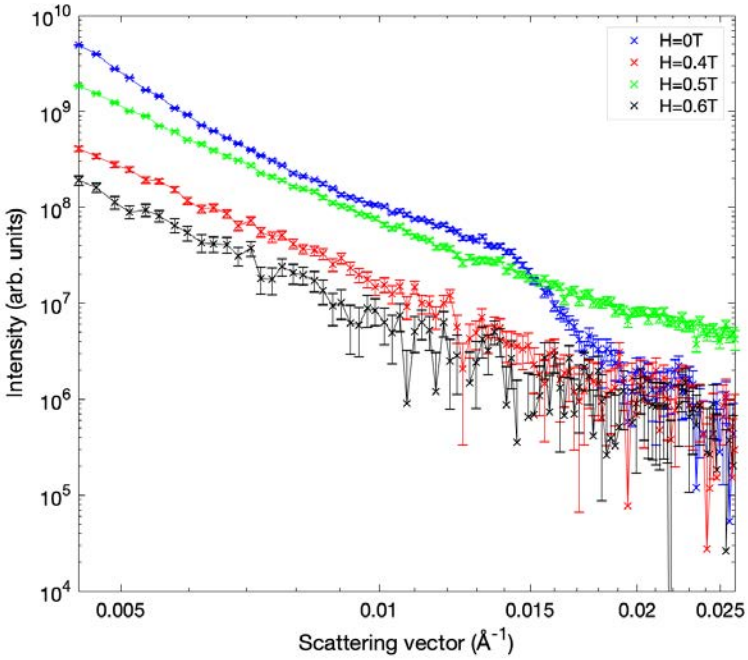

Figure 7.7: Intensity against scattering vector for the medium q arrangement at RT. Fields were selected to investigate specific points of interest.

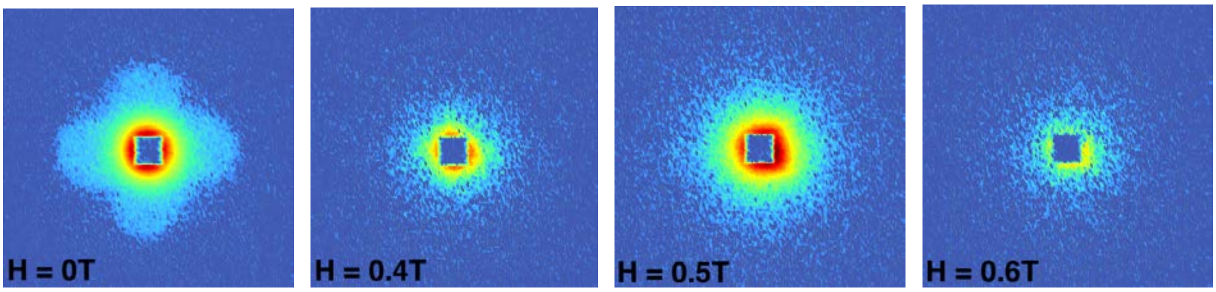

Figure 7.8: Detector images showing the varying directionality of the scattering signal as a function of field, for the medium q region at room temperature. Colour scale is as in previous figures.

Study of the 2D detector images for fields preceding the peak at H=0.5 T show a distinct four-fold anisotropy for H<H_{Sat}, which then collapses after saturation, before intensity is recorded in an isotropic manner at the H=0.5 T peak and finally the intensity collapses again in the high field regions. Figure 7.8 summarises the detector images for this results series. To further investigate the directionality, Figure 7.9 shows the averaged intensity as a function of the azimuthal (or analysis) angle, elucidating that the intensity change is stronger for some angular directions than others as field is changed from H=0 T to H=0.2 T. H=0.4 T is included in this plot to highlight the transition to isotropic scattering at this value of field and the background data used for reduction is H=0.6 T.

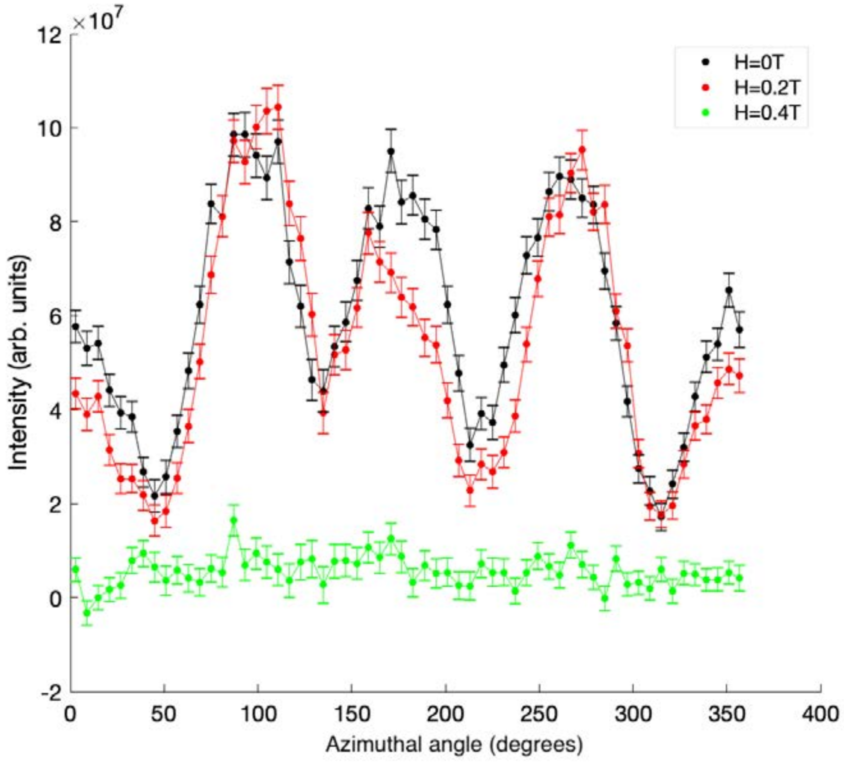

Figure 7.9: Intensity as a function of azimuthal angle for varying magnitudes of magnetic field strength at RT.

To analyse these peculiar effects and attempt to determine the underlying mechanism for this anisotropy, one can employ the use of split analysis sectors to focus on both 'on anisotropy' and 'off anisotropy' scattering. Henceforth, sectors taken at 0°, 90°, 180° & 270° will be summed together and displayed as + scattering and correspond to the 'on anisotropy' scattering. Conversely, sectors at 45°, 135°, 225° & 315° are summed to form **x** scattering, corresponding to the 'off anisotropy' scattering. Example sectors are shown in Figure 7.10 and Figure 7.11 shows the intensity as a function of the scattering vector from this analysis.

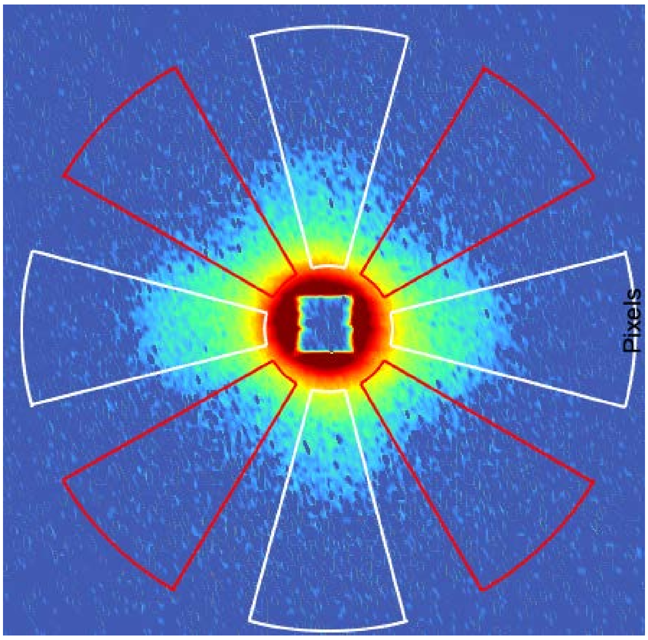

Figure 7.10: Example sectors used to investigate the anisotropy seen at 0 T and 0.2 T in the MQ region. White is the + sectors and red is the x sectors.

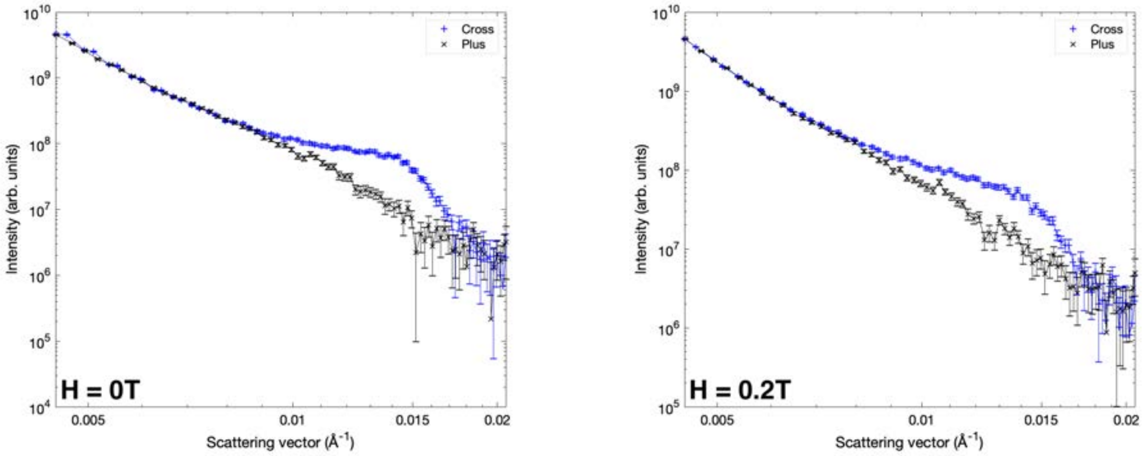

Figure 7.11: Intensity as a function of scattering vector at RT for the split sector analysis (Figure 7.10) for the low values of field which exhibit the four-fold anisotropy.

It is clear that there is a peak in the scattered intensity within the anisotropy (+) as opposed to outside of the anisotropy (**x**). This peak is shown to broaden slightly with increasing field. Outside of the peak, the scattering data lines up well for both sector summations, reinforcing that the scattering feature causing the anisotropy appears within a specific length scale, along specific crystallographic directions.

By using the **x** scattering signal as a background, the anisotropic peak can be plotted on a standard I vs q plot (not log scales) where the data shows a clear Gaussian-like shape. Fitting this data to a standard Gaussian function and using the error bars to contribute to the weight of the fitting, the centroid position of the peak can be converted to determine a physical size of the scattering object. Eq. 7.1 shows the fitting model used:

$$Y = A\,exp\left[-\left(\frac{x-b}{c}\right)^2\right] \tag{7.1}$$

where A is the peak height, b is the centroid position and c is the full width at half maximum (FWHM) of the peak.

Figure 7.12 shows the results from this peak fitting. At zero applied field, the centroid position of the peak fitting corresponds to a physical size of 50 nm (determined using Eq. 6.4) for the scattering object, whilst at H=0.2 T the peak is shifted towards a lower q value, suggesting that the scattering object has a physical size of 57 nm. The q values taken from the fitting to determine these sizes were of high precision (8 decimal places from instrument) however for this work, it is reasonable to round to 4 d.p, therefore estimating physical sizes to the nearest nanometer. The increase in scattered signal at the extreme low q ($0.005 < q < 0.010$) arises from the increased ΔM due to application of field - as the material is slightly hysteretic and had previously been magnetised in the negative direction, it is anticipated that this low q scattering is nothing of note with regards to the anisotropy-inducing scattering object.

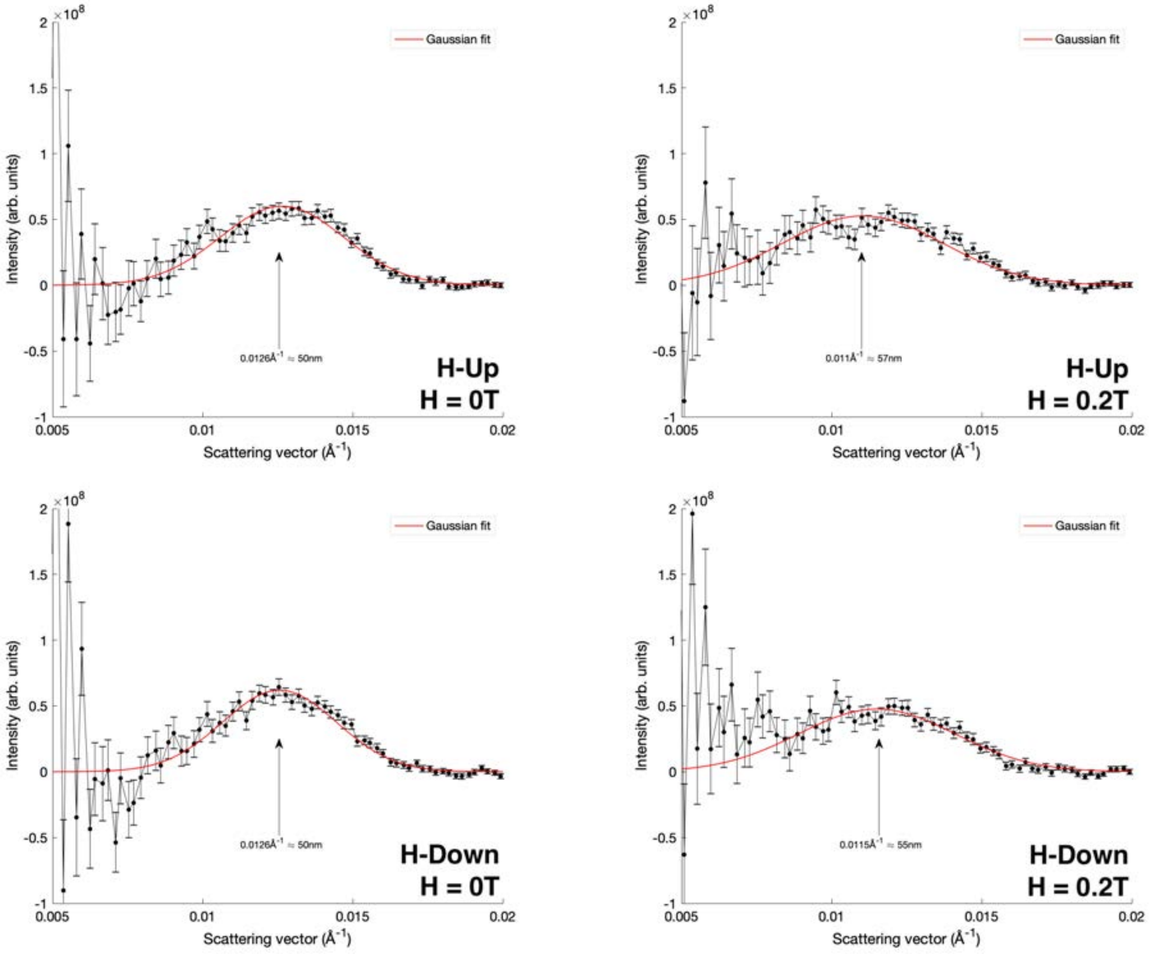

Figure 7.12: Gaussian peak fitting of the reduced data from the split sector analysis for both the H-Up and H-Down measurements.

No difference is seen between the peak shape and the resultant centroid position for both the H-Up and H-Down results. While the centroid position is consistent, there is clearly a broadening in the peak width (approximately 20% on the FWHM) for the H-Down fitting, suggesting that there is more of a range in size of the scattering feature upon reduction of the applied field.

For the second experiment, the introduction of a cryostat allowed for temperature dependency to be investigated. Figure 7.13 shows the zero field resultant temperature dependency for both cooling and warming. A clear ferromagnetic-like change in intensity occurs around 230 K which is unusual given that FePd is ferromagnetic at room temperature as shown in Figure 7.2. Further to the large increase in scattered intensity below

≈230 K, there is a precursor increase in scattering beginning at ≈250 K, which is roughly the temperature that the material returns to a background level of intensity.

Due to the instrumental inaccuracies in the heating and cooling data (thermal lag and poor control settings), it is important to analyse the scattering vector dependence for more definitive information on the transition temperature. By plotting the intensity as a function of q for various temperatures, the difference in slope can illuminate the transition temperature more clearly. Figure 7.13 shows the results of this, using the zero field cooling (ZFC) data to present that the transition temperature lies between 230 K and 240 K and that after the transition the dependence on scattering vector changes, suggesting a different scattering mode. Furthermore, it is intriguing that the dependency is the same at 260 K, which is equivalent to a background level, as for 250 K and 240 K which has slightly raised intensity.

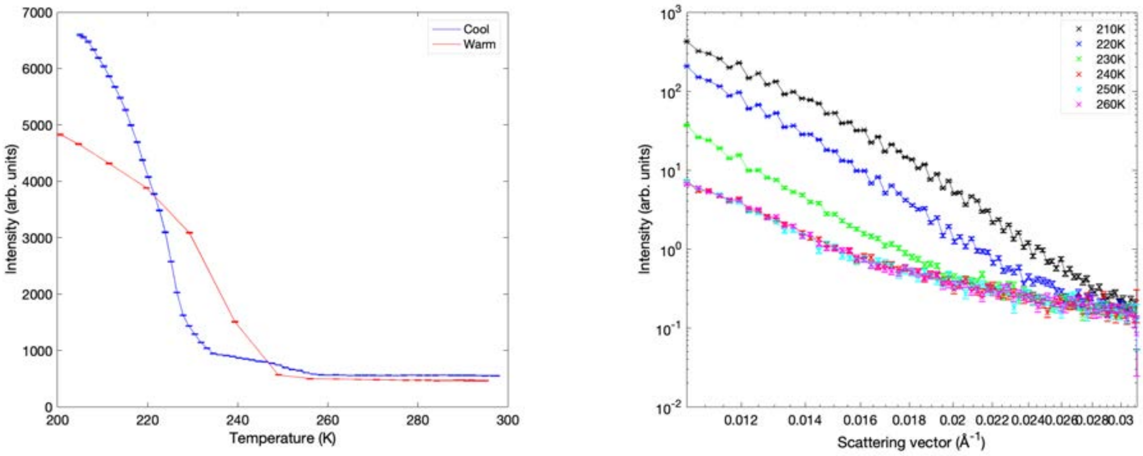

Figure 7.13: **Left** Zero field temperature dependence of FePd, both cooling and warming, across a temperature range of 200 K to 300 K. **Right** Scattering vector dependence as a function of temperature (ZFC) for the MQ arrangement.

Examples of the raw detector images for cooling are given as Figure 7.14 and it is clear that at T=270 K (and RT) that the four-fold anisotropy previously seen in the first experiment is reproducible. As temperature is reduced, the four-fold anisotropy gets slightly stronger at higher values of q but becomes significantly sharper in its directionality.

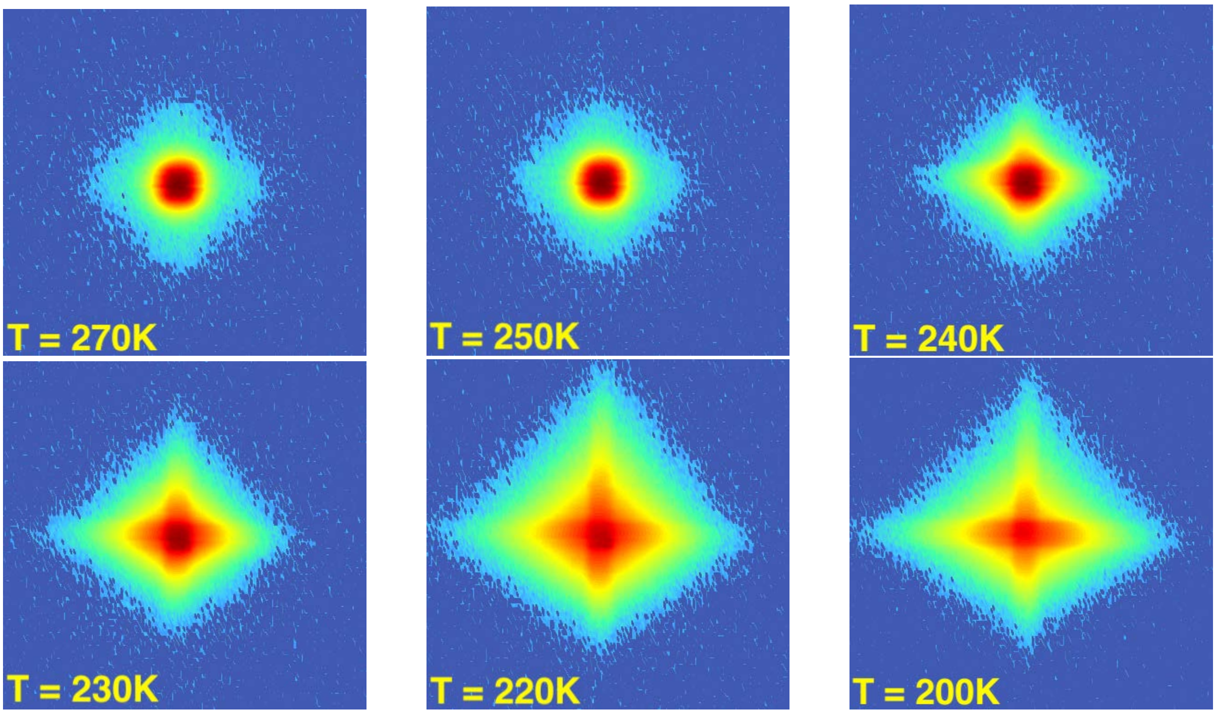

Figure 7.14: Raw detector images taken upon zero field cooling from 300 K towards 200 K.

To investigate the magnetic properties in the lower temperature region, Figure 7.15 shows the split sector analysis for the magnetic field dependence at 200 K. As seen at lower values of q at RT, the horizontal direction is dominant at 200 K for all fields but shows a peak around H=0.2 T - this was previously unseen in the low q data. The small peak seen in the MQ field dependency at RT (prior experiment) is no longer visible at 200 K. Suppression of this predominantly HQ feature may be due to reduced temperature.

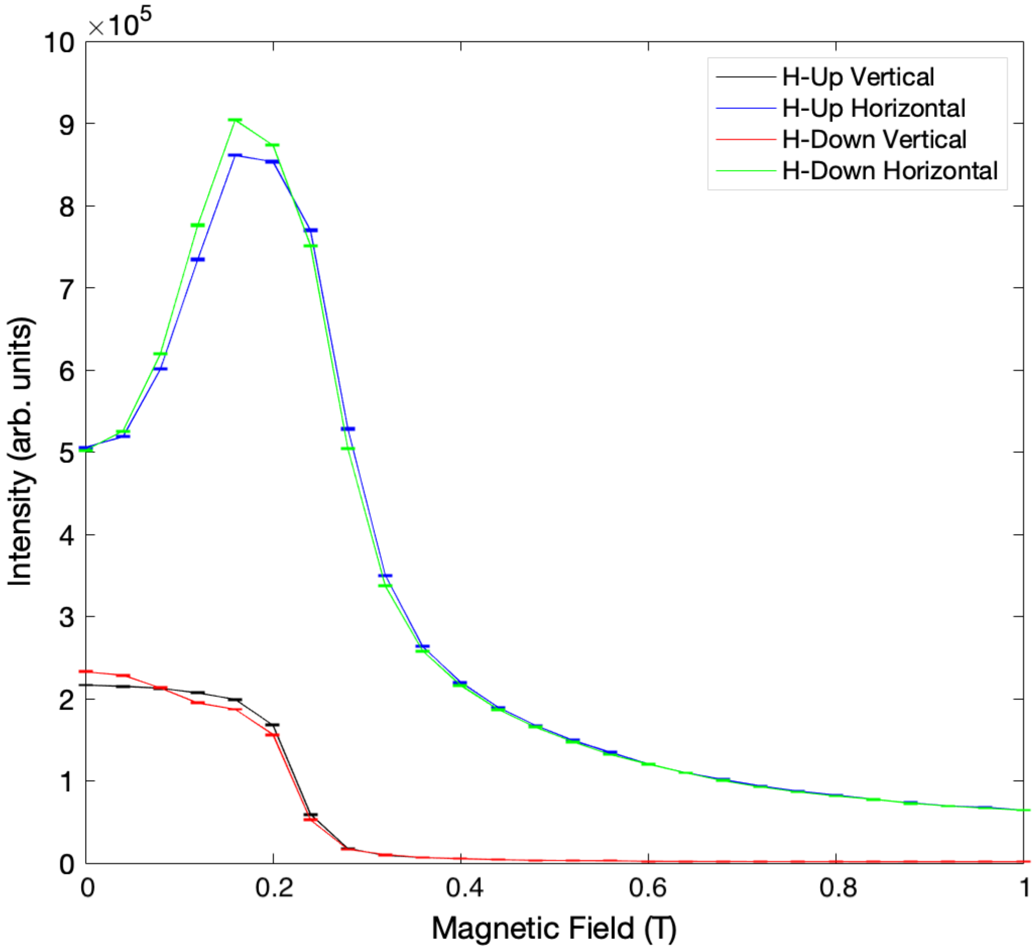

Figure 7.15: Split sector analysis of the magnetic field dependence at 200 K. The definitions of H-Up and H-Down (Figure 7.6) and sector analysis method (Figure 7.10) remain consistent.

7.1.3 High q (HQ) - ILL

Beginning in the new high q (HQ) range with measurements as a function of applied field, it was found that the unexpected peak at H=0.5 T in the MQ range was more strongly pronounced in the HQ range - specifically the intensity at the peak is ≈ 2 orders of magnitude larger than the intensity surrounding the peak. From this, it is clear that this appearing feature is by far the dominant scattering mode and warrants investigation. Figure 7.16 shows a split sector investigation into the field dependence of the intensity.

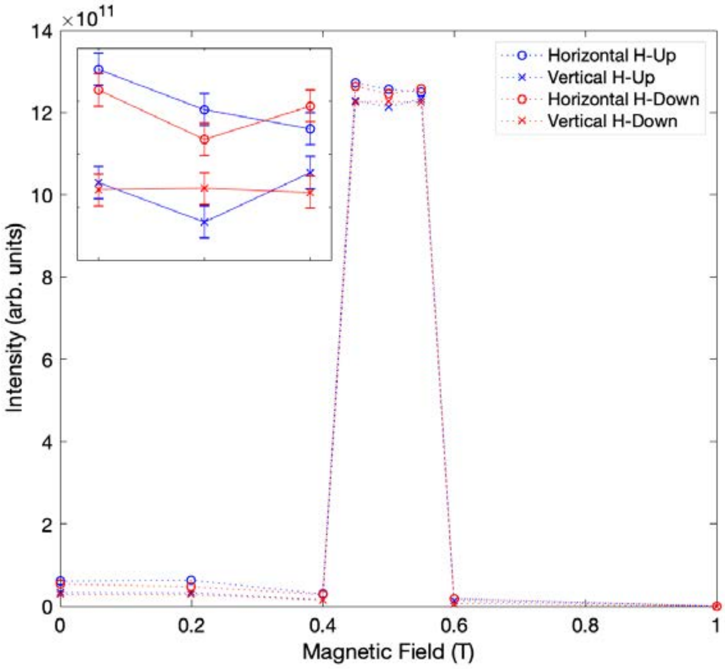

Figure 7.16: Split sector analysis of the intensity as a function of applied field for the HQ range at room temperature. The inset is a magnified view of the data points that make up the peak from 0.45 T to 0.55 T.

As seen in the LQ region, the direction which goes with the magnetic field (horizontal) exhibits a larger scattering signal for both H-Up and H-Down. One point of note is that amongst this 'top shelf' of data points, both the 'vertical H-Up' and 'horizontal H-Down' share a peculiar U-shape. It is particularly intriguing given that previous data has never shown the off-field direction to show dominance over the direction aligned with the magnetic field and this directional switching highlights that large fields (H>H_{Sat})) may break symmetry in the material.

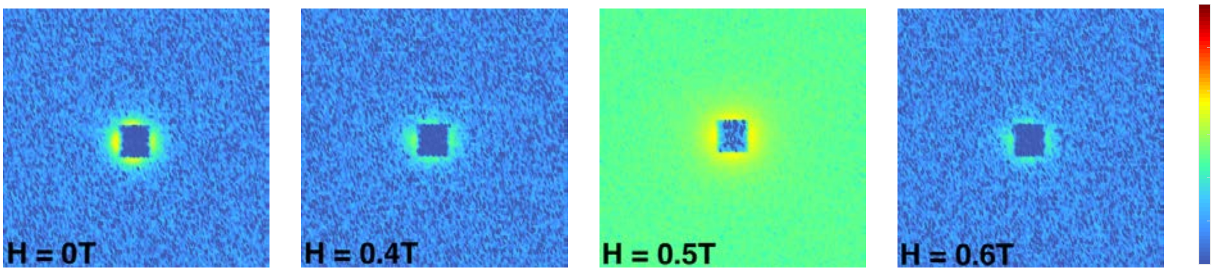

Figure 7.17: Detector images showing the varying directionality of the scattering signal as a function of field, for the high q region. The colour bar is given to show the difference in scattered intensity at H=0.5 T.

The 2D detector images for some key fields are given as Figure 7.17. It is clear to see that the increase in scattering is significant and seemingly isotropic. The area of scattering immediately around the beam centre is shown to decrease almost linearly with field (outside of the peak) as is the case for low q signal from ferromagnetic saturation. The dependency on the scattering vector for these key fields is given as Figure 7.18, which shows that the increased signal for H=0.5 T extends across the whole range and is indeed isotropic as the detector image shows. The upper limit of this HQ range translates to a scattering object of approximately $\approx$ 5 nm. The abrupt appearance and disappearance of this enhanced isotropic signal is intriguing.

Moving onwards to analyse the potential hysteresis in signal, the difference between H-Up and H-Down for the intensity against scattering vector is shown in Figure 7.19. Here it is seen that the hysteresis shown in the HQ region is generally mild. For the H=0 T data, there is a slight hysteresis in favour of H-Down in the lower end of the range and this would correspond to the signal seen in the MQ range, with H-Down being $\approx$ 10% larger than H-Up on return to zero applied field. In contrast to this, there is seemingly no hysteresis at H=0.5 T, suggesting that whatever the dominant scattering feature is at this field it is completely reversible. At the lower end of the range, the H-Up can be seen to be *slightly* larger than H-Down (as was seen in Figure 7.6) however the error bars overlap and would require extremely long counting times to clarify this to a reasonable degree. These results suggest that the hysteresis seen arises from the large scattering features (magnetic domains) and that the process occurring around H=0.5 T is reversible

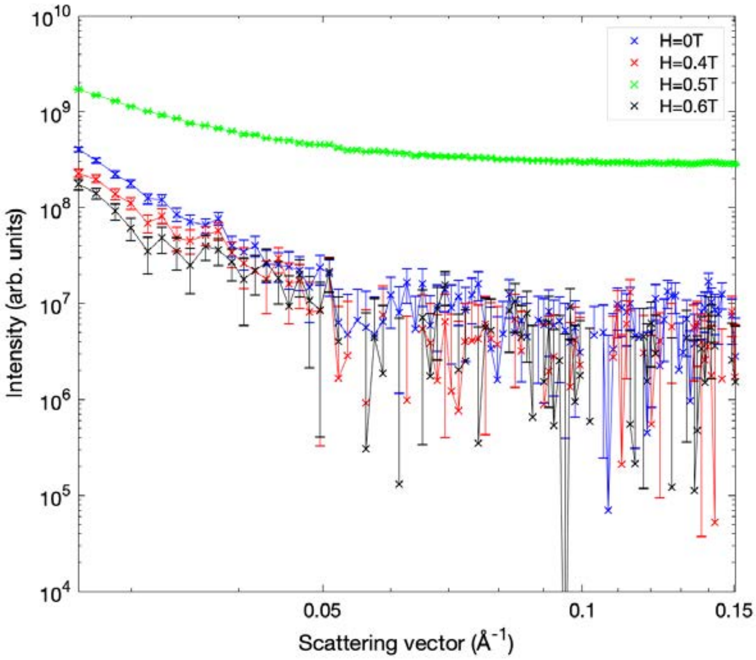

Figure 7.18: Scattered intensity as a function of scattering vector, for key fields within the data range. Errors are large at the higher end of the range due to a low signal and Poisson statistics.

and lacks definitive hysteresis in the HQ range.

Finally the directionality of the scattered signal at H=0 T and H=0.5 T is shown in Figure 7.20. There is no exhibited anisotropy at H=0 T, suggesting that the small scale features in the material have no directional bias without application of magnetic field. This behaviour largely continues as the field is increased to H=0.5 T, where only the lower end of the HQ range shows any directional preference to align with the field direction.

The clear separation in scattered intensity between H=0 T and H=0.5 T warrants investigation into the effect of temperature on this feature. An altered q range was used during the second experiment, probing features from 40 nm to a minimum size of 10 nm. Figure 7.21 shows the field dependence in this updated q setting as a function of temperature. The H=1 T files were used as a background, hence why all scans terminate at zero intensity. Figure 7.21 shows a clear peak at H=0.5 T which appears at 220 K (after the FCC to FCT transition) which grows in prominence as temperature is further reduced to 200 K. The zero field intensity for both the 200 K and 210 K measurements is extremely

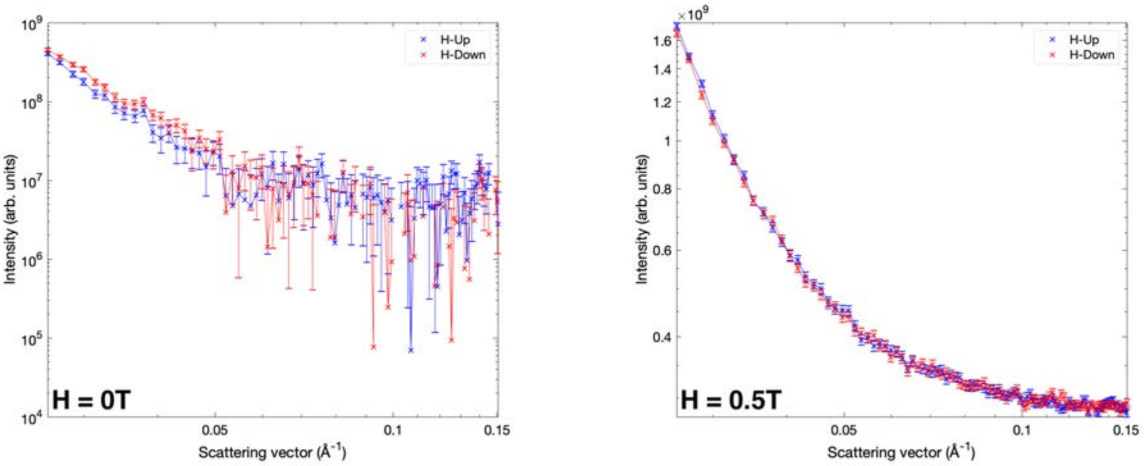

Figure 7.19: Intensity as a function of scattering vector for both H-Up and H-Down at room temperature, comparing the scattering dependence outside of, and within the HQ peak.

similar however there is a clear separation between the two at H=0.5 T, implying that cooling to 200 K induces some additional magnetic character which is only observed at fields exceeding saturation.

Finally for the $n \parallel [001]$ arrangement, an investigation into the directional scattering vector dependence at low temperatures (FCT phase) was performed. Figure 7.22 compares the vertical and horizontal sectors of the H=0 T and H=0.5 T data, it can be seen that at 230 K there is a very slight bias in the horizontal direction. Upon cooling through 230 K, the directional separation is reversed and becomes more prominent, in that the vertical sectors become dominant for both fields.

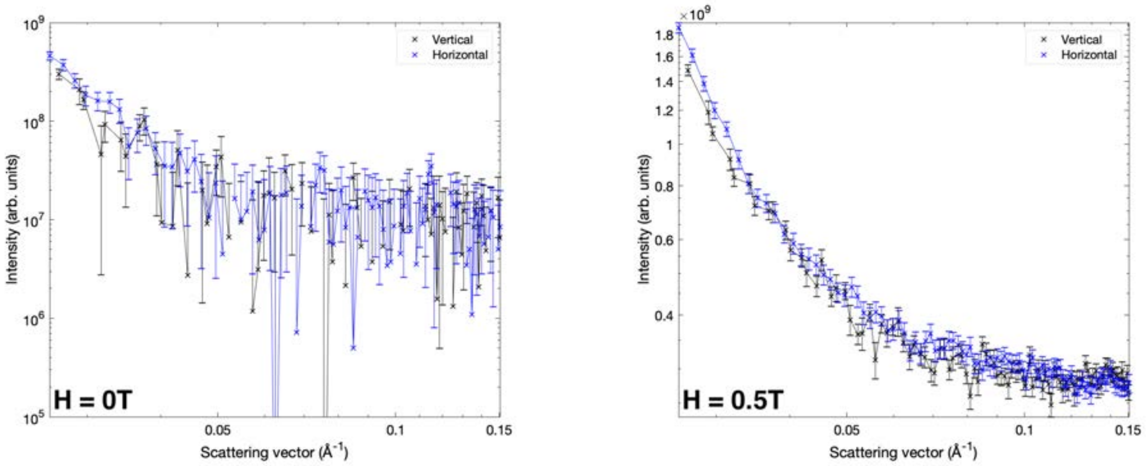

Figure 7.20: Split sector analysis of the intensity as a function of scattering vector at room temperature.

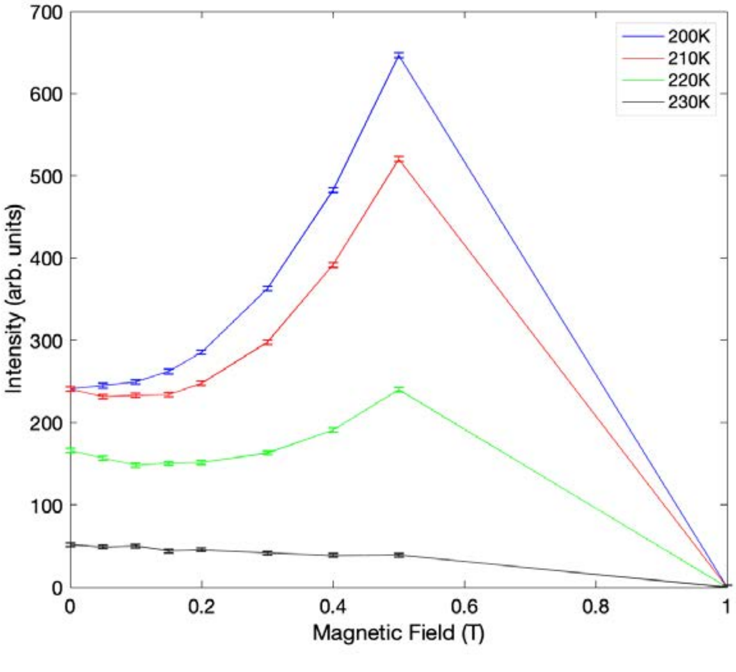

Figure 7.21: Intensity as a function of magnetic field for multiple temperatures during cooling. Time was critical during this experimentation phase and due to the long counting times at high q, where saturation of the magnetisation drastically reduces signal, no data was collected between 0.5 T and 1 T.

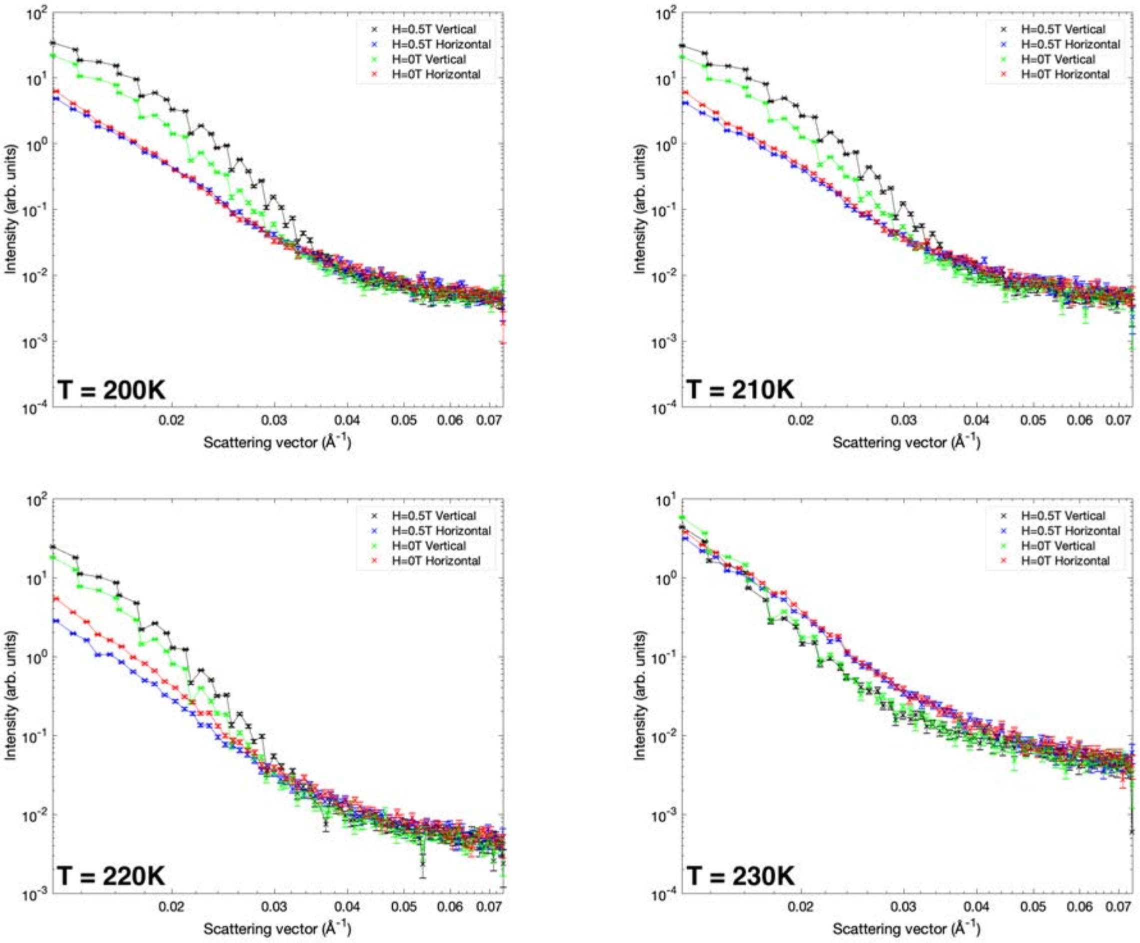

Figure 7.22: Split sector evaluation of the intensity as a function of scattering vector, for H=0 T and H=0.5 T, at different temperatures upon cooling from 300 K to 200 K.

7.2 Results - $\boldsymbol{n} \parallel [110]$

To further investigate the directionality of FePd at different ranges, a small study was performed with the beam direction parallel to [110]. After zero field cooling to 200 K, the hysteresis and field dependence of the material was measured. Figure 7.23 shows the results from this MQ scan, specifically a peak in the intensity at ≈H=0.15 T and almost negligible hysteresis.

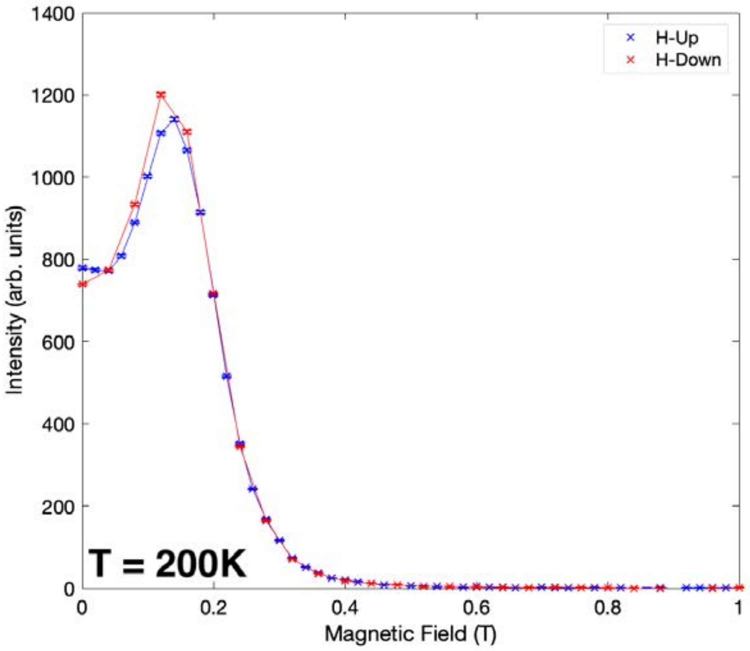

Figure 7.23: Intensity as a function of scattering vector at 200 K in the MQ range.

Following this, a warming temperature series (again MQ) was performed to determine the effect of temperature on the field response and Figure 7.24 presents the results. A reduction in temperature through the transition leads to a saturation-like decline in intensity with increasing field, however as temperature is reduced further towards 200 K there is an emergence of the peak centred at ≈H=0.15 T. Finally for this orientation, Figure 7.24 shows the hysteresis of the field response at both 200 K and 240 K. It is apparent that for this q range (a MQ/HQ hybrid), the peak centred at ≈H=0.15 T is incredibly dominant at 200 K but is seemingly not appearing at 240 K. Otherwise, the low temperature regions of this material are hysteresis free.

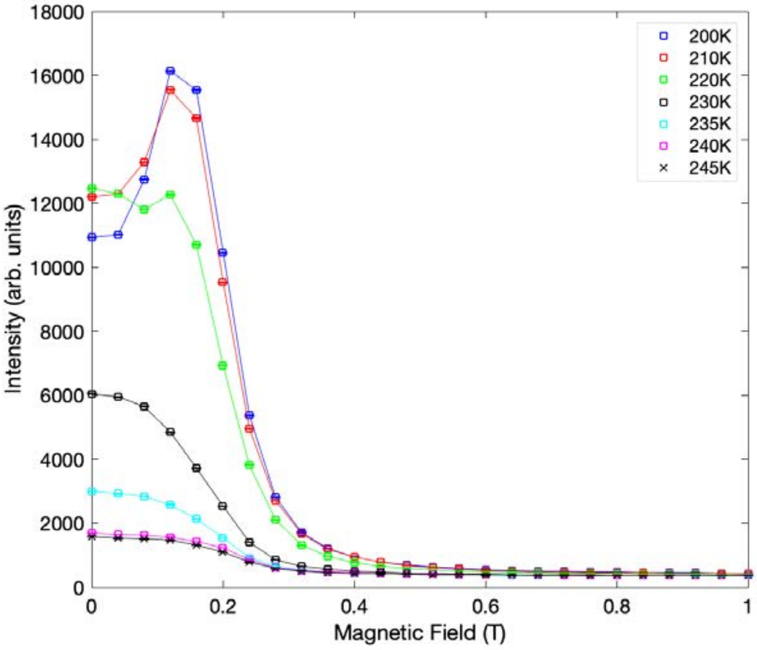

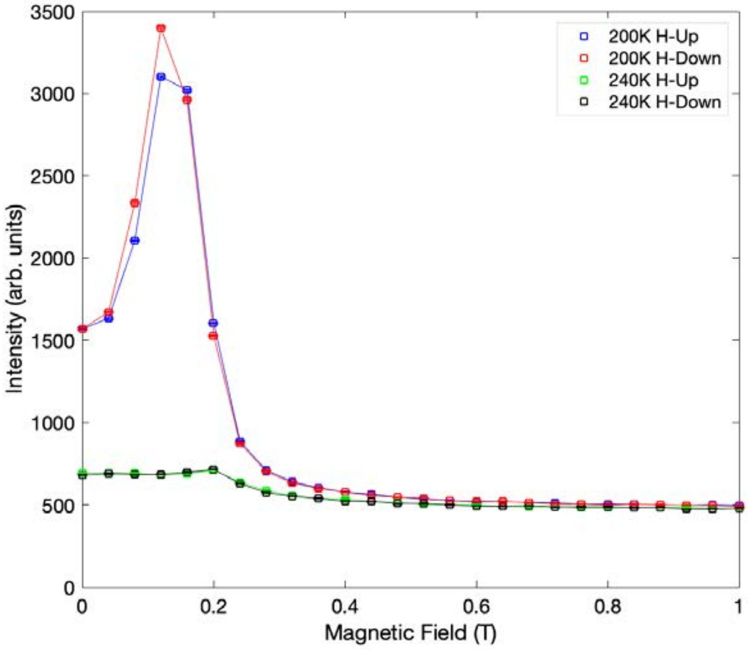

Figure 7.24: **Top** The field dependence (MQ) on intensity, for varying warming temperatures. **Bottom** Field dependence in the hybrid q range for temperatures of 240 K and 200 K.

7.3 Discussion

The results presented above clearly outline that FePd is a material which is heavily affected by temperature, applied field and directionality. At room temperature, the material is ferromagnetic as is evidenced by the non-linear decrease in scattering with increasing field. Magnetic domain walls are the likely cause for this scattering due to the length scales upon which this decrease is most prominent - the LQ range used at the FRM-II corresponds roughly to physical sizes in the range of 50 nm to 250 nm. The alignment of magnetic domains reaches saturation at $\approx$H=0.3 T, a feature which has been verified by magnetisation measurements previously.[35] Approaching saturation, the directionality of FePd is found to shift, i.e. there appears a directional bias in scattered intensity which is maximised at H=0.2 T. The dominant direction lies with the applied magnetic field. The room temperature hysteresis is fairly large, being on the order of 10% and despite the directionality influence with increasing field, there are no directional factors in hysteresis suggesting that the separation of the 'on' and 'off' field direction is itself reversible.

At higher q ranges (MQ corresponds to 25 nm$< d <$125 nm) the room temperature field dependence continues to provide information of note, specifically a low H four-fold anisotropy and a peak in the scattering at H=0.5 T. The four-fold anisotropy is aligned along the four [110] flavour directions, has a well defined + shape and persists until H=0.2 T. It is suspected that this anisotropy continues until saturation at which point the scattering collapses, which has been observed to occur at H=0.4 T for these measurements. The intensity of the four-fold anisotropy can be plotted as a function of the azimuthal angle where it bears a significant resemblance to magnetic torque measurements in the literature (Figure 7.25).[35] While the contrast between real and reciprocal space is apparent and therefore the magnetic torque changes recorded previously cannot directly be the cause of the scattering pattern measured in this work, it does however suggest at an underlying mechanism that reinforces the importance of both field and direction analysis.

Within the low field four-fold anisotropy, careful choice of analysis sectors and reduc-

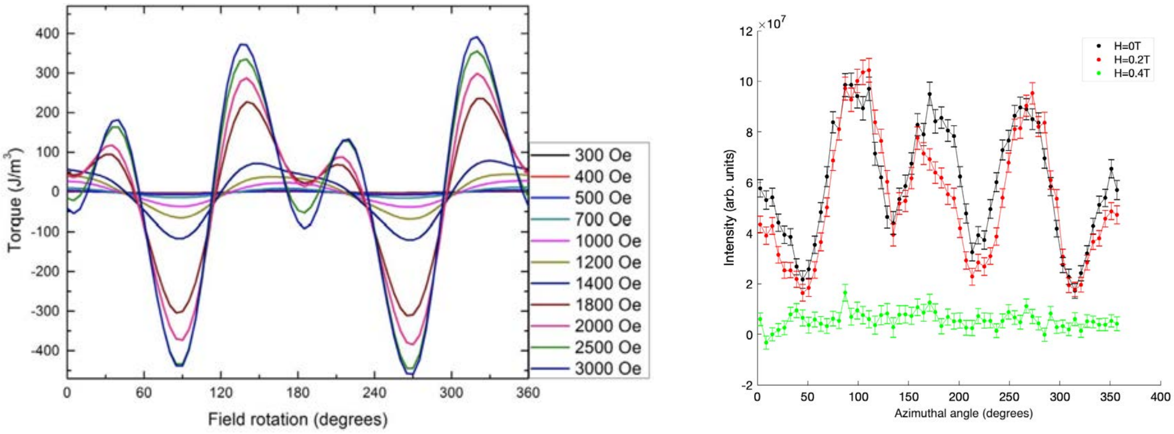

Figure 7.25: **Left** Magnetic torque measurements performed by Steiner et al. **Right** Azimuthal plot of the intensity. MQ, H=0T. Particular attention should be directed to the 0.2 T, or 2000 Oe, data which shows a combination of two- and four-fold anisotropy for both results.

tion reveals the existence of a peak in intensity as a function of scattering vector. The peaks are distinctly Gaussian in shape with a reasonably wide FWHM. Fitting of these peaks (present at H=0 T and H=0.2 T, H-Up and H-Down) yields a centroid position equivalent to 50 nm at H=0 T. This is reproducible for H-Up and H-Down, with the peaks broadening and shifting to a larger centroid relating size of approximately 55 nm.

As temperature is lowered from 300 K to 200 K (which should be significantly into the FCT phase) there is a clear two-step transition in the region of 250 K to 230 K. The higher temperature feature has a minimal impact on the scattered intensity, suggesting that the change in the magnetic response of the material is not significant within the adaptive (or pseudo-orthorhombic) phase. The hypothesised driving force for the phase transition in FePd is the coalescence and growth of the twinning clusters, which exist in the bulk at room temperature and are stabilised with decreasing temperature. It appears that the magnetic and symmetry properties (two-fold and four-fold combination discussed above) of these twinning clusters is a contributing factor to the physical properties, even at room temperatures where their physical size and volume density is small.

The second transition seen as a function of temperature, occurring around 230 K, is significantly more pronounced as the scattering intensity rises in a Landau-manner which is representative of a material cooling through T_C. This is peculiar as FePd is a known ferromagnet at room temperature, albeit with negligible hysteresis and coercivity. This large degree of magnetic reversibility is attributed to the presence of the twinning clusters, which have been found in other systems to 'fold and unfold' to reduce the magnetic anisotropy in their local region.[100] Following coalescence and growth through the adaptive phase region, the crystal structure becomes tetragonal and therefore one would expect a [001] maximisation for the strain. This is however not the case and below 240 K, the [110] direction remains the dominant magnetostrictive direction for all fields. The [001] strain is actually maximised within the adaptive phase region, specifically near the boundary with the FCT phase - it could be that the bulk emergence of twinning clusters, which are known to be elastically soft at the FCC-FCT transition, have an isotropic relaxing effect on the crystal which in turn yields increased strain for the [001] direction.

The magnitude of the two-step transition is visible in the scattering patterns, with the four-fold anisotropy becoming intrinsically more diamond shaped (i.e. losing its roundness at the + positions and instead evolving to assume a non-symmetrical square shape, orientated 45° off angle) below 250 K. Despite the changes to the pattern, the four-fold anisotropy remains prominent and increasing the field at 200 K is found to collapse the signal onto the field direction.

At low temperatures, FePd continues to exhibit almost zero hysteresis between increasing and decreasing field. Directionality effects persist though, with the peak at H=0.2 T only existing in the [110] direction aligned with the magnetic field. There is an assumption that this peak corresponds to magnetic saturation as it correlates well to the room temperature magnetic properties however it is intriguing that the change in crystal structure did not affect the saturating field. Furthermore, the increase in scattering from zero field up to H=0.2 T suggests that the features in this range have some resistance to magnetisation in low amounts. It may be the case that the martensitic phase (existing of long range ordering of twin clusters) maintains its isotropic demagnetisation field up to fields of H=0.2 T, at which point the demagnetisation field is quenched and bulk saturation occurs. This is backed up by the fact that the scattering in the [110] direction perpendicular to the applied field is almost flat until H=0.2 T, at which point the magnetisation collapses to zero.

Probing the smaller length scales (high q) elucidates some intriguing directional properties of FePd, hinting at an intimately linked phenomena between crystallographic direction, magnetisation and temperature. Twinning striations (of character $\{110\}/\langle 110\rangle$) have been detected in FePd at room temperature, with striation separation of approximately 5 nm. When converted to a reciprocal space value, the striations (assuming 5 nm spacing) will correspond to an approximate value of q=0.1 $\AA^{-1}$. The high q measurements showed a strong, isotropic peak in the field dependence at room temperature, with the peak centred at H=0.5 T and with a width of 0.1 T. Analysis of the scattering vector dependence at this peak position and comparison to H=0 T show negligible difference in the hysteresis response, directionality and general scattering vector dependence - seemingly the only difference is one of increased scattering. As temperature is lowered, the prominence of the beam is reduced through the transition, to such an extent that there is no discernible peak in the field dependence at 230 K. Continuation of cooling causes the reemergence of the H=0.5 T peak, which becomes quite pronounced (taking almost Lorentzian-like shape). Note that the zero field intensity is uniform for 200 K and 210 K, whilst the H=0.5 T peak shows higher intensity for 200 K than for 210 K, potentially highlighting that the feature causing an intensity peak at H=0.5 T has a different thermal behaviour to the bulk.

Shifting orientation to neutrons parallel to the [110] direction (therefore the in-plane directions of the disk are another [110] and [001] direction, respectively vertical and horizontal on the scattering pattern). Tracking these directions with reducing temperature, it has been found that the [110] direction becomes the dominant scattering direction below 230 K - more specifically, there is bulk isotropy within the adaptive phase region which is independent of field. For T<230 K the [110] direction is dominant for all values of field, likely due to the FCT phase itself having a directional preference in this directions, a feature which likely holds from the precursor twinning clusters.

Cooling to 200 K shows that FePd remains free of magnetic hysteresis even after a phase change, something which is ideal as a long term application. As seen in the MQ range, there is a well defined peak in the field dependent intensity at H=0.2 T. It has been previously noted that the twin clusters in FePd are highly mobile and have an unusually high demagnetisation field - these clusters will mobilise to minimise the magnetisation, eventually de-twinning at saturation. The lack of peak appearance at H=0.5 T for this beam direction (H $\parallel$ [001]) is in direct contrast to the previous measurements which show the aforementioned peak when H $\parallel$ [001]. Clearly this HQ feature has a very specific field response, yet also seems to undergo the elastic softening at the transition.

7.3.1 Key Findings and Evaluation

- Iron-palladium exhibits magnetic saturation at H=0.2 T - coinciding with magnetisation measurements performed in literature and visible in reciprocal space as a Landau-like increase in scattering with decreasing temperature.

- Presence of an anisotropy in the scattering pattern, which bears similarities to a combination of two- and four-fold anisotropy observed in the magnetic torque of FePd. Isolating this anisotropy along the [110] directions shows a clear peak in the intensity, with scattering features of size 50 nm at zero field. Application of low field (H=0.2 T) increases the size of this feature to 55 nm, before the feature seemingly collapses upwards of H=0.4 T.

- A two-step, thermally induced transition which confirms the presence of an adaptive phase, consisting of a co-existence of FCC and FCT phases, before a bulk transition into FCT. The FCT phase produces significantly larger scattered intensity in a manner that appears ferromagnetic in nature - a reduction in temperature produces a significant increase in signal, reminiscent of the second-order transition seen when a material is cooled below its Curie temperature. The mixed FCC-FCT phase does not contribute as strongly to the intensity increase as the volume fraction of FCT is presumed to be low and yet to dominate the magnetic response, however the growth of the adapting does lead to a small signal increase. At 200 K, the field dependence produces a peak at saturation (H=0.2 T) before proceeding to fall to zero as field is ramped further.

- A crystal direction dependent peak in the high q region at H=0.5 T. This peak is present when the field is aligned along a [110] direction but fails to appear when H $\parallel$ [001], suggesting a strong reliance on magnetocrystalline anisotropy for the feature inducing this scattering interaction. The peak is shown to stand out significantly from the background at 200 K and 300 K but is indistinguishable around the transition temperature. Finally, the [110] direction remains dominant in intensity despite field direction being applied parallel to [001] in this geometry.

These results clearly show that the precursor twinning clusters, or martensitic tweed, play a crucial role in the physical properties of iron-palladium. It has already been highlighted that the resistance to magnetisation of these clusters, arising from a unique demagnetisation field, play a significant role in the minimisation of magnetic energy within the material. It is likely that the twinning clusters continue to play a crucial role in the material following the transition to a bulk FCT phase.

Room temperature analysis of the four-fold anisotropy clearly reveals a group of scattering features with an average size of 50 nm at 0 T and 55 nm at 0.2 T. These features are reversible with applied field and exist solely along all of the [110] flavour directions. As temperature is reduced, the [110] directions preserve their anisotropy however there is a growth in intensity in the intermediate directions. This arises from the bulk coalescence of clusters at the phase transition and makes the twinning clusters hard to detect using SANS, with the anisotropy becoming sharper in q and not in azimuthal angle. These twinning clusters are highly mobile and significantly larger than those previously seen using TEM, with these results suggesting cluster size of 50 nm in comparison to tweed striations seen on the 2 nm length scale.

The high q range, covering physical sizes from ≈ 5 nm up to ≈ 30 nm show a peak in the magnetisation at H=0.5 T, when applied field is along a [110] direction. For the orientation when $H \parallel [001]$, this peak does not appear. Given this information and supported by the knowledge of twinning striations within FePd,[100] it appears that there is also a distribution of striations which exist along, and are incredibly resistant to magnetisation, along the [110] directions. Given their small physical size, their net contribution to the bulk magnetic properties will be small and likely undetectable using conventional methods. However, with SANS, direct evidence has been observed for some transition at 0.5 T whose length scale corresponds directly to that of the twinning striations. As field is ramped, the striations will resist magnetisation (due to their mobility and extremely low anisotropy) until such point when the magnetism is able to 'override' the twin character, forcing alignment along the [110] directions. At this override point, the striations produce a peak in scattering intensity whose character is currently undetermined - it may arise from a magnetic or crystal structure effect, more likely a combination of both.

As FePd is cooled to 200 K it clearly passes through the expected adaptive phase before becoming FCT in the bulk. The two phases show different levels of scattering intensity, with the latter FCT producing a very dominant degree of scattering upon cooling. Saturating field remains constant at H=0.2 T for all values of temperature, although the intensity of signal is more pronounced outside of the transition than within it, likely arising from the softening of the phonon coupling during co-existence of the FCC and FCT phases. The same is true for the high q peak at H=0.5 T, suggesting that the peak in scattering at saturation is a feature of the FCT phase regardless of its physical form, i.e. bulk or striations.

7.4 Further fundamental material investigations

It is fairly typical for Doctoral programmes with a focus on beamline/large-scale facility techniques to include investigations that span multiple scientific strands - the work included in this thesis is no different, presenting studies on two specific alloy systems. Other work performed in this thesis includes but is not limited to:

Irradiation induced precipitation in reactor pressure vessel steels Precipitation clusters, comprising mainly of Cu, Mn and Ni, have been found to negatively affect the key properties of reactor pressure vessels in the nuclear industry. These clusters form due to the large irradiation and time at temperature experience near the core of nuclear reactors. The cluster size and changing magnetic character make them detectable on the SANS scale. Work in this project involved an experimental SANS study, coinciding with a metallurgical characterisation of reactor pressure vessel steels.

Search for magnetic polarons in europium hexaboride and europium telluride Polarons are a hypothesised quasiparticle, consisting of a cage of lattice distortions and a drifting conduction electron. Exchange interactions between the conduction electron and local lattice moments may give rise to the existence of magnetic polarons. These local regions of ferromagnetism have been speculated to play a crucial role in the insulator to metal transition in europium hexaboride/telluride and therefore could be the underlying mechanism behind the colossal magnetoresistance seen in this compound. Multiple SANS studies on this compound have been performed in the pursuit of direct evidence for magnetic polarons. Given the experimental difficulties in measuring Eu based samples (large neutron absorption), it has proved troublesome to achieve these desired results in a typical transmission SANS orientation.

Polarised SANS on FePd In addition to the work presented in this chapter, a polarised neutron scattering study on FePd has been attempted. The aim of the experiment was to isolate the contributions from the four channels of polarised scattering (++,+-,-+,–) which in turn would allow for the determination of the precise magnetic and structural contributions to the scattering pattern. Unfortunately, given the ferromagnetic nature of FePd and the desire to probe features at magnetic fields exceeding saturation (i.e. the 0.5 T peak), the results from these measurements remain inconclusive.

Chapter 8

Functional materials ($Tb_{1-x}Dy_xFe_2$): Results & Discussion

This chapter recounts the results of the synchrotron XRD study on various compositions of $Tb_{1-x}Dy_xFe_2$ samples. Results are presented in this chapter firstly as individual samples, before a summary of the MPB position is delivered. When discussing temperature regions, these are are divided as 'low', 'intermediate' and 'high', relative specifically to the sample environment used to achieve them. Table 8.1 summarises these temperature ranges.

Table 8.1: Definition of the temperature regions described in this analysis.

Region name	**Sample environment**	**Temperature range**
Low	Cryostat	10 K to 120 K
Intermediate	Cryostream	90 K to 300 K
High	Hot air blower	300 K to 700 K

The two main methods of data presentation and analysis in this chapter are: colour maps, covering a wide temperature and angle range, with the intensity displayed as an overlaid colour, and individual scans of the (222), (440) and (800) reflections, displaying intensity as a function of angle. Colour maps allow for easy visualisation and determination of transition temperature and character and follow a typical 'temperature' scale; blue or 'cold' represent a minimum in intensity, while dark red or 'hot', represent the maximum intensity values for that figure. Due to the reflection sites chosen, new or changing appearances of colour/intensity (rapid or slowly with temperature) are signals of a change in phase structure. Discontinuities in the centroid positions and/or intensity hint at the existence of first-order phase transitions, or 'sharp' boundaries. While colour maps are particularly effective at highlighting the presence and position of phase transitions, they are not so effective at presenting the specific peak splitting which occurs over very small angle ranges (an example is four separate features within an angular range of 0.5°) - individual intensity scans at various temperatures addressed this problem. Plotting the intensity as a function of angle for individual temperatures (or occasionally multiple temperatures where appropriate) the nature of the phases and/or phase mixing at that composition & temperature position can be assessed. The ratio of peak amplitudes is used as an indicator of both the degree of phase mixing, however peak fitting is only performed for defined regions of two peaks, with a double pseudo-Voigt profile (see Chapter 6.4.2). The metric of 'amplitude ratio' visible on the figures in this Chapter, is defined in Eq. 8.1 and Table 8.2 presents a summary of the expected peak amplitude ratios for rhombohedral, tetragonal and cubic phases. Amplitude ratio is used to show a 'trend' in the peak splitting behaviour, in that it is shown to highlight when a set of reflections is distorting towards a given phase.

$$Amplitude\ Ratio = \frac{High\ angle\ intensity}{Low\ angle\ intensity} \tag{8.1}$$

Table 8.2: Expected peak amplitude ratios for the rhombohedral, tetragonal and cubic phases. Unity represents no splitting, or one single peak in the intensity. Otherwise, peaks are listed in order of ascending angle, such that the ratio is *Low angle intensity:High angle intensity*. The value of the amplitude ratio metric, calculated using Eq. 8.1, is given in brackets.

	(222)	**(440)**	**(800)**
Tetragonal	Unity	1:2 *(2)*	2:1 *(0.5)*
Rhombohedral	1:3 *(3)*	1:1 *(1)*	Unity
Cubic	Unity	Unity	Unity

8.1 Sample 1 - $\mathbf{Tb_{0.44}Dy_{0.56}Fe_{2.01}}$

Given that this composition has a relatively high Tb content, the measurements were focused on monitoring the low temperature region, where the $TbFe_2$ parent phase should induce a rhombohedral distortion which will in turn generate a peak splitting in the amplitude ratio of 1:3. There are no corresponding Mossbauer results relating to this composition, however by extrapolation between the known easy axis results, the MPB is anticipated to appear at approximately 50 K.[32] By probing temperatures between 10 K and 90 K, evidence has been uncovered for a previously undiscovered low symmetry, low temperature phase where the peak transformations and resultant positions do not coincide with either of the parent phases. A further discovery is that of a first-order transition from the co-existence of rhombohedral and low symmetry phases, signalled by a spontaneous 'jump' in the peak amplitudes at 50 K, which heralds a second-order growth in dominance of the rhombohedral phase. The shift to a fully rhombohedral structure appears to still be occurring at 86 K.

Figure 8.1 shows the peak intensity as a function of temperature and two theta angle for all three reflection sites, where there is a sharp discontinuity in the region of 50 K. Below the discontinuity, the (222) reflection site shows four key features at 14 K (Figure 8.2) - two peaks at approximate positions of 9.60° and 9.62°, as well as two well defined shoulders at ≈9.58° and 9.63°. The presence of these additional features suggests the existence of some low symmetry phase. As temperature is increased to 46 K, there is minimal change in the reflection site other than an increase in signal at the ≈9.58° shoulder. Between 46 K and 54 K, there is a sharp transition above which the resultant angular dependence on intensity is characteristic of a rhombohedral lattice distortion (two peaks at 9.58° and 9.62°), although there remains some dilution of the lower angle peak in that its intensity is higher than expected. Rhombohedral lattice distortions will cause a 1:3 splitting ratio in the (222) reflection. Analysis of the peak intensities at T=86 K for this reflection yield an approximate value to the amplitude ratio metric (Eq. 8.1) of 1.67. At T=82 K, this metric is 1.36. This discrepancy in the peak amplitude ratio suggests that phase mixing

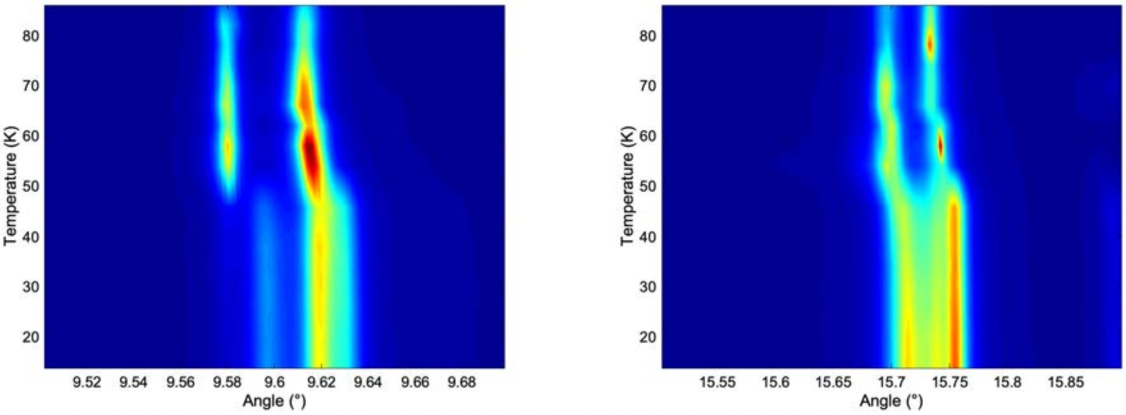

(a) (222) reflection

(b) (440) reflection

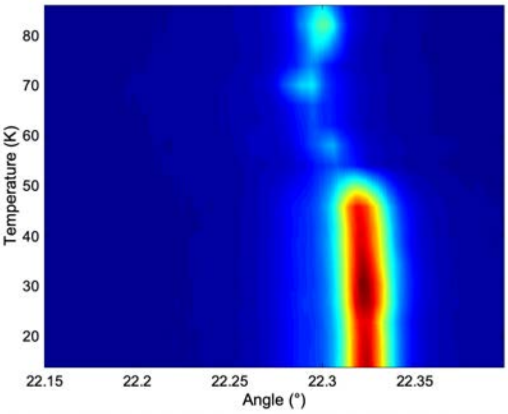

(c) (800) reflection

Figure 8.1: Low temperature intensity mapping at the specific reflection angles of interest for $Tb_{0.44}Dy_{0.56}Fe_{2.01}$ for a temperature range of 14 K to 86 K

is preserved with increasing temperature and is still significant at T=86 K. The intensity vs angle scans for temperatures in the range 14 K to 86 K, at the (222) reflection site are given as Figure 8.2.

Similarly, the (440) reflection exhibits a co-existence of phases at 14 K with approximate peak positions of 15.72°, 15.74° and 15.76°. The outer peaks are expected for a rhombohedral lattice distortion, while the centre peak is not. All three peaks share roughly similar amplitudes. Increasing temperature to 46 K results in amplitude changes to two of the peaks - relative to the 15.72° peak, the centre-most peak shows reduced amplitude while the high angle peak intensity is enhanced. Across the supposed boundary, the transition is sharp and at 54 K the low angle peak has become dominant while the centre peak (attributed to arise from a low symmetry phase) is reduced to exist within the background. Further temperature increase reverts the peak dominance to the high angle peak. The (440) reflection peaks should take a ratio of 1:1 under a rhombohedral distortion and, as in the case of the (222) reflection for this sample, this amplitude ratio is not yet seen at 86 K suggesting co-existence of phases at this temperature. Figure 8.3 summarises these (440) reflection scans.

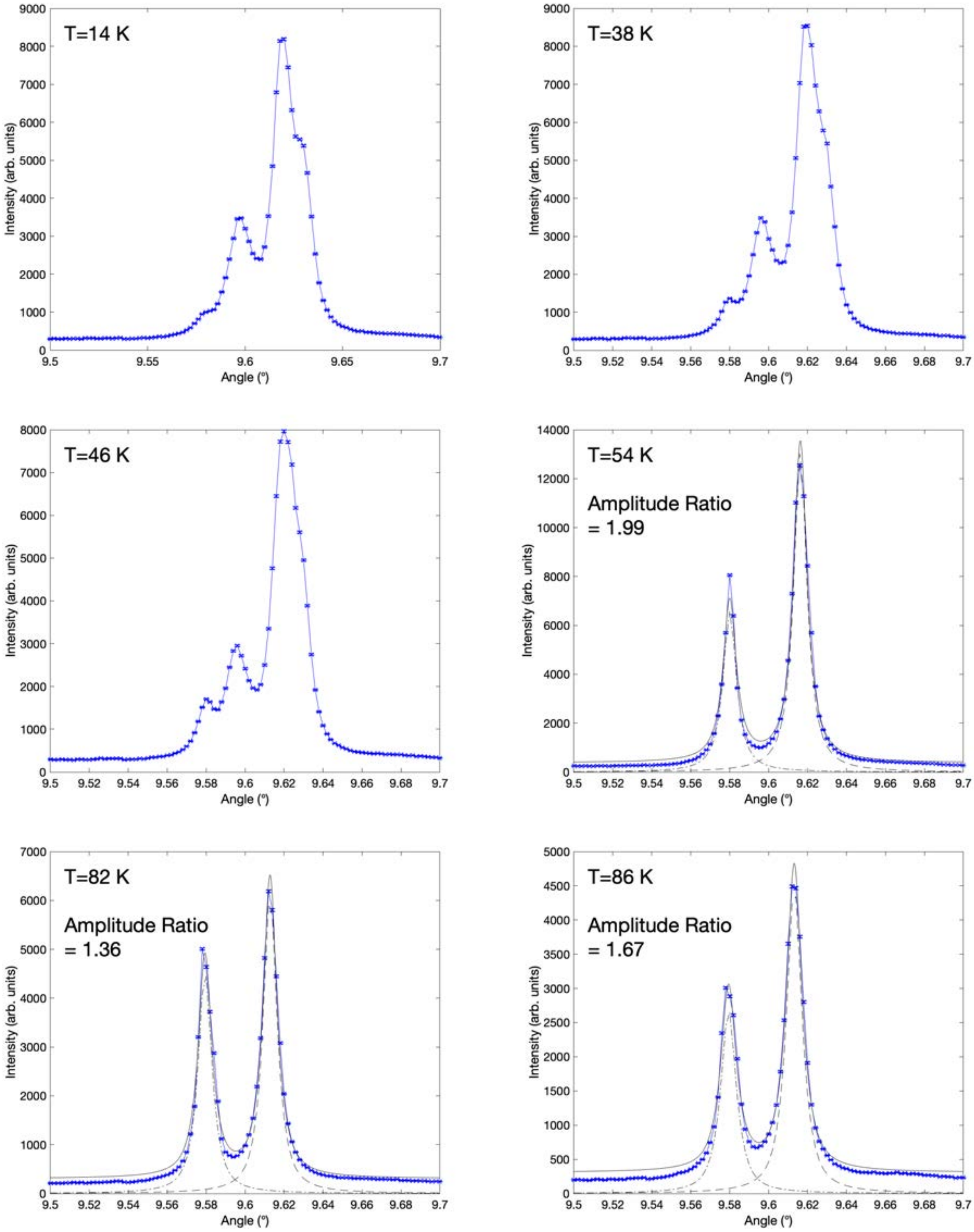

Figure 8.2: Intensity as a function of two theta angle at the (222) reflection site, for key temperatures within the range 14 K to 86 K.

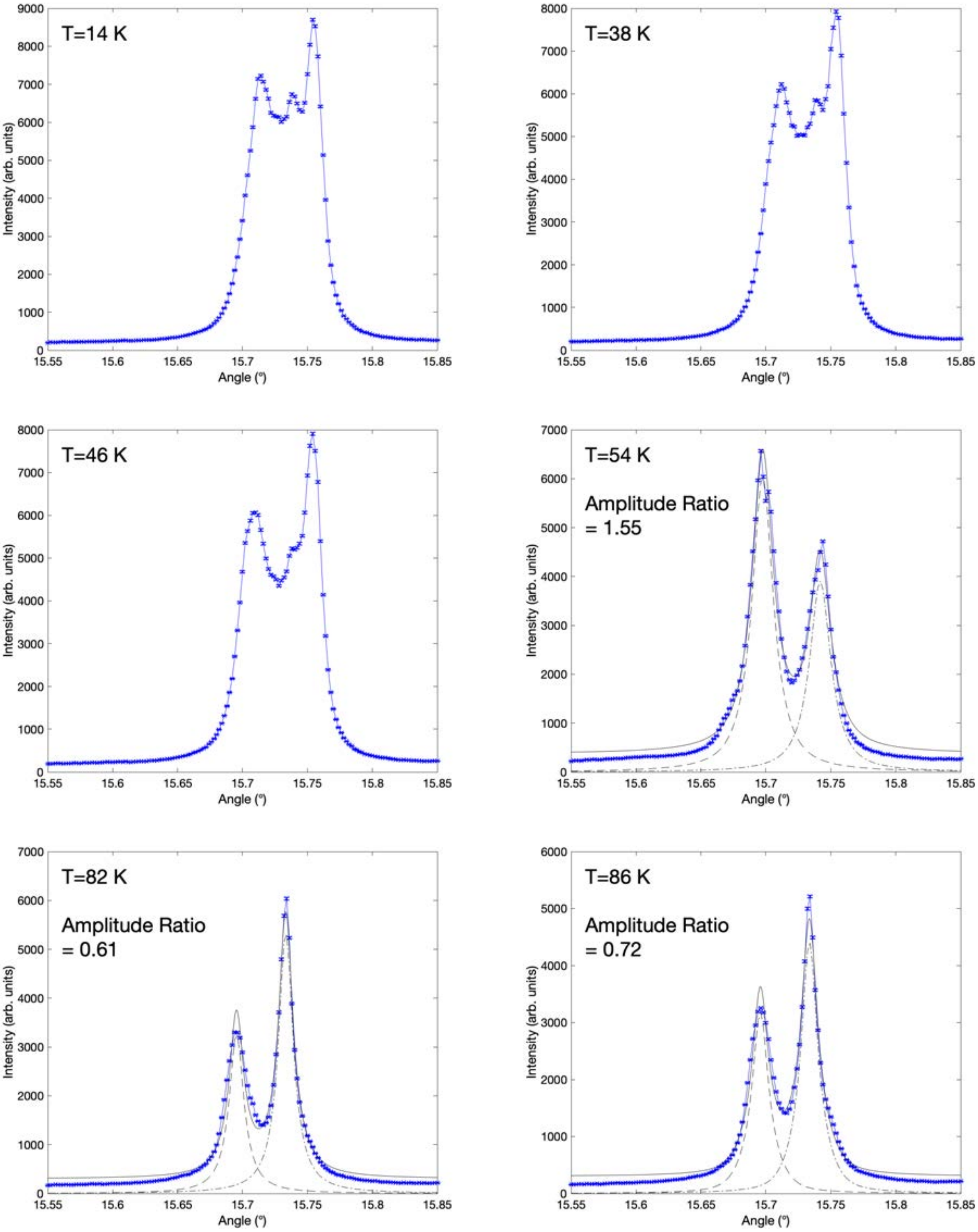

Figure 8.3: Intensity as a function of two theta angle at the (440) reflection site, for key temperatures in the range of 14 K to 86 K.

8.2 Sample 2 - $\mathbf{Tb_{0.40}Dy_{0.60}Fe_{2.01}}$

For this sample, the aim was to track the reflection positions through a larger region of interest, namely from 10 K (using the cryostat) up to 300 K (using the Cryostream). The results are divided into two approximate ranges, the low temperature range (10 K to 70 K) and an intermediate temperature range (100 K to 300 K). The low temperature colour plots (Figure 8.4) show reproducible evidence from Sample 1 that there is a transition to a low symmetry phase at around 50 K, demonstrated by the existence of two additional peaks (at 9.60° and 9.63°) whose intensities fade into background above 50 K. All three reflection sites show a clear discontinuity in the centroid positions of the main intensity peaks, with a centroid shift to the lower angle on the order of 0.01° at 50 K. A summary array of the (222), (440) and (800) reflections, where the peak fitting results are plotted and amplitude ratio is presented, are given respectively as Figures 8.6, 8.7 and 8.8.

The intensity profiles exhibited above 50 K are well defined - the (222) reflection shows two pronounced peaks, with the higher angle peak being significantly stronger in intensity than the peak at ≈9.58°. The (440) reflection shows a uniform, even splitting above 50 K with only slight variation in intensity (the lower angle peak shows stronger intensity) and a separation of 0.05°. Finally, the (800) reflection shows a single peak with considerable width; some degree of increased peak width is expected as scattering angle is increased, however the non-symmetrical intensity profile for this reflection is characteristic of peak shouldering, which appears unchanged with increasing temperature (from 10 K to 68 K).

Continuing into the intermediate temperature range of 95 K to 300 K, the intensity profiles and centroid positions at 95 K agree well with the 68 K information from the low temperature data set (Figure 8.5). The (222) reflection maintains its intensity imbalance character, while the (440) reflection appears to be more evenly split and the shouldering on the (800) reflection remains unchanged with temperature. The width on the low angle side of the (800) reflection is approximately 0.05°, significantly larger than that on the high angle side (≈0.01°).

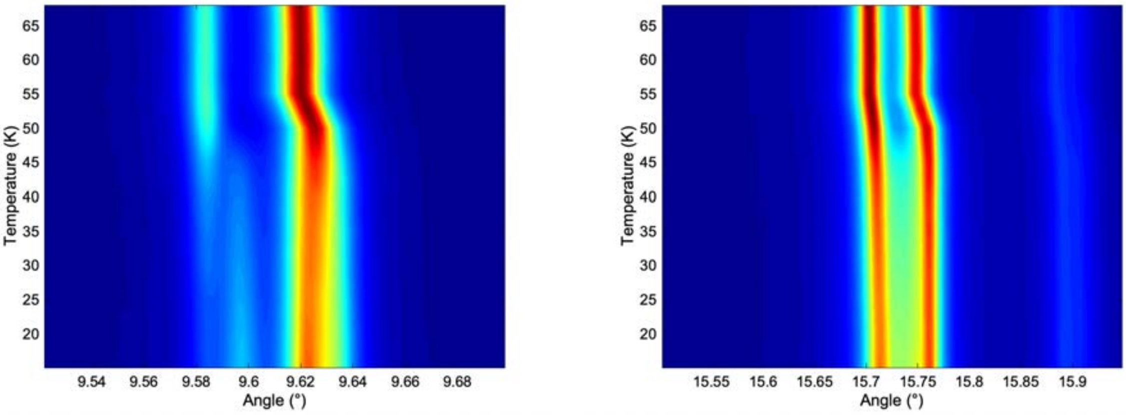

(a) (222) reflection

(b) (440) reflection

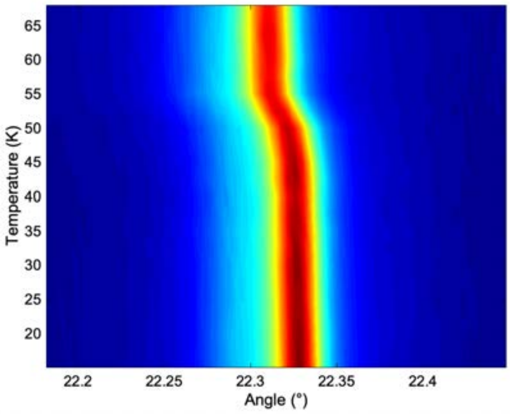

(c) (800) reflection

Figure 8.4: Intensity mapping at the specific reflection angles of interest for $Tb_{0.40}Dy_{0.60}Fe_{2.01}$, for a temperature range of 10 K to 68 K.

For the two reflections with a discernible peak splitting, specifically the (222) and (440) reflections, the centroid separation decreases in a linear fashion with increased temperature such that the peak splitting appears to 'close' with warming.

Analysis of the individual intensity vs angle scans (Figures 8.6, 8.7 and 8.8) shows that for the (222) reflection above 50 K, the amplitude ratio metric tracks well towards the expected value of 3, confirming the rhombohedral character. Alongside this, the (440) reflection shows dual peak character across a wide temperature range (15 K to 293 K) with the expected amplitude ratio metric of 1. It is important to highlight however that the goodness of fit is increasingly poor for temperatures below the transition, suggesting that as seen in Sample 1, there is a third peak feature in the angle region of 15.74°, which 'pollutes' the rhombohedral distortion at low temperatures. The change in the (800) reflection is minimal with temperature, although the statistics suffer at higher temperatures where the increased thermal vibrations cause problems at high angle peaks.

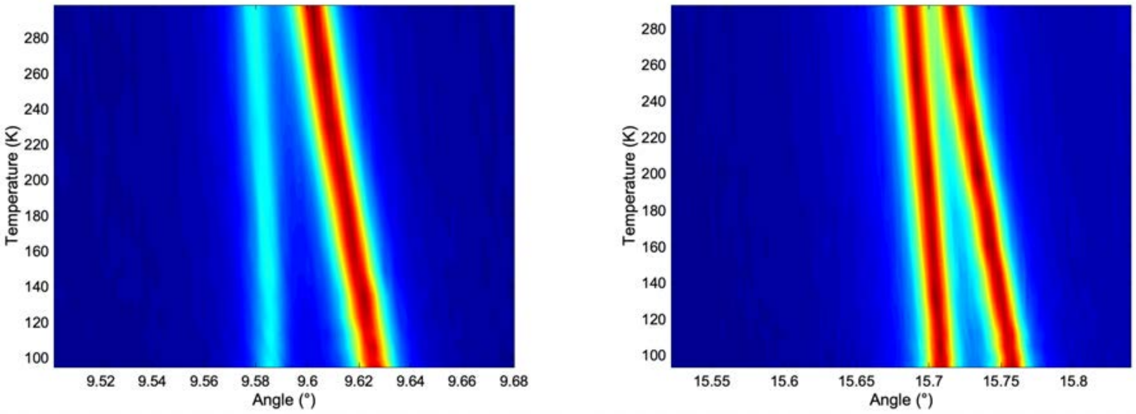

(a) (222) reflection

(b) (440) reflection

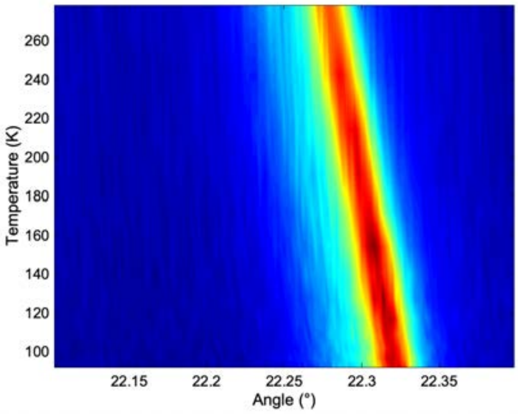

(c) (800) reflection

Figure 8.5: Intermediate temperature intensity mapping at the specific reflection angles of interest for $Tb_{0.40}Dy_{0.60}Fe_{2.01}$, for an approximate temperature range of 100 K to 300 K.

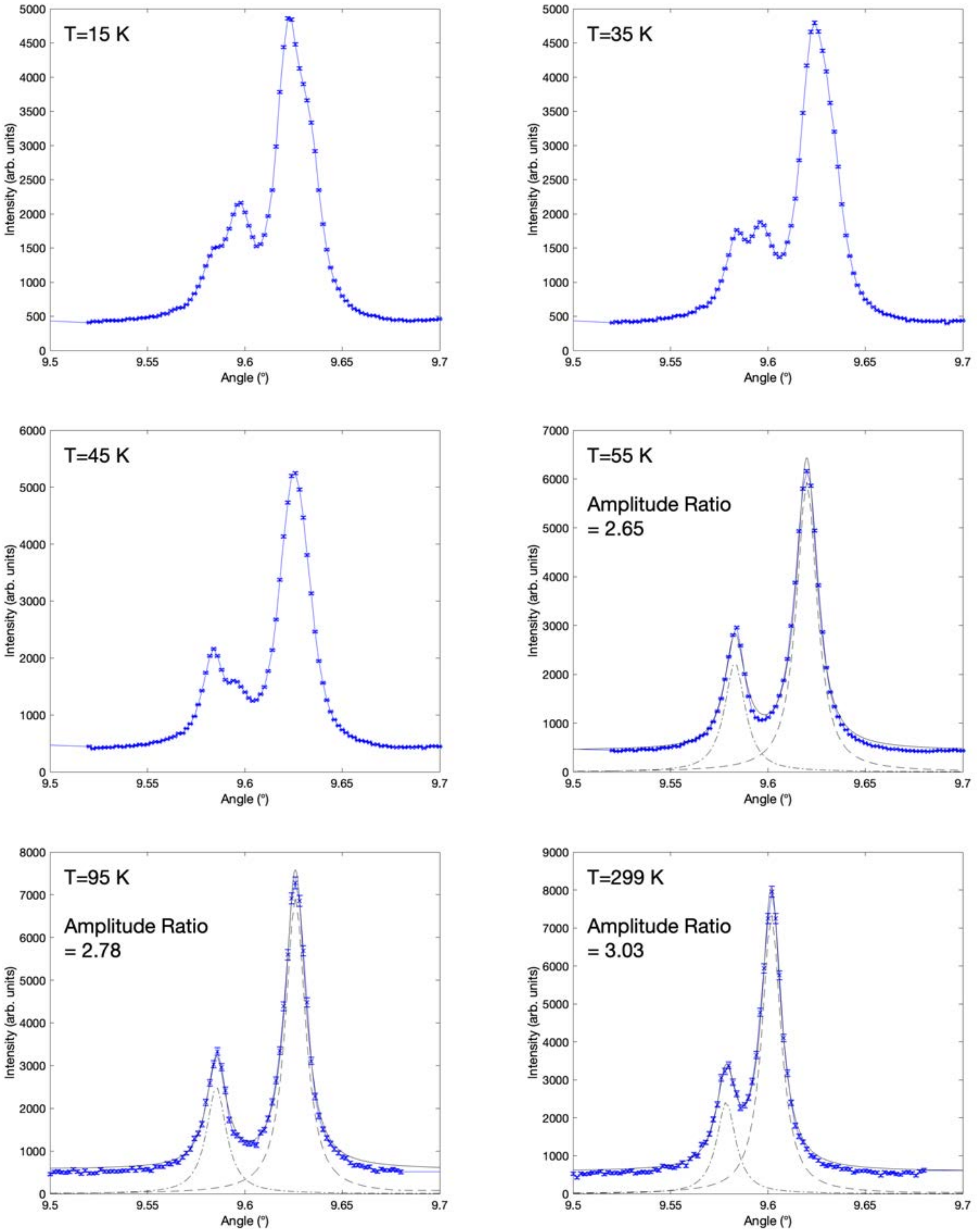

Figure 8.6: Intensity as a function of two theta angle for multiple temperatures at the (222) reflection site.

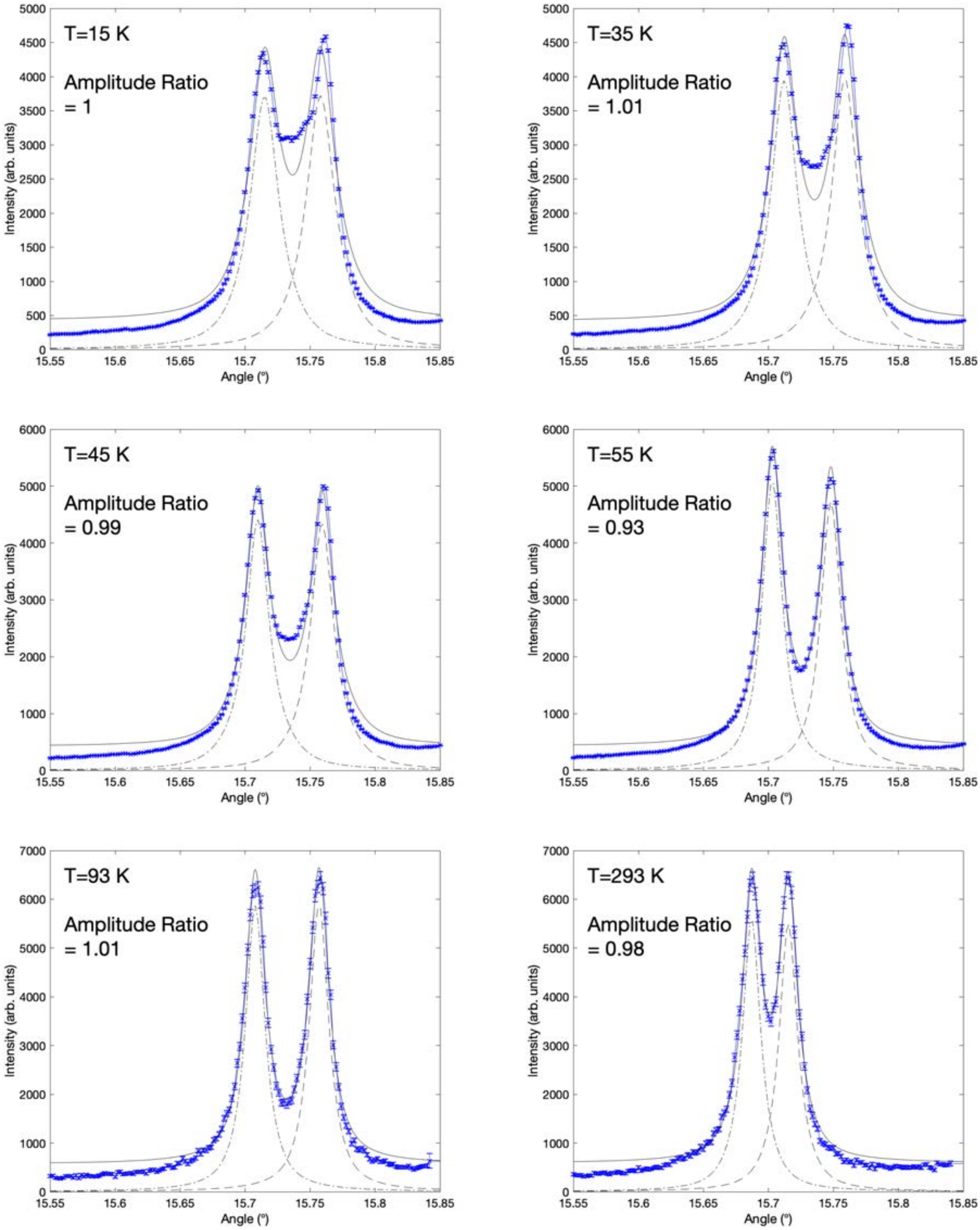

Figure 8.7: Intensity as a function of two theta angle for multiple temperatures at the (440) reflection site.

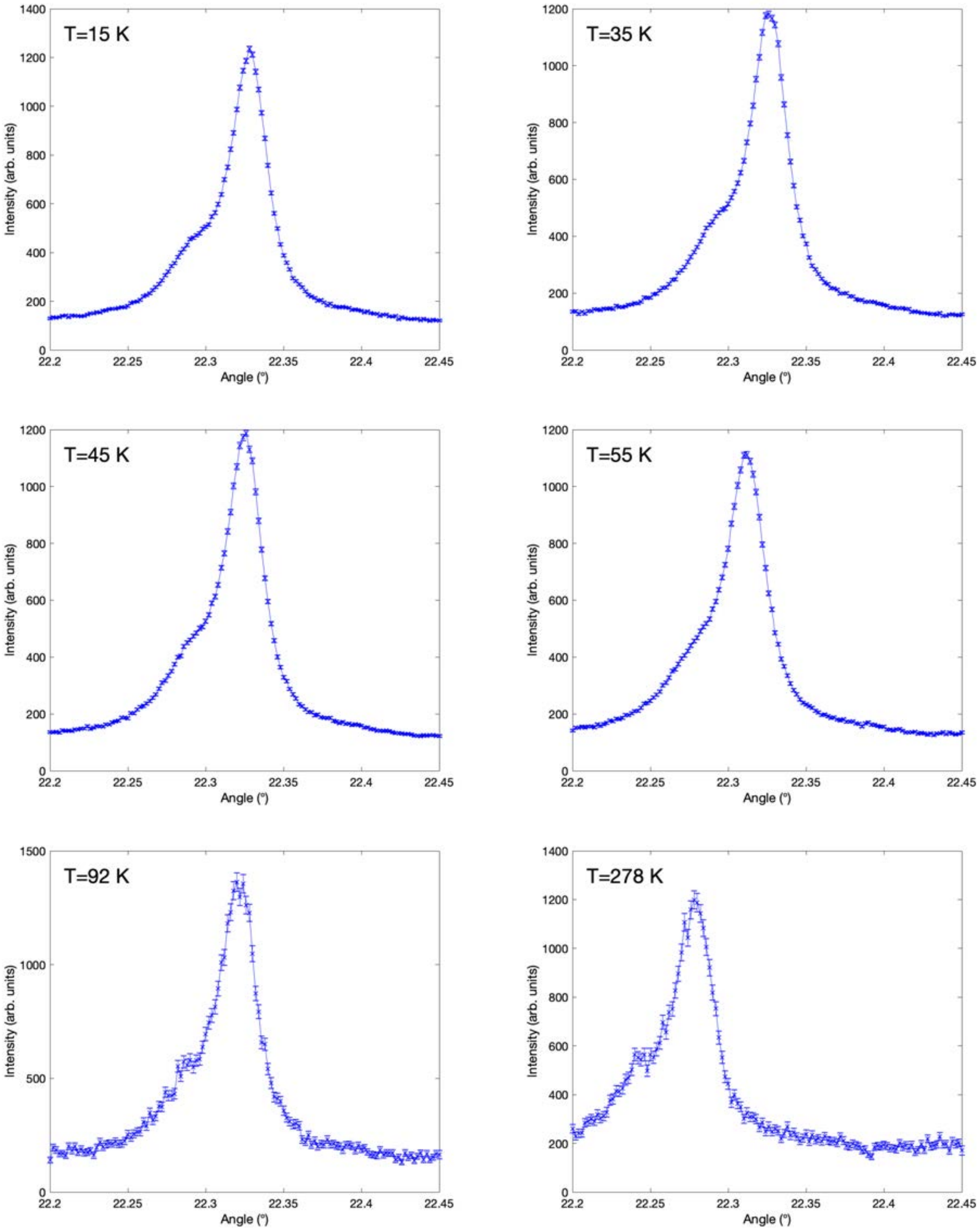

Figure 8.8: Intensity as a function of two theta angle for multiple temperatures at the (800) reflection site.

8.3 Sample 3 - $\mathbf{Tb}_{0.36}\mathbf{Dy}_{0.64}\mathbf{Fe}_{2.02}$

This sample is of particular interest as it encompasses a large range of features: the expected rhombohedral-tetragonal MPB but also low T Mossbauer results either side of this composition (x=0.6 and x=0.7) show different easy axes of magnetisation,[32] suggesting that some transition takes place in the low temperature region. Given the intrigue in this region of the phase diagram, a full temperature scan (10 K to 700 K) was performed and also temperature hysteresis scans in certain ranges to assess the effect of cooling and warming on certain transitions.

Beginning with the low temperature region, Figure 8.9 shows there is a clear hysteresis between cooling and warming - transition appears to occur around 50 K for cooling but not until approximately 110 K for warming, although there is a slight peak shoulder, visible as a smear on the colour plot, extending down to around 50 K for warming. It is important to highlight that the discontinuity, or first-order 'jump' in the centroid peak position at 50 K (seen in Samples 1 and 2) is again shown for this sample, however the magnitude of said centroid shift to low angle is lessened (approximately 0.005°, as opposed to 0.01° for Sample 1). The hysteresis response is summarised in Figure 8.10, which shows the overlaid cooling and warming (222) peaks as a function of temperature. While the centroid positions of the peaks remain within error for cooling and warming, there is approximately a 50 K difference between the transition temperature, found in both the (222) and (440) reflections.

Figure 8.11 shows the colour map array for warming in the intermediate and high temperature ranges, while Figure 8.12 shows the three reflection sites at key temperatures through the whole temperature range. The transitions in this sample are particularly noteworthy and intriguing. The peak reflections at 20 K are all unity, signalling that this phase is neither rhombohedral, tetragonal or the low symmetry phase observed in Samples 1 and 2. Based purely on the reflection measurements, it would be assumed that this low temperature phase is cubic in nature (due to its high symmetry and lack of distortion driven peak splitting), however the presence of a low temperature cubic structure in this alloy series has not thus far been suggested - in all likelihood the distortion is below the detectable limit, a reality that may occur from poor sample quality. Furthermore, it is peculiar that the previous low symmetry to rhombohedral transition (Samples 1 and 2) exhibit no hysteresis for warming and cooling. This sample, where the peaks are reflective of a high symmetry system, has a transition with well quantifiable hysteresis and this further adds to the intrigue for this phase.

Trending upwards through the transition, the peaks shift to take on a rhombohedral like reflection pattern (i.e. splitting of the (222) and (440) but not the (800) reflections), which then persists through the intermediate temperature range. The (440) amplitude ratio shows consistent agreement with the expected value of 1 for the majority of rhombohedral region, however the (222) reflection exhibits more fluctuation in the peak splitting, with the amplitude ratio varying from 4 at 98 K before trending towards, and decreasing below, a value of 3 at 406 K. Upon further heating, centroid position separation is reduced until such a point that the peak splitting is no longer observable - the peaks merge back to unity. Further to this, there exists a slight discontinuity in angle at approximately 600 K. This discontinuity takes a similar form to that seen in the low temperature data of Samples 1 & 2, and is seemingly a first-order transition, one which is more in line with a transition to a high temperature cubic structure.

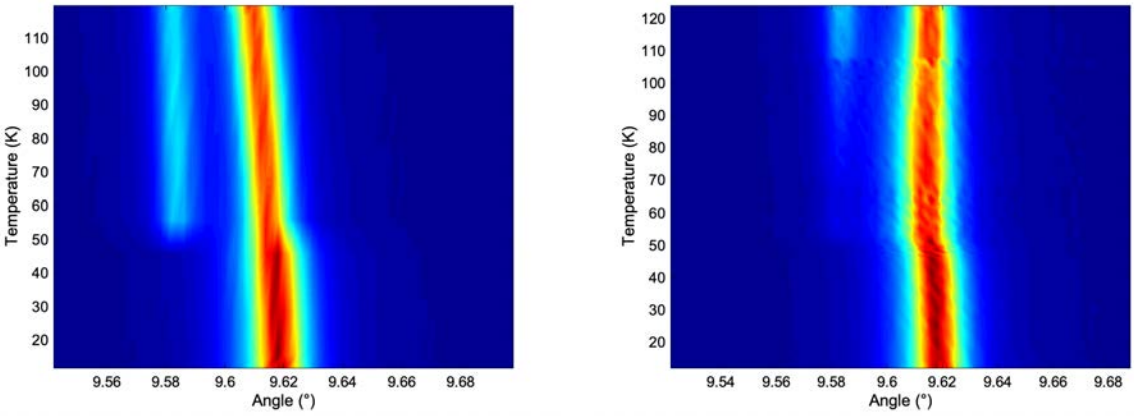

(a) (222) Cooling

(b) (222) Warming

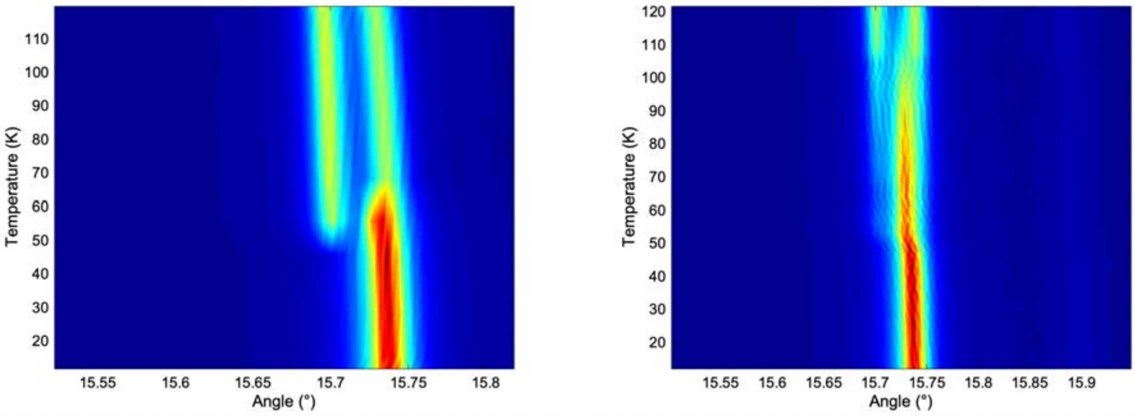

(c) (440) Cooling

(d) (440) Warming

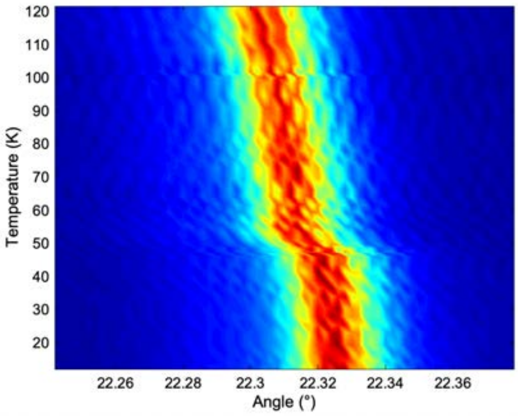

(e) (800) Warming

Figure 8.9: Low temperature intensity mapping at the specific reflection angles of interest for $Tb_{0.36}Dy_{0.64}Fe_{2.02}$. Note that a cooling run for the (800) reflection was not performed due to early errors in experimental set-up, another of which is the reduced resolution unfortunately visible in the (800) warming results.

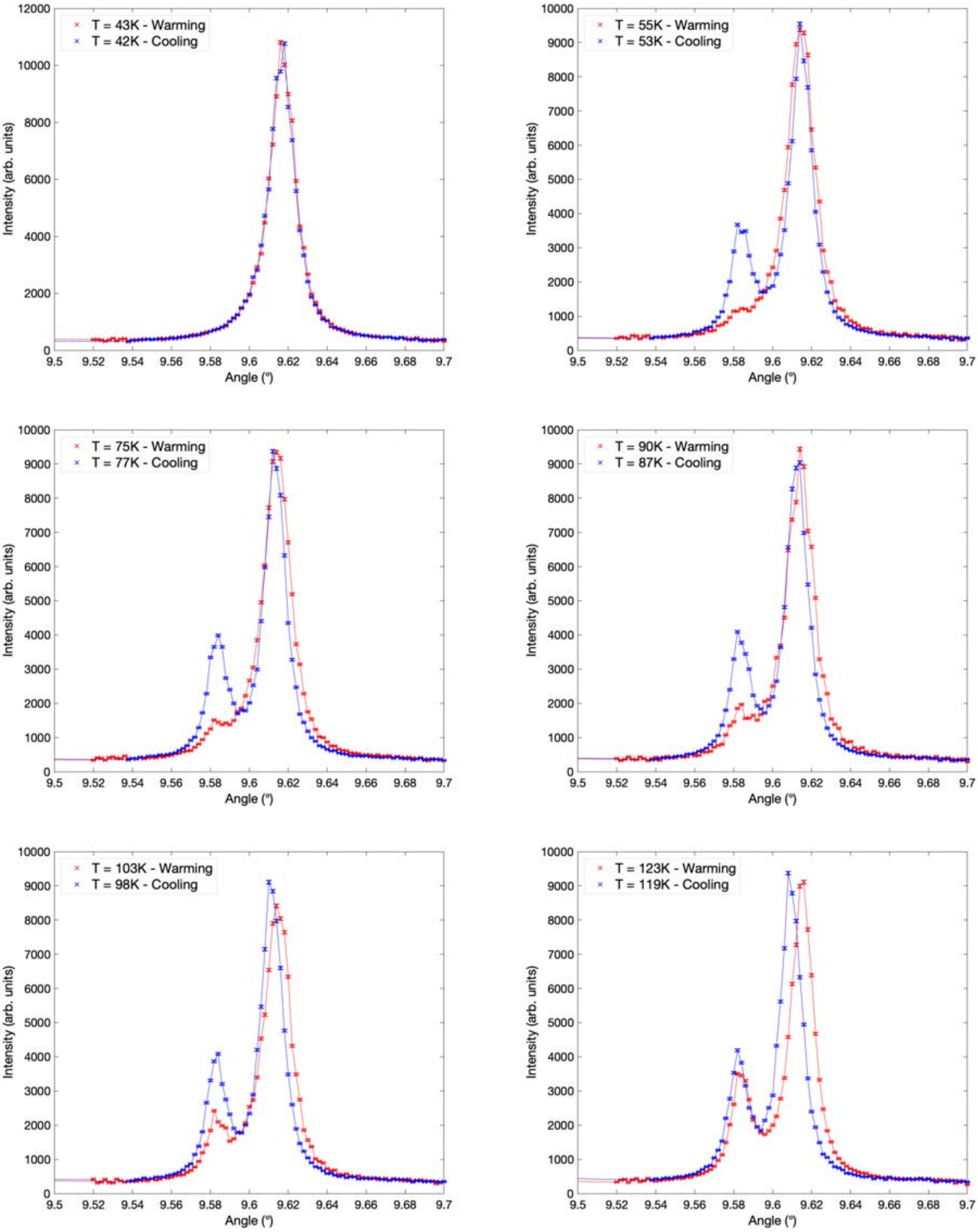

Figure 8.10: (222) reflection peaks as a function of temperature, for both cooling and warming cycles, showing the hysteresis in the transition temperature. The slight variation in temperatures at each point is due to slight inaccuracies between regulator and sample space thermocouples.

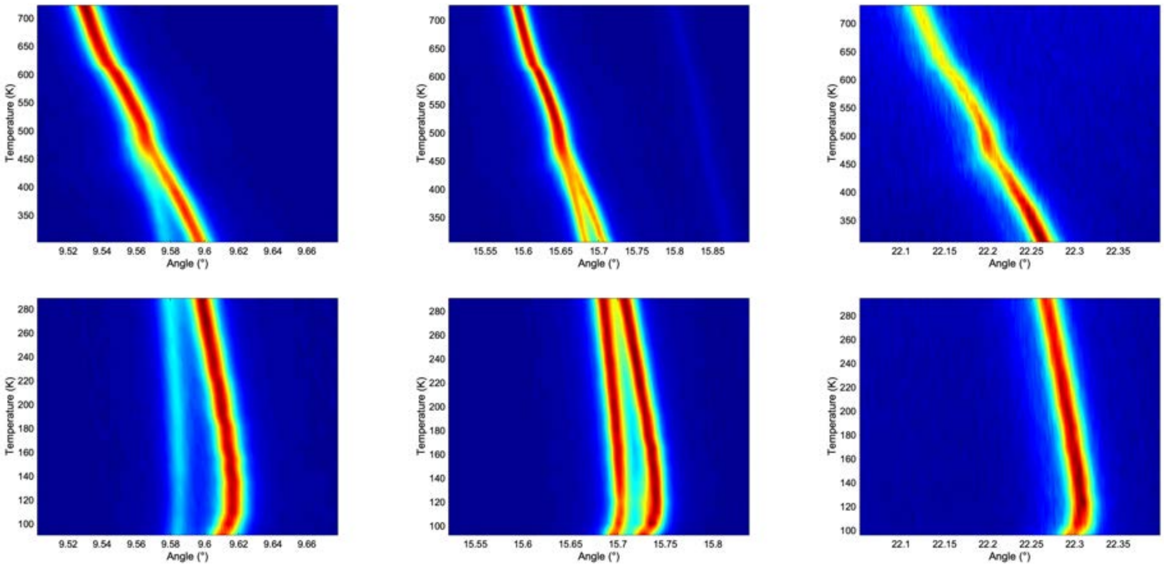

Figure 8.11: Colour map array for the **Left** (222), **Centre** (440) and **Right** (800) reflections sites, in the high (**Top**) and intermediate (**Bottom**) temperature ranges.

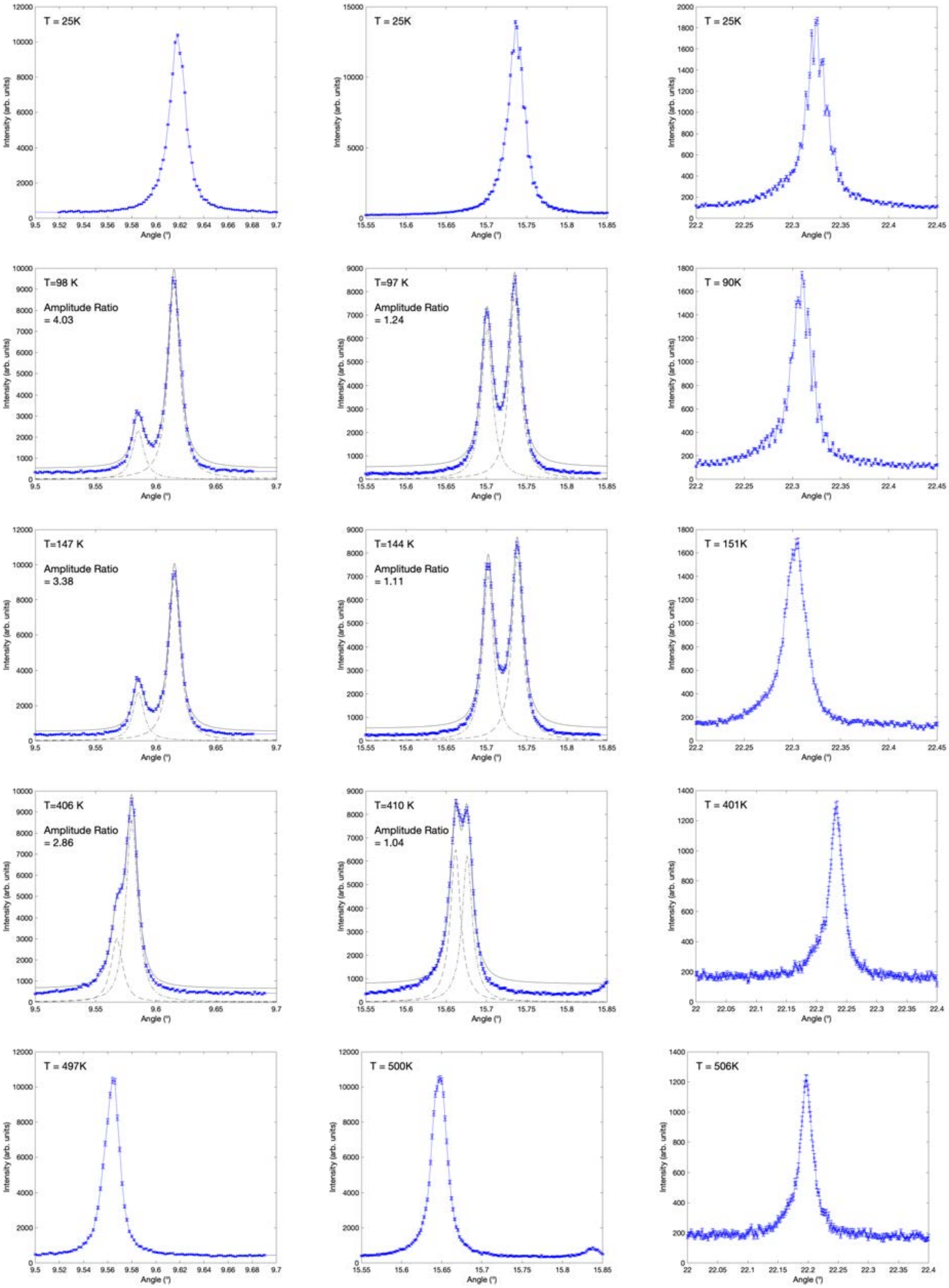

Figure 8.12: Intensity as a function of two theta angle at key points across the temperature range, for **Left** (222), **Centre** (440), and **Right** (800) reflections. Note that the slight low angle shoulder on the (800) peak is attributed to a small amount of impurity present within the sample, as the shoulder is constant across the full temperature range.

8.4 Sample 4 - $Tb_{0.35}Dy_{0.65}Fe_{2.05}$

The composition of Sample 4 matches that used in previous synchrotron XRD studies and marked the composition lowest in x from those studies. Based on this previous data,[29] the MPB transition is anticipated to occur around 150 K. It is important to note that this sample had the highest Fe content of the nine alloys studied - a factor which may contribute to a small degree of impurities as RE-Fe_3 is known to form readily.[154] Figure 8.13 shows the generated colour plots from the measurements in the intermediate temperature region, for both cooling and warming, where the transition temperature is observed to onset at 180 K. Below the transition temperature, the reflections are all unity albeit with some significant shouldering. The angular separation of the split reflections above the transition temperature remains distinct. At the transition temperature and for the reflections which undergo a splitting (i.e. (222) and (440)), it is found that the unity peak intensity (low temperature) consistently tracks towards the higher angle reflection. Figure 8.14 shows the three reflection sites at key temperatures around the MPB and where applicable, the associated fitting results. Aside from the presence of two minor impurity peaks (attributed to excess iron and the formation of minor undesirable phases) affecting the low angle shoulder on the (222) and (800) reflections, the observed peak splitting is characteristic of the MPB. However, the transition temperature appears higher than that seen in Sample 3 which is similar in composition - 180 K for Sample 4 as opposed to ≈120 K (warming). A further point of interest arises in the 'flavour' of the (440) reflections at 90 K. For Samples 1 and 2, the low temperature region of the (440) reflection exhibited three distinct peaks of roughly equivalent intensity, the centre-most of which is attributed to the presence of a low symmetry phase. For this sample, the central peak (15.73°) is significantly larger in intensities than the peaks either side (15.50° and 15.75°) and the peak intensity remains constant with increasing temperature, eventually collapsing between ≈110 K and 150 K. A tetragonal structure would exhibit a 1:2 splitting and therefore these measurements may suggest a co-existence of T and R phases (dominant T at 90 K, evolving to dominant R with increasing temperature).

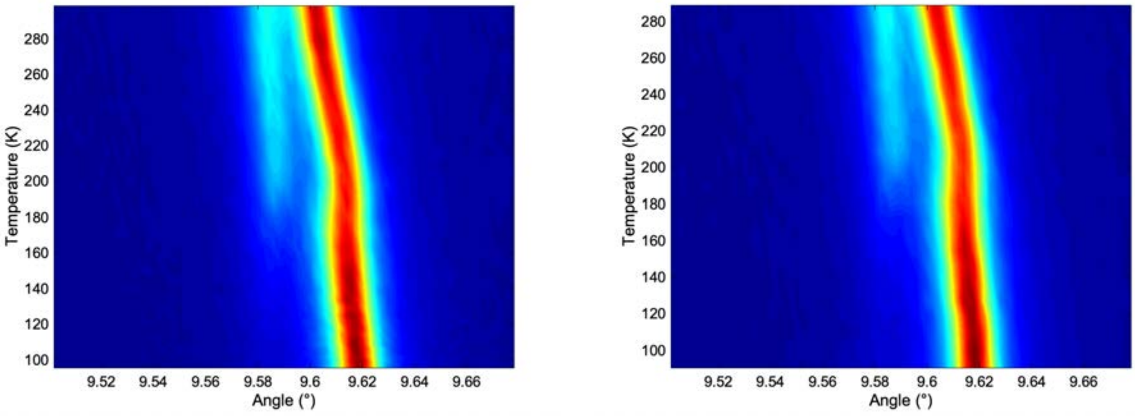

(a) (222) Cooling

(b) (222) Warming

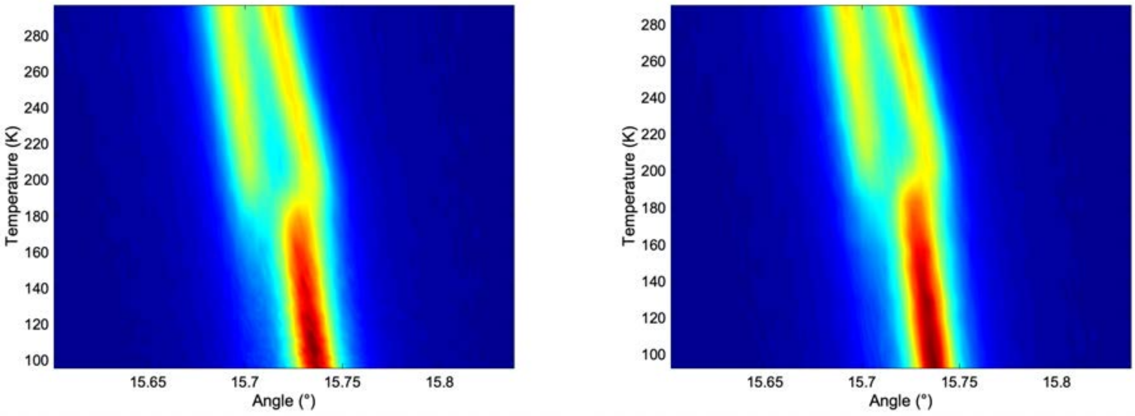

(c) (440) Cooling

(d) (440) Warming

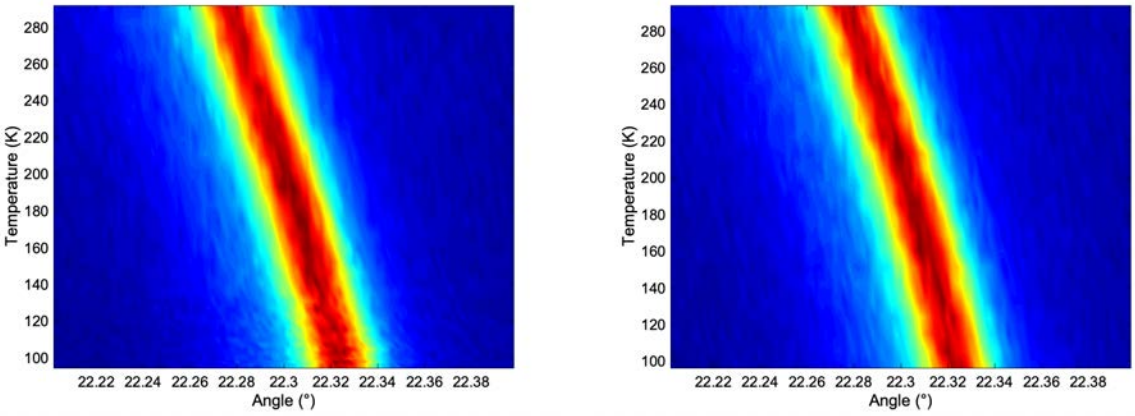

(e) (800) Cooling

(f) (800) Warming

Figure 8.13: Intermediate temperature intensity mapping at the specific reflection angles of interest for $Tb_{0.35}Dy_{0.65}Fe_{2.05}$. Both cooling and warming is shown

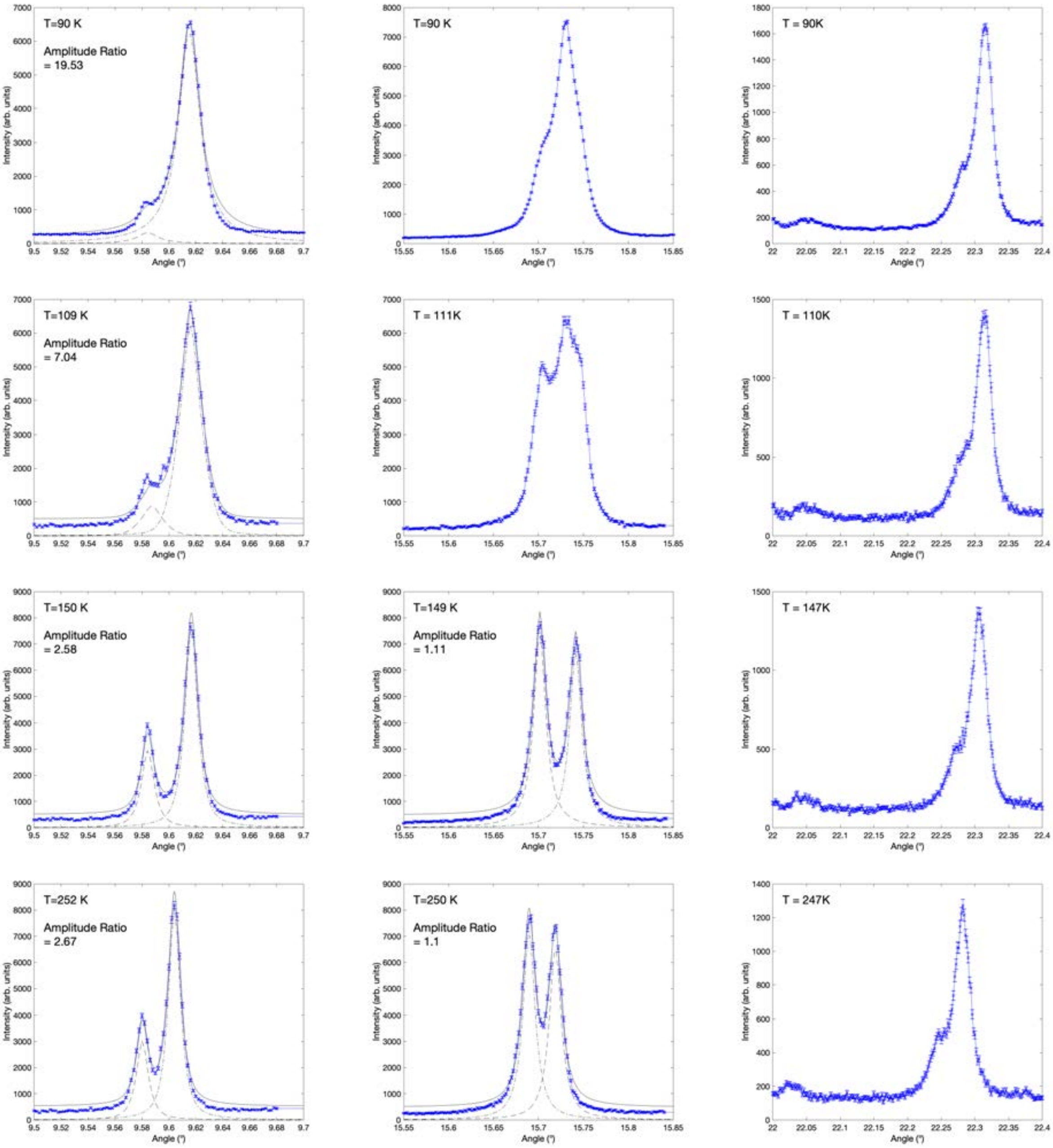

Figure 8.14: Intensity as a function of two theta angle across the high temperature range, for **Left** (222), **Centre** (440), and **Right** (800) reflections observed in $Tb_{0.35}Dy_{0.65}Fe_{2.05}$. Amplitude ratio tracking is not performed for (800) as the low angle peak is unchanging with temperature and assumed to derive from an impurity.

8.5 Sample 5 - $\mathbf{Tb_{0.34}Dy_{0.66}Fe_{2.03}}$

$Tb_{0.34}Dy_{0.66}Fe_{2.03}$ is very similar in composition to Samples 3 & 4. Sample 5 acts as a compositional accuracy check for the other samples in this region. Figure 8.15 shows the resultant colour plots, which feature a relatively sharp transition to rhombohedral structure at ≈120 K. This transition is free of hysteresis between cooling and warming cycles, with the MPB transition temperature for this sample having an onset of around 120 K and appears relatively sharp in its transition from tetragonal to rhombohedral.
Figure 8.16 shows the reflections at approximately 95 K, 150 K and 200 K. At 90 K all three reflection sites exhibit peak unity, a feature which has already been discussed for Sample 3, is characteristic of a high symmetry cubic structure. While it may be the case that the tetragonal distortion is not of significant magnitude to split the (800) reflection, a 1:2 splitting in the (440) reflection is expected and the lack of such a feature does provide evidence for a low temperature cubic structure. Centroid separation after the transition is shown to close with increasing temperature and the non-symmetrical, low angle shouldering on the (800) reflection is observed for this sample - a reproducible feature from Sample 2. A further point of note for Sample 5 is that it shows a good degree of 'purity', specifically that the peak reflections behave as expected with minimal impurity shouldering and sharp transitions. This may imply that MPB width is more intimately tied to composition than originally thought, with the previous perception being that MPB width is only a function of temperature.

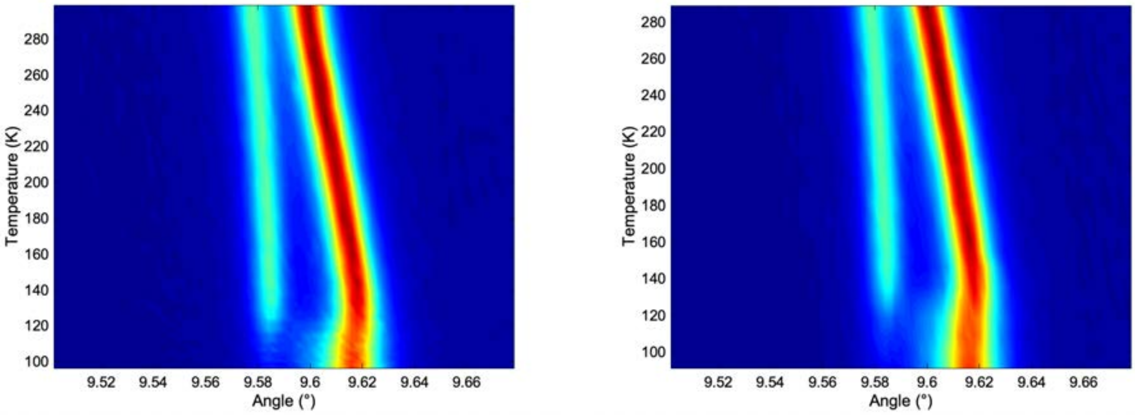

(a) (222) Cooling (b) (222) Warming

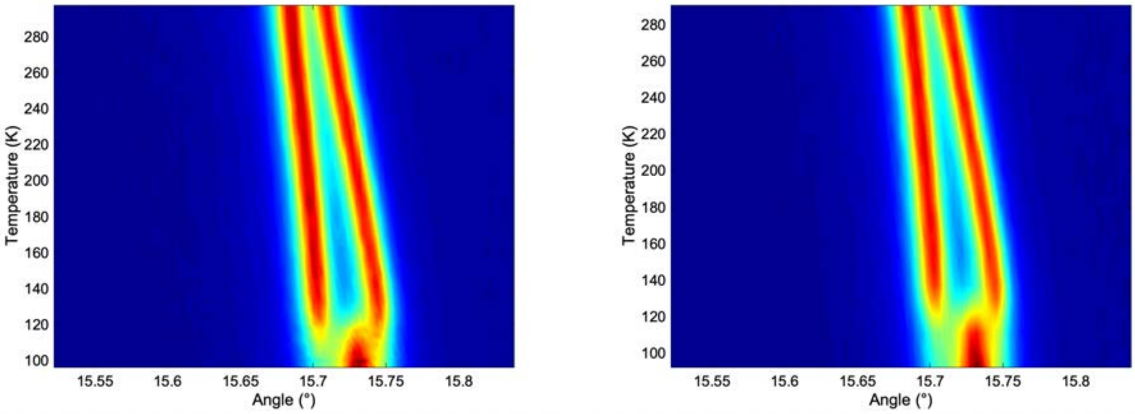

(c) (440) Cooling (d) (440) Warming

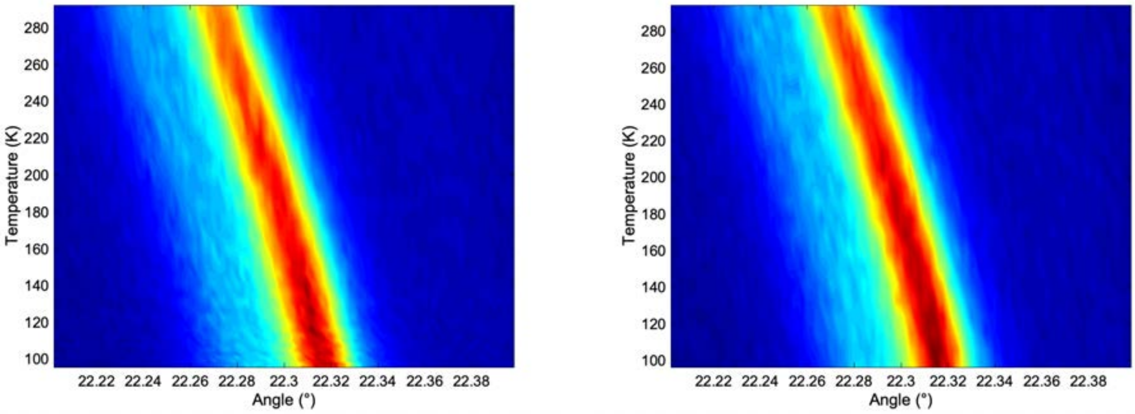

(e) (800) Cooling (f) (800) Warming

Figure 8.15: Intermediate temperature intensity mapping at the specific reflection angles of interest for $Tb_{0.34}Dy_{0.66}Fe_{2.03}$. Measurements are shown for both cooling and warming.

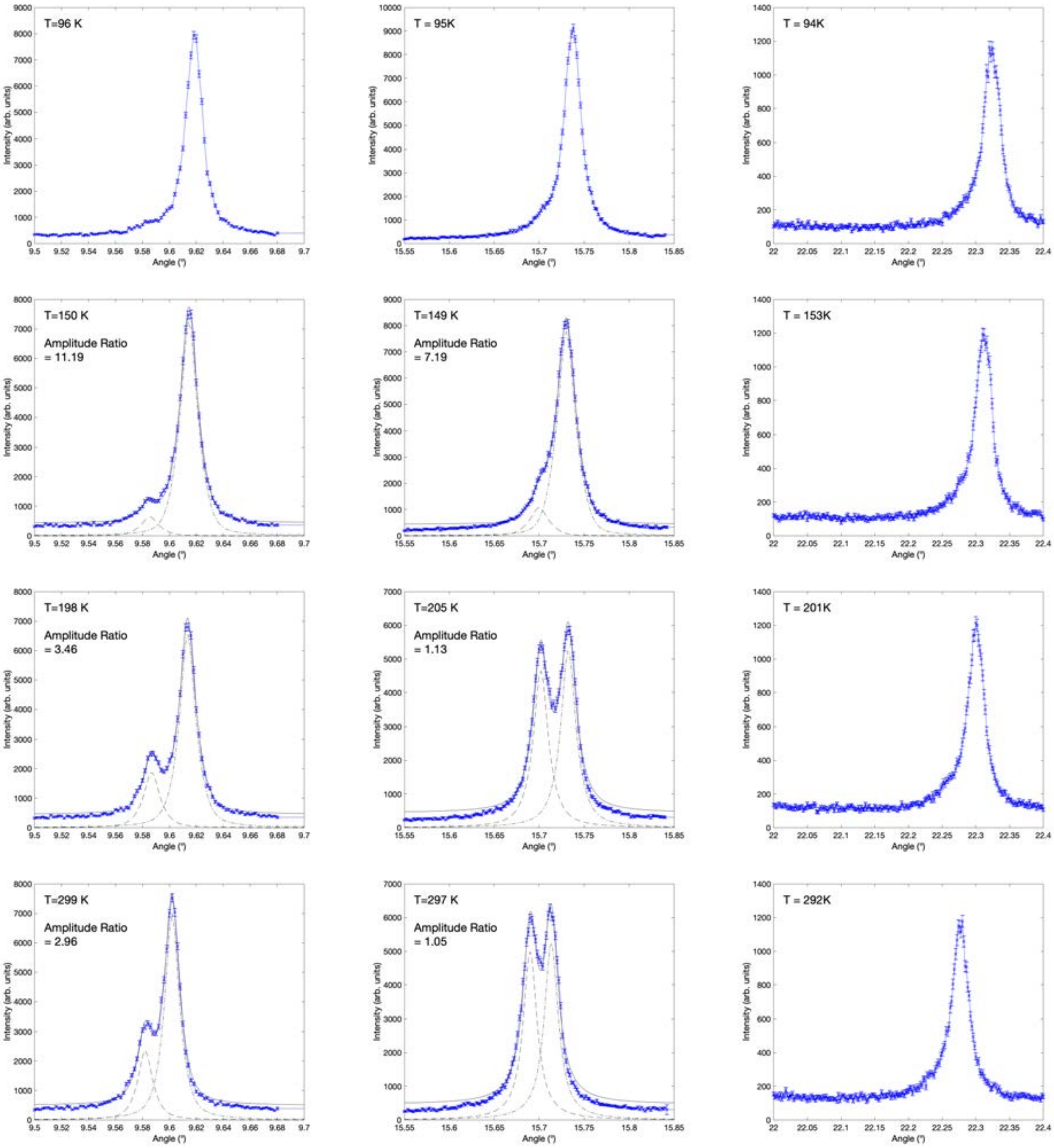

Figure 8.16: Intensity as a function of two theta angle across the high temperature range, for **Left** (222), **Centre** (440), and **Right** (800) reflections observed in $Tb_{0.34}Dy_{0.66}Fe_{2.03}$.

8.6 Sample 6 - $Tb_{0.30}Dy_{0.70}Fe_{2.01}$

Sample 6 sits firmly within the region of composition that has previously been documented using synchrotron XRD, with an expected MPB position at around 230 K. This sample was only studied in a small temperature range of 230 K to 280 K - a choice which in hindsight, was an experimental misstep. Figure 8.17 shows the colour plots for cooling across that narrow temperature range. There is a smearing across all angle ranges between 255 K and 260 K - it is believed this arises from poor instrumental setup and/or an artefact from interpolation between data points, rather than any transitions within this temperature range. The most likely cause of this experimental error is a small degree of thermal expansion in a poorly ground powder, causing a slight shift in the powder (within the capillary).

Due to the smearing and low resolution of the colour plots, it is even more paramount than in other samples to study the individual plots of intensity as a function of angle - Figure 8.18 does this. While resolution remains poor in comparison to other samples (it is not uncommon for instrument parameters to be optimised more with increasing experiment time) it is still sufficient to show that the material is rhombohedral across this whole temperature range. Furthermore, the poor resolution of this data set raised issues with the fitting and analysis of the amplitude ratio. Throughout this analysis, the DPV fitting has been performed using a consistent peak shape - more specifically, the ratio of Lorentzian and Gaussian contribution within the Pseudo-Voigt is constant for both peaks, meaning the fitting is based only around changes to centroid, amplitude and peak width. This is the most robust method for fitting peak splitting, based on the assumption that the reflections are splitting only due to distortion from phase changing which is uniform across the sample. An example of the poor statistics is visible in the (800) reflection, where the large error bars cast doubt on whether the feature at $\approx 22.27°$ is two fine peaks or one single peak with considerable width.

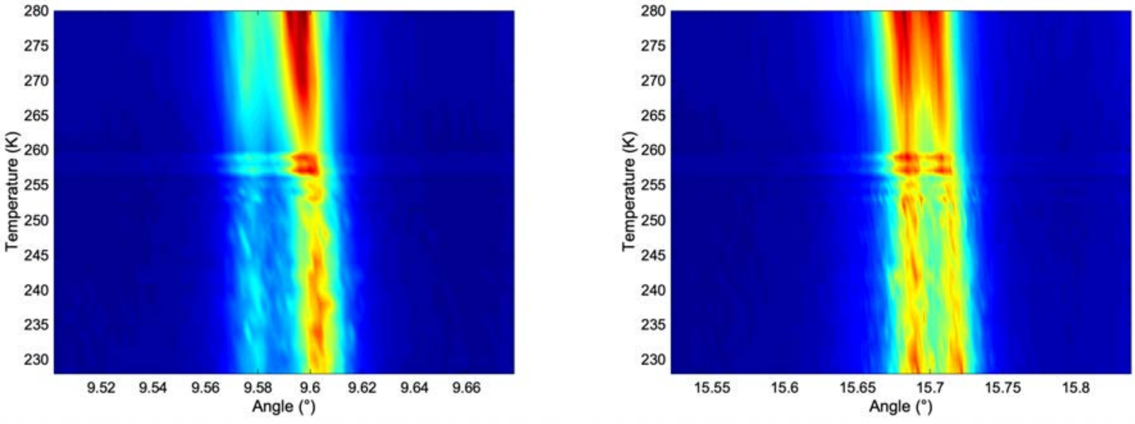

(a) (222) Reflection

(b) (440) Reflection

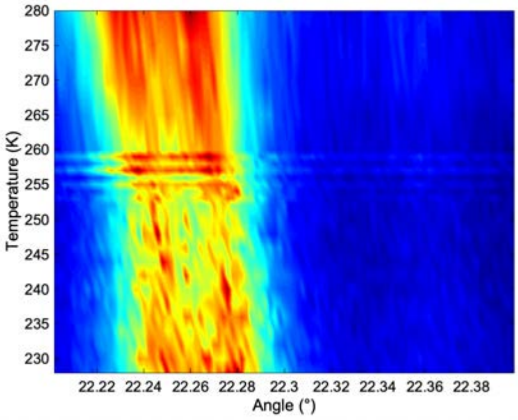

(c) (800) Reflection

Figure 8.17: Intermediate temperature intensity mapping at the specific reflection angles of interest for $Tb_{0.30}Dy_{0.70}Fe_{2.01}$. Measurements were taken upon cooling.

The MPB transition is expected at around 230 K, previous evidence within this study suggests that the rhombohedral peak splitting can begin to emerge at temperatures lower than expected - likely due to the large [111] strain of $TbFe_2$ being significantly larger than the [001] strain of $DyFe_2$, approximately 75 times stronger at 250 K.[25] Therefore, this data set can only affirm that this composition is wholly rhombohedral across this narrow temperature range.

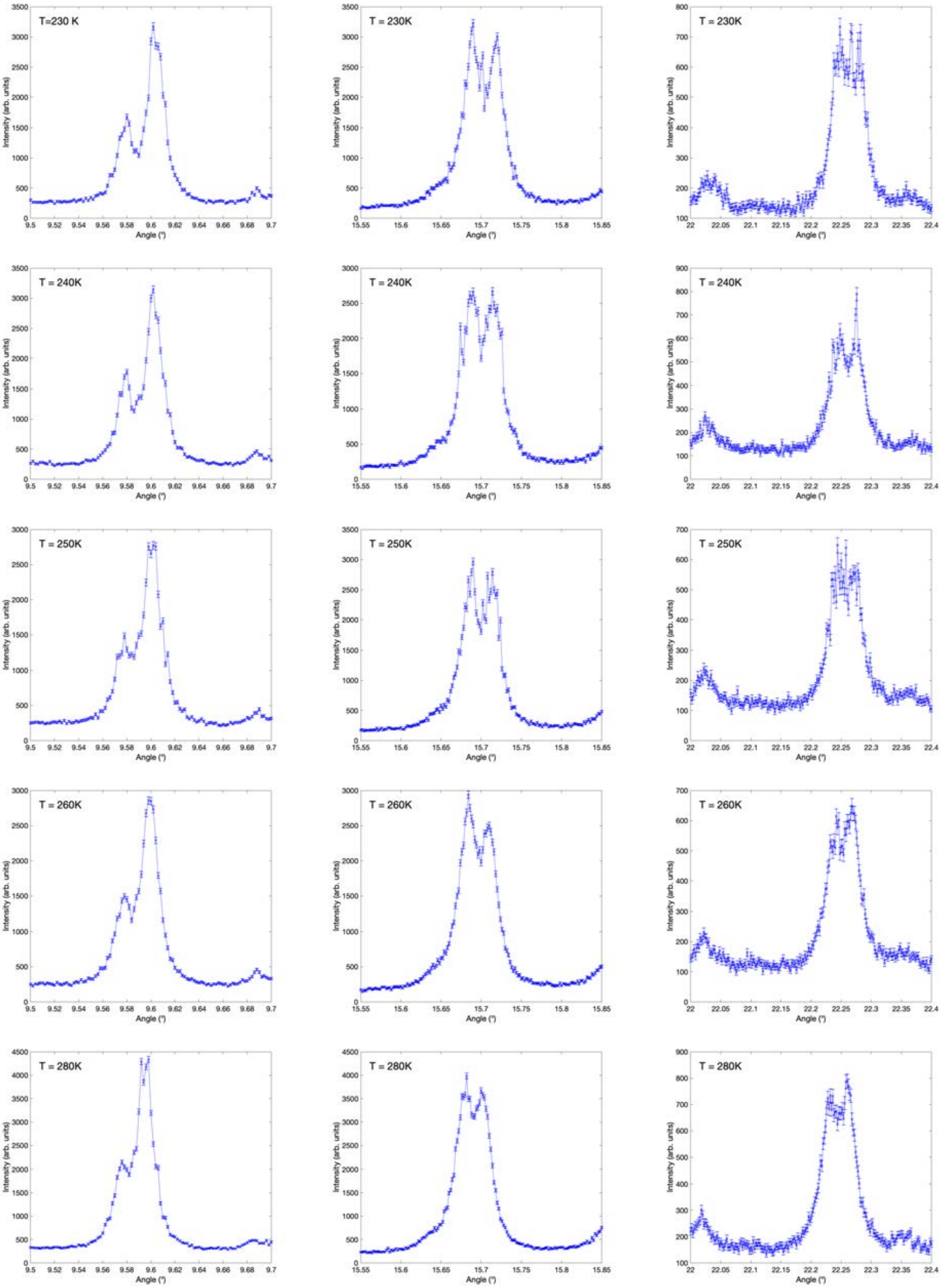

Figure 8.18: Intensity as a function of two theta angle across a focused temperature range, for **Left** (222), **Centre** (440), and **Right** (800) reflections observed in $Tb_{0.30}Dy_{0.70}Fe_{2.01}$.

8.7 Sample 7 - $Tb_{0.25}Dy_{0.75}Fe_{2.01}$

$Tb_{0.25}Dy_{0.75}Fe_{2.01}$ exists firmly within the region of samples previously studied with synchrotron XRD and of the samples studied is arguably closest to Terfenol-D in composition.[29] The expected MPB position is in the region of 250 K to 300 K and Figure 8.19 shows the resultant colour plots for this intermediate temperature range, for both cooling and warming.

Figure 8.19 shows a discrepancy between cooling and warming, a feature which has not been seen thus far for the MPB transition. The cooling run shows a continuous transition from tetragonal to rhombohedral, beginning around 250 K and continuing with increasing temperature, however the warming run shows more of a 'jump' in the data. This mild discontinuity at 250 K appears first-order in nature and shares significant similarities to the low temperature transition observed in Samples 1 and 2. Otherwise, there is negligible hysteresis between warming and cooling.

Above the transition temperature, the three reflection sites do not exhibit the normal splitting for an 'above MPB', or rhombohedral, position - a direct contrast to what has been seen in the samples preceding this one. Consulting the colour maps, it has become common in these measurements to observe a clear separation between the low and high angle peaks of the (222) and (440) reflections. For this sample, this is not the case and above the transition temperature the colour maps show one feature with considerable, non-symmetrical width, rather than individual features.

Figure 8.20 shows the reflection sites at key temperatures - before, during and after the MPB transition (increasing temperature). Firstly, it is important to highlight that the (800) reflection shows a consistent, temperature independent, low angle shoulder which is separated from the main peak by approximately 0.03°. While the intensity of this feature does fluctuate slightly, i.e. more pronounced at 304 K than at 268 K, it is most likely that this feature arises from a small amount of impurity phase. Despite this, the remaining reflections are fairly conclusive. From approximately 100 K up to $\approx$220 K, the reflections are at unity; this has been observed and discussed prior (for example in Sample 5) and provides further evidence for a low temperature cubic phase on the Dy-side of the phase diagram. At 220 K and onwards to a temperature in excess of 300 K, the (222) and (440) reflections split in the expected manner, taking respective amplitude ratio metrics of 3.25 and 1.31, at 300 K. These agree reasonably well with the expected values of 3 and 1. The top end of this data set is ≈440 K and at this temperature, the (222) and (440) reflections have returned to unity, whereas the (800) reflection continues to contain the low angle shoulder hypothesised to arise from impurities. While the peaks at this temperature are not yet symmetric, it is clear that either: the lattice distortion is drastically reducing with increasing temperature, therefore reducing the degree of peak splitting, or that the transition to the high temperature cubic structure (documented to occur at approximately 700 K depending on x) is happening at temperatures far lower than expected. Given the high temperature discontinuity seen at 600 K for Sample 3, it is anticipated that the cause of centroid merging is a reduction in lattice distortion, a suggestion which is also backed up by a lack of, or immeasurable amount of, [001] lattice distortion in the tetragonal phase.

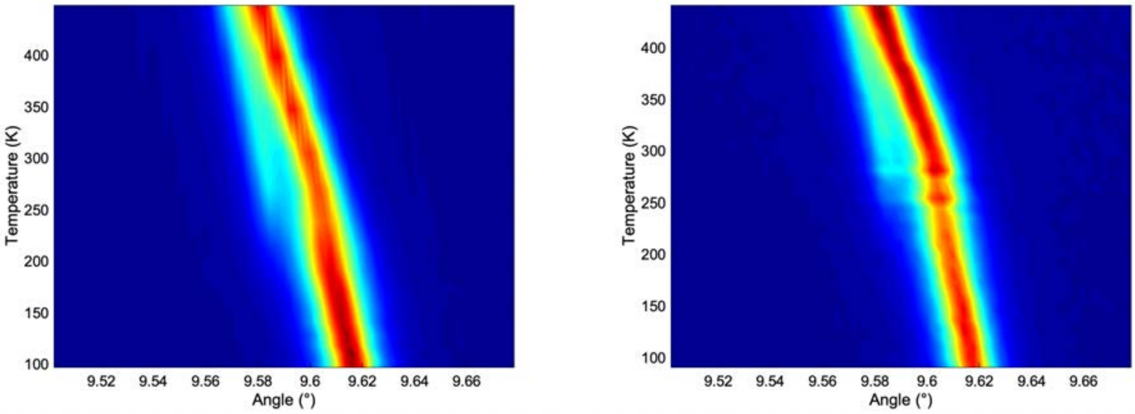

(a) (222) Cooling (b) (222) Warming

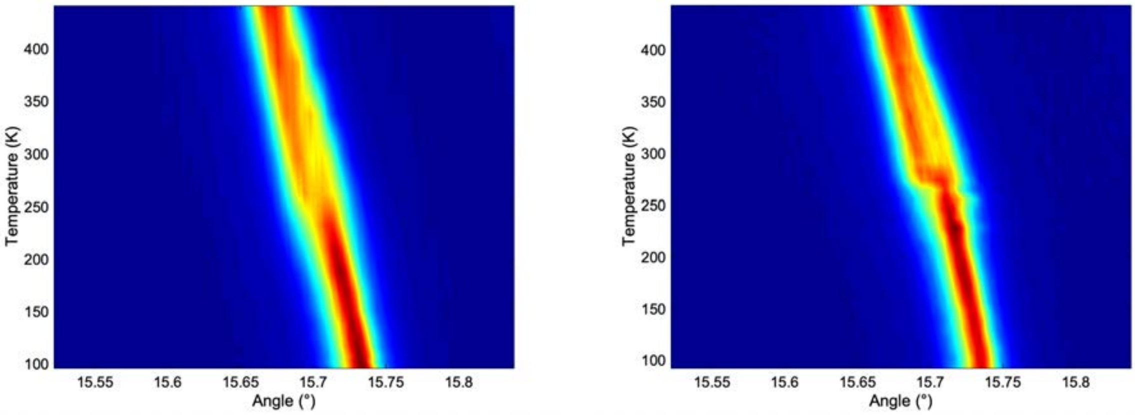

(c) (440) Cooling (d) (440) Warming

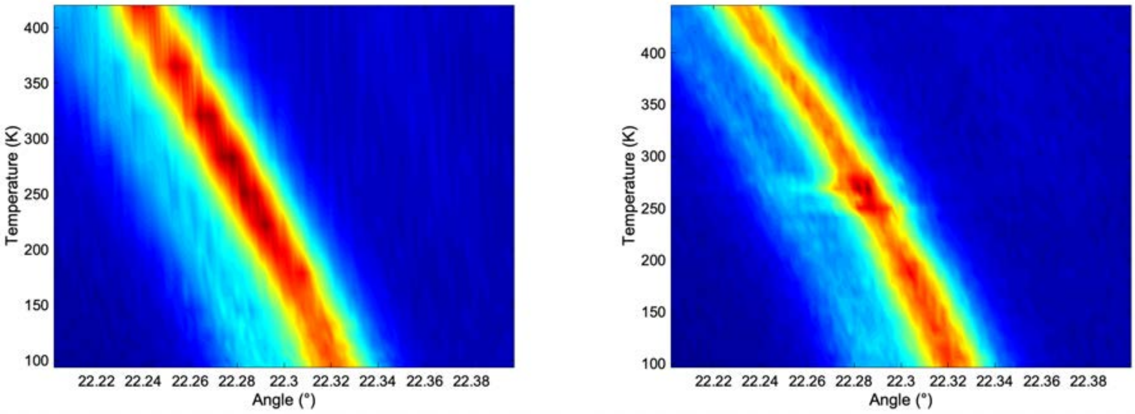

(e) (800) Cooling (f) (800) Warming

Figure 8.19: Intermediate temperature intensity mapping at the specific reflection angles of interest for $Tb_{0.21}Dy_{0.79}Fe_{2.02}$, for a temperature range of 100 K to approximately 450 K.

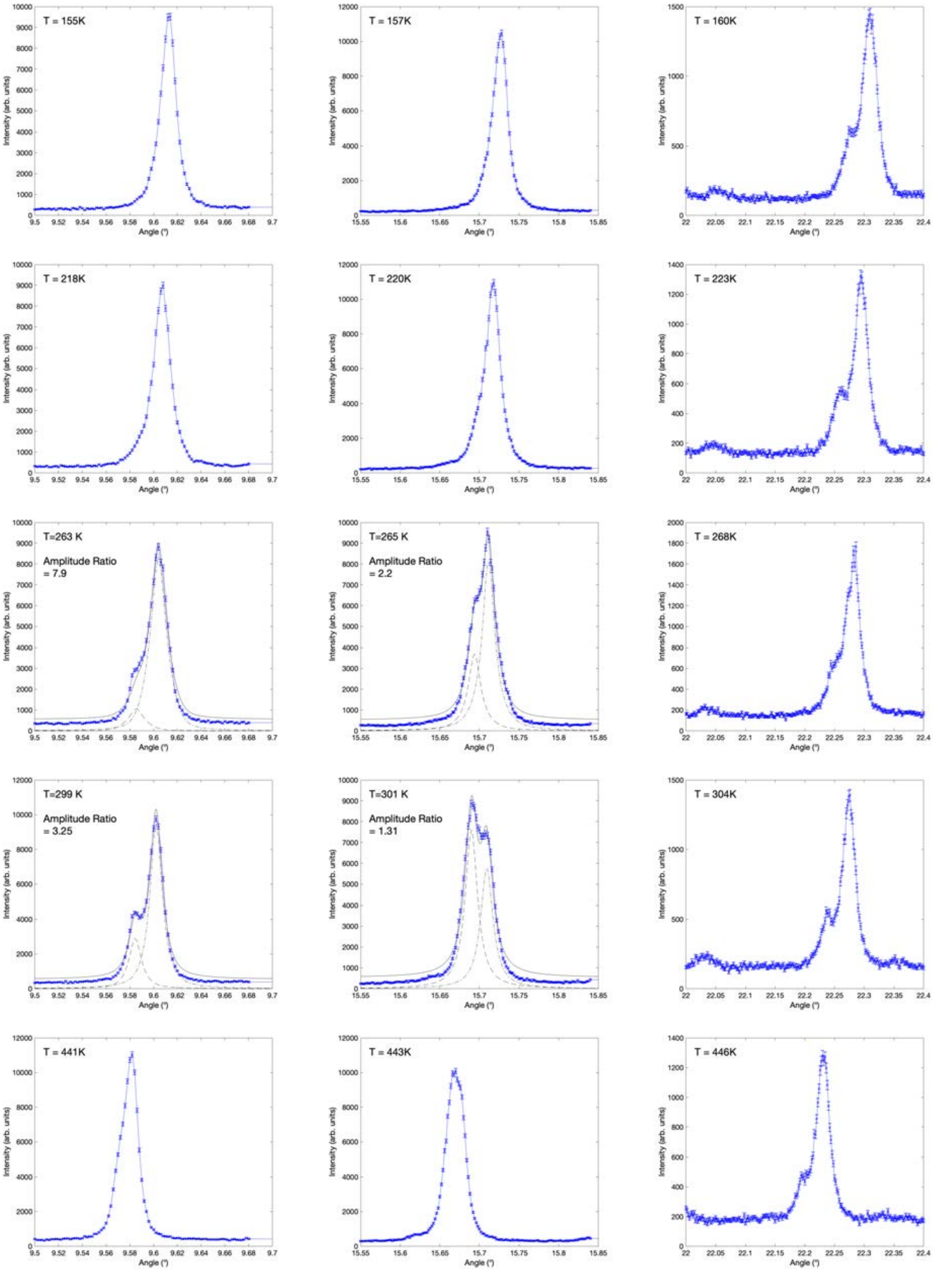

Figure 8.20: Intensity as a function of two theta angle across the high temperature range, for **Left** (222), **Centre** (440), and **Right** (800) reflections observed in $Tb_{0.25}Dy_{0.75}Fe_{2.01}$.

8.8 Sample 8 - $\mathbf{Tb_{0.21}Dy_{0.79}Fe_{2.02}}$

With an x ratio slightly higher than that previously studied using XRD (Bergstrom), Sample 8 provides a crucial comparison between previous work and this study. The high Dy content in this alloy leads to an expectation for the MPB to exist at temperatures not too dissimilar from room temperature, as the Dy content for Sample 8 is higher than that for Terfenol-D and it has been previously explained that Terfenol-D is a market leader for room temperature magnetostrictive applications (see Chapter 4). Therefore, for this sample the intermediate and high temperature ranges were studied. Figure 8.21 shows the cooling data for all three reflection sites, in the intermediate and high temperature ranges.

Figure 8.21 shows that there are three transitions occurring in this sample - two positioned approximately at 300 K and 450 K, which are both continuous in their nature, and a final at approximately 620 K that behaves similarly to that seen in Sample 3, albeit with a larger magnitude shift to lower angle. The higher temperature transition agrees well with the other samples and given the reflections are all unity above this, it seems apparent that this is the cubic transition temperature. Cooling from 600 K, the peaks remain fairly singlet in nature until 450 K, at which point the (222) and (440) peaks gain a lower angle shoulder (≈0.01°) and increased width respectively (Figure 8.22). A lack of distinct rhombohedral peak splitting suggests that for this composition, there is a large region of rhombohedral and tetragonal phase co-existence - more completely, the MPB nature is clear and has a large width for this large value of Dy content. Below 300 K all three reflections are at unity. Given the continued observation of unity peaks in what is anticipated to be a tetragonal region, it is becoming apparent that the magnitude of tetragonal distortion in these samples is not significant enough to promote peak splitting, particularly at temperatures greater than 100 K. Reasons for this may include changing elastic constants with temperature, or that the polycrystalline nature of these samples is resulting in reduced degree of distortion.

Terfenol-D (≈$Tb_{0.3}Dy_{0.7}Fe_2$) exhibits desirable properties due to the minimisation of the opposing magnetocrystalline anisotropies of the parent phases and the large strain of the [111] distortion (Section 4). At this composition, the MCA will be significantly large on the Dy side and furthermore, the [001] distortion is approximately two orders of magnitude smaller than the [111] distortion from the $TbFe_2$ phase.

In the 100 K region, there is a peculiar shifting of the two theta angle with temperature. Increasing temperature promotes lattice expansion, increasing the lattice parameters and shifting the reflection to lower angle. It appears that from low temperature up to ≈100 K, the opposite is true and that all three reflections shift to higher angle, suggesting that the shifting anisotropy constants (Figures 2.2 and 4.5) are leading to negative magnetostriction. Unfortunately, the low temperature region was not probed for this sample and therefore cannot offer any indication as to the cause of this feature.

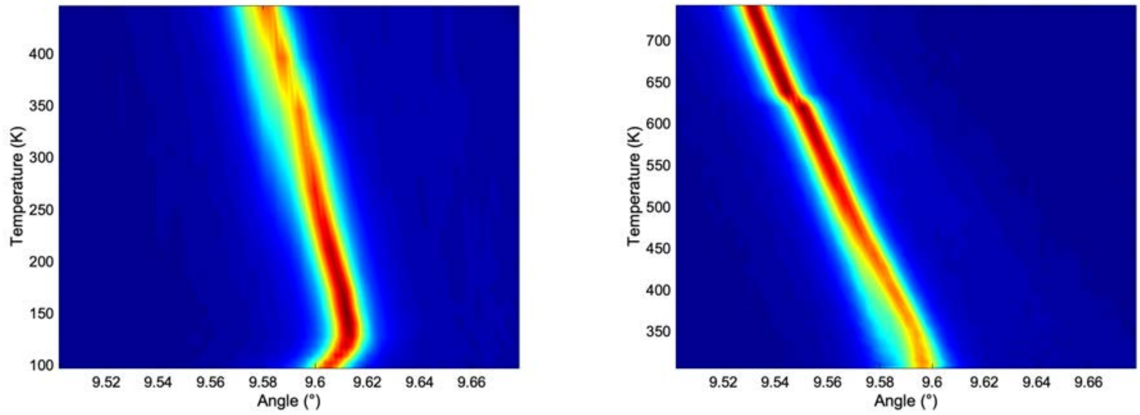

(a) (222) Intermediate Temperature
(b) (222) High Temperature

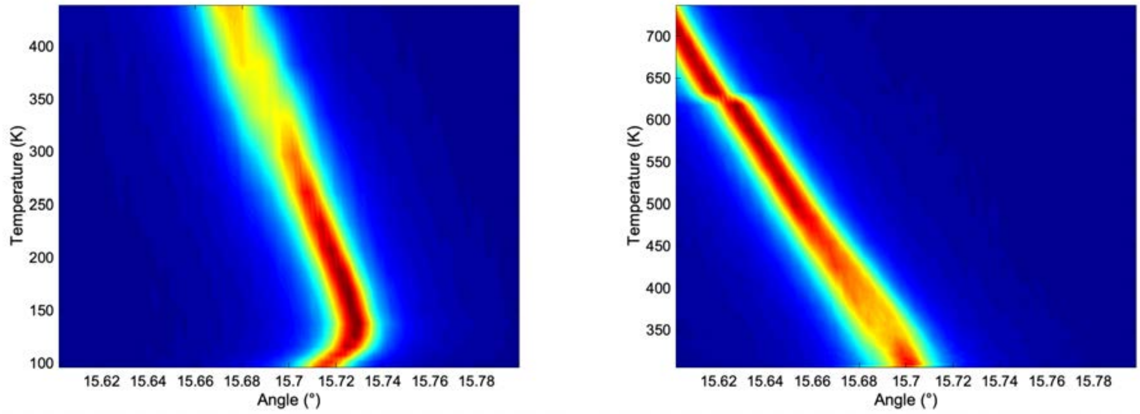

(c) (440) Intermediate Temperature
(d) (440) High Temperature

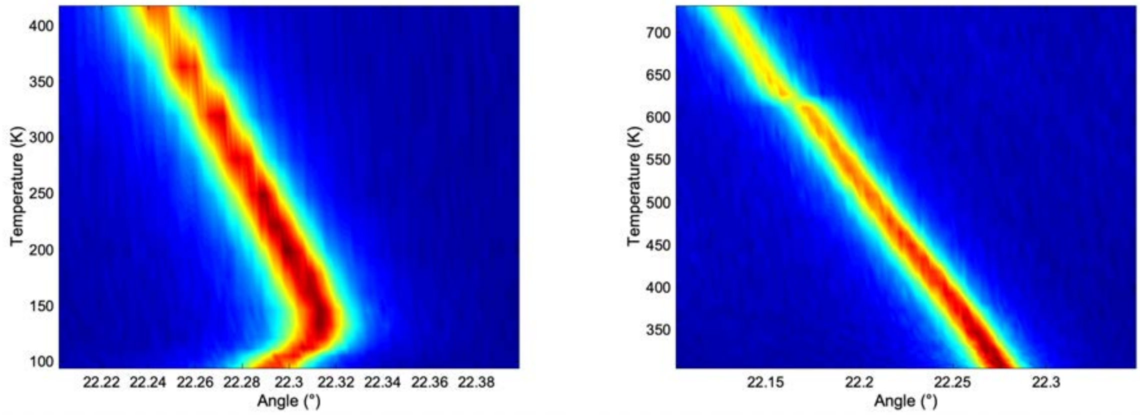

(e) (800) Intermediate Temperature
(f) (800) High Temperature

Figure 8.21: Intermediate and high temperature intensity mapping at the specific reflection angles of interest for $Tb_{0.21}Dy_{0.79}Fe_{2.02}$. Measurements were taken upon cooling.

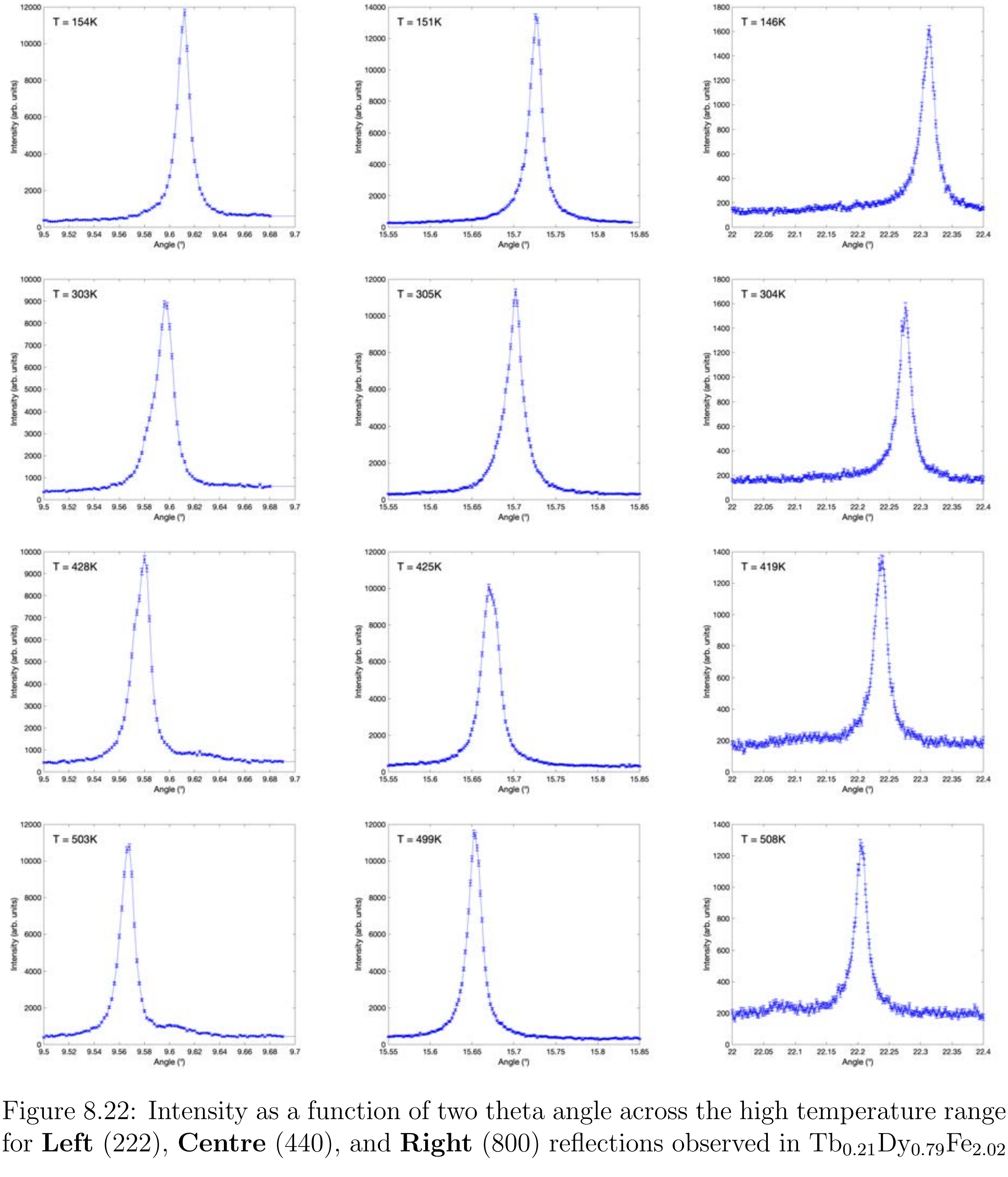

Figure 8.22: Intensity as a function of two theta angle across the high temperature range, for **Left** (222), **Centre** (440), and **Right** (800) reflections observed in $Tb_{0.21}Dy_{0.79}Fe_{2.02}$.

8.9 Sample 9 - $Tb_{0.13}Dy_{0.87}Fe_{2.01}$

Sample 9 falls firmly onto the Dy side of the existing phase diagram and has not previously been studied by synchrotron XRD. Mossbauer results for x=0.85 show tetragonal structure at 0 K but at 300 K the structure becomes non-trivial and therefore not well defined. Figure 8.23 shows the colour plots for the three reflection sites of interest.

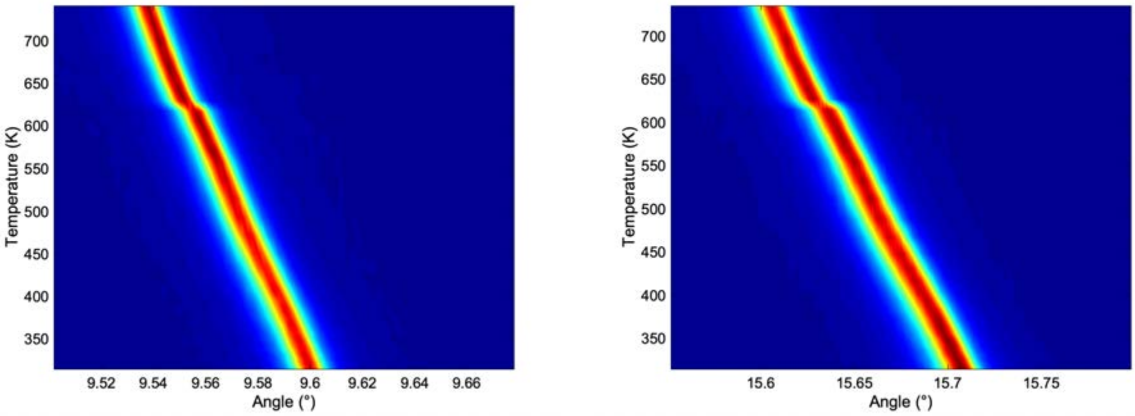

(a) (222) reflection

(b) (440) reflection

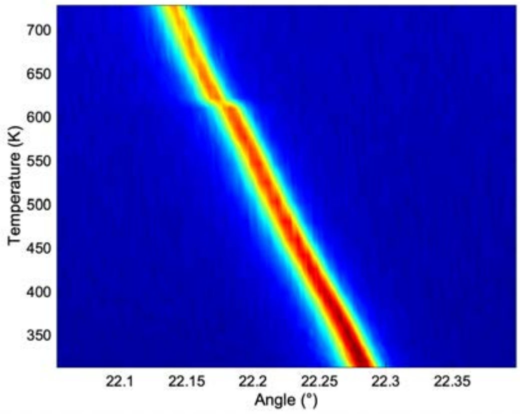

(c) (800) reflection

Figure 8.23: High temperature intensity mapping at the specific reflection angles of interest for $Tb_{0.13}Dy_{0.87}Fe_{2.01}$. Measurements were taken upon cooling.

Figure 8.23 clearly shows uniformity with increasing temperature, aside from a slight discontinuity or 'jump' in the data at approximately 600 K. The cubic transition temperature for $DyFe_2$ is in that region, previously stated as 635 K, therefore this discontinuity likely corresponds to the first order phase change from tetragonal to cubic - as the lattice parameters unify, the reflection angle is shifted slightly to represent that.

Figure 8.24 shows the reflections as a function of temperature. In comparison to other compositions near the MPB (i.e. those with less Dy), there is no clear transition from 300 K up to 700 K and a single measurement performed at ≈90 K shows that this peak unity continues down through the intermediate range. Unity peaks in this high temperature region would seem to suggest that the structure is cubic and the lack of a clear transition in this composition is striking. As discussed for Sample 8, it is fair to propose that the material is indeed tetragonal from 89 K to the cubic transition but the [001] distortion is sufficiently small to not promote significant peak splitting.

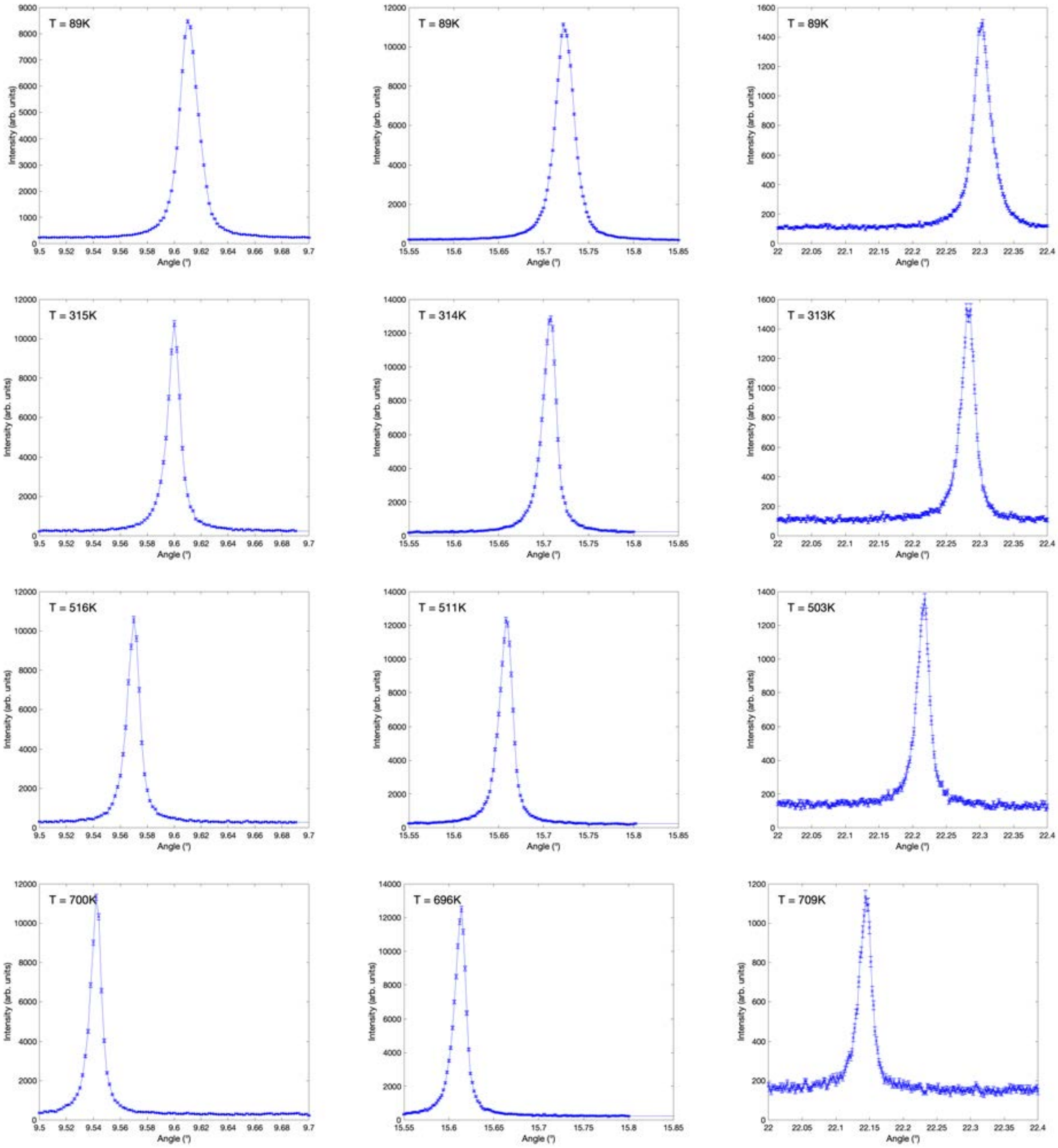

Figure 8.24: Intensity as a function of two theta angle across the high temperature range, for **Left** (222), **Centre** (440), and **Right** (800) reflections.

8.10 Discussion

The results presented in this chapter have shown a considerable expansion on the previous synchrotron XRD results for $Tb_{1-x}Dy_xFe_2$ alloys. Table 8.3 summarises these results, showing the different phase regions and transitions identified during this study.

Table 8.3: Table summary of the phase regions determined within this study. x represents the at% of Dy. ***LS***, ***R***, ***T*** and ***C*** represent low symmetry, rhombohedral, tetragonal and cubic phases respectively. ***MPB*** is used in place of a ***T+R*** co-existence.

Sample Number	x	Summary
1	0.56	15 K<***R+LS***<54 K, 54 K<***R***<86 K
2	0.6	10 K<***R+LS***<50 K, 50 K<***R***<300 K
3	0.64	15 K<***LS***<110 K, 110 K<***R***<450 K, 450 K<***C***
4	0.65	90 K<***R+LS***<160 K, 160 K<***R***
5	0.66	90 K<***T***<170 K, 170 K<***MPB***<210 K, 210 K<***R***<300 K
6	0.7	230 K<***R***<280 K
7	0.75	90 K<***T***<245 K, 245 K<***MPB***<300 K, 300 K<***R***<440 K, 440 K<***C***
8	0.79	90 K<***T***<300 K, 300 K<***MPB***<460 K, 460 K<***C***
9	0.87	90 K<***T/C***<700 K

Here new evidence is shown for the existence of a low temperature, low symmetry phase which appears in compositions with 0.5<x<0.65. Furthermore, these results have expanded the synchrotron XRD phase diagram for this material, particularly focused around the morphotropic phase boundary that exists between the tetragonal and rhombohedral phases. Focused studies within the MPB region show a second-order transformation through the boundary, with no evidence to suggest that monoclinic phases form and/or are stable within the MPB region - therefore, MPBs in this material are a co-existence of the two phases either side of the boundary. The high temperature results suggest that the cubic transition, previously thought to exist at 700 K, is occurring at slightly reduced temperatures in the region of 600 K to 650 K, signified by a first-order discontinuity in the angular positions. Meanwhile, the peak centroids merge to unity in a 'cubic-like manner' at temperatures significantly below the cubic transition (approximately 450 K) - an indicating factor that the spontaneous lattice distortion of the rhombohedral and tetragonal phases are drastically reduced with increasing temperature.

It is important to preface this discussion by saying that minor compositional inaccuracies may lead to some discrepancy between samples. An attempt has been made to confirm the Tb/Dy ratio of the samples measured (using Reitveld refinement in the high temperature region) however these have proved unsuccessful due to the highly similar electron clouds of the two elements. Previous arc melting experience and preliminary compositional analysis of samples produced earlier in the production cycle (where errors in fabrication are expected to be most apparent) show good agreement with calculated composition, therefore it is reasonable to assume an error of $\boldsymbol{\sigma x} = \pm 0.01$ to the Tb/Dy ratio, which ultimately dictates the position on the phase diagram. The presence of any impurities provides minimal impact to these results as the experimentation focuses in on specific reflections, where the amplitude ratios are well defined - any impurity peaks are visible and can be accounted for.

The existence of low symmetry phases in MPB-containing materials has long been speculated and work which has been previously discussed in this thesis has paved the way for ever developing knowledge. Monoclinic phases have been suggested to exist within the MPB, forming an adaptive phase across which the easy axis transition can occur - this is contrary to the findings of this work, which show a continuous, or second-order, transition through the MPB, facilitated by a co-existence of tetragonal and rhombohedral phases. Interestingly, evidence has been found to support the existence of a low temperature, low symmetry phase which may be monoclinic in nature but would require a separate study to determine the complex nature of this newly discovered phase.

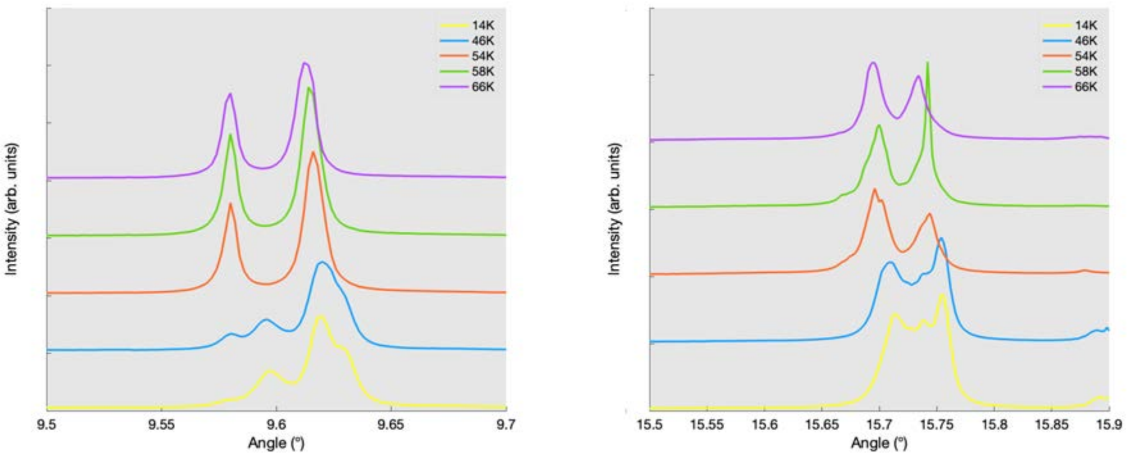

Figure 8.25: **Left** The (222) and **Right** (440) reflections for multiple temperatures in the low temperature range, showing the changing co-existence of the rhombohedral and low symmetry phases, observed in Sample 1. Offset is provided for clarity.

Figure 8.25 portrays an example of the low symmetry phase, and its co-existence with a rhombohedral phase, for both the (222) and (440) reflections in Sample 1. It is clear from the 66 K results, that the rhombohedral peak splitting take positions of approximately 9.57° and 9.62°. As temperature is reduced, the intensity of these peaks decreases in a non-linear fashion - the change in peak intensity is of no particular note between 66 K and 54 K, however the data at 46 K shows a significant reduction in the intensity of the rhombohedral peaks. At the same time, two new features appear (at ≈9.60° and 9.63°) which become more pronounced as temperature is further decreased to 14 K. A similar phenomena is also visible in the (440) reflection, although the low symmetry feature here exists between the two rhombohedral peaks, at an approximate position of 15.74°.

It may be a fair assumption to say that given there is some evidence (simulation and practical in PZT[170, 188]) that the low symmetry phase seen may be monoclinic in nature. Monoclinic phases are found to exist when the anisotropy energy is low and the magnetostatic and exchange energies dominate - it may be the case that the complex balance of the parent phases and their respective changing anisotropy constants, combined with a reduction in thermal fluctuations (which increases exchange energy), causes the creation of low symmetry phases.

This low temperature, low symmetry transition has been found to exhibit significant hysteresis between cooling and warming (Figure 8.26), with a thermal lag of approximately 50 K. Particularly in the low temperature transitions, there appears a discontinuity in the peak centroid at the onset transition temperature (low temperature, at which point the transition would begin for warming from 0 K). It has previously been reported that the MPB transition is a two-step process with increasing temperature - a second-order, continuous transition away from the [001] tetragonal easy axis to some arbitrary crystal direction, before a first-order transition to the [111] rhombohedral easy axis, as shown in Figure 8.27.[29] This theory may prove true for the transition between low symmetry and rhombohedral phases (as in the low temperature region for ≈ x=0.5), where the observed discontinuity for cooling is typically preceded by a continuous decrease in the rhombohedral phase intensities, before a sharp transition to a mixed state at ≈50 K. In contrast, the warming results show a more second-order transition through the whole temperature range, likely caused by favourable energetics of the rhombohedral phase at increasing temperatures.

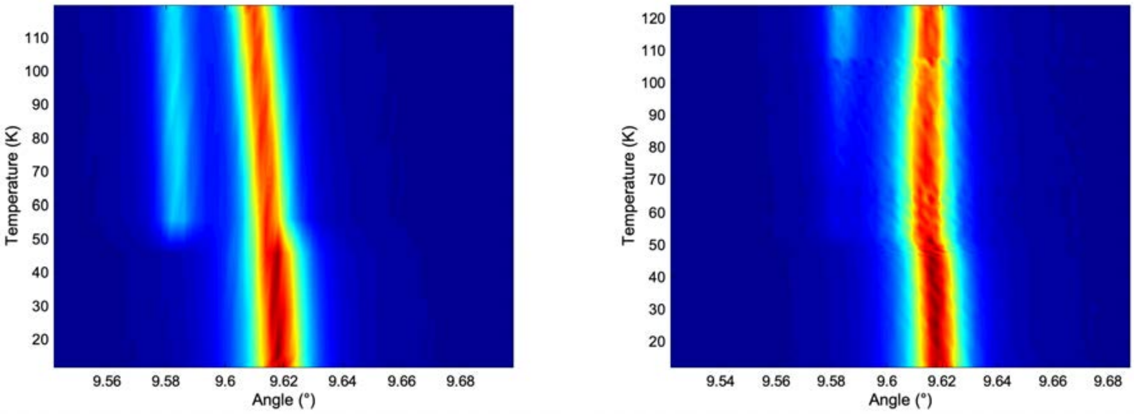

(a) (222) Cooling

(b) (222) Warming

Figure 8.26: Example of the thermal hysteresis seen between **Left** cooling and **Right** warming, for Sample 3.

The peak splitting behaviour through the MPB and indeed the MPB width (the temperature range across which the transition takes place) suggests a slow 'melting' of one phase into the other, such as is shown in Figure 8.28 where the (440) reflection peak splitting

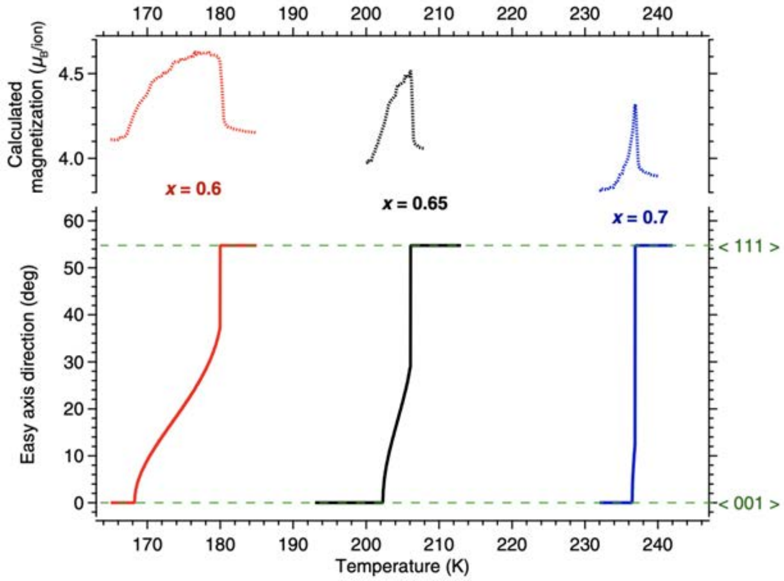

Figure 8.27: Single ion crystal field theory for the thermal width in MPB transition as a function of composition.[29]

is shown at the extremities and centre of the MPB. It transpires that the co-existence of rhombohedral and tetragonal phases in the MPB, are a function of composition and temperature and it is expected that these two properties are intrinsically linked. The increase in MPB width at high values of composition and temperature provides some level of analytical problems, where for some higher x sample the reflections show only light rhombohedral character and are not well defined because the shift to peak unity (likely arising from a reduction in magnitude of lattice distortion) occurs. The lack of any rhombohedral character in Sample 9, where x=0.87, may suggest that the MPB forms a vertical or near vertical boundary at some high Dy composition values, therefore the transition becomes simply a tetragonal to cubic shift (which is difficult to detect due to minimal lattice distortion, especially at high temperatures).

These measurements help to elucidate the transformation to a high temperature cubic phase in this alloy. The parent phases of $TbFe_2$ and $DyFe_2$ are expected to undergo a transition to cubic structure at approximately 700 K, however these results instead show that any split peaks are found to merge over a wide temperature range - a phenomenon which would normally signal a transition to a high symmetry, in this case cubic, structure.

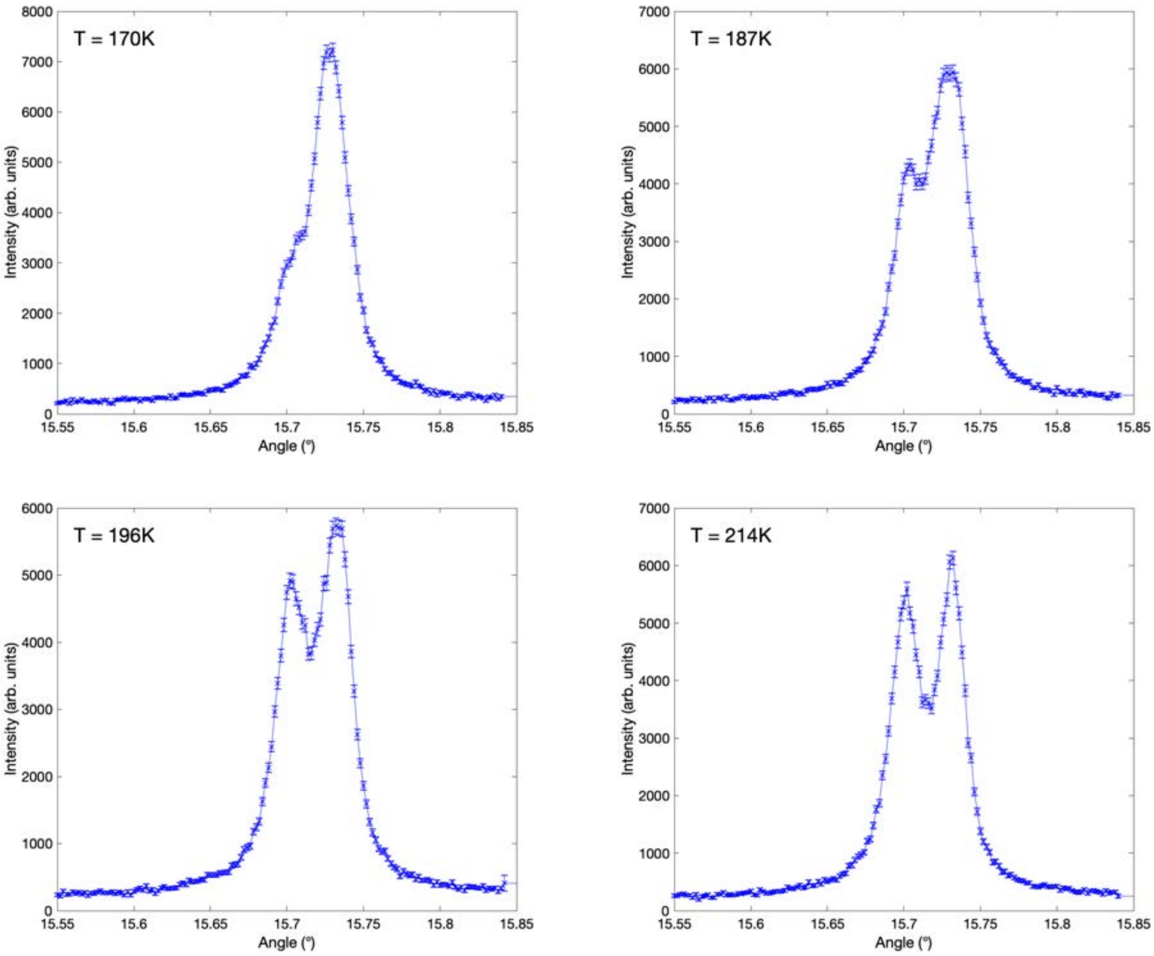

Figure 8.28: Intensity as a function of two theta angle across the MPB region, for the (440) reflection, observed in $Tb_{0.34}Dy_{0.66}Fe_{2.03}$.

There are two potential causes for this, either the alloying of parent phases causes a large reduction in the cubic transition temperature (a feature which is somewhat supported by the discontinuities observed for some samples in the region of 600 K to 650 K), or that the lattice distortions caused by the parent phases, which determine the degree of peak splitting and allow phase examination using synchrotron XRD, is vastly reduced above room temperature. Given that the parent phases are well understood, it is more likely the latter. Small amounts of undesirable phases (RE-Fe_3) may exist and are known to reduce the produced strain - it may be the case that these phases are present and reduce the distortion to such a level that the cubic transition is smeared.

To conclude, a summary of these results is shown in the form of a synchrotron XRD phase diagram, presented as Figure 8.29. These results use the analysis presented previously in this chapter, to outline the phase regions for each sample in this study. The presence of low symmetry phases prompts further study, with determination of the crystal structure and mechanism for formation being paramount. It appears to be the case that MPB containing materials often contain more complex transitions than a simple MPB, as is seen in PZT materials (among others).[28, 188]

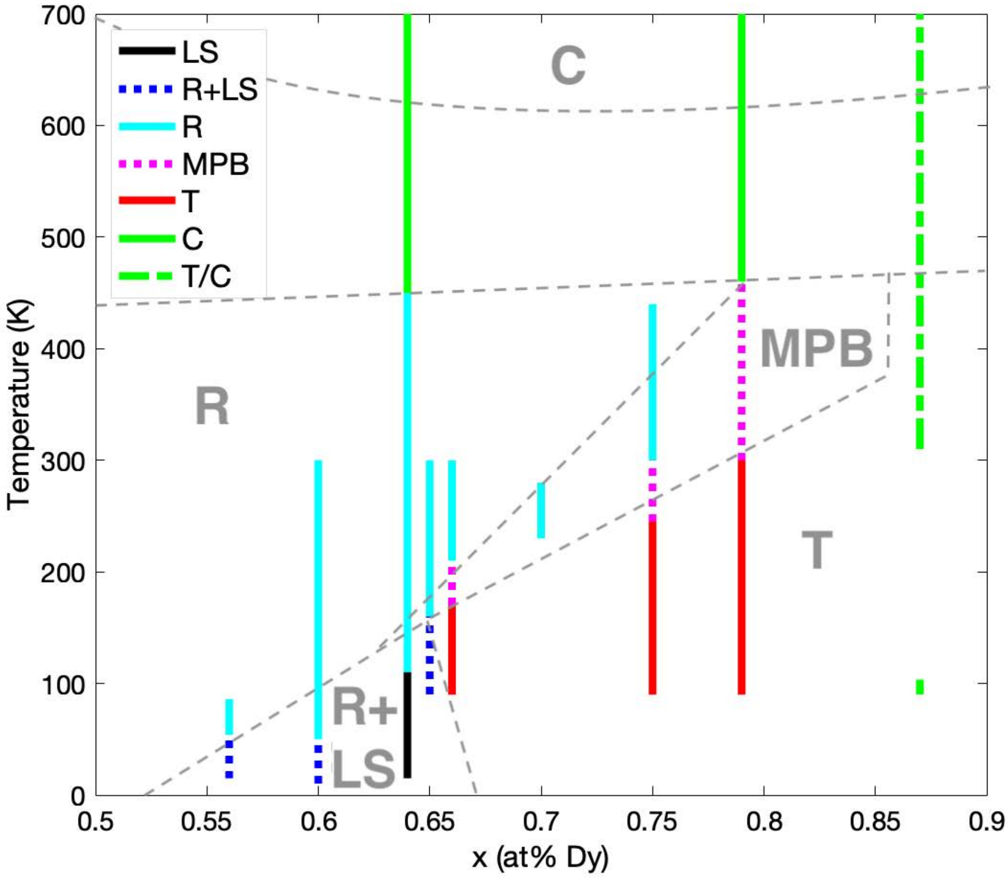

Figure 8.29: Results of the synchrotron XRD experiments, showing an updated phase diagram for comparison with that shown in Bergstrom et al (Figure 5.17). Vertical bars correspond to the direct results of phase determination from synchrotron XRD analysis. Grey dashed lines and letters act as guides to highlight the phase regions present. MPB is used here to denote a rhombohedral and tetragonal co-existence, while the unmarked phase region is left such as no distortion was detected, however the cubic transition temperature is well documented for the parent materials.
LS: **L**ow **S**ymmetry, **R+LS**: Co-existence of **R**hombohedral and **L**ow **S**ymmetry, **R**: **R**hombohedral, **MPB**: **M**orphotropic **P**hase **B**oundary, **T**: **T**etragonal, **C**: **C**ubic, **T/C**: Assumed direct transition of **T**etragonal to **C**ubic

Chapter 9

Conclusions and future work

Functional materials have become a cornerstone of modern society, with the advent of the technological age providing, and thriving in, the continuous development of new alloys for practical purposes. Magnetostrictive materials are one such example of a functional material, within which application of an external magnetic field will induce a strain.[193] Desirable magnetostrictive materials exhibit large magnitudes of strain, for minimum values of applied field and have low coercivity; a combination of these properties allows for easy switching 'on' and 'off' of the strain, which can then be used in applications such as sensors, actuators and transducers.[1,3,4] The future state of all functional materials, not just magnetostrictive materials, is reliant on both optimisation of existing materials and the synthesis of new materials. To achieve this, it is crucial to investigate, characterise and understand the underlying physics and material properties in existing materials, the path to future materials is highlighted.

To elucidate future alloy development, the aim of this thesis was to perform comprehensive analysis on two samples of magnetostrictive material - the binary alloy, iron-palladium, and the Laves phase compound, $Tb_{1-x}Dy_xFe_2$, using reciprocal space analysis techniques. These studies are linked via their shared interplay between magnetic and crystal structures. To achieve these aims, a series of neutron scattering experiments into the ferromagnetic shape memory alloy $Fe_{68.8}Pd_{31.2}$ have been performed, alongside a synchrotron X-ray diffraction study on a range of $Tb_{1-x}Dy_xFe_2$ alloys, wherein a barrier between crystal structures known as a morphotropic phase boundary (MPB) exists, which provides enhanced physical properties if the alloy fabrication is carefully controlled.[25,90]

Iron-palladium is a magnetostrictive material wherein the large strain at reduced temperature is attributed to a change in crystal structure from a face centred cubic to that of a face centred tetragonal, via an adaptive phase. A pre-martensitic tweed phenomena is known to exist as a minor phase at room temperature. These twinning clusters have been found to be adaptive to both applied magnetic field and temperature changes.[35,94]

Neutron scattering has been used to investigate the various temperature and magnetic field responses of this material, using two samples of identical composition. The results from these experiments show good agreement with physical property measurements in the literature, showing a clear magnetic saturation at H=0.2 T. At low values of applied field, up to and including the saturating field, a strong anisotropy is visible in the medium scattering vector (q) range. Analysis of this anisotropy reveals a peak in intensity as a function of scattering vector, which when converted to a physical size, suggests a strongly scattering feature with a median size of 50 nm at zero applied field. As field is increased to 0.2 T, the median size is shown to grow to approximately 55 nm. These sizes are significantly larger than that expected for twinning clusters (previously seen to be 2-3 nm in iron-palladium[13]), are reversible with applied field, and exist solely along [110] directions. At larger fields, this collapse of this anisotropy infers that the scattering feature is drastically changed, hinting at a significant change to either the magnetisation or crystal structure of the alloy at some threshold value of applied field.

Investigation of the intensity as a function of temperature clearly shows a transition, which appears to be a two step process where the latter is characteristic of a transformation to a ferromagnetic material, in that scattering intensity is enhanced due to the increase in magnetic scattering. This is peculiar as FePd is known to be ferromagnetic at room temperature. These findings suggest that the FCT phase of this material may have significantly stronger magnetic properties than the room temperature FCC phase, implying that the increased strain at low temperatures may not arise purely from changes to the elasticity of the material. Exceeding saturation, at H=0.5 T, there is an unexpected peak in the scattering intensity for the high q range. This peak has been found to be heavily influenced by directionality, only appearing when the magnetic field is aligned along a [110] direction. Thermal analysis of this peak shows that it is clearly pronounced at both 200 K and 300 K but is negligible at the transition temperature ($\approx$240 K).

It arises that FePd actually contains two specific sizes of precursor tweed - 'large' twinning clusters, on the order of 50 nm, which are crucial to the adaptive phase transformation as they coalesce together, and smaller twinning striations aligned along the [110] direction which strongly resist magnetisation until 0.5 T at which point they are the cause of the anisotropic scattering visible in high q.

$Tb_{1-x}Dy_xFe_2$ is a family of magnetostrictive alloys largely used in functional applications, most notably for sensors and actuators. The market leading Terfenol-D material is one such alloy in this family, with a composition of $Tb_{0.27}Dy_{0.73}Fe_2$, its desirable physical properties are found to exist near the morphotropic phase boundary between the two parent phases of $TbFe_2$ and $DyFe_2$, where it is known that the anisotropy is minimised and strain remains high, owed to the precise balance of the parent materials $TbFe_2$ and $DyFe_2$ which have rhombohedral and tetragonal structures respectively.[33] This synchrotron XRD study has been aimed at increasing the current knowledge on phases and phase transitions, specifically the morphotropic phase boundary, across multiple compositions of the functional material $Tb_{1-x}Dy_xFe_2$. A range of samples were fabricated using the arc melting method, before the most promising were identified using a preliminary 'sample study', employed to confirm that impurity concentration is minimal and that the desired phases were present. To determine the crystal structure as a function of composition and temperature, three main reflection sites were monitored so as to study the observed peak splitting, caused by inherent lattice distortions. Clear evidence is obtained for a low temperature, low symmetry phase which may be monoclinic in nature due to the reduction in anisotropy energy and increase in exchange energy in these regions. This low symmetry phase is found to co-exist with the rhombohedral phase at multiple compositions and may potentially suppress the formation of the tetragonal phase, in turn causing a reduction in [001] lattice distortion (which is already dwarfed by its [111] counterpart by approximately two orders of magnitude, at room temperature). Furthermore, evidence has been obtained in this thesis which confirms that morphotropic phase boundaries are in fact a co-existence of rhombohedral and tetragonal phases, visible by their shifting character across the boundary. It is also shown that MPB width may be a function of composition and temperature, with the MPB width being significantly larger for samples with high Dy content, potentially allowing for greater application potential, particularly so where phase co-existence is desirable and the MPB could be designed to exist as a functionally metastable region.

Finally, these results highlight the high temperature region of these alloys. The transition to a cubic structure for both of the parent phases is expected at approximately 700 K - this is in direct contrast to the results obtained within this work, where the crystal structure is shown to 'melt' towards cubic across a large temperature range before eventually settling in a cubic fashion around 450/500 K. Given that the cubic transition temperatures for the parent compounds are well documented,[102] these findings provide confirmation that the degree of lattice distortion is significantly reduced at high temperatures away from the MPB composition.

By increasing the understanding of the response to temperature, applied magnetic field and compositional changes, the application potential of these two compounds is widened significantly. While the low symmetry phase in $Tb_{1-x}Dy_xFe_2$ alloys is found to appear at temperatures well below those feasible for application (less than 100 K), the knowledge of phase co-existence provides a significant insight into the nature of phase boundaries in this alloy system, which is not specific to the morphotropic phase boundary. With regards to the MPB, its position has been further mapped (both wider in composition and temperature than previously measured) and the nature of the MPB has been cemented as a phase co-existence of rhombohedral and tetragonal symmetries, information which can be exploited to achieve increased performance at boundary positions. The importance of directionality within the iron-palladium system brings to light a realm of new possibilities for magnetostrictive materials of this type, specifically those which take on a 'strain glass' structure. The highly mobile and influential twinning clusters may provide a mechanism for significant enhancement to the physical properties, while the new information regarding the magnetic and temperature response can be used to aid in the optimisation of any future employment.

9.1 Future work

9.1.1 Iron-Palladium

Suggested future work for this material is largely based around new sample synthesis and physical property measurements. A new range of single crystal samples, fabricated to provide a focused range of compositions either side of that studied in this thesis, should be thoroughly characterised to determine their directions. Following this, physical property measurements of the magnetisation, magnetostriction and AC susceptibility will help to determine the nature of the magnetisation in the FCT phase, and also potentially unlock the secret behind the peak in the high q region at 0.5 T. By confirming the cause of this peculiar extremity in scattering intensity, the magnetic response of iron-palladium can be accounted for across every length scale. Cementing the cause of this feature, hypothesised to arise from forced magnetic rotation of the nanoscale striations, will provide clues to the ideal fabrication methods for these materials.

Polarised small-angle neutron scattering has already been attempted in a bid to isolate the nuclear and magnetic components of scattering, albeit with limited success. Future attempts at this experimentation should account more for depolarisation at the sample position, a feat which would require increasingly fine control of the instrumentation, but would lead to determination of the specific contributions to the scattering intensity, allowing for a more comprehensive analysis of the magnetisation anisotropy. A newly fabricated sample with higher saturation field (dependent on results of magnetic analysis) may allow these measurements to be performed. Finally, to analyse the structural features within this sample, transmission electron microscopy or atom probe tomography provide the best resolution in the size region of interest. Studying single crystal samples with well aligned growth directions, will allow for a complete picture on both the size and directionality of the tweed striations, which can in turn be combined with the polarisation study previously suggested.

9.1.2 $Tb_{1-x}Dy_xFe_2$ alloys

For this material, the existence of a low symmetry phase prompts strong interest, as the anisotropy compensation and drastic reduction in thermal fluctuations stabilises a previously unseen crystal structure. Therefore, the suggested approach is fabrication of a new range of samples (preferably single crystal such as to maximise distortion magnitude) within a tighter region of interest, specifically $0.5< x <0.7$ to encompass all compositions which feature the low symmetry phase - Bridgman or floating zone methods would be ideal for this. Following fabrication, a comprehensive microstructure and compositional study of the samples should be performed. By checking for the presence of any impurity phases, examining the microstructure, cementing the composition and confirming the phases present are as expected (particularly important would be to determine volume fractions of the phases, particularly when near MPB composition) this work can be elevated to finer detail, particularly relating to the finer points of the underlying physics. To achieve this, the following techniques are suggested - ICP-OES will be used to determine sample composition and should be combined with light element compositional analysis (notably oxygen) to ensure sample purity. Microscopy work should then include topographical work and compositional work (EDS, WDS), where the distribution of RE elements and/or oxides may highlight any problems during fabrication. To aid the subsequent XRD measurements, particle size analysis of the ground samples would allow for an optimum particle size to be assessed and achieved, therefore maximising the instrument resolution. Finally, a combination of low temperature synchrotron XRD measurements (consisting of both peak monitoring and full angle scans) and magnetostriction measurements should be performed - this would allow for a new type of 3D phase diagram to be generated, i.e. adding a z component to express regions of enhanced strain. This phase diagram would serve as a new benchmark figure-of-merit for functional materials whose optimisation relies on MPB enhancement. Full angle scans will allow for refinement and determination of the low symmetry phase. Low symmetry phases provide unique potential for study of anisotropy in non-trivial directions and if characterised correctly, could provide insight that is invaluable for the study of low symmetry phases in other functional materials.

Bibliography

[1] S. Aksoy, "Magnetostrictive actuators," in *Reference Module in Materials Science and Materials Engineering*, Elsevier, 2021.

[2] A. Sankara Subramanian, P. Meenalochini, S. Suba Bala Sathiya, and G. Ram Prakash, "A review on selection of soft magnetic materials for industrial drives," *Materials Today: Proceedings*, 2020.

[3] S. Yusuf, "3 - functional magnetic materials: Fundamental and technological aspects," in *Functional Materials* (S. Banerjee and A. Tyagi, eds.), pp. 111–154, London: Elsevier, 2012.

[4] E. Hristoforou, A. Ktena, and S. Angelopoulos, "Magnetostrictive materials for sensing applications," in *Reference Module in Materials Science and Materials Engineering*, Elsevier, 2020.

[5] S. Trolier-McKinstry, S. Zhang, A. J. Bell, and X. Tan, "High-performance piezoelectric crystals, ceramics, and films," *Annual Review of Materials Research*, vol. 48, no. 1, pp. 191–217, 2018.

[6] H. Liu, J. Zhong, C. Lee, S.-W. Lee, and L. Lin, "A comprehensive review on piezoelectric energy harvesting technology: Materials, mechanisms, and applications," *Applied Physics Reviews*, vol. 5, no. 4, p. 041306, 2018.

[7] N. Sezer and M. Koç, "A comprehensive review on the state-of-the-art of piezoelectric energy harvesting," *Nano Energy*, vol. 80, p. 105567, 2021.

[8] Z. Deng and M. J. Dapino, "Review of magnetostrictive materials for structural vibration control," *Smart Materials and Structures*, vol. 27, p. 113001, oct 2018.

[9] J. Atulasimha and A. B. Flatau, "A review of magnetostrictive iron–gallium alloys," *Smart Materials and Structures*, vol. 20, p. 043001, mar 2011.

[10] F. Narita and M. Fox, "A review on piezoelectric, magnetostrictive, and magnetoelectric materials and device technologies for energy harvesting applications," *Advanced Engineering Materials*, vol. 20, no. 5, p. 1700743, 2018.

[11] O. G. Heinonen, E. W. Singleton, B. W. Karr, Z. Gao, H. S. Cho, and Y. Chen, "Review of the physics of magnetoresistive readers," *IEEE Transactions on Magnetics*, vol. 44, no. 11, pp. 2465–2471, 2008.

[12] H. Gu, X. Zhang, H. Wei, Y. Huang, S. Wei, and Z. Guo, "An overview of the magnetoresistance phenomenon in molecular systems," *Chem. Soc. Rev.*, vol. 42, pp. 5907–5943, 2013.

[13] R. Oshima, M. Sugiyama, and F. E. Fujita, "Tweed structures associated with Fcc-Fct transformations in Fe-Pd alloys," *Metallurgical Transactions A*, vol. 19, no. 4, pp. 803–810, 1988.

[14] M. B. Moffett, A. E. Clark, M. Wun-Fogle, J. Linberg, J. P. Teter, and E. A. McLaughlin, "Characterization of Terfenol-D for magnetostrictive transducers," *The Journal of the Acoustical Society of America*, vol. 89, no. 3, pp. 1448–1455, 1991.

[15] M. Ahart, M. Somayazulu, R. E. Cohen, P. Ganesh, P. Dera, H.-k. Mao, R. J. Hemley, Y. Ren, P. Liermann, and Z. Wu, "Origin of morphotropic phase boundaries in ferroelectrics," *Nature*, vol. 451, no. 7178, pp. 545–548, 2008.

[16] I. O. Troyanchuk, N. V. Tereshko, D. V. Karpinsky, V. V. Fedotova, and C. Kozak, "Morphotropic phase boundary in $Bi_{1-x}Ca_xFe_{\frac{1-x}{2}}Nb_{\frac{x}{2}}O_3$ multiferroics," *New Electrical and Electronic Technologies and their Industrial Implementation*, p. 44, 2013.

[17] G. L. Squires, *Introduction to the Theory of Thermal Neutron Scattering*. Cambridge University Press, 3 ed., 2012.

[18] P. Sedigh Rahimabadi, M. Khodaei, and K. R. Koswattage, "Review on applications of synchrotron-based x-ray techniques in materials characterization," *X-Ray Spectrometry*, vol. 49, no. 3, pp. 348–373, 2020.

[19] B. Jacrot, "The study of biological structures by neutron scattering from solution," *Reports on Progress in Physics*, vol. 39, pp. 911–953, oct 1976.

[20] A. P. Radlinski, "Small-Angle Neutron Scattering and the Microstructure of Rocks," *Reviews in Mineralogy and Geochemistry*, vol. 63, pp. 363–397, 01 2006.

[21] C. B. Larsen, A. T. Rømer, S. Janas, F. Treue, B. Mønsted, N. E. Shaik, H. M. Rønnow, and K. Lefmann, "Exact diagonalization study of the hubbard-parametrized four-spin ring exchange model on a square lattice," *Physical Review B*, vol. 99, Feb 2019.

[22] J. Joule, "On a new class of magnetic forces," *Ann. Electr. Magn. Chem*, vol. 8, no. 1842, pp. 219–224, 1842.

[23] O. Heinonen, "Magnetoresistive materials and devices," in *Introduction to Nanoscale Science and Technology*, pp. 327–353, Boston, MA: Springer US, 2004.

[24] A. Clark, R. Abbundi, and W. Gillmor, "Magnetization and magnetic anisotropy of $TbFe_2$, $DyFe_2$, $Tb_{0.27}Dy_{0.73}Fe_2$ and $TmFe_2$," *IEEE Transactions on Magnetics*, vol. 14, no. 5, pp. 542–544, 1978.

[25] A. Clark, "Chapter 7 magnetostrictive rare earth-Fe2 compounds," vol. 1 of *Handbook of Ferromagnetic Materials*, pp. 531–589, Elsevier, 1980.

[26] S. Yang, H. Bao, C. Zhou, Y. Wang, X. Ren, Y. Matsushita, Y. Katsuya, M. Tanaka, K. Kobayashi, X. Song, and J. Gao, "Large magnetostriction from morphotropic phase boundary in ferromagnets," *Phys. Rev. Lett.*, vol. 104, p. 197201, May 2010.

[27] K. Uchino, *Ferroelectric devices.* CRC press, 2018.

[28] B. Jaffe, W. R. Cook, and H. Jaffe, "Chapter 7 - solid solutions of Pb(Ti, Zr, Sn, Hf)O_3," in *Piezoelectric Ceramics* (B. Jaffe, W. R. Cook, and H. Jaffe, eds.), pp. 135–183, Academic Press, 1971.

[29] R. Bergstrom, M. Wuttig, J. Cullen, P. Zavalij, R. Briber, C. Dennis, V. O. Garlea, and M. Laver, "Morphotropic phase boundaries in ferromagnets: $Tb_{1-x}Dy_xFe_2$ alloys," *Phys. Rev. Lett.*, vol. 111, p. 017203, Jul 2013.

[30] B. Jaffe, R. S. Roth, and S. Marzullo, "Piezoelectric properties of lead zirconate-lead titanate solid-solution ceramics," *Journal of Applied Physics*, vol. 25, no. 6, pp. 809–810, 1954.

[31] T. Asada and Y. Koyama, "Ferroelectric domain structures around the morphotropic phase boundary of the piezoelectric material $PbZr_{1-x}Ti_xO_3$," *Physical Review B*, vol. 75, no. 21, p. 214111, 2007.

[32] U. Atzmony, M. P. Dariel, and G. Dublon, "Spin-orientation diagram of the pseudobinary $Tb_{1-x}Dy_xFe_2$ Laves compounds," *Phys. Rev. B*, vol. 15, pp. 3565–3566, Apr 1977.

[33] A. Clark and D. Crowder, "High temperature magnetostriction of $TbFe_2$ and $Tb_{.27}Dy_{.73}Fe_2$," *IEEE Transactions on Magnetics*, vol. 21, no. 5, pp. 1945–1947, 1985.

[34] R. A. Kellogg and A. B. Flatau, "Stress-strain relationship in terfenol-d," in *Smart Structures and Materials 2001: Smart Structures and Integrated Systems*, vol. 4327, pp. 541–549, International Society for Optics and Photonics, 2001.

[35] J. Steiner, A. Lisfi, T. Kakeshita, T. Fukuda, and M. Wuttig, "Unique magnetostriction of $Fe_{68.8}Pd_{31.2}$ attributable to twinning," *Scientific Reports*, vol. 6, no. 1, p. 34259, 2016.

[36] A. Aharoni, *Introduction to the Theory of Ferromagnetism.* International Series of Monographs on Physics, Clarendon Press, 2000.

[37] G. H. O. Daalderop, P. J. Kelly, and M. F. H. Schuurmans, "First-principles calculation of the magnetocrystalline anisotropy energy of iron, cobalt, and nickel," *Phys. Rev. B*, vol. 41, pp. 11919–11937, Jun 1990.

[38] L. Landau and E. Lifshitz, *Course of Theoretical Physics.* Elsevier, 2013.

[39] B. K. Sharma, *Electrical and Electronic Materials Science, Ch7 Magnetic Materials.* 2014.

[40] O. Dunlop, D. J. & Ozdemir, "Rock magnetism. fundamentals and frontiers. isbn 0 521 32514 5," *Geological Magazine*, vol. 135, no. 2, p. 287–300, 1998.

[41] *Magnetic Anisotropy*, ch. 7, pp. 197–239. John Wiley & Sons, Ltd, 2008.

[42] K. Martin, P. Groot, B. Rainford, K. Wang, G. Bowden, J. Zimmermann, and H. Fangohr, "Magnetic anisotropy in the cubic laves RE-Fe_2 intermetallic compounds," *Journal of Physics: Condensed Matter*, vol. 18, p. 459, 12 2005.

[43] D. Kendall and A. R. Piercy, "Magnetisation processes and temperature dependence of the magnetomechanical properties of $Tb_{0.27}Dy_{0.73}Fe_{1.9}$," *IEEE Transactions on Magnetics*, vol. 26, no. 5, pp. 1837–1839, 1990.

[44] J. Stöhr and H. Siegmann, *Magnetism: From Fundamentals to Nanoscale Dynamics.* Springer Series in Solid-State Sciences, Springer Berlin Heidelberg, 2007.

[45] J. Jackson, *Classical Electrodynamics.* Wiley, 1963.

[46] M. T. Johnson, P. J. H. Bloemen, F. J. A. den Broeder, and J. J. de Vries, "Magnetic anisotropy in metallic multilayers," *Reports on Progress in Physics*, vol. 59, pp. 1409–1458, nov 1996.

[47] H. Kirchmayr, "Magnetic anisotropy," in *Encyclopedia of Materials: Science and Technology* (K. J. Buschow, R. W. Cahn, M. C. Flemings, B. Ilschner, E. J. Kramer, S. Mahajan, and P. Veyssière, eds.), pp. 4754–4757, Oxford: Elsevier, 2001.

[48] M. Nematov, I. Baraban, N. Yudanov, V. Rodionova, F. Qin, H.-X. Peng, and L. Panina, "Evolution of the magnetic anisotropy and magnetostriction in Co-based amorphous alloys microwires due to current annealing and stress-sensory applications," *Journal of Alloys and Compounds*, vol. 837, p. 155584, 2020.

[49] R. Bozorth, *Ferromagnetism.* The Bell Telephone Laboratories Series, IEEE Press, 1993.

[50] C. Zhang, T. Ma, and M. Yan, "Induced additional anisotropy influences on magnetostriction of giant magnetostrictive materials," *Journal of Applied Physics*, vol. 112, no. 10, p. 103908, 2012.

[51] P. A. M. Dirac and R. H. Fowler, "The quantum theory of the electron," *Proceedings of the Royal Society of London. Series A, Containing Papers of a Mathematical and Physical Character*, vol. 117, no. 778, pp. 610–624, 1928.

[52] W. Pauli, "Über den zusammenhang des abschlusses der elektronengruppen im atom mit der komplexstruktur der spektren," *Zeitschrift für Physik*, vol. 31, no. 1, pp. 765–783, 1925.

[53] J. Rohlf, *Modern Physics from alpha to Z0.* Wiley, 1994.

[54] J. Coey, *Magnetism and Magnetic Materials.* Knovel Library, Cambridge University Press, 2010.

[55] Q. Liu, C. Deng, Y. Yu, J. Torrent, M. J. Jackson, S. K. Banerjee, and R. Zhu, "Temperature dependence of magnetic susceptibility in an argon environment: implications for pedogenesis of Chinese loess/palaeosols," *Geophysical Journal International*, vol. 161, no. 1, pp. 102–112, 2005.

[56] C. Kittel and P. McEuen, *Introduction to Solid State Physics.* John Wiley & Sons, 2019.

[57] S. Sendelbach, D. Hover, A. Kittel, M. Mück, J. M. Martinis, and R. McDermott, "Magnetism in squids at millikelvin temperatures," *Physical Review Letters*, vol. 100, Jun 2008.

[58] P. A. M. Dirac and R. H. Fowler, "On the theory of quantum mechanics," *Proceedings of the Royal Society of London. Series A, Containing Papers of a Mathematical and Physical Character*, vol. 112, no. 762, pp. 661–677, 1926.

[59] D. Griffiths, *Introduction to Quantum Mechanics.* Cambridge University Press, 2017.

[60] W. Heisenberg, "Mehrkörperproblem und resonanz in der quantenmechanik," *Zeitschrift für Physik*, vol. 38, no. 6, pp. 411–426, 1926.

[61] C. Kittel and J. Galt, "Ferromagnetic domain theory," vol. 3 of *Solid State Physics*, pp. 437–564, Academic Press, 1956.

[62] J. S. Galsin, "Chapter 19 - ferromagnetism," in *Solid State Physics* (J. S. Galsin, ed.), pp. 407–430, Academic Press, 2019.

[63] N. Nakotte, A. Purwanto, R. A. Robinson, R. B. Von Dreele, L. Havela, K. Prokeš, V. Sechovsky, L. C. J. Pereira, J. C. Spirlet, and J. Rebizant, "On the relationship between crystal structure and magnetism in U_2Pd_2Sn and U_2Ni_2In ," *Journal of Applied Physics*, vol. 81, no. 8, pp. 4927–4927, 1997.

[64] L. A. Shuvalov, "Magnetic properties of crystals," in *Modern Crystallography IV* (L. A. Shuvalov, ed.), (Berlin, Heidelberg), pp. 267–347, Springer Berlin Heidelberg, 1988.

[65] H. Sakai, S. Yokoyama, A. Kuwabara, J. S. White, E. Canévet, H. M. Rønnow, T. Koretsune, R. Arita, A. Miyake, M. Tokunaga, Y. Tokura, and S. Ishiwata, "Negative-pressure-induced helimagnetism in ferromagnetic cubic perovskites $Sr_{1-x}Ba_xCoO_3$," *Phys. Rev. Materials*, vol. 2, p. 104412, Oct 2018.

[66] R. H. Yu, S. Basu, Y. Zhang, A. Parvizi-Majidi, and J. Q. Xiao, "Pinning effect of the grain boundaries on magnetic domain wall in FeCo-based magnetic alloys," *Journal of Applied Physics*, vol. 85, no. 9, pp. 6655–6659, 1999.

[67] J. A. Dooley, C. A. Lindensmith, R. G. Chave, N. Good, J. Graetz, and B. Fultz, "Magnetostriction of single crystal and polycrystalline $Tb_{0.60}Dy_{0.40}$ at cryogenic temperatures," *Journal of Applied Physics*, vol. 85, no. 8, pp. 6256–6258, 1999.

[68] S. Blundell and K. Blundell, *Concepts in Thermal Physics.* OUP Oxford, 2010.

[69] M. Suzuki, "A Theory of the Second Order Phase Transitions in Spin Systems. III: Critical Behavior of Correlation Functions in Ising Ferromagnets," *Progress of Theoretical Physics*, vol. 39, no. 2, pp. 349–364, 1968.

[70] I. K. Kamilov and K. K. Aliev, “Second-order phase transitions in ferromagnetic materials in weak fields near the curie point,” *Soviet Physics Uspekhi*, vol. 26, pp. 696–712, aug 1983.

[71] R. Indeck and M. Muller, “Magnetic recording measurements,” in *Encyclopedia of Materials: Science and Technology* (K. J. Buschow, R. W. Cahn, M. C. Flemings, B. Ilschner, E. J. Kramer, S. Mahajan, and P. Veyssière, eds.), pp. 1–14, Oxford: Elsevier, 2002.

[72] T. Oguchi, “A theory of antiferromagnetism, ii,” *Progress of Theoretical Physics*, vol. 13, no. 2, pp. 148–159, 1955.

[73] M. Gottschilch, O. Gourdon, J. Persson, C. de la Cruz, V. Petricek, and T. Brueckel, “Study of the antiferromagnetism of Mn_5Si_3: an inverse magnetocaloric effect material,” *Journal of materials chemistry*, vol. 22, no. 30, pp. 15275–15284, 2012.

[74] C. Sürgers, G. Fischer, P. Winkel, and H. v. Löhneysen, “Large topological hall effect in the non-collinear phase of an antiferromagnet,” *Nature communications*, vol. 5, no. 1, pp. 1–8, 2014.

[75] W. H. Meiklejohn and C. P. Bean, “New magnetic anisotropy,” *Phys. Rev.*, vol. 105, pp. 904–913, Feb 1957.

[76] J. S. Smart, “The Néel theory of ferrimagnetism,” *American Journal of Physics*, vol. 23, no. 6, pp. 356–370, 1955.

[77] L. B. Kong, L. Liu, Z. Yang, S. Li, T. Zhang, and C. Wang, “15 - theory of ferrimagnetism and ferrimagnetic metal oxides,” in *Magnetic, Ferroelectric, and Multiferroic Metal Oxides* (B. D. Stojanovic, ed.), Metal Oxides, pp. 287–311, Elsevier, 2018.

[78] R. Jackson, “John tyndall and the early history of diamagnetism,” *Annals of science*, vol. 72, no. 4, pp. 435–489, 2015.

[79] F. Luborsky, J. Livingston, and G. Chin, “Chapter 29 - Magnetic properties of metals and alloys,” in *Physical Metallurgy (Fourth Edition)* (R. W. Cahn and P. Haasen, eds.), pp. 2501–2565, Oxford: North-Holland, fourth edition ed., 1996.

[80] A. del Moral, *Magnetostriction and Magnetoelasticity Theory: A Modern View.* American Cancer Society, 2007.

[81] A. Olabi and A. Grunwald, “Design and application of magnetostrictive materials,” *Materials & Design*, vol. 29, no. 2, pp. 469–483, 2008.

[82] N. Ekreem, A. G. Olabi, T. Prescott, A. Rafferty, and M. Hashmi, “An overview of magnetostriction, its use and methods to measure these properties,” *Journal of Materials Processing Technology*, vol. 191, pp. 96–101, 08 2007.

[83] E. Lee and M. Asgar, “The magnetostriction of nickel,” *Proceedings of the Royal Society of London. A. Mathematical and Physical Sciences*, vol. 326, no. 1564, pp. 73–85, 1971.

[84] R. Birss and E. Lee, “The saturation magnetostriction constants of nickel within the temperature range -196 to 365°C,” *Proceedings of the Physical Society (1958-1967)*, vol. 76, no. 4, p. 502, 1960.

[85] S. Legvold, “Chapter 3 rare earth metals and alloys,” vol. 1 of *Handbook of Ferromagnetic Materials*, pp. 183–295, Elsevier, 1980.

[86] J. J. Rhyne and S. Legvold, “Magnetostriction of Tb single crystals,” *Phys. Rev.*, vol. 138, pp. A507–A514, Apr 1965.

[87] J. J. Rhyne, “Chapter 16 amorphous magnetic rare earth alloys,” in *Alloys and Intermetallics*, vol. 2 of *Handbook on the Physics and Chemistry of Rare Earths*, pp. 259–294, Elsevier, 1979.

[88] A. T. Aldred, “Magnetization of iron-gallium and iron-arsenic alloys,” *Journal of Applied Physics*, vol. 37, no. 3, pp. 1344–1346, 1966.

[89] “Magnetostrictive coefficient values for iron, nickel, and cobalt. `https://eng.libretexts.org/Bookshelves/Materials_Science/Supplemental_Modules_(Materials_Science)/Magnetic_Properties/Magnetostriction`.” [Online; accessed 2021-07-19].

[90] A. Clark, “Magnetic and magnetoelastic properties of highly magnetostrictive rare earth-iron laves phase compounds,” in *AIP Conference Proceedings*, vol. 18, pp. 1015–1029, American Institute of Physics, 1974.

[91] E. Semenova, V. Svetlana, J. Fedotova, and V. Bayev, “Iron-palladium composite nanoparticles,” pp. 289–292, 06 2013.

[92] R. C. Hall, “Magnetic anisotropy and magnetostriction of ordered and disordered cobalt-iron alloys,” *Journal of Applied Physics*, vol. 31, no. 5, pp. S157–S158, 1960.

[93] S. Ren, D. Xue, Y. Ji, X. Liu, S. Yang, and X. Ren, “Low-field-triggered large magnetostriction in iron-palladium strain glass alloys,” *Phys. Rev. Lett.*, vol. 119, p. 125701, Sep 2017.

[94] J. Cui, T. Shield, and R. James, “Phase transformation and magnetic anisotropy of an iron–palladium ferromagnetic shape-memory alloy,” *Acta Materialia*, vol. 52, no. 1, pp. 35–47, 2004.

[95] B. Zhang and W. A. Soffa, “Structure and properties of rapidly-solidified iron-platinum and iron-palladium alloys,” *IEEE Transactions on Magnetics*, vol. 26, no. 5, pp. 1388–1390, 1990.

[96] J. E. Schmidt and L. Berger, “Magnetostriction of Pd-Fe alloys,” *Journal of applied physics*, vol. 55, no. 4, pp. 1073–1080, 1984.

[97] A. Y. Volkov, “Structure and mechanical properties of CuAu and CuAuPd ordered alloys,” *Gold Bulletin*, vol. 37, no. 3, pp. 208–215, 2004.

[98] P. Vlaic and E. Burzo, “Magnetic behaviour of iron-platinum alloys,” *Journal of Optoelectronics and Advanced Materials*, vol. 12, pp. 1114–1124, 05 2010.

[99] H. Seiner, V. Kopecký, M. Landa, and O. Heczko, “Elasticity and magnetism of Ni_2MnGa premartensitic tweed,” *physica status solidi (b)*, vol. 251, no. 10, pp. 2097–2103, 2014.

[100] M. E. Gruner, S. Fähler, and P. Entel, “Magnetoelastic coupling and the formation of adaptive martensite in magnetic shape memory alloys,” *physica status solidi (b)*, vol. 251, no. 10, pp. 2067–2079, 2014.

[101] M. Sugiyama, R. Oshima, and F. E. Fujita, “Mechanism of fcc-fct thermoelastic martensite transformation in Fe & Pd alloys,” *Transactions of the Japan Institute of Metals*, vol. 27, no. 10, pp. 719–730, 1986.

[102] J. Alexander and O. Myers, “Microstructure properties and strengthening mechanisms of the as4-3501-6 polymeric resin with embedded terfenol-d particles,” *ASME 2014 Conference on Smart Materials, Adaptive Structures and Intelligent Systems, SMASIS 2014*, vol. 1, 09 2014.

[103] J. Verhoeven, E. Gibson, O. McMasters, and J. Ostenson, “Directional solidification and heat treatment of terfenol-d magnetostrictive materials,” *Metallurgical Transactions A*, vol. 21, no. 8, pp. 2249–2255, 1990.

[104] P. Burr, S. Middleburgh, and R. Grimes, “Crystal structure, thermodynamics, magnetics and disorder properties of Be-Fe-Al intermetallics,” *Journal of Alloys and Compounds*, vol. 639, 07 2014.

[105] E. Hellner, “Fritz laves 27.2.1906 - 12.8.1978,” *Zeitschrift fur Kristallographie - Crystalline Materials*, vol. 151, no. 1-4, pp. 1–20, 1980.

[106] F. Stein, M. Palm, and G. Sauthoff, “Structure and stability of laves phases. part i. critical assessment of factors controlling laves phase stability,” *Intermetallics*, vol. 12, no. 7, pp. 713–720, 2004. Intermetallic and Advanced Metallic Materials - A Symposium Dedicated to Dr. C.T. Liu, 3-6 March 2003, San Diego, CA, USA.

[107] R. Parr and Y. Weitao, *Density-Functional Theory of Atoms and Molecules.* International Series of Monographs on Chemistry, Oxford University Press, 1994.

[108] L. Rabahi, B. Alili, D. Bradai, T. Grosdidier, and A. Kellou, “Dft calculations of structural, magnetic and thermal properties of c15, c14 and c36 laves phases in Fe-Nb-Zr,” *Intermetallics*, vol. 83, pp. 92–100, 2017.

[109] C. E. Patrick, G. A. Marchant, and J. B. Staunton, “Spin orientation and magnetostriction of $Tb_{1-x}Dy_xFe_2$ from first principles,” *Phys. Rev. Applied*, vol. 14, p. 014091, Jul 2020.

[110] S. Yang and X. Ren, “Noncubic crystallographic symmetry of a cubic ferromagnet: Simultaneous structural change at the ferromagnetic transition,” *Phys. Rev. B*, vol. 77, p. 014407, Jan 2008.

[111] Y. Chen and B. Zheng, "What happens after the rare earth crisis: a systematic literature review," *Sustainability*, vol. 11, no. 5, p. 1288, 2019.

[112] A. E. Clark and H. S. Belson, "Giant room-temperature magnetostrictions in $TbFe_2$ and $DyFe_2$," *Physical Review B*, vol. 5, no. 9, p. 3642, 1972.

[113] J. J. Rhyne, J. H. Schelleng, and N. C. Koon, "Anomalous magnetization of amorphous $TbFe_2$, $GdFe_2$, and YFe_2," *Phys. Rev. B*, vol. 10, pp. 4672–4679, Dec 1974.

[114] A. E. Clark, J. P. Teter, and O. D. McMasters, "Magnetostriction "jumps" in twinned $Tb_{0.3}Dy_{0.7}Fe_{1.9}$," *Journal of Applied Physics*, vol. 63, no. 8, pp. 3910–3912, 1988.

[115] A. Clark, R. Abbundi, H. Savage, and O. McMasters, "Magnetostriction of rare earth-Fe_2 Laves phase compounds," *Physica B+C*, vol. 86-88, pp. 73–74, 1977.

[116] "`http://www.tdvib.com/wp-content/uploads/2015/09/Terfenol-D-alloys-vs-Temperature.png`," 2021. [Online; accessed 2021-07-19].

[117] K. Strnat, "The hard magnetic properties of rare earth-transition metal alloys," *IEEE Transactions on Magnetics*, vol. 8, no. 3, pp. 511–516, 1972.

[118] X. Liu, J. Liu, Z. Pan, X. Song, Z. Zhang, J. Du, and W. Ren, "Optimisation on magnetic anisotropy and magnetostriction in $Tb_xHo_{0.8-x}Pr_{0.2}(Fe_{0.8}Co_{0.2})_{1.93}$ compounds," *Journal of Magnetism and Magnetic Materials*, vol. 391, pp. 60–64, 2015.

[119] "`https://www.instituteofmaking.org.uk/materials-library/material/terfenol-d`," 2021. [Online; accessed 2021-07-19].

[120] G. Müller and J. Friedrich, "Crystal growth, bulk: Methods," in *Encyclopedia of Condensed Matter Physics* (F. Bassani, G. L. Liedl, and P. Wyder, eds.), pp. 262–274, Oxford: Elsevier, 2005.

[121] H. Ozoe and S. Tanaka, "Finite element analyses of a simplified model for floating zone crystallization method," in *Transport Phenomena in Heat and Mass Transfer* (J. REIZES, ed.), pp. 663–674, Amsterdam: Elsevier, 1992.

[122] O. McMasters, J. Verhoeven, and E. Gibson, "Preparation of terfenol-d by float zone solidification," *Journal of Magnetism and Magnetic Materials*, vol. 54-57, pp. 849–850, 1986.

[123] J. Verhoeven, E. Gibson, O. McMasters, and H. Baker, "The growth of single crystal terfenol-d crystals," *Metallurgical and Materials Transactions A*, vol. 18, no. 2, pp. 223–231, 1987.

[124] J. D. Snodgrass and O. McMasters, "Optimized terfenol-d manufacturing processes," *Journal of alloys and compounds*, vol. 258, no. 1-2, pp. 24–29, 1997.

[125] W. Paul, "Chapter 1 high pressure in semiconductor physics: A historical overview," vol. 54 of *Semiconductors and Semimetals*, pp. 1–48, Elsevier, 1998.

[126] P. Han, J. Tian, and W. Yan, "1 - bridgman growth and properties of pmn–pt-based single crystals," in *Handbook of Advanced Dielectric, Piezoelectric and Ferroelectric Materials* (Z.-G. Ye, ed.), Woodhead Publishing Series in Electronic and Optical Materials, pp. 3–37, Woodhead Publishing, 2008.

[127] W. J. Park, J. C. Kim, B. J. Ye, and Z. H. Lee, "Macrosegregation in bridgman growth of terfenol-d and effects of annealing," *Journal of Crystal Growth*, vol. 212, no. 1, pp. 283–290, 2000.

[128] P.-Z. Wong, "A simple method for in-situ purification and bridgman growth of anhydrous xCl2 single crystals (x = Fe, Co, Mg) and their mixed crystals," *Journal of Crystal Growth*, vol. 58, no. 3, pp. 534–536, 1982.

[129] C. Ferraz, M. Armelin, R. Oliveira, L. Otubo, J. Trencher Martins, R. Santos, F. Costa, D. Vergaças de Sousa Carvalho, N. Omi, C. Mesquita, and M. Hamada, "Purification and crystal growth of the bismuth (iii) iodide-influence of trace impurities on the crystal quality," *Studies in Engineering and Technology*, vol. 4, p. 70, 07 2017.

[130] L. A. Goryainov, "Impurity diffusion in the melt in crystal production by bridgman's method," *Journal of engineering physics*, vol. 20, no. 5, pp. 609–614, 1971.

[131] B. Davies, R. Mottram, and I. Harris, "Recent developments in the sintering of ndfeb," *Materials Chemistry and Physics*, vol. 67, no. 1, pp. 272–281, 2001.

[132] S. Zhao, H. Liu, X. Han, X. Meng, J. Qu, Y. Li, and S. Li, "Study on the sintering method of terfenol-d," *Journal of Applied Physics*, vol. 99, no. 8, p. 08M708, 2006.

[133] V. Issindou, B. Viala, L. Gimeno, O. Cugat, C. Rado, and S. Bouat, "Fabrication methods for high-performance miniature disks of terfenol-d for energy harvesting," *Sensors and Actuators A: Physical*, vol. 284, pp. 1–5, 2018.

[134] C. Rodríguez, A. Barrio, I. Orue, J. Vilas, L. León, J. M. Barandiarán, and M. Fdez-Gubieda Ruiz, "High magnetostriction polymer-bonded terfenol-d composites," *Sensors and Actuators A: Physical*, vol. 142, no. 2, pp. 538–541, 2008. The sixth European Magnetic Sensor and Actuator conference.

[135] G. P. McKnight and G. P. Carman, "[112] oriented terfenol-d composites," *Materials Transactions*, vol. 43, no. 5, pp. 1008–1014, 2002.

[136] S. Lim, S. Kim, S. Kang, J. Park, J. Nam, and D. Son, "Magnetostrictive properties of polymer-bonded terfenol-d composites," *Journal of Magnetism and Magnetic Materials*, vol. 191, no. 1, pp. 113–121, 1999.

[137] N.-j. Wang, Y. Liu, H.-w. Zhang, X. Chen, and Y.-x. Li, "Fabrication, magnetostriction properties and applications of Tb-Dy-Fe alloys: a review," *China Foundry*, vol. 13, no. 2, pp. 75–84, 2016.

[138] J. Liu, Z. Pan, X. Liu, Z. Zhang, X. Song, and W. Ren, "Large magnetostriction and direct experimental evidence for anisotropy compensation in

$Tb_{0.4-x}Nd_xDy_{0.6}(Fe_{0.8}Co_{0.2})_{1.93}$ Laves compounds," *Materials Letters*, vol. 137, pp. 274–276, 2014.

[139] H. Yin, J. Liu, Z. Pan, X. Liu, X. Liu, L. Liu, J. Du, and P. Si, "Magnetostriction of $Tb_xDy_{0.9-x}Nd_{0.1}(Fe_{0.8}Co_{0.2})_{1.93}$ compounds and their composites ($0.20 < x < 0.60$)," *Journal of Alloys and Compounds*, vol. 582, pp. 583–587, 2014.

[140] M. Wun-Fogle, J. Restorff, A. Clark, and J. Lindberg, "Magnetization and magnetostriction of dendritic [112] $Tb_xDy_yHo_zFe_{1.95}$ ($x+y+z = 1$) rods under compressive stress," *Journal of applied physics*, vol. 83, no. 11, pp. 7279–7281, 1998.

[141] J. Restorff, M. Wun-Fogle, and A. Clark, "Temperature and stress dependences of the magnetostriction in ternary and quaternary terfenol alloys," *Journal of Applied Physics*, vol. 87, no. 9, pp. 5786–5788, 2000.

[142] B. Wang, Y. Lv, G. Li, W. Huang, Y. Sun, and B. Cui, "The magnetostriction and its ratio to hysteresis for Tb-Dy-Ho-Fe alloys," *Journal of Applied Physics*, vol. 115, no. 17, p. 17A902, 2014.

[143] Z. Guo, S. Busbridge, Z. Zhang, X. Zhao, D. Geng, and B. Wang, "Microstructure, magnetic properties and spontaneous magnetostriction of $Tb_{0.2}Pr_{0.8}(Fe_{0.4}Co_{0.6})_x$," *IEEE transactions on magnetics*, vol. 36, pp. 3217–3218, Sept. 2000.

[144] B. W. Wang, S. L. Tang, X. M. Jin, L. Z. Cheng, and K. Y. He, "Microstructure and magnetostriction of $(Dy_{0.7}Tb_{0.3})_{1-x}Pr_xFe_{1.85}$ and $(Dy_{0.7}Tb_{0.3})_{0.7}Pr_{0.3}Fe_y$ alloys," *Applied Physics Letters*, vol. 69, no. 22, pp. 3429–3431, 1996.

[145] X. Zhao, J. Li, S. Liu, S. Ji, and K. Jia, "Magnetic properties and thermal stability of PrFe2 compound," *Journal of Alloys and Compounds*, vol. 258, no. 1, pp. 39–41, 1997.

[146] H. Yin and J. Liu, "Research progress of $MgCu_2$-type giant magnetostrictive materials with Pr," *Xiyou Jinshu Cailiao Yu Gongcheng/Rare Metal Materials and Engineering*, vol. 43, pp. 1275–1280, 05 2014.

[147] J. Du, J. Wang, C. Tang, Y. Li, G. Wu, and W. Zhan, "Magnetostriction in twin-free single crystals $Tb_yDy_{1-y}Fe_2$ with the addition of aluminum or manganese," *Applied physics letters*, vol. 72, no. 4, pp. 489–491, 1998.

[148] J. Liu, P. Zhongbin, X. Liu, Z. Zhang, X. Song, and W. Ren, "Large magnetostriction and direct experimental evidence for anisotropy compensation in $Tb_{0.4-x}Nd_xDy_{0.6}(Fe_{0.8}Co_{0.2})_{1.93}$ Laves compounds," *Materials Letters*, vol. 137, pp. 274–276, 12 2014.

[149] Z. J. Guo, S. C. Busbridge, B. W. Wang, Z. D. Zhang, and X. G. Zhao, "Structure and magnetic and magnetostrictive properties of $(Tb_{0.7}Dy_{0.3})_{0.7}Pr_{0.3}(Fe_{1-x}Co_x)_{1.85}$ ($0 < x < 0.6$)," *IEEE Transactions on Magnetics*, vol. 37, no. 4, pp. 3025–3027, 2001.

[150] X.-C. Li, Y.-T. Ding, and Y. Hu, "Effects of Zr addition on the microstructure and magnetostriction of the as cast $Tb_{0.3}Dy_{0.7}Fe_{1.95}$ alloys," *Gongneng Cailiao/Journal of Functional Materials*, vol. 42, pp. 2257–2260+2264, 12 2011.

[151] L. Xu, C. Jiang, and H. Xu, "Magnetostriction and electrical resistivity of Si doped $Tb_{0.3}Dy_{0.7}Fe_{1.95}$ oriented crystals," *Applied physics letters*, vol. 89, no. 19, p. 192507, 2006.

[152] D. Kim, O. Kwon, J. Kim, and Z. Lee, "Effect of oxygen impurity on magnetostriction of directionally solidified $Tb_{0.3}Dy_{0.7}Fe_{1.8}$," *Magnetics, IEEE Transactions on*, vol. 40, pp. 2781 – 2783, 08 2004.

[153] Y. dong Kwon, O. yeoul Kwon, M. chul Kim, and D. moon Wee, "Reaction of terfenol-d melts with SiO_2 crucibles," *Materials Science and Engineering: B*, vol. 129, no. 1, pp. 18–21, 2006.

[154] S. Fischer, M. Kelsch, and H. Kronmüller, "Optimization of magnetostriction, coercive field and magnetic transition temperature in nanocrystalline TbDyFe+ Zr/Nb multilayers," *Journal of magnetism and magnetic materials*, vol. 195, no. 3, pp. 545–554, 1999.

[155] Y. Yamashita, "Large electromechanical coupling factors in perovskite binary material system," *Japanese journal of applied physics*, vol. 33, no. 9S, p. 5328, 1994.

[156] W. Cao and L. E. Cross, "Theoretical model for the morphotropic phase boundary in lead zirconate–lead titanate solid solution," *Physical Review B*, vol. 47, no. 9, p. 4825, 1993.

[157] C.-C. Hu, T.-N. Yang, H.-B. Huang, J.-M. Hu, J.-J. Wang, Y.-G. Shi, D.-N. Shi, and L.-Q. Chen, "Phase-field simulation of domain structures and magnetostrictive response in $Tb_{1-x}Dy_xFe_2$ alloys near morphotropic phase boundary," *Applied Physics Letters*, vol. 108, no. 14, p. 141908, 2016.

[158] T. Ma, X. Liu, X. Pan, X. Li, Y. Jiang, M. Yan, H. Li, M. Fang, and X. Ren, "Local rhombohedral symmetry in $Tb_{0.3}Dy_{0.7}Fe_2$ near the morphotropic phase boundary," *Applied Physics Letters*, vol. 105, no. 19, p. 192407, 2014.

[159] C. Hu, Y. Shi, D. Shi, S. Tang, J. Fan, and Y. Du, "Anisotropy compensation and magnetostrictive properties in $Tb_xDy_{1-x}(Fe_{0.9}Mn_{0.1})_{1.93}$ Laves compounds: Experimental and theoretical analysis," *Journal of Applied Physics*, vol. 113, no. 20, p. 203906, 2013.

[160] C. Zhou, S. Ren, H. Bao, S. Yang, Y. Yao, Y. Ji, X. Ren, Y. Matsushita, Y. Katsuya, M. Tanaka, and K. Kobayashi, "Inverse effect of morphotropic phase boundary on the magnetostriction of ferromagnetic $Tb_{1-x}Gd_xCo_2$," *Phys. Rev. B*, vol. 89, p. 100101, Mar 2014.

[161] A. Devonshire, "Theory of ferroelectrics," *Advances in physics*, vol. 3, no. 10, pp. 85–130, 1954.

[162] P. K. Mukherjee, "Ferroelectric and antiferroelectric liquid crystals," in *Reference Module in Materials Science and Materials Engineering*, Elsevier, 2021.

[163] F. Craciun, "Dielectric, ferroelectric, antiferroelectric, relaxor, piezoelectric ceramics: Definitions and main applications," in *Reference Module in Materials Science and Materials Engineering*, Elsevier, 2020.

[164] S. Said, M. Sabri, and F. Salleh, "Ferroelectrics and their applications," in *Reference Module in Materials Science and Materials Engineering*, Elsevier, 2017.

[165] J. F. Ihlefeld, "Chapter 1 - fundamentals of ferroelectric and piezoelectric properties," in *Ferroelectricity in Doped Hafnium Oxide: Materials, Properties and Devices* (U. Schroeder, C. S. Hwang, and H. Funakubo, eds.), Woodhead Publishing Series in Electronic and Optical Materials, pp. 1–24, Woodhead Publishing, 2019.

[166] A. Chauhan, S. Patel, R. Vaish, and C. R. Bowen, "Anti-ferroelectric ceramics for high energy density capacitors," *Materials*, vol. 8, no. 12, pp. 8009–8031, 2015.

[167] Y. Liu, H. Aziguli, B. Zhang, W. Xu, W. Lu, J. Bernholc, and Q. Wang, "Ferroelectric polymers exhibiting behaviour reminiscent of a morphotropic phase boundary," *Nature*, vol. 562, no. 7725, pp. 96–100, 2018.

[168] G. Xu, H. Luo, H. Xu, and Z. Yin, "Third ferroelectric phase in pmnt single crystals near the morphotropic phase boundary composition," *Physical Review B*, vol. 64, no. 2, p. 020102, 2001.

[169] J. Walker, H. Simons, D. O. Alikin, A. P. Turygin, V. Y. Shur, A. L. Kholkin, H. Ursic, A. Bencan, B. Malic, V. Nagarajan, *et al.*, "Dual strain mechanisms in a lead-free morphotropic phase boundary ferroelectric," *Scientific reports*, vol. 6, no. 1, pp. 1–8, 2016.

[170] N. Zhang, H. Yokota, A. M. Glazer, Z. Ren, D. A. Keen, D. S. Keeble, P. A. Thomas, and Z. G. Ye, "The missing boundary in the phase diagram of $\mathrm{PbZr}_{1-x}\mathrm{Ti}_x\mathrm{O}_3$," *Nature Communications*, vol. 5, no. 1, p. 5231, 2014.

[171] C. Wu, X. Wang, and X. Yao, "Comparative study on the phase transitions in pzt-based ceramics by mechanical and dielectric analyses," *Ceramics International*, vol. 38, pp. S13–S16, 2012.

[172] S. Samanta, V. Sankaranarayanan, and K. Sethupathi, "Effect of successive multiple doping of La, Nb and Fe on structure and lattice vibration of MPB PZT," *Materials Today: Proceedings*, vol. 5, no. 14, pp. 27919–27927, 2018.

[173] T. Takenaka, K.-i. Maruyama, and K. Sakata, "$(\mathrm{Bi}_{0.5}\mathrm{Na}_{0.5})\mathrm{TiO}_3$-$\mathrm{BaTiO}_3$ system for lead-free piezoelectric ceramics," *Japanese journal of applied physics*, vol. 30, no. 9S, p. 2236, 1991.

[174] A. Sasaki, T. Chiba, Y. Mamiya, and E. Otsuki, "Dielectric and piezoelectric properties of $(\mathrm{Bi}_{0.5}\mathrm{Na}_{0.5})\mathrm{TiO}_3$ - $(\mathrm{Bi}_{0.5}\mathrm{K}_{0.5})\mathrm{TiO}_3$ Systems," *Japanese Journal of Applied Physics*, vol. 38, pp. 5564–5567, sep 1999.

[175] H. Nagata, M. Yoshida, Y. Makiuchi, and T. Takenaka, "Large piezoelectric constant and high curie temperature of lead-free piezoelectric ceramic ternary system based on bismuth sodium titanate-bismuth potassium titanate-barium titanate near the morphotropic phase boundary," *Japanese journal of applied physics*, vol. 42, no. 12R, p. 7401, 2003.

[176] T.-B. Xu, "Energy harvesting using piezoelectric materials in aerospace structures," in *Structural Health Monitoring (SHM) in Aerospace Structures*, pp. 175–212, Elsevier, 2016.

[177] K. Uchino, *Advanced Piezoelectric Materials: Science and Technology*. Woodhead Publishing Series in Electronic and Optical Materials, Elsevier Science, 2017.

[178] Y. Hiruma, K. Yoshii, R. Aoyagi, H. Nagata, and T. Takenaka, "Piezoelectric properties and depolarization temperatures of $(Bi_{0.5}Na_{0.5})TiO_3$ - $(Bi_{0.5}K_{0.5})TiO_3$ - $BaTiO_3$ lead-free piezoelectric ceramics," in *Key Engineering Materials*, vol. 320, pp. 23–26, Trans Tech Publ, 2006.

[179] Y. Hiruma, Y. Makiuchi, R. Aoyagi, H. Nagata, and T. Takenaka, "Lead-free piezoelectric ceramic based on $(Bi_{0.5}Na_{0.5})TiO_3$ - $(Bi_{0.5}K_{0.5})TiO_3$ - $BaTiO_3$ solid solution," *Ceramic transactions*, vol. 174, pp. 139–146, 2006.

[180] B. Noheda, J. A. Gonzalo, L. E. Cross, R. Guo, S.-E. Park, D. E. Cox, and G. Shirane, "Tetragonal-to-monoclinic phase transition in a ferroelectric perovskite: The structure of $PbZr_{0.52}Ti_{0.48}O_3$," *Phys. Rev. B*, vol. 61, pp. 8687–8695, Apr 2000.

[181] Y. Wang, D. Wang, G. Yuan, H. Ma, F. Xu, J. Li, D. Viehland, and P. M. Gehring, "Fragile morphotropic phase boundary and phase stability in the near-surface region of the relaxor ferroelectric $(1-x)\mathrm{Pb}(\mathrm{Zn}_{1/3}\mathrm{Nb}_{2/3})\mathrm{O}_3 - x\mathrm{PbTiO}_3$: [001] field-cooled phase diagrams," *Phys. Rev. B*, vol. 94, p. 174103, Nov 2016.

[182] R. S. Solanki, S. Mishra, Y. Kuroiwa, C. Moriyoshi, and D. Pandey, "Evidence for a tricritical point coinciding with the triple point in $(\mathrm{Pb}_{0.94}\mathrm{Sr}_{0.06})(\mathrm{Zr}_x\mathrm{Ti}_{1-x})\mathrm{O}_3$: A combined synchrotron x-ray diffraction, dielectric, and landau theory study," *Physical Review B*, vol. 88, no. 18, p. 184109, 2013.

[183] B. Noheda, J. A. Gonzalo, R. Guo, S.-E. Park, L. E. Cross, D. E. Cox, and G. Shirane, "The monoclinic phase in pzt: New light on morphotropic phase boundaries," *AIP Conference Proceedings*, vol. 535, no. 1, pp. 304–313, 2000.

[184] P. Marton, I. Rychetsky, and J. Hlinka, "Domain walls of ferroelectric $BaTiO_3$ within the Ginzburg-Landau-Devonshire phenomenological model," *Physical Review B*, vol. 81, 01 2010.

[185] H.-Y. Ye, J.-Z. Ge, Y.-Y. Tang, P.-F. Li, Y. Zhang, Y.-M. You, and R.-G. Xiong, "Molecular ferroelectric with most equivalent polarization directions induced by the plastic phase transition," *Journal of the American Chemical Society*, vol. 138, pp. 13175–13178, 10 2016.

[186] A. Kumar, A. K. Kalyani, R. Ranjan, K. J. Raju, J. Ryu, N. Park, and A. James, "Evidence of monoclinic phase and its variation with temperature at morphotropic phase boundary of plzt ceramics," *Journal of Alloys and Compounds*, vol. 816, p. 152613, 2020.

[187] C. Wieser, A. Walnsch, W. Hügel, and A. Leineweber, "The monoclinic lattice distortion of η-Cu_6Sn_5," *Journal of Alloys and Compounds*, vol. 794, pp. 491–500, 2019.

[188] S. Gorfman, D. S. Keeble, A. M. Glazer, X. Long, Y. Xie, Z.-G. Ye, S. Collins, and P. A. Thomas, "High-resolution x-ray diffraction study of single crystals of lead zirconate titanate," *Phys. Rev. B*, vol. 84, p. 020102, Jul 2011.

[189] S. K. Mishra, D. Pandey, and A. P. Singh, "Effect of phase coexistence at morphotropic phase boundary on the properties of $Pb(Zr_xTi_{1-x})O_3$ ceramics," *Applied Physics Letters*, vol. 69, no. 12, pp. 1707–1709, 1996.

[190] Y. Zhang, D. Xue, H. Wu, X. Ding, T. Lookman, and X. Ren, "Adaptive ferroelectric state at morphotropic phase boundary: Coexisting tetragonal and rhombohedral phases," *Acta Materialia*, vol. 71, pp. 176–184, 2014.

[191] X. Q. Ke, D. Wang, X. Ren, and Y. Wang, "Formation of monoclinic nanodomains at the morphotropic phase boundary of ferroelectric systems," *Phys. Rev. B*, vol. 88, p. 214105, Dec 2013.

[192] R. E. Newnham, "Phase Transformations in Smart Materials," *Acta Crystallographica Section A*, vol. 54, pp. 729–737, Nov 1998.

[193] E. du Tremolet DeLacheisserie, *Magnetostriction Theory and Applications of Magnetoelasticity.* CRC-Press, 1993.

[194] M. Brooks, L. Nordström, and B. Johansson, "Rare-earth transition-metal intermetallics," *Physica B: Condensed Matter*, vol. 172, no. 1, pp. 95–100, 1991.

[195] M. Adil, S. Yang, M. Mi, C. Zhou, J. Wang, R. Zhang, X. Liao, Y. Wang, X. Ren, X. Song, and Y. Ren, "Morphotropic phase boundary and magnetoelastic behaviour in ferromagnetic $Tb_{1-x}Gd_xFe_2$ system," *Applied Physics Letters*, vol. 106, no. 13, p. 132403, 2015.

[196] T. Leist, T. Granzow, W. Jo, and J. Rödel, "Effect of tetragonal distortion on ferroelectric domain switching: A case study on La-doped $BiFeO_3$–$PbTiO_3$ ceramics," *Journal of Applied Physics*, vol. 108, no. 1, p. 014103, 2010.

[197] A. Murtaza, S. Yang, M. T. Khan, A. Ghani, C. Zhou, and X. Song, "Temperature dependent magnetization and coercivity in morphotropic phase boundary involved ferromagnetic $Tb_{1-x}Gd_xFe_2$ system," *Materials Chemistry and Physics*, vol. 217, pp. 278–284, 2018.

[198] A. Murtaza, S. Yang, C. Zhou, T. Chang, K. Chen, F. Tian, X. Song, M. R. Suchomel, and Y. Ren, "Anomalous magnetoelastic behaviour near morphotropic

phase boundary in ferromagnetic $Tb_{1-x}Nd_xCo_2$ system," *Applied Physics Letters*, vol. 109, no. 5, p. 052904, 2016.

[199] S. Wei, S. Yang, D. Wang, X. Song, X. Ke, Y. Gao, X. Liao, and Y. Wang, "Monte carlo simulation of magnetic domain structure and magnetic properties near the morphotropic phase boundary," *Phys. Chem. Chem. Phys.*, vol. 19, pp. 7236–7244, 2017.

[200] U. Atzmony, M. P. Dariel, E. R. Bauminger, D. Lebenbaum, I. Nowik, and S. Ofer, "Spin-orientation diagrams and magnetic anisotropy of rare-earth-iron ternary cubic laves compounds," *Phys. Rev. B*, vol. 7, pp. 4220–4232, May 1973.

[201] R. L. Owen, J. Juanhuix, and M. Fuchs, "Current advances in synchrotron radiation instrumentation for mx experiments," *Archives of Biochemistry and Biophysics*, vol. 602, pp. 21–31, 2016. Protein Crystallography.

[202] T. Mason, "Neutron scattering studies of spin fluctuations in high-temperature superconductors," *Handbook on the Physics and Chemistry of Rare Earths*, vol. 31, pp. 281–314, 2001.

[203] M. R. Johnson and G. J. Kearley, "Chapter 6 - dynamics of atoms and molecules," in *Neutron Scattering – Fundamentals* (F. Fernandez-Alonso and D. L. Price, eds.), vol. 44 of *Experimental Methods in the Physical Sciences*, pp. 415–469, Academic Press, 2013.

[204] S. W. Lovesey, *Theory of neutron scattering from condensed matter.* United Kingdom: Clarendon Press, 1984.

[205] S. M. Yusuf and A. Kumar, "Neutron scattering of advanced magnetic materials," *Applied Physics Reviews*, vol. 4, no. 3, p. 031303, 2017.

[206] "`https://www.ill.eu/users/instruments/instruments-list/d11/description/instrument-layout`." [Online; accessed 2021-07-19].

[207] I. Bailey, "A review of sample environments in neutron scattering," *Zeitschrift für Kristallographie-Crystalline Materials*, vol. 218, no. 2, pp. 84–95, 2003.

[208] "`https://www.ill.eu/users/support-labs-infrastructure/software-scientific-tools/grasp`." [Online; accessed 2021-07-19].

[209] V. I. Iveronova and G. P. Revkevich, "Theory of X-ray scattering /2nd revised and enlarged edition/," *Moscow Izdatel Moskovskogo Universiteta Pt*, Jan. 1978.

[210] "`https://www.esrf.eu/id22`." [Online; accessed 2021-07-19].

[211] MATLAB, *version 7.10.0 (R2010a).* Natick, Massachusetts: The MathWorks Inc., 2010.

[212] G. Pagnini and R. Saxena, "A note on the voigt profile function," *arXiv preprint arXiv:0805.2274*, 2008.

[213] T. Ida, M. Ando, and H. Toraya, "Extended pseudo-voigt function for approximating the voigt profile," *Journal of Applied Crystallography*, vol. 33, no. 6, pp. 1311–1316, 2000.